Imperial College of Science, Technology and Medicine
Department of Materials

Optical characterisation of diamonds and simulations for maser and quantum devices

Yongqiang Wen

Submitted in part fulfilment of the requirements for the degree of
Doctor of Philosophy in Materials of Imperial College London

Abstract

Quantum technology has revolutionised academia and industry by potentially solving many problems that are not feasible and accessible for conventional technology. Quantum materials like colour centres in diamonds are a promising quantum technology platform in research and industry. Herein, the development of the room-temperature diamond maser as a quantum device for oscillators and low noise amplifiers is presented. This thesis investigates both experimental and analytical research in characterising diamonds, mainly Nitrogen-Vacancy (NV) centres, for masing and maser devices, as well as theoretical and simulation work in designing masers and threshold conditions. Besides the research specifically into the maser, optical characterisation of these quantum materials is conducted. This thesis primarily focuses on the maser, but the defect centres characterised have wider use in quantum technology. To push forward the analytical methods for diamond optical characterisation, this thesis employs multiple algorithms in fluorescence lifetime imaging that improve the performance of conventional methods. Furthermore, a hybrid quantum algorithm is employed to aid the analysis of optical data, which utilises unconventional quantum properties of quantum circuits and simulators to analyse quantum materials for developing quantum devices.

Acknowledgements

I would like to express my genuine gratitude to my supervisors, Daan Arroo and Neil Alford, for their invaluable support and guidance during my PhD study. I also wish to thank the department for the funding opportunity to support my living. I also thank my previous supervisor, Jon Breeze, who introduced me to the subject of maser and his guidance in the first year of my Ph.D. I would like to thank Daniel Jones for building the early version of the optical system. I would like to thank Phil Diggle for building the later version of the optical system and for a lot of guidance in diamond and optics with his extensive knowledge and patience. I would like to thank Wern Ng for helping me with electronics and microwave engineering, as well as constructing masers and his experimental data. I would also like to thank Despina for helping me in the lab and setting up maser experiments.

I would like to thank Mark Oxborrow for his advice and knowledge in maser and microwave engineering, as well as COMSOL simulations. I would like to thank Norbert Klein for the usage of CST software. I would like to thank Louis Chen for discussing interesting research topics and collaborations. I want to thank Max and Michael for sharing many ideas in masers. I would like to thank Mike Lennon for his stunning work in making cavities. I would also like to thank Element Six for providing diamond samples. I also want to thank Irena who helped me at the Spin-LAB and the use of electromagnet. I would like to thank the Imperial College HPC facility for allowing me to use the computational resources for my thesis. I would like to thanks my family for supporting me and my girlfriend, Yan for her countless supports. I profusely thank my friends, Peter, Yuxuan, and many others, in London.

Dedication

Dedicated to all those who have provided unwavering support.

'I think that modern physics has definitely decided in favor of Plato. In fact the smallest units of matter are not physical objects in the ordinary sense; they are forms, ideas which can be expressed unambiguously only in mathematical language.'

Werner Heisenberg

Declaration

I declare that the work is done by the author, and the collaborative works are indicated in the text.

The copyright of this thesis rests with the author. Unless otherwise indicated, its contents are licensed under a Creative Commons Attribution-NonCommercial 4.0 International Licence (CC BY-NC).

Under this licence, you may copy and redistribute the material in any medium or format. You may also create and distribute modified versions of the work. This is on the condition that: you credit the author and do not use it, or any derivative works, for a commercial purpose.

When reusing or sharing this work, ensure you make the licence terms clear to others by naming the licence and linking to the licence text. Where a work has been adapted, you should indicate that the work has been changed and describe those changes. Please seek permission from the copyright holder for uses of this work that are not included in this licence or permitted under UK Copyright Law.

Contents

Abstract **i**

Acknowledgements **iii**

1 Introduction **1**

1.1 Motivation and objectives 1

1.2 Overview 3

1.3 Statement of originality 4

2 Background Theory **6**

2.1 Maser 6

2.1.1 Gaseous maser 7

2.1.2 Solid-state maser 9

2.1.3 Room temperature maser 10

2.1.4 Working principle 11

2.2 Dielectric resonator 19

2.3 Microwave system charaterisation 25

2.4 Microstrip antenna 27

2.5 Diamond 29

2.5.1 Defects in diamond 30

2.5.2 Diamond synthesis process 32

2.5.3 NV centre properties 33

3 Experimental Methods and Apparatus **38**

3.1 Optical characterisation methods 38

3.1.1 Scanning laser confocal microscope 39

3.1.2 Fluorescence lifetime imaging 42

3.1.3 ODMR 44

3.1.4 Spin lattice relaxation time imaging 45

3.2 Optical characterisation setup 45

3.2.1 CW-laser section 47

3.2.2 Supercontinuum laser section 51

3.2.3 Sample stage and detection section 51

3.2.4 Apparatus specifications 54

3.3 Maser 64

3.3.1 Dielectric resonator and cavity 64

3.3.2 DC magnetic field characterisations 77

3.3.3 Diamond maser 80

4 Optical Characterisation Results **83**

4.1 Samples 83

4.2 Fluorescence lifetime imaging of diamond samples for maser 86

4.2.1 Random search for lifetime components and phasor method for diamond 100

4.2.2 Deep learning for defects in diamonds 116

4.3 Spin-lattice relaxation time imaging of diamond samples 130

4.4 ODMR 132

4.5 Conclusion 134

5 Modelling Methods and Simulations 135

5.1 Extended rate equations simulation of spin dynamics and ODMR of NV^- 135

5.2 Exploring the Spin Dynamics of a Room-Temperature Diamond Maser using an Extended Rate Equation Model 144

5.2.1 Introduction 144

5.2.2 Theoretical model 147

5.2.3 Maser simulation 149

5.2.4 Conclusion 161

6 Maser Results 163

6.1 Diamond based maser 163

6.1.1 Bruker magnet-based system 163

6.1.2 GMW based system 170

6.2 Conclusion 177

7 Conclusion 178

7.1 Summary of Thesis Achievements 178

7.2 Future Work 180

A Appendix **185**

A.1

Hybrid quantum transfer learning for phasor analysis 185

A.2

Fluorescence lifetime results 189

A.3

Phasor analysis 201

A.4

Halbach array PSO optimisation and experimental field characterisation 204

Bibliography **215**

List of Tables

3.1 A list of dielectric constant and dielectric loss of various dielectric materials. . . 75

3.2 A summary of the performance of different dielectric resonators. 75

4.1 A table of the four-diamond samples used in this thesis. The [NV^-] concentration is not rigorously determined in this thesis, the concentration of the NID_{02} and D09 are quantified by EPR measurements, not included in this thesis. 84

4.2 A summary of lifetime measurement at 532 nm based on the least square method. 99

4.3 A Tukey's Honestly Significant Difference test of the four samples. It shows the difference in mean between any two samples and the upper bound and lower bound of the 95% CI and the P value. It shows that there is statistical significance of the τ_1 values between the samples except for the 10BB and NID_{02}. It confirms that there is a positive correlation among the thin sample. 99

4.4 A summary of lifetime measurement at 532 nm based on the phasor method using global binning. 105

4.5 A summary of lifetime measurement at 532 nm based on the random search method. 108

4.6 A summary of lifetime measurement at 532 nm based on the deep learning method.118

4.7 A summary of lifetime measurement at 532 nm based on the phasor method. . . 128

4.8 A summary of lifetime measurement at 532 nm based on the phasor method. . . 128

5.1 Transition rates used to describe the time evolution of the ensemble of NV^- centres in a cavity to produce the results presented in Figures 3-8. The values are based on experimental results from Ref. [1]. 146

5.2 Variable parameters used in the rate equations to describe the time evolution of the ensemble of NV^- centres in a cavity. The number of available NV^-, the maser frequency, ω, the dephasing time, T_2^* and the Q factor is from [2]. The V_m and η are obtained in a CST MICROWAVE STUDIO simulation. The Δ_l is the detuning in frequency between the 532 nm excitation laser and the zero phonon line at 637 nm and Ω_L is the estimated pump strength at 400 mW of excitation power. 151

5.3 Definition of the three masing regimes using the number of photons and the logarithm gradient. 159

6.1 A summary of maser performance of NID_{02} sample in the Bruker electromagnet. 165

6.2 A summary of maser performance of NID_{02} sample in the Bruker electromagnet. 176

A.1 A summary of Halbach array simulations. 215

List of Figures

2.1 The E and B fields of the $TE_{01\delta}$ mode in a cylindrical dielectric resonator. . . . 24

2.2 (a) The diamond lattice unit cell. The carbon atoms are represented by the black sphere. (b)The NV centre in a diamond lattice unit cell. The carbon atoms are represented by the black spheres, the vacancy is in purple and the nitrogen atom is in cyan. 31

2.3 The SiV centre in a diamond lattice unit cell. The carbon atoms are represented by the black spheres, the vacancy is in purple and the silicon atom is in brown. . 32

2.4 The energy levels of the NV centre. NV^-: The triplet states are on the left, showing the 532 nm excitation and the 637 nm zero-phonon line. The spin-conserving intersystem crossing to the singlet states on the right, shown in the dotted lines. NV^0: The doublet ground state, the excited state and the metastable state. . . . 35

3.1 This diagram shows the confocal microscope setup. 41

3.2 A schematic diagram of the optical confocal microscope with MW, pulse control using the pulse streamer and the time tagger for counting signal from the detectors. 46

3.3 This diagram shows the experimental setup with the 532 nm laser in operation. 49

3.4 This diagram shows the experimental setup with the supercontinuum laser in operation. 50

3.5 This diagram shows the ODMR experimental setup with a cylindrical permanent magnet container and three motorised stages. A magnet can be loaded on or off to do ODMR with or without a magnetic field. The black curves with arrows on both ends indicate the motion of the motors. The motorised states provide movements so that the magnet can align to the sample with the desired angles and radial distance. 52

3.6 The spectral information of the output beam is obtained using the Andor Kymera 328i spectrometer. 53

3.7 The S_{11} of the microstrip antenna, where R = 7 mm, g = 0.1 mm, s = 3.9 mm and r = 0.5 mm. 60

3.8 (a)The tangential H field of the microstrip antenna at 2.87 GHz, where R = 7 mm, g = 0.1 mm, g = 3.9 mm and r = 0.5 mm. (b)The cross-sectional view of the tangential H field of the microstrip antenna at 2.87 GHz, where R = 7 mm, g= 0.1 mm, g = 3.9 mm and r = 0.5 mm. The colour scale indicates the strength of the magnetic field. 61

3.9 The cross-sectional view of the tangential H field of the microstrip antenna at 2.87 GHz, where R = 7 mm, g = 0.1 mm, g = 3.9 mm and r = 0.5 mm. 61

3.10 (a)The microstrip antenna has a resonant frequency of 2.87 GHz. The diameter of the circular antenna is R = 7 mm. The diameter, r, of the small hole, is 0.5 mm. The width of the gap, g, is 0.2 mm and the length, s, is 3.9 mm. (b)The manufactured microstrip antenna used in this thesis. 62

3.11 The S12 of the design cavity and resonator, the results are averaged based on 128 measurements. The loaded Q is above 35,576. 66

3.12 The 3D H field the E field of the $TE_{01\delta}$ mode, which is computed using the eigenmode method in CST, in a sapphire cylindrical dielectric resonator, inner diameter of 5 mm, outer diameter of 10 mm, height of 6 mm, on a quartz post in a copper cavity, inner diameter of 31 mm. 68

3.13 Top: The E field. Bottom: the H field of the $TE_{01\delta}$ mode, which is computed using the eigenmode method in CST, in a sapphire cylindrical dielectric resonator, inner diameter of 5 mm, outer diameter of 10 mm, height of 6 mm, on a quartz post in a copper cavity, inner diameter of 31 mm. 69

3.14 These figures show the relation of the inner radius of the sapphire resonator and the Q factor and the mode volume. The last subfigure shows the plot of the inner diameter of the copper cavity against the unloaded Q factor. It is shown that at 31 mm, the Q factor is optimised, provided that the outer diameter of the sapphire resonator is 10 mm. 70

3.15 The drawings for the "coffee cup" design. This is designed for diamond maser using the EPR electromagnet. 71

3.16 The drawings for the GMW cavity design. This is designed for diamond maser using the GMW electromagnet. 71

3.17 (a) The electric field profile of the $TEM_{01\delta}$ of the sapphire resonator shown in logarithmic scale. (b) The magnetic field profile of the $TEM_{01\delta}$ of the sapphire resonator shown in logarithmic scale. 73

3.18 The magnetic field profile of the $TEM_{01\delta}$ of the (a) Rutile (b) BMT (c) Rutile with a thicker wall (d) BZT. 74

3.19 The field reading of the teslameter at a stationary point in a magnetic field. . . 78

3.20 The magnetic field map of the GMW electromagnet, the field difference is too small to be detected by the teslameter. 79

3.21 A schematic diagram of the diamond maser with the GMW electromagnet. The diamond inside a dielectric resonator and a copper cavity are fitted inside the pole pieces of the electromagnet. The output signal is detected by the spectrum analyser and the VNA, which can be used to check the resonance of the resonator before masing. The switch is used to select which detector to be used. 81

3.22 A schematic diagram of the diamond maser with the GMW electromagnet. The diamond inside a dielectric resonator and a copper cavity are fitted inside the pole pieces of the electromagnet. The output signal is detected by the spectrum analyser and the VNA, which can be used to check the resonance of the resonator before masing. The switch is used to select which detector to be used. 82

4.1 The image of the samples (a) D09 (b) 10BA (c) 10BB (d) NID_{02}. 85

4.2 The fluorescence lifetime decay profile using the least square method to analyse the sample D09 at 532 nm excitation. The dots are the data and the red curve is the fit. 88

4.3 The fluorescence lifetime map using the least square method to analyse the sample D09 at 532 nm excitation. The subfigures show the integrated decay intensity which is the fluorescence mapping. The first and the second-lifetime components, τ_1 and τ_2, and the reduced χ^2 mapping and the amplitude, A_1 and A_2, of the first and the second components respectively. 89

4.4 The fluorescence lifetime map using the least square method to analyse the sample D09 at 502 nm excitation. The subfigures show the integrated decay intensity which is the fluorescence mapping. The first and the second-lifetime components, τ_1 and τ_2, and the reduced χ^2 mapping and the amplitude, A_1 and A_2, of the first and the second components respectively. 90

4.5 The fluorescence lifetime map using the least square method to analyse the sample D09 at 592 nm excitation. The subfigures show the integrated decay intensity which is the fluorescence mapping. The first and the second lifetime components, τ_1 and τ_2, and the reduced χ^2 mapping and the amplitude, A_1 and A_2, of the first and the second components respectively. 91

4.6 The fluorescence lifetime map using the least square method to analyse the sample D09 at 402 nm excitation. The subfigures show the integrated decay intensity which is the fluorescence mapping. The first and the second-lifetime components, τ_1 and τ_2, and the reduced χ^2 mapping and the amplitude, A_1 and A_2, of the first and the second components respectively. 92

4.7 The image shows the pixel where NV^- is dominant over NV^0 under (a) 532 nm, (b) 502 nm and (c) 592 nm excitation. 93

4.8 The plots show the mean and the dispersion of τ_1 and τ_2 of D09 sample with various excitation wavelengths. 94

4.9 The plots show the mean and the dispersion of τ_1 and τ_2 of the four samples. From the upper plot, there is a positive correlation with the concentration and the τ_1 among the thin samples. 98

4.10 The plots show the phasor-transformed data point as a green dot and the red dots show the corresponding lifetime components on the circle. (a) Mono-exponential. (b) Bi-exponential (c) Tri-exponential. (d) Tetra-exponential. 101

4.11 The phasor diagram of the 10BA sample, (a) for 532 nm, (c) for 502 nm, (e) for 562 nm and the angular histograms of the 10BA sample (b) for the 532 nm, (d) for the 502 nm and (f) for the 562 nm. 103

4.12 (a) The plots show the phasor-transformed data point from sample D09, with an excitation of a range of excitation wavelengths. (b) The plots show the phasor-transformed data point from sample D09, with an excitation of a range of depths from the top surface from 6.57 mm at 532 nm excitation. 105

4.13 The plots show the blind determination in phasor space data point as a green dot and the red dots show the corresponding lifetime components on the circle. The cyan line and the cyan dots are the second harmonics of the corresponding lifetime components. The dark blue dot is the second harmonic of the data point. d is the distance between the second harmonics of the line and the data point. (a) Initial guess of the lifetime components (b) Second harmonic of the initial guess (c) The ideal lifetime components (d) Second harmonic of the ideal lifetime components that the line perfectly intercepts the data point. 107

4.14 The plots show the lifetime component imaging of the D09 sample using the random search method. 109

4.15 The plots show the lifetime component imaging of the NID_{02} sample using the random search method. 110

4.16 The plots show the lifetime component imaging of the 10BA sample using the random search method. 111

4.17 The plots show the lifetime component imaging of the 10BB sample using the random search method. 112

4.18 The plots show the mean and the dispersion of τ_1 and τ_2 of the D09 sample using the random search method. By varying the wavelength, the distribution varies from a uniform distribution to a transition, where it is similar to a normal distribution with a long tail at one end to a bimodal distribution. The distribution is opposite in direction between the τ_1 and τ_2. 113

4.19 The plots show the lifetime components distribution in the pixel level of the 4 samples using the random search method. 114

4.20 The image shows the flow chart of training and inferring the fluorescence lifetime imaging data. The architecture of the model is made of a main branch that consists of 3D CNN layers that extract the features on both the spatial and the temporal domain and 2D CNN layers. The main branch is separated into small branches for each parameter. 119

4.21 (a) The image shows the percentage errors of the trained model for a non-existent lifetime component. (b) The histogram shows the percentage errors of the trained model for a non-existent lifetime component. 120

4.22 The images show the lifetime components of the trained model for D09 sample at 592 nm. 120

4.23 The images show the lifetime components predicted and reconstructed using the trained model for NID_{02} sample at 532 nm. 121

4.24 The images show the lifetime components predicted and reconstructed using the trained model for 10BA sample at 532 nm. 122

4.25 The images show the lifetime components predicted and reconstructed using the trained model for 10BB sample at 532 nm. 123

4.26 The distribution of the lifetimes and the amplitudes: (a) τ_1 and τ_2 and (b) A_1 and A_2, of the four samples using the deep learning method. 124

4.27 The distribution of the lifetimes and the amplitudes: (a) τ_1 and τ_2 and (b) A_1 and A_2, of the d09 sample excited with 7 difference excitation wavelengths using the deep learning method. 124

4.28 GT1. The image shows the predicted values of τ_1 and τ_2 (a), A_1 and A_2 (c), using four different analyses and the ground truth value as a black line and the shaded area represents the standard deviation. The pixel difference between the predicted values and the ground truth values,(b)τ_1 and τ_2 (d) A_1 and A_2. . . . 125

4.29 GT2. The image shows the predicted values of τ_1 and τ_2 (a), A_1 and A_2 (c), using four different analyses and the ground truth value as a black line and the shaded area represents the standard deviation. The pixel difference between the predicted values and the ground truth values,(b)τ_1 and τ_2 (d) A_1 and A_2. . . . 126

4.30 The plots show the T_1 lifetime imaging of NID_{02} sample. The step size is 50 μm. 130

4.31 The plots show the T_1 lifetime imaging of 10BA sample. The X and Y are the steps. The step size is 100 μm. 131

4.32 The plots show the CW-ODMR of the sample 10BB at 532 nm excitation and with various optical power. 132

4.33 The plots show the CW-ODMR of the sample 10BB at 532 nm excitation and with a magnetic field aligned to one of the NV axes. 133

4.34 The plots show the pulsed-ODMR of the sample 10BA at 532 nm excitation. . 133

5.1 This diagram shows the energy levels, decay rate and pumping rate of the 7-level model. 139

5.2 (a) Optical pumping of the 7-level system. 140

5.3 This diagram showing the population oscillates between the m=0 and m=$\pm$1 states when the Ω_m=4 MHz and the dephasing γ_m is zero. The π pulse has a duration, τ_π, of 786 ns which agrees with $\tau_\pi = \pi/\Omega_m$. 141

5.4 (a) This diagram showing the CW-ODMR spectrum when the Ω_m=4 MHz, Ω_l=1 MHz without any magnetic field. The spectrum is fitted using a Voigt function. The spectrum is almost a Lorentzian. The linewidth is about 6.39 MHz. (b) This diagram shows the MW power broadening of the CW-ODMR spectrum when the Ω_m=12 MHz, Ω_l=1 MHz without any magnetic field. The spectrum is fitted using a Voigt function. The broadened spectrum is more Gaussian. (c) This diagram showing the CW-ODMR spectrum when the Ω_m=4 MHz, Ω_l=4 MHz without any magnetic field. The spectrum is fitted using a Voigt function. The linewidth is narrower and the Lorentzian is more significant. (d) This diagram shows the inhomogeneous broadening of the power broadened CW-ODMR spectrum when the Ω_m=12 MHz, Ω_l=1 MHz. The spectrum is the combination of five NV centres sub-species that experience a slightly different magnetic field. The spectrum is fitted using a Voigt function. The broadened spectrum is more Gaussian. 142

5.5 (a) This diagram showing the CW-ODMR spectrum when the Ω_m=4 MHz, Ω_l=1 MHz. The magnetic field is 0.5 mT. The spectrum is fitted using two Voigt functions. (b) This diagram shows the MW power broadening of the CW-ODMR spectrum when the Ω_m=12 MHz, Ω_l=1 MHz. The magnetic field is 0.5 mT. The spectrum is fitted using two Voigt functions. (c) This diagram showing the pulsed ODMR spectrum when the system is polaried by Ω_l=1 MHz laser for 100 μs, then a π pulse, Ω_m=4 MHz, for 0.786 μs, without any magnetic field, and a final readout by a Ω_l=1 MHz laser for 10 μs. The spectrum is fitted using a Voigt function. The spectrum is almost a Lorentzian. The linewidth is about 3.06 MHz. (d) This diagram shows the pulsed ODMR spectrum when the system is polarised by Ω_l=1 MHz laser for 100 μs, then a π pulse, Ω_m=4 MHz, for 0.786 μs, with a 0.5 mT magnetic field, and a final readout by a Ω_l=1 MHz laser for 10 μs. The spectrum is fitted using a Voigt function. The spectrum is almost a Lorentzian. The linewidth is about 3.06 MHz. 143

5.6 This NV^- energy level diagram indicating pumping and decay rates of the 7-level model with excited phonon bands shown by the grey area in levels $|4\rangle$, $|5\rangle$ and $|6\rangle$. Here, the green dashed line represents the energy of the excitation wavelength (532 nm, 2.33 eV) promoting population to the phonon bands, whereas the green solid line is the transition represented by the pump strength Ω_L. Decay rates are indicated by κ_{ij} (the values for these rates used to generate our results are provided in Table 1) for the decay from the initial electronic state i to the new state j, $\gamma\hbar B$ is the Zeeman splitting, W_{st} and W_{sp} is the stimulated emission rate and the spontaneous emission rate. Non-radiative decays are also shown to, and from, $|7\rangle$ where the bold line denotes the faster decay rate. Reproduced from AIP Publishing [3]. 145

5.7 The energy density of the magnetic field of the $TE_{01\delta}$ mode of a cylindrical copper cavity simulated using CST MICROWAVE STUDIO. The solid white outlines show the boundaries of a sapphire resonator and post and the dashed white outlines the inner boundaries. The walls of the copper cavity are shown as the enclosure that bounds the image. Reproduced from AIP Publishing [3]. . 152

5.8 The steady-state number of photons as a function of the cavity Q factor. The photon number shows threshold behaviour with respect to the Q factor, with the onset of masing at around $Q = 29000$ for the parameters listed in Table 5.1. The inset shows the onset on a logarithmic scale. Reproduced from AIP Publishing [3]153

5.9 The steady-state number of photons as a function of the optical pump power. For the parameters listed in Table 5.1, the threshold pump power is about 370 mW. Reproduced from AIP Publishing [3]. 154

5.10 The steady-state number of microwave photons as a function of the cavity mode volume for the parameters listed in Table 5.1. The masing threshold occurs at a mode volume of about 0.26 cm^3. The inset shows the onset on a logarithmic scale. Reproduced from AIP Publishing [3] 155

5.11 The steady-state microwave photon number as a function of the optical pump strength and the loaded cavity Q factor. It is possible to identify a masing action regime, a no masing regime and an intermediate "incipient masing" regime in which stimulated emission dominates spontaneous emission, but the maser cannot achieve self-sustaining oscillations. At all pump strengths, the photon number increases monotonically with the Q-factor as expected. Reproduced from AIP Publishing [3] 156

5.12 The log gradient map of Figure 5.11 shows the incipient masing regime, where the increase of number of photons with respect to the change in Q factor and the pump power is significant, on the order of 1 or more, the number of photons is moderate. In the no masing regime on the bottom and left, both the number of photons and the log gradient is low. In the masing regime on the top right, the number of photons is high but the log gradient is low. 157

5.13 The number of microwave photons in the cavity as a function of the filling factor, defined by Eq. 4. The number of photons becomes saturated above $\eta = 0.3$. The inset shows the onset of masing at a filling factor of 0.03. Reproduced from AIP Publishing [3]. 158

6.1 The maser signal of the left peak (a), middle peak (b) and the right peak(c) from the NID_{02} sample were measured in the spectrum analyser. (d) is the S_{11} of the maser resonator. 167

6.2 The distribution of (a) the maximum power, (b) the 3 dB width and (c) the frequency of data taken from the traces of the NID_{02} sample using the Bruker electromagnet with various optical pump powers. 168

6.3 The maser signal of the left peak (a) middle peak accumulated traces (b) the 3D histogram of the maximum power and the frequency (c) the autocorrelation of the frequency and the amplitude (maximum power) of the traces as a time series and (d) is the frequency against the maximum power from the D09 sample were measured in the spectrum analyser. 169

6.4 The accumulated maser signals were collected for 10 seconds, containing 325 traces, on a GMW electromagnet at 4.0 V laser power. (a) the left peak, (b) the middle peak, (c) the right peak. (d) The accumulated maser signals were collected for 10 seconds, containing 325 traces, on a GMW electromagnet at 1.2 V laser power of the middle peak. 172

6.5 The maser signal of the left peak (a) the accumulated traces, showing the jitter during a 10 s measurement. (b) the positions of each peak in the frequency spectrum. (c) 3D histogram of the maximum power and the counts of the peak in the frequency spectrum. (d) the histogram of maximum power. 173

6.6 The autocorrelation of maser signals was collected for 10 seconds, containing 325 traces, on a GMW electromagnet at 4.0 V laser power. 174

6.7 The distribution of (a) the maximum power, (b) the 3 dB width and (c) the frequency of data taken from the traces of the D09 sample using the GMW electromagnet with various optical pump powers. 175

A.1 The architecture of the hybrid classical-quantum classifier for phasor analysis. The knowledge of the generic phasor network can be transferred to a diamond defect network containing a trainable quantum layer at the end to predict the results. The generic phasor network has the knowledge of various lifetime components, whereas the diamond defects network only have the knowledge of the lifetime components specific to the diamond. 187

A.2 The image shows the generated data from bi-exponential and tri-exponential functions with labels. 187

A.3 (a) The image shows the predicted class for the NID_{02} diamond sample under 532 nm excitation. (b) The image shows the predicted class for the D09 diamond sample under 532 nm excitation. (c) The image shows the predicted class for the 10BA diamond sample under 532 nm excitation. (d) The image shows the predicted class for the 10BB diamond sample under 532 nm excitation. 188

A.4 The fluorescence lifetime mapping using the least square method to analyse the sample 10BA at 532 nm excitation. The subfigures show the integrated decay intensity which is the fluorescence mapping. The first and the second lifetime components, τ_1 and τ_2, and the reduced χ^2 mapping and the amplitude, A_1 and A_2, of the first and the second components respectively. 190

A.5 The fluorescence lifetime mapping using the least square method to analyse the sample 10BA at 502 nm excitation. The subfigures show the integrated decay intensity which is the fluorescence mapping. The first and the second lifetime components, τ_1 and τ_2, and the reduced χ^2 mapping and the amplitude, A_1 and A_2, of the first and the second components respectively. 191

A.6 The fluorescence lifetime mapping using the least square method to analyse the sample 10BA at 562 nm excitation. The subfigures show the integrated decay intensity which is the fluorescence mapping. The first and the second lifetime components, τ_1 and τ_2, and the reduced χ^2 mapping and the amplitude, A_1 and A_2, of the first and the second components respectively. 192

A.7 The fluorescence lifetime mapping using the least square method to analyse the sample 10BB at 532 nm excitation. The subfigures show the integrated decay intensity which is the fluorescence mapping. The first and the second lifetime components, τ_1 and τ_2, and the reduced χ^2 mapping and the amplitude, A_1 and A_2, of the first and the second components respectively. 193

A.8 The fluorescence lifetime mapping using the least square method to analyse the sample 10BB at 592 nm excitation. The subfigures show the integrated decay intensity which is the fluorescence mapping. The first and the second lifetime components, τ_1 and τ_2, and the reduced χ^2 mapping and the amplitude, A_1 and A_2, of the first and the second components respectively. 194

A.9 The fluorescence lifetime mapping using the least square method to analyse the sample 10BB at 482 nm excitation. The subfigures show the integrated decay intensity which is the fluorescence mapping. The first and the second lifetime components, τ_1 and τ_2, and the reduced χ^2 mapping and the amplitude, A_1 and A_2, of the first and the second components respectively. 195

A.10 The fluorescence lifetime mapping using the least square method to analyse the sample NID_{02} at 532 nm excitation. The subfigures show the integrated decay intensity which is the fluorescence mapping. The first and the second lifetime components, τ_1 and τ_2, and the reduced χ^2 mapping and the amplitude, A_1 and A_2, of the first and the second components respectively. 197

A.11 The fluorescence lifetime mapping using the least square method to analyse the sample NID_{02} at 562 nm excitation. The subfigures show the integrated decay intensity which is the fluorescence mapping. The first and the second lifetime components, τ_1 and τ_2, and the reduced χ^2 mapping and the amplitude, A_1 and A_2, of the first and the second components respectively. 198

A.12 The fluorescence lifetime mapping using the least square method to analyse the sample NID_{02} at 502 nm excitation. The subfigures show the integrated decay intensity which is the fluorescence mapping. The first and the second lifetime components, τ_1 and τ_2, and the reduced χ^2 mapping and the amplitude, A_1 and A_2, of the first and the second components respectively. 199

A.13 The phasor diagram of the 10BB sample, (a) for 532 nm, (c) for 482 nm, (e) for 572 nm and the angular histograms of the 10BB sample (b) for the 532 nm, (d) for the 482 nm and (f) for the 572 nm. 200

A.14 The phasor diagram of the D09 sample, (a) for 532 nm, (c) for 502 nm, (e) for 562 nm and the angular histograms of the D09 sample (b) for the 532 nm, (d) for the 502 nm and (f) for the 562 nm. 202

A.15 The phasor diagram of the NID_{02} sample, (a) for 532 nm, (c) for 502 nm, (e) for 562 nm and the angular histograms of the NID_{02} sample (b) for the 532 nm, (d) for the 502 nm and (f) for the 562 nm. 203

A.16 The PSO algorithm flowchart for optimisation of Halbach arrays for maser application. 206

A.17 10-magnet Halbach array (a) 3D model (b) The X-Y magnetic field map without applying demagnetisation method (c) The X-Y magnetic field map with applying demagnetisation method (d) The Y-Z magnetic field map (e) The X-Z magnetic field map (f) The X-Z magnetic field map of the 3D printed Halbach array, measured by a teslameter. 207

A.18 The histogram of the field map of the Halbach array in a 3 mm × 3 mm × 3 mm cube. 208

A.19 The 3-dimensional magnetic field map of the Halbach array in a 3 mm × 3 mm × 3 mm cube. 208

A.20 8-magnet Halbach arrays (a) 3D model of a single layer (b) Stack of 3 layers (c) The X-Y magnetic field map (d) The Y-Z magnetic field map (e) The X-Z magnetic field map. 210

A.21 (a) The 3-dimensional magnetic field map of the Halbach array in a 3 mm × 3 mm × 3 mm cube. (b) Field difference and mean field with random deviation of position and rotation from the ideal Halbach array, ± 1 mm in position and ± 1 °.211

A.22 (a) The PSO-optimised Halbach array. (b) The 3-dimensional magnetic field map of the Halbach array in a 3 mm × 3 mm × 3 mm cube. 213

A.23 The 2-dimensional magnetic field map of the angle-position-optimised Halbach array in a 3 mm × 3 mm plane. 214

A.24 The teslameter is mounted on the X stage which is mounted on the Z stage. The teslameter scans across a small square at the centre, the size is 2x2 mm. The Halbach array is an 8 prism-shaped Halbach array from Magnetic Solutions. The GMW electromagnet is shown in the background. 216

A.25 The rendered image of the magnetic field mapper. 217

A.26 (a) The field profile of the Halbach array. The Halbach array provides a 0.345 T field at the centre, the greatest difference in the field is about 0.3 mT. (b) The 3D magnetic field slice map of the Halbach array. (c) The 3D magnetic field map of the Halbach array with an inclined plane represents the sample along the <111> plane. (d) The histogram of the magnetic field profile in terms of Zeeman shift. The curve represents the lineshape of the maser resonator, represented by a 1 MHz lineshape. It is assumed that the total number of emitters is $4{\cdot}10^{14}$ and only the MW emitter within the lineshape contributes to the maser. 218

A.27 **Magnetic field histogram.** The histogram of the magnetic field profile in terms of Zeeman shift. The curve represents the lineshape of the maser resonator, represented by a 1 MHz lineshape. It is assumed that the total number of emitters is $4{\cdot}10^{13}$ and only the MW emitter within the lineshape contributes to the maser. 219

Chapter 1

Introduction

1.1 Motivation and objectives

Quantum mechanics is an extraordinary theory that studies quantum phenomena, such as atomic theory and quantised electromagnetic radiation, that are not able to be solved using classical mechanics. After years of theoretical studies and scientific exploration in quantum mechanics, quantum technologies that utilise quantum phenomena are becoming useful tools in every aspect of society.

Microwave amplification by stimulated emission of radiation (Maser) is the microwave counterpart of the laser. The underlying principle is based on a quantum theory of radiation. The maser has greatly impacted pure science and the industry since its invention. However, in comparison with lasers, masers have a lesser impact and attraction than the laser due to the difficulty in building an efficient and compact maser at room temperature or at atmospheric pressure. Typical masers will require cryogenic temperature and vacuum conditions for operation and only find niche markets in space communication and radio astronomy. A route to realise a stable room temperature maser is to extend the spin-lattice relaxation time and the spin decoherence time of spin defects in solid materials. One of the candidates is the nitrogen-vacancy (NV) centre, which is a point defect in diamonds consisting of a substitutional nitrogen atom adjacent to a vacancy. The negatively charged NV^- centres have many extraordinary properties such as long spin coherent time at room temperature [4], energy levels that are sensitive to the environment, optical readout of spin states, which have been proposed to be used as qubits in

quantum computers [5], quantum sensors [6, 7]. In addition, the NV^- centre can be used as the gain medium for masers, which has been proposed and demonstrated [8, 9, 2].

A recent study on the maser has paved the way to a more reliable solid-state maser that works at room temperature and at ambient pressure, [10, 2]. However, there are still improvements needed to build a more reliable and efficient maser.

This thesis aims to develop a model to simulate the spin dynamics of NV centres interacting with an optical excitation, external magnetic field and microwave excitation, as well as various parameters, including the number of defects, the optical pump rate and the decoherence of the defects. This will help design a diamond-based cavity maser by finding the threshold conditions. Secondly, the thesis aims to design different cavities for a diamond-based maser for a small electromagnet, a small Halbach array and a large commercial electron paramagnetic resonance (EPR) magnet. In particular, the cavity designed for the small electromagnet is a crucial component in miniaturising diamond masers. A Halbach array is one of the solutions for further miniaturisation after the small electromagnet. Thus, it is critical to model, simulate and optimise the Halbach array, in order to achieve a high field and high homogeneity, specifically for a diamond maser.

Thirdly, the optical characterisation of diamond samples is conducted. This can identify the characteristics and intrinsic parameters, and links to the performance of the diamond-based masers. Thus, it can tell what the intrinsic parameters of the diamond sample are good for masing, such as the spin relaxation time. Combining the modelling, experiment and the multi-dimensional optical characterisation of NV centre in diamond as a maser gain material, this thesis hopes to unravel the mystery of building a more efficient and powerful diamond-based maser.

Lastly, in optical characterisation, especially the lifetime fitting of multiple lifetime components. The traditional least-square method used is biased and can be computationally expensive for high-resolution images. The aim is to develop a new method, using higher harmonics and classical-quantum hybrid algorithms in phasor analysis and deep neural networks, for diamond-based fluorescence lifetime characterisation. These resolve the bias problem due to the lack of information about the samples and the time-consuming fitting process. The thesis introduces a classical-quantum hybrid algorithm to aid the analysis of optical characterisation.

1.2 Overview

This thesis focuses on the optical characterisation and spin properties of NV centres in diamonds, and the realisation of masers based on NV centres and the performance of the diamonds as the gain media of masers. This thesis is organised into seven chapters. The first chapter gives an introduction, an overview and a statement of the originality of the thesis. The second chapter describes the background theory and a short literature review about the maser. There follows a background for both the dielectric resonator and microwave antenna, microwave characterisation and background of diamond and the optical and spin properties of NV centres.

The third chapter describes the experimental technique, setup and apparatus for characterising the optical and spin properties of NV centres, such as the confocal microscope, fluorescence lifetime imaging, ODMR and T_1 imaging. The other half of this chapter describes the design of the dielectric resonator and the cavities used, as well as the magnetic field homogeneity characterisation of the electromagnet and the setup of the diamond maser.

The fourth chapter presents the results of the optical characterisation: fluorescence lifetime imaging of diamond, which contains two sections about the novel analytical methods, the spin-lattice relaxation time imaging of the diamond samples and the ODMR of the diamond samples.

The fifth chapter discusses the modelling techniques and simulation methods and results. These include the extended-7 level rate equations for spin dynamics, optically detected magnetic resonance (ODMR) and the determination of the masing threshold.

The sixth chapter presents the masing results of the diamond-based maser, and the results are divided into the EPR-based system, which uses a large electromagnet from a Bruker EPR system, and the GMW-based system, which uses a small dipole electromagnet from GMW Associates. It verifies the simulation and modeling in the previous chapter.

The seventh chapter concludes the work and proposes future works based on the current results. In the appendix, there is a detailed section about hybrid quantum transfer learning on diamond, more optical data for each sample and the algorithm for swarm intelligent optimisation, which solves complex optimisation with the collective behaviour of many individuals that have a correlative behaviour with others, inspired by biological systems, of Halbach array.

1.3 Statement of originality

- The thesis shows a 7-level extended rate equation that is based on semi-classical Maxwell-Bloch equations to predict the threshold conditions of diamond masers with various parameters, such as the Q factor, mode volume, and pump power. It defines no-masing, incipient masing and masing action regimes, as well as the linear and saturation masing regimes that is verified by the experimental results. These results formed the basis of a publication [11].

- The thesis demonstrates the modelling of optimised Halbach arrays for diamond-based masers. The Halbach array design simulation implements a particle swarm optimisation algorithm (PSO), which relies on swarm intelligence, for automatically optimising the structure and the field homogeneity. The algorithm is based on analytical and vectorised calculation with a demagnetisation meshing technique. Furthermore, the algorithm implements optimisation on each individual magnet, such as the position and the rotation angle to find the optimal placement of each magnet. The algorithm can discover new structures that differ from the conventional structure with high field inhomogeneity.

- The thesis discusses new cavity designs and simulations that are specifically designed for the Bruker electromagnet and a small cavity for the GMW electromagnet, which can fit inside the poles of the magnet and optimise the dimension for a high Q factor. Furthermore, various dielectric materials are simulated at around 9.5 GHz for masing applications.

- The thesis presents the linear and saturation regimes in both the masers using the Bruker electromagnet and the GMW electromagnet, and the extended rate equations simulate a similar saturation regime at a similar excitation power.

- The thesis presents the corresponding optical characterisation of the diamonds that are used for masing, such as spin-lattice relaxation time mapping and fluorescent lifetime mapping at various excitation wavelengths.

- The thesis presents a novel fluorescent lifetime analysis technique based on phasor analysis in the study of diamonds, which is the blind-determination method with a random search technique that uses high harmonics to estimate the lifetime of a sample, as well as an angled-resolved histogram.

- A deep learning method, based on high-dimension convolutional and residual networks, is introduced into diamond-based fluorescent lifetime mapping that is trained on various fluorescent defects in diamonds, so it provides an efficient way to extract the lifetimes and the proportions of each pixel from the map and help distinguish the number of lifetime components. Another benefit is to avoid the use of initial guesses and the models to be used for fitting and trained with more variety of defects which would reduce the bias when doing a fitting. It outperforms the traditional least square method.

- T_1 relaxation mapping is implemented on the diamond samples to visualise the distribution of region of high and low T_1 relaxation time that is essential for a maser. This thesis shows the relation between the T_1 time and the masing threshold experimentally as well as theoretically.

Chapter 2

Background Theory

2.1 Maser

Microwave radiation is electromagnetic radiation with frequencies ranging from 300 MHz to 300 GHz. Microwave and its related technologies have revolutionised many fields across industry, academia and everyday lives, such as wireless communications, astronomy, medical and military applications [12]. A maser, which is the acronym for microwave amplification by stimulated emission of radiation, generates coherent microwave radiation similar to a laser that generates optical radiation from stimulated emission. Masers can act as microwave oscillators, high-resolution spectrometers and low noise amplifiers in the microwave spectrum [13]. The fundamental quantum theory of radiation behind masers was developed by Einstein in 1917 [14]. Although the maser was invented before the laser, the development of the maser lagged behind the laser. The primary reason is that the operation condition of the maser is very restricted as it typically requires vacuum and cryogenic temperature, usually at liquid helium temperature and only a few at liquid nitrogen temperature [15]. Although the maser requires cryogenic and vacuum systems, it is still employed in deep space communication, such as the Goldstone Deep Space Communications Complex which uses cryogenic ruby masers [16]. It also finds uses in astronomy and atomic clock. Passive hydrogen masers are used on Galileo satellites and active hydrogen masers on Beidou satellites. Radar systems use masers due to exceptional performance in low noise amplification compared with other conventional amplifiers such as vacuum tubes, travelling wave tube amplifiers (TWT), field effect transistors (FET)

and high-electron-mobility transistors (HEMTs) which exhibit electronic shot noise and thermal noise [13, 2]. The key difference is that masers lie in the quantum regime, which uses stimulated emission arising from the light-matter interaction to amplify MW signals as microwave photons, whereas conventional amplifiers use electron beams or currents in semiconductors relying on charge which has intrinsic noise.

For example, ultra-low noise Indium phosphide (InP) HEMTs have a gain of 27 dB and a noise temperature of about 31 K at room temperature and 1.4 K when it is cooled down to 15 K between 4 GHz and 8 GHz [17]. A room-temperature pentacene maser has a noise temperature of well below 30 K [10].

Masers can operate at various MW frequencies depending on the available energy levels in the gain materials, but at low frequencies, the performance might not be optimal for many reasons, such as the cross-relaxation; thus the low noise amplification performance below 1 GHz might be worse than other competitors [15]. Beyond the Earth, cosmic masers, such as methanol masers at 6.6 GHz [18] and water masers at 22.21 GHz [19], exist at a large scale and they are closely related to comets, stellar atmosphere and molecular clouds. The interstellar medium has an extremely low density, and non-equilibrium states and permits population inversion [20].

Another benefit of masers is the linearity of amplification, which does not suffer from inter-modulation from interference of strong signals with weak signals.

2.1.1 Gaseous maser

The first maser, using a beam of ammonia molecules at 78 K in a vacuum chamber, at a frequency of 23.87 GHz, was built 7 years before the first laser [21], by Charles Townes, James Gordon and Herbert Zeiger in 1954 [22]. The ammonia maser relied on a directional molecular beam source and a non-uniform electrostatic field, via a 30,000 DC voltage [15], to focus the molecules that are excited into a resonant cavity at 23.87 GHz where the excited molecules release the energy via photons and return to the ground state by an electric field of an external MW source at the resonant frequency. Since the excited state and the ground state ammonia molecules have different charge distributions, the nonuniform electrostatic field can divert or focus the ground state and the excited state molecules respectively. The power output of the maser oscillator was estimated to be about $5 \cdot 10^{-10}$ W [23].

The energy levels of ammonia masers are intrinsic vibrations and rotation of the molecules. The linewidth is sharp and stable and is used for frequency standards. The linewidth is proportional to the velocity of the molecules, which is about 200 Hz [24]. The frequency deviation of the oscillator is inversely proportional to the power. This limits the ammonia maser to a narrow-band amplifier in amplifier operation.

Later, the atomic hydrogen maser, masing at 1.42 GHz, was built which had a longer lifetime than the ammonia [25]. In contrast, the atomic hydrogen maser relies on the magnetic dipole interaction which is inherently weak. The atomic hydrogen maser consists of a Woods's discharge source, which produces a beam of atomic hydrogen, an inhomogeneous magnetic field from a six-pole magnet to select the atoms in the two hyperfine levels, (F = 1, m = 0) and (F = 1, m = 1) and a resonant cavity at 1.42 GHz [26]. The maser operation is triggered by the spontaneous emission. The maximum power is about 10^{-12} W, and the linewidth is about 1 Hz, considerably narrower than the ammonia maser [26] [27].

Apart from the hydrogen atom, hydrogen cyanide (HCN) is another type of gas maser material. HCN molecules have a large electric dipole moment and the ability to be separated by the excited and the ground states using a nonuniform electric field. The masing transition is at 88.6 GHz. The HCN maser relies on the rotational energy of the HCN molecules. The HCN maser consists of a multichannel nozzle as the molecule source, an eight-rod electric focuser and a cavity with loaded Q of 6300 cooled by liquid nitrogen and in a vacuum of about 10^{-6} mm Hg. The ^{14}N nuclear electric quadruple interacts with the electric field gradient of the molecule and produces three hyperfine sub-levels at 88.630 GHz, 88.631 GHz and 88.633 GHz [28]. The maximum transmission coefficient is about -8 dB [28].

The gas masers tend to have a narrow linewidth due to the intrinsic property of the atom and molecule, the quality is limited by collision and the frequency is untunable. The "Electric" maser such as the ammonia and HCN relies on the electric dipole moment of the molecules to be selected by the focuser and mase, and the transition frequency is much higher than the hydrogen maser. Masers can also be realised using free electrons that generate stimulated cyclotron radiation. The benefit is that the structure of the cyclotron maser is not directly linked to the wavelength of the microwave radiation.

2.1.2 Solid-state maser

Solid state maser materials contain paramagnetic ions or atoms that have a permanent magnetic dipole moment from unpaired electrons doped in a crystal that is diamagnetic and not interacting with the ions, such as ruby and rutile [29]. With an external magnetic field, such a paramagnetic system can achieve population inversion. Transition metal ions tend to have magnetic dipole moments such as chromium ions, Cr^{3+}, doped in ruby, as well as Gd^{3+} in gadolinium ethyl sulfate and nickel fluorosilicate that amplified at 9 GHz [30]. The chromium-doped ruby at cryogenic temperature was proposed as a maser gain material, which laid the foundation for robust solid-state systems as opposed to the gaseous masers introduced earlier [31]. Solid-state masers are robust and do not need high vacuum and molecule sources. The ruby masers have been constructed and used at Deep Space Network since 1960. The masers are based on either a cavity system or a travelling-wave system, operating at 4.5 K. The gain is between 20 to 50 dB, the bandwidth is between 0.75 up to 300 MHz, and the noise temperature ranges from 1.9 K up to 30 K [16]. The cavity used for these type of maser oscillator is often the superconducting cavity, and the maser oscillator is referred to 'superconducting cavity maser oscillator' (SCMO) [32], which is a sapphire cylindrical resonator coated with lead [33].

The transition frequency of the paramagnetic impurities is tunable via the Zeeman effect. The Zeeman effect occurs when an external magnetic field interacts with a magnetic dipole. The energy is given by $E = -M_J g_J \mu_B B$, where M_J is the total angular moment quantum number, g_J is the Lande g factor, μ_B is the Bohr magneton and B is the magnetic field. However, the linewidth is broader than the gas maser due to the effect of the magnetic environment of the lattice and the external magnetic field.

Cryogenic temperatures are essential for a sufficiently long spin-lattice relaxation time, T_1, which is the time that the spins take to relax back to thermal equilibrium, and the spin-spin relaxation time, T_2, to keep the population inversion of the spin states [31]. In particular, the T_1 relaxation time plays an important role in maser operation. The longer T_1 allows the spin population inversion to maintain for a sufficient amount of time without re-polarising the material. Another reason is that the Boltzmann distribution is temperature dependent, proportional to $e^{E/k_B T}$, the distribution between the spin states at room temperature is nearly the same due to the small energy difference, the factor $E/k_B T$ is very small. Thus, the populations between the ground and the excited states are very similar at thermal equilibrium. The masing requires

a highly non-equilibrium state.

Seeking a long T_1 at room temperature is a main interest in building a room temperature solid-state maser. Phonon scattering is the dominant effect causing the short T_1 time at room temperature [15]. Materials with weak spin-orbit coupling, such as carbon-based materials like diamond and organic materials, show weak phonon scattering and long T_1 time [8]. Another approach is to increase the pump power so that the population inversion increases and thus the masing power [13], or increases the concentration of the spin active impurities. But higher concentration will lead to a reduction of T_2 time, as there is a dephasing interaction between the spins and impurities.

2.1.3 Room temperature maser

The search for room-temperature masers has been active since the discovery of the first maser. The advance in organic materials and semiconductors accelerated the discovery of new maser materials and microwave materials. The dissolved C_{60} and porphyrin molecules in the organic nematic liquid crystal under a strong DC magnetic field and optical excitation have been realised as gain materials for microwave amplification at room temperature [34]. The C_{60} molecules in nematic liquid crystals have a complex permeability over a 27 MHz bandwidth at 253 K, the imaginary part of the permeability can be either positive or negative, which corresponds to emission and absorption [34]. Bouregeois et al. demonstrated a sapphire maser, at 12.038 GHz, based on the EPR resonance of the Fe^{3+} ion doped in the sapphire with a concentration of a few ppb [35]. This maser oscillates without a DC magnetic field and with a microwave excitation at 31.34 GHz.

In 2012, a pulsed room temperature maser operating in the Earth's magnetic field was built using pentacene-doped p-terphenyl as the gain material [10]. The maser output was found to be -10 dBm. The optical threshold pump power was 230 W from a 585 nm pulsed laser.

Population inversion and stimulated emission from negatively charged V_{si} defects, which are optically pumped, in silicon carbide (SiC), both 4H-SiC and 6H-SiC, at room temperature are reported [36, 37]. The V_{si} defect is an atomic spin defect that is a missing silicon in the silicon carbide lattice. The V_{si} defect has a weak spin-orbit interaction, and the T_1 relaxation time is very long, which is about a few milliseconds [38].

Masing at room temperature using NV^- centres in diamond was proposed in 2015 [8, 39]. Similar to SiC, NV^- centres are atomic defects in diamond lattices that consist of a substitutional nitrogen atom and a vacancy replacing a missing carbon. Three years later, a continuous-wave maser at room temperature was built using NV^- centres in diamond [2]. The output power was about -90 dBm, and the threshold pump power was 180 mW [2]. The organic maser gain media relies on the spin active molecules doped in inactive solid materials such as pentacene in p-terphenyl, phenazine/1,2,4,5-tetracyanobenzene, with Q-boosting, [40] and 1,3,5-tri(naphthyl)benzene [41]. Different combinations of spin-active molecules and host solids have been studied, such as different derivatives of nitrogen-substituted tetracene are studied [42]. Recently, 6,13-diazapentacene-doped para-terphenyl has been demonstrated as a maser gain medium, having an output power of -10 dBm at 1478 MHz [43].

2.1.4 Working principle

The maser can operate in either an oscillator mode or an amplifier mode. Microwave oscillators and microwave amplifiers are key components used in communication and metrology. Amplifiers amplify small signals that are hard to detect to a strong signal that can be used in communication systems. Oscillators are used as local oscillators and frequency standards in many systems.

In the early 20^{th} century, vacuum tube technology dominated the field of microwave oscillators and amplifiers, such as travelling-wave tubes, klystrons and cavity magnetrons. For example, klystrons are a widely used microwave oscillator and amplifier that use an electron beam in a resonant cavity interacting with a microwave signal and subsequently converts its kinetic energy to amplify the microwave signal at the second resonant cavity that outputs the signal. When the output signal is feedback into the system, it works as an oscillator. The advantages are the high power, over a MW, and high gain, which can go up to 60 dB. However, vacuum tube technology suffers from low efficiency, bulky size, non-linearity and high noise. In the late 1970s, semiconductor oscillators became dominant due to their compact size. Maser technology on the other hand has a very low noise and high linearity.

In the amplifier mode, the maser amplifies small microwave signals within the bandwidth of the maser resonant frequency. The maser frequency bandwidth is very narrow and it is typically

50 Hz and with a gain of 20 dB for a high Q cavity maser. The benefit of the maser amplifier is it has a very low added noise, unlike conventional electronic amplifiers, such as HEMTs, which have electronic noise, flicker noise and thermal noise. Bipolar transistors, operational amplifiers and field effect transistors are used to amplify signals. Due to impurities and phonon scattering, the thermal noise is high. Thus, HEMTs often rely on the 2D electron gas in a heterostructure interface.

The maser amplifier uses the stimulated emission and with special cavity design to select a specific mode. The primary noise source is the spontaneous emission and thermal photons. Thus, a maser amplifier can achieve a lower noise figure at room temperature than HEMTs. To achieve low noise performance, the input matching network with the maser optimised input impedance has to be used, and it is used as a first stage of amplification and followed by other amplifiers that improve the cumulative gain. The bandwidth can be improved using successive amplifiers that amplify different spectral part of the signal.

The working principle is based on the quantum theory of radiation. This relies on the interaction between the electromagnetic field and a quantised system such as a spin system. The quantised system has many discrete energy levels. For example, in an atom, the electron can transit between two different energy levels by emitting or absorbing a quanta of electromagnetic field energy such as a photon. The amount of energy matches the energy difference between the energy levels. For lasers, the energy corresponds to the electronic transition between the energy levels in atoms. For masers, the energy is much lower than the electronic transition in atoms. The energy of the hyperfine transition in atoms is low enough for microwave photons. For example, the hydrogen atom has four distinct spectral lines in the visible, corresponding to the electronic transition between the n = 2 and n = 3, 4, 5 energy levels [44]; a distinct microwave spectral line at 1.42 GHz, corresponding to the hyperfine energy levels of the 1s orbit. The hyperfine interaction relies on the magnetic dipole of the electrons [44].

Suppose that in an atomic or molecular system, there are three energy levels with $E_3 > E_2 > E_1$. Each energy level has certain populations, N_3, N_2 and N_1. The Boltzmann distribution determines the population ratio between two of the energy levels at thermal equilibrium, $e^{(E_1-E_2)/k_BT}$ and $E_1 - E_2 = hf_{21}$, where h is the Planck constant and f_{21} is the frequency difference between the two energy levels. The population preferentially occupies lower energy levels, thus, $N_1 > N_2 > N_3$. The population can transfer between levels via the absorption or

emission of quantised energy that matches the energy difference between the levels, such as a photon. There is spontaneous emission, stimulated emission and stimulated absorption. The spontaneous emission process is when an electron at a higher energy level moves to a lower energy level and emits a photon corresponding to the energy difference spontaneously. The phase and the direction of the emission is random. On the other hand, in the stimulated emission process, an electron in a higher energy level interacts with a photon that matches the energy difference and moves to the lower energy level by emitting a photon with the same energy, phase and direction. The probability of the stimulated emission process is determined by the energy density and the linewidth of the incoming photons and the transition property of the emitter which is determined by the Einstein B_{21} coefficients. Stimulated absorption happens when an electron in a lower energy level absorbs a photon corresponding to the energy difference and moves to the higher energy level. The absorption rate is determined by the energy density and the linewidth of the incoming photons and the Einstein B_{12} coefficients. The spontaneous emission can be thought of as an emission stimulated by vacuum fluctuation of the electromagnetic field. The probability of the spontaneous emission process is determined by the electromagnetic environment and the transition property of the emitter. The spontaneous emission rate is different when the emitter is in free space and a cavity. Focusing on two of the levels from the systems, the rate of change of the population is modelled using rate equations. The population from the lower state can absorb pumping photons to move to the higher state. However, the population will relax back to the thermal equilibrium via spin-lattice relaxation. The spins are not isolated, they couple to the crystal lattice. The energy can transfer to the lattice as a phonon. The harder the pumping, the more the population will be in the higher state, until it reaches saturation when the populations are equal in the lower and the higher states.

$$\frac{dN_1}{dt} = A_{21}N_2 + B_{21}N_2\rho(\omega) - B_{12}N_1\rho(\omega) + k_{21}N_2 - k_{12}N_1 \tag{2.1}$$

$$\frac{dN_2}{dt} = -A_{21}N_2 - B_{21}N_2\rho(\omega) + B_{12}N_1\rho(\omega) - k_{21}N_2 + k_{12}N_1 \tag{2.2}$$

$$\frac{d\Delta N}{dt} = 2A_{21}N_2 - 2B_{21}\Delta N\rho(\omega) + (k_{21} - k_{12})N - (k_{12} + k_{21})\Delta N \tag{2.3}$$

where A_{21} is the Einstein A coefficient that gives the probability of spontaneous emission from N_2 to N_1, B_{21} is the Einstein B coefficient that gives the probability of stimulated emission,

B_{21} gives the probability of stimulated absorption and $\rho(\omega)$ is the energy density of the electromagnetic field. k_{12} and k_{21} are the spin-lattice relaxation rate from level 1 to level 2 and from level 2 to level 1, respectively. $\Delta N = N_1 - N_2$ is the population inversion and $N = N_1 + N_2$ is the total number of population. From the equations above, the decay rate of the population inversion is determined by the spin-lattice relaxation term, $k_{21} + k_{12}$. The spin-lattice relaxation time is $T_1 = \frac{1}{k_{21} + k_{12}}$. The ratio of the upward and the downward spin-lattice relaxation rate is determined by $e^{\frac{hf_{21}}{k_B T}}$, where hf_{21} is the energy difference between the two states. For simplicity, the subscript of the frequency between the two states is dropped. It is about 1 at room temperature for microwave frequency. The Einstein B coefficient is derived from the stimulated transition rate, W, from [15].

$$W = \frac{1}{4}(\frac{2\pi g \mu_0 \mu_B}{h})^2 g(f) |\langle i|\mathbf{H}^* \cdot \mathbf{S}|j\rangle|^2 \tag{2.4}$$

where μ_B is the Bohr magneton, g(f) is the lineshape function, which can be assumed to be Lorentzian for simplicity. The normalised Lorentzian lineshape function can be expressed as below [15].

$$g(f) = \frac{2T_2}{1 + (2\pi T_2)^2 (f - f_0)^2} \tag{2.5}$$

where T_2 is the spin relaxation time and f_0 is the resonant frequency. At resonance ($f = f_0$), the lineshape function is $g(f) = 2T_2$ and the linewidth is inversely proportional to the T_2 relaxation time.

$|\langle|i|\mathbf{H}^* \cdot \mathbf{S}|j\rangle|^2$ is the transition matrix element of the magnetic dipole interaction between states i and j. The transition matrix element can be further simplified, as the H^* is not a quantum mechanical operator, leaving the term $\langle|\mathbf{S}|\rangle = \sigma_{ij}$ that determines the transition. After some algebra [15], the stimulated transition rate can be expressed:

$$W = \frac{1}{4}(\frac{2\pi g \mu_0 \mu_B H}{h})^2 g(f) \sigma^2 \tag{2.6}$$

where $\sigma^2 = \dfrac{\mathbf{H}^* \cdot \sigma\sigma^* \cdot \mathbf{H}}{\mathbf{H}^* \cdot \mathbf{H}}$, for a linearly polarised microwave field and a triplet spin system, the maximum σ^2 is 0.5. Provided that the magnetic field energy density is $H^2 = nhf\mu_0/V_m$, where

V_m is the mode volume and n is the number of photons in the mode and $W = Bn$, the Einstein B coefficient at resonant is given:

$$B = \frac{1}{4}(\frac{2\pi g\mu_B}{h})^2 \frac{\mu_0 T_2 h f \eta}{V_m} \tag{2.7}$$

where η is the filling factor.

$$B \approx 6.4544 \cdot 10^{-18} \frac{T_2 f \eta}{V_m} \tag{2.8}$$

Assuming that η=1, V_m= 0.1 cm^{-3}, T_2=4 μs and f= 9.22 GHz, the B coefficient is approximately 2.38·10^{-6} s^{-1}. The spontaneous rate is given by [15]:

$$A = \frac{8\pi^3 \mu_0 f^3 (g\mu_B)^2}{3hc^3} \tag{2.9}$$

At 9.22 GHz, the spontaneous rate is about 1.57·10^{-12} s^{-1}, which is much slower than the stimulated transition rate and the spin relaxation rate. From the 2-level model, the maximum population inversion is near where the two populations are equalised under strong pumping. To achieve population inversion, the minimum number of levels required is 3. The extra level will act as an auxiliary level.

The maser can operate as an amplifier or an oscillator. In the amplifier mode, an input signal photon stimulates the population inverted system and triggers the stimulated emission, resulting in more photons that are the same as the input photon. Usually, the number of spins is large, so the amplification is smooth and coherent. If the number of spins or the number of input photons is small, the situation is different, as the stimulated emission is a probabilistic process. The phase of the output signal might become a problem [15]. In the oscillator mode, the thermal photons and the spontaneous emission act as the input, and the power gain is large enough to overcome all the losses in the cavity.

In order to make a maser, an excitation source is required to bring the electrons into the excited state; stimuli photons are required to trigger the stimulated emission; A sufficient amount of population inversion so that the stimulated emission is the dominant emission type.

The threshold pump rate, thus, the threshold optical pump power is inversely proportional to

the T_1 [2].

$$W_t = \frac{\alpha}{T_1(C-1)} \tag{2.10}$$

$$P_t = W_t \frac{A\hbar\omega}{\sigma} \tag{2.11}$$

where W_t is the threshold pump rate, P_t is the threshold pump power, A is the spot size of the laser, $\hbar$ is the reduced Planck constant, ω is the frequency of the laser, σ is the one-photon absorption cross-section, C=$4g^2N/(\kappa_s\kappa_c)$ is the cooperativity, where κ_s is the spin decay rate and κ_c is the cavity decay rate, and the α is the scaling factor related to the number of photons required to change the population inversion by one [2]. The output power of the maser is proportional to the cavity decay rate, $\kappa_c = \omega_c/Q$ where the frequency of the cavity is defined as ω_c and the number of microwave photons.

Increasing the cooperativity can reduce the threshold pump power for masing. The cooperativity is proportional to the number of active gain molecules. Increasing the density of the gain material can reduce the threshold pump power. However, there is more interaction between the molecules that reduces the spin relaxation time. The cooperativity is proportional to the square of the coupling strength, g, between the spin and the cavity field. At resonance, the coupling strength, g, is expressed below.

$$g = \gamma\sqrt{\frac{\kappa_s\mu_0\hbar\omega_c}{2V(\kappa_s+\kappa_c)}} \tag{2.12}$$

where V=$\int_V |H|^2/|H_{max}|^2 dV$ is the mode volume. The coupling strength can be improved by decreasing the mode volume of the cavity. Suitable gain materials should have energy levels within the microwave spectrum, and a magnetic matrix element between the levels making it feasible to establish population inversion.

A microwave resonator is used to select the desired frequency. For constructing a cavity maser, there are two configurations: one-port maser and two-port maser. In a one-port maser, there is only one port for the input signal and output signal, the measurement is reflection. A circulator is used at the port to direct the input signal in and the output signals out from the coupling port. In a two-port maser, there is an input port and an output port, the measurement is

transmissive. However, about half of the output signal will reflect back to the input port, which leads to a reduction in gain-bandwidth product by a factor of 2. For this thesis, the one-port masers are constructed and the gain media used is NV diamond.

Spin Relaxation

Spin relaxation is a phenomenon in which spins interact with different spins or interact with the lattice, known as spin-spin relaxation and spin-lattice relaxation, respectively. The relaxation leads to the return of the thermal equilibrium after any perturbations. The relaxation caused by the spin-lattice interaction is determined by the time constant T_1 relaxation time. The relaxation caused by the spin-spin interaction is determined by the time constant T_2 relaxation time.

Spin relaxation times are very important, as they limit the coherence for quantum control and quantum sensing by restoring the thermal equilibrium from the desired states. This process can be described by the Bloch model.

$$\frac{dM_x}{dt} = \gamma_e B\mathbf{M}_y - \frac{\mathbf{M}_x}{T_2} \tag{2.13}$$

$$\frac{dM_y}{dt} = \gamma_e B\mathbf{M}_x - \frac{\mathbf{M}_y}{T_2} \tag{2.14}$$

$$\frac{dM_z}{dt} = \frac{\mathbf{M}_{z0} - \mathbf{M}_z}{T_1} \tag{2.15}$$

$$\tag{2.16}$$

where the $\mathbf{M}_i$ is the macroscopic magnetisation along the i axis, which i = x, y, z, $\mathbf{M}_{z0}$ is the initial magnetisation along the z axis, γ_e is the geyomagnetic ratio of an electron, B is the magnetic field, T_1 and T_2 is the spin-lattice relaxation time and the spin-spin relaxation time.

This process is determined by the energy transfer between the spin system and the environment such as the lattice. At room temperature, the spin-lattice relaxation time is dominantly limited by the phonons [45]. The cross relaxation time is the relaxation time to reach thermal equilibrium between two spin systems that have a similar transition frequency and are close in space. If the spin-lattice relaxations are different between the two spin systems, the cross-relaxation

process can alter the spin-lattice relaxations, as the spin system with the longer spin-lattice relaxation time will relax via the cross-relaxation process to the other spin system [15].

To measure the T_1 of NV centres, a laser is used to initialise the NV centres to the m = 0 state, then readout using the laser after a period of free evolution τ. After the initialisation, the NV centres will relax back to the thermal equilibrium, which is roughly the same population in the m = 0 and the m = $\pm$1 states at room temperature.

As the period of free evolution increases, the photoluminescent intensity exponentially decreases as the population in the m = 0 state decreases as a longer period of free evolution will allow more spins to relax. The T_1 is the time it takes to decay to 1/e of its intensity. The inverse pulse method can also be used to measure the T_1. After the initialisation, an MW inversion pulse (π pulse) pumps all the population to the m = $\pm$1 states from the m = 0 state. The population will take some time to relax back to the thermal equilibrium. The T_1 can be estimated by fitting the exponential decay data over the period of free evolution.

When a MW π pulse is applied, the spins rotate 90°, perpendicular to the external magnetic field, which is along the Z direction. After the pulse, the magnetisation of the spins is in the XY plane, denoted as M_{xy}. The M_{xy} will gradually decrease to zero. Due to the interactions between the spins, the phase of each spin will gradually move out of phase with each other, and the M_{xy} will decrease more rapidly. The relaxation time is characterised by the spin-spin relaxation time, T_2. In reality, the magnetic field is inhomogeneous, which leads to inhomogeneous dephasing, the M_{xy} relaxation time is determined by the dephasing time, T_2^*, the profile rapidly decreased because each spin experiences a different field. The T_2 can be measured by applying the Hahn echo sequence, $\pi/2 - \tau - \pi - \tau - echo$. Hahn echo sequence removes the dephasing effect by applying a π pulse that flips all the spins. The spins with faster rates will have an extra distance to rotate, whereas the spins with slower rates have a shorter distance to rotate and catch up to the faster spins which leads to the cancellation of the dephasing. By comparing the initial intensity, the time and the echo intensity, the T_2 can be obtained.

In an inhomogeneous magnetic field environment, each spin interacts with the field differently, this causes the dephasing effect. The lifetime of the coherence is characterised by the dephasing time, T_2^*. There are a few methods to measure the T_2^*: Ramsey sequence, $\pi/2-\tau-\pi/2$, is similar to the Hahn sequence, but without the π pulse for removing the dephasing; To extrapolate the linear fit of the resonant linewidth and the MW power down to zero power, since the linewidth

is inversely proportional to the dephasing time and it is power broadened by the MW pulse [2] [46]. The T_2 and T_2^* are limited by the concentration of the spin defects. The higher the concentration, the more interactions between the defects.

Zeeman Effect

Some atoms, ions and spin defects have magnetic dipole moments. The magnetic dipole moment arises from the unpaired electrons that have orbital and spin angular momentum. The orbital magnetic dipole moment is μ_l, and the spin magnetic dipole moment is μ_s and can be combined to form the total magnetic dipole moment μ_J.

$$\mu_J = -g\mu_B J \tag{2.17}$$

where g is the Lande g factor and μ_B is the Bohr magneton. When the g factor is 2.0023 for a single free electron, the magnetic dipole moment is mainly spin, whereas the magnetic dipole moment is mainly orbital when it is near one. In an external magnetic field parallel to the axis of the magnetic dipole, with a strength B. The energy of the magnetic dipole is:

$$E = m_J g\mu_B B. \tag{2.18}$$

where m_J is the total spin quantum number that has a value of 2J + 1. For a S = 1 spin defect, the Zeeman shift in frequency is f = $2\mu_B B/h$ or simply f/B = 28 GHz/T, the energy levels are split into m_J = +1, 0, -1 levels. Similarly, a nucleus possesses magnetic dipole moment if it has an odd number of protons and an even number of neutrons or an odd number of neutrons and an even number of protons or both that will leave an unpaired proton or neutron. For example, the Zeeman shift in frequency of ^{14}N is f/B = 3.1 MHz/T, which is much smaller than the electron Zeeman shift and it is often neglected.

2.2 Dielectric resonator

Electromagnetic resonators are important devices for confining and storing electromagnetic fields at specific frequencies. A dielectric resonator is often made of dielectric ceramics that

have low dielectric loss and a high dielectric constant that will confine electromagnetic energy in a small volume for a long period of time. The main difference between the dielectric resonator and the metallic cavity is that there is radiation leakage at the edges of the resonator, due to the air/dielectric boundary. The solution is to use a larger copper cavity to enclose the dielectric resonator. The proposal of such a dielectric resonator can be dated back to 1939 [47]. The realisation of dielectric resonators that exhibit a microwave resonance was in the 1960s, the first dielectric resonators were made of single-crystal rutile (TiO_2)[48][49]. However, the temperature stability is very poor and it was not used in practice. The dielectric materials that construct the resonator can be single crystal or polycrystalline [50], or even a composite of different dielectric materials [51].

The thermal coefficient, which is determined by the temperature coefficient of the relative permittivity, is an important factor to be considered. The resonator will be heated up if a pump laser is illuminated through the resonator, and this results in a frequency shift. For rutile, the coefficient for permittivity is 760 ppmK^{-1} and 1200 ppmK^{-1}, for the components perpendicular and parallel to the c-axis, respectively [52]. Sapphire is a single crystal form of alumina, Al_2O_3, which has a dielectric constant of 9.3 perpendicular to the C-axis and 11.5 parallel to the C-axis at 10^9 Hz, a dielectric loss of $3 \cdot 10^{-5}$ and temperature coefficient of the resonant frequency is -60 ppm/K at room temperature. Rutile has a dielectric constant of 170, parallel to the c-axis, a dielectric loss of 10^{-4} and a temperature coefficient of ca 500 ppm/K at room temperature [53], the resonant spectrum is in the range of radio waves and microwaves. Barium Titanate [54], Lanthanum aluminate [55], Barium Magnesium Titanate (BMO) [56], Barium Zinc Titanate (BZT) [57], $BaTi_4O_9$, (BTO) and Strontium Titanate, $SrTiO_3$, (STO) are microwaves dielectrics with perovskite structures, the dielectric constants are 38 and 300, respectively, the TCF is 14 ppm/K and the thermal expansion is 40 ppm/K. Furthermore, a composite of materials with different signs of the thermal coefficient might be used to cancel the expansion or reduction. These are the potential dielectric materials for maser applications.

The resonant frequencies are determined by the dielectric constant, ϵ, ranging from 3 to 300, of the commonly used dielectric materials, which is proportional to $\sqrt{\epsilon}$. The change in the dielectric constant at the interface between the air and the dielectric material allows the electromagnetic fields to be confined within the materials.

The Q factor is pre-dominantly determined by the Q dielectric loss. The dielectric loss in

crystal might be due to extrinsic loss, such as the defects, doping [58], porosity, grain size [59] and the intrinsic loss such as the anharmonic phonon interaction with the crystal with the electromagnetic field [60][61]. Sapphire, which is the single crystal form of aluminum oxide, is a low loss dielectric material commonly used in dielectric resonators. Sapphire exhibits temperature and frequency-dependent dielectric loss, which is 10^{-8} at liquid helium temperature [61]. The dielectric loss is still very low at room temperature, $\tan\delta = 10^{-6}$ [62].

In this thesis, the dielectric resonators and the posts that support the resonators are made of sapphire. The Q factor is the ratio of the maximum energy stored, E, in one cycle to the average energy dissipated in one cycle, P. The higher the Q factor, the less dissipation in the cavity.

$$Q = \frac{2\omega W}{P} \tag{2.19}$$

$$W_e = \frac{\epsilon_0 \epsilon_r}{2} \int_V |E|^2 dV \tag{2.20}$$

$$W_h = \frac{\mu_0 \mu_r}{2} \int_V |H|^2 dV \tag{2.21}$$

The W_e is the electric energy stored in the resonator with a volume, V, and W_h is the magnetic energy stored in the resonator with a volume, V.

The unloaded Q factor encompasses the dielectric, the conductor, and the radiation losses, while the loaded Q factor takes into account the external Q factor, which is determined by the coupling to the external systems, in addition to the unloaded Q.

The loaded Q factor measured using a VNA is inversely proportional to the bandwidth, $\Delta\omega$, in an approximation, Q=$\omega/\Delta\omega$, where ω is the resonant frequency [63]. The relation between the loaded Q factor, Q_L, and the unloaded Q factor, Q_U, is expressed below.

$$\frac{1}{Q_L} = \frac{1}{Q_U} + \frac{1}{Q_{ext}} \tag{2.22}$$

$$\frac{1}{Q_U} = \frac{1}{Q_c} + \frac{1}{Q_d} + \frac{1}{Q_r} \tag{2.23}$$

where Q_{ext} is the external Q factor that accounts for the external loss, Q_c is the conductive Q factor, which accounts for the conductor loss and Q_d is the dielectric Q factor, which accounts

for the loss due to the dielectric and Q_r is the radiation Q factor, which accounts for the loss due to radiation.

$$P_c = \sqrt{\frac{\pi f \mu_0}{\sigma}} \frac{1}{2} \int_V |H|^2 dV \tag{2.24}$$

where f is the frequency, σ is the conductivity of the conductor.

A material with low loss at the resonant frequency allows the electromagnetic fields to be confined for a longer time, thus, realising a high Q factor. In contrast, metallic resonators are lossy at microwave frequency. The common problem encountered when using a dielectric resonator is the sensitivity to the temperature [64]. Dielectric has a complex-valued dielectric constant and a finite conductivity which both induce losses in the MW field. The conductivity loss results in heating of the dielectric materials. The imaginary part of the dielectric constant induces loss which is due to the polarisation damping of the electric and magnetic dipoles which respond to the MW field. The loss tangent is defined by these two contributions [63].

$$tan\delta = \frac{\sigma}{\omega \epsilon'} + \frac{\epsilon''}{\epsilon'} \tag{2.25}$$

$$P_d = \frac{\omega tan\delta \epsilon'}{2} \int_V |E|^2 dV \tag{2.26}$$

$$Q_d = \frac{W}{W_d tan\delta} \tag{2.27}$$

where ϵ' and ϵ'' are the real and the imaginary part of the dielectric constant, σ is the conductivity and ω is the frequency of the field. The dielectric Q factor is $Q_d = (tan\delta)^{-1}$. Typically, the higher the frequency the lower the Q_d as the ϵ'' will increase, the dominant term in the loss tangent, $tan\delta$ is ϵ''/ϵ', [63]. The power dissipation due to the dielectric is P_d and the Q_d can be expressed in terms of the loss tangent, total stored energy and the stored energy within the dielectric materials.

In addition, the resonant frequency and the performance are determined by the geometrical shape and the size of the resonator. The usual parameters for modelling and designing a resonator are the geometry, the size and the materials with a certain dielectric constant and loss tangent which determine the dielectric loss.

Let us consider a cylindrical dielectric resonator, it can be considered as a two-open-end waveguide with a length of L along the z-axis. The field propagates along the axis, while the field is evanescently decaying outside the resonator, which leads to a radiation loss. The mode used in this thesis is the $TE_{01\delta}$ mode, where the magnetic field, H_z, is along the cavity z-axis at the centre and radially outward at the interfaces and the electric field, E_ϕ, is encircling the z-axis forming concentric circles [63]. This mode is dominant if the length, L$<\lambda/2$, is much shorter than the wavelength of the resonant mode, λ. The field components of the TE mode are expressed below.

$$H_z = H_0 J_0(kr) e^{i\beta z} \tag{2.28}$$

$$E_\psi = \frac{i\omega H_0 \mu_0}{k} J_0'(kr) e^{i\beta z} \tag{2.29}$$

$$H_r = -\frac{i\beta H_0 \mu_0}{k} J_0'(kr) e^{i\beta z} \tag{2.30}$$

$$\tag{2.31}$$

where H_0 is the magnetic field amplitude, $\beta = \sqrt{\epsilon k_0^2 - k^2}$ is the propagation constant, k is the wave-number in the resonator, J_0 is the zero order Bessel function and J_0' is the derivatives of the zero order Bessel function. Figure 2.1 shows the magnetic field and the electric field configuration of the $TEM_{01\delta}$ mode in a cylindrical resonator. At the open-ends, z=$\pm$L/2, the E_ψ and the H_r are continuous in the dielectric region and the air region. By substituting the equations above, the equations can be rearranged to a transcendental equation below that the resonant frequency is determined by the k_0 [12].

$$tan(\frac{\beta L}{2}) = \frac{\sqrt{k^2 - k_0^2}}{\beta} \tag{2.32}$$

The resonant frequency of the $TE_{01\delta}$ is expressed as

$$f = \frac{1}{2\pi\sqrt{\mu\epsilon}} \sqrt{(\frac{x_{01}'}{r})^2 + (\frac{\pi}{L})^2} \tag{2.33}$$

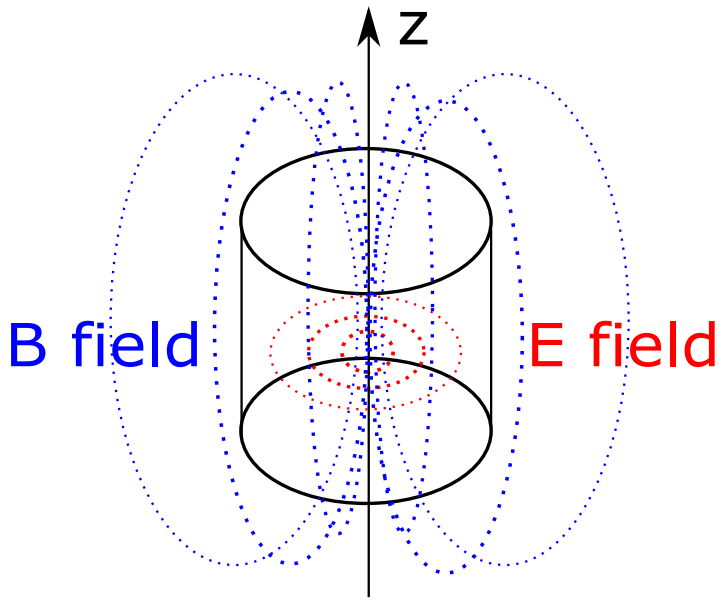


Figure 2.1: The E and B fields of the $TE_{01\delta}$ mode in a cylindrical dielectric resonator.

where r is the radius of the resonator, L is the length of the resonator, x'_{01} is the first zero of the derivative of the zeroth order Bessel function of the first kind [63]. From the equation, the resonant frequency is inversely proportional to the square root of the dielectric constant.

In order to put any samples inside the resonator, the centre region along the axis is empty space. Since the electric field is not strong along the centre axis, this hollow region will not affect the $TE_{01\delta}$ mode much. The hollow region will increase the frequency separation between the $TE_{01\delta}$ and the $TM_{01\delta}$ modes, as the electric field is tightly focused along the axis in the $TM_{01\delta}$ mode, which is the opposite of the $TE_{01\delta}$ mode [63].

To prevent radiation loss, the dielectric resonator is placed inside a copper cavity made of oxygen-free copper. The metal cavity will perturb the fields and shift the resonant frequency. The shift in frequency depends on the stored energy type. If it is electric, the frequency will shift to the lower part of the spectrum. If it is magnetic, the frequency will shift to the higher part of the spectrum [63]. There is a moveable top plate, which is a copper plate attached to a M6 screw, placed in the copper cavity to tune the cavity resonant frequency.

The copper cavity and the dielectric resonators are simulated using the eigenmode frequency

domain simulation in CST microwave studio, results shown in Chapter 3. The inner diameter of the cavity is optimised to produce the highest Q factor using the CST.

The dielectric resonator is made of sapphire, ϵ_d= 11.5 parallel to the C-axis and ϵ_d=9.3 perpendicular to the C-axis, in the microwave spectrum. Sapphire is used as it has a relatively low dielectric loss at room temperature.

2.3 Microwave system charaterisation

Scattering parameters (S parameters) are important parameters that characterise linear microwave systems such as the dielectric resonators and the microstrip antenna used in this thesis. At high frequencies such as microwave frequencies, the measurements of voltage and current become more difficult compared to low frequencies. In addition, the short-circuit and open-circuit termination will introduce unwanted inductance and capacitance during characterisation of the microwave systems. Therefore, the conventional Z-parameters and ABCD-parameters methods for low frequencies are not generally employed in microwaves systems. In S parameters measurements, the microwave power at a port is measured with respect to another port. For example, in a two-port network, there are two input ports, a_1 and a_2 and two output ports, b_1 and b_2 by assuming that the ports are all terminated with the reference impedance [65].

$$a_1 = \frac{V_1^+}{\sqrt{Z_0}} \qquad (2.34)$$
$$b_1 = \frac{V_1^-}{\sqrt{Z_0}}$$

where V_1 is the incoming wave in the forward and backward direction and Z_0 is the port impedance. The S parameters are defined as:

$$\begin{aligned} S_{11} &= \frac{b_1}{a_1} \\ S_{12} &= \frac{b_1}{a_2} \\ S_{21} &= \frac{b_2}{a_1} \\ S_{22} &= \frac{b_2}{a_2} \end{aligned} \tag{2.35}$$

S_{11} and S_{22} are the reflection coefficients for port 1 and port 2, whereas S_{12} and S_{21} are the transmission coefficients from port 1 to port 2 and from port 2 to port 1. In general, the S parameters are complex and contain the phase response of the systems. The phase response is more important in communication systems and not in this thesis. The insertion loss of a system can be extracted from the transmission coefficients and the reflection coefficients are related to the input impedance. The reference impedance is usually 50 Ω. For an arbitrary impedance terminated system, the input and output impedance, Γ_i and Γ_o, of a system is defined as [66]:

$$\begin{aligned} \Gamma_i &= S_{11} + \frac{S_{12}S_{21}a_2}{b_2 - S_{22}a_2} \\ \Gamma_o &= S_{22} + \frac{S_{12}S_{21}\Gamma_s}{1 - S_{11}\Gamma_s} \end{aligned} \tag{2.36}$$

where Γ_s is the source impedance. In the impedance-matched condition, the insertion loss is defined as:

$$IL = -20log_{10}(S_{21}) \tag{2.37}$$

It is important to note that when the impedance of the source and the impedance of the load are matched, the reflection is minimised or complex conjugate matched that the power delivered to the load is maximised.

2.4 Microstrip antenna

Microstrip antennas consist of metallic patches on a grounded dielectric substrate, which is fabricated using printed circuit technology. The idea was proposed in the 1950s [67][68]. Microstrip antennas are extensively used in the microwave industry due to the small form factor, cheap of fabrication, and ease of integration to microwave integrated circuits. These features allow more customisability and variants to be developed for different applications. In this thesis, custom-designed microstrip antennas are used for providing the modulating electromagnetic field interacting with defects. The antennas are designed to support a broad-band microwave frequency centred at 2.87 GHz that correpond to the zero-field splitting of the NV^- centre. The broad-band feature is required as it accounts for any frequency shift by a small external magnetic field which is a few hundred MHz, around 10%, as well as manufacturing errors. Microstrip antennas can be modeled analytically using a cavity model with magnetic walls, an open-ended transmission line model or with a dyadic Green's function method [69] [70][71]. Generally, the permittivity of the substrate is small, as the bandwidth will decrease with a higher permittivity, and the thickness of the substrate is positively correlated to the bandwidth [70]. Provided that the substrate is not too thin, $<0.01\ \lambda$, surface wave excitation is usually considered the primary loss factor for microstrip antennas [72]. When the substrate are getting thicker, the energy will couple to those modes instead of the radiation modes. This will lead to a decrease in radiation efficiency. The upper limit of the thickness is defined as 0.11λ, which is about 11.5 mm for 2.87 GHz, as the input might become inductive entirely. The feeding method used is a tapered microstrip line that is impedance matched. Proximity feeding is another popular feeding method that allows a wider bandwidth and reduced spurious emission and reduced inductive effect, but it is difficult to fabricate and align, and it is excluded.

The antenna design is based on a circular patch [73]. The dimensions and the design of the antenna are found by using the electromagnetic simulations in CST Microwave Studio. The details of the simulation is discussed in Chapter 3. The microstrip antenna consists of only the conducting patches made of copper, the FR-4 substrate and the copper ground plane. The microstrip antenna supports hybrid fields consisting of TE and TM modes [12]. The resonant frequency of TM_{nm} modes of a circular patch antenna is given as [74]:

$$f_{nm} = \frac{A_{nm}c}{2\pi r\sqrt{\epsilon_r}} \tag{2.38}$$

where A_{nm} is the roots of the eigenmode, r is the radius of the circular patch and the ϵ_r is the dielectric constant of the substrate. The small hole introduces an inductance and the slot introduces capacitance. The feed line is impedance matched to 50 Ω.

The characterisation methods are the S-parameters, the voltage standing wave ratio, the field profiles and the line impedance at the port interface. The S-parameter, S_{11}, measures the reflected signal from the stimulated signal from port 1 at the same port. The signal from the port transmits through the coplanar waveguide and is reflected back to the port. The S_{11} is expressed as the power of the reflected signal and the frequency. In order to maximise the field strength, most of the signal should not reflect back to the port. The reflection coefficient of the interface is determined by the ratio of the impedance of the port, which is 50 Ω, and the impedance of the coplanar waveguide.

$$\Gamma = \frac{Z_s - Z_0}{Z_s + Z_0} \tag{2.39}$$

where Z_0 is the impedance of the port and the Z_s is the impedance of the antenna. The reflection coefficient is minimised as the impedance of the port equals the impedance of the system, assuming that the source is real. The impedance is matched by adjusting the w, S and the geometry of the tracks.

For the microstrip antenna, the track is tapered to match the impedance at the port and the resonant frequency design of the antenna. The antenna consists of a small hole acting as an inductor and a narrow gap acting as a capacitor. The sample is placed in the hole. The sizes of the hole and the gap are adjusted to fit the resonant frequency at 2.87 GHz. The thickness of the ground plane and the top copper layer is 0.018 mm. The thickness of the substrate is 1.6 mm. The radius of the circular antenna is R = 20 mm. The radius of the small hole is r = 2.05 mm. The width of the gap is g = 0.3 mm and the length is l = 6.25 mm. Another parameter, s = l-R is introduced, it is the distance between the centre of the antenna to the centre of the hole. The antenna can be modelled as an LC circuit, where the resonant frequency is determined by all the parameters, the inductance L $\propto$ r is determined by the small hole, the capacitance C $\propto$ l/g is determined by the size of the gap and the resistance R $\propto$ 1/(R-s-r) [73]. The resonant frequency of the antenna is f = $\frac{1}{2\pi\sqrt{LC}}$ and the bandwidth is δ f = $\frac{R}{L}$ [73].

2.5 Diamond

Diamonds are important materials that have excellent mechanical and optical properties. The properties of diamonds depend on their lattice structure and structural defects. Ideally, diamonds are made of purely carbon atoms, which form a diamond cubic structure, which is face-centred, the schematic diagram of the unit cell of a diamond is shown in Figure 2.2. The covalent bonding between the carbon atoms is the sp^3 hybridised bonds provided by the 4 outer unpaired electrons of a carbon atom.

The pure diamond is colourless and transparent over the visible spectrum. In natural diamonds, many impurities are present in diamonds such as nitrogen and silicon. These impurities impact the colour. Thus, it is important to investigate the absorption and luminescent properties of the defects. Moreover, defects have charges and spins that provide a way to study the interaction with electromagnetic fields and quantum phenomena. Furthermore, the defects in diamonds provide a place to study the theoretical works on point defects, symmetry and quantum physics.

Nitrogen is the most dominant impurity present, as it is rich in the environment and similar in size to carbon. Based on the amount of impurities in the diamond, there are four classes of diamond: type Ia, type Ib, type IIa and type IIb. The type I diamond, which is the most common type, consists of a substantial amount of nitrogen impurity that the nitrogen can be detected in IR spectroscopy. The nitrogen concentration is about 0.1 %. About 98 % of diamonds are type Ia, and the nitrogen concentration is up to 0.3 % [75]. It can be subdivided into type IaA and type IaB. The type IaA diamond consists of A-centres, which is a pair of nitrogen atoms and does not affect the colour of the diamonds, while the type IaB diamonds consist of aggregates of nitrogen atoms such as the B-centres, which is a vacancy surrounded by four nitrogen atoms [76]. Type Ib diamonds are much rarer than type Ia in nature, about 0.1 % of natural diamonds, consist of C-centres, which is a substitutional nitrogen atom. The nitrogen concentration is up to 500 ppm. The Type II diamonds contain only a trace amount of nitrogen, which is less than 1000 ppb. Usually, the nitrogen content is not measurable. Type IIa diamonds are the purest type of diamond with almost no impurities. They are colourless. The type IIb diamond consists of boron impurities. The boron atoms have one fewer outer electron than the carbon atoms. The presence of boron atoms, about 1000 ppb, causes the diamond to become a p-type semiconductor [75].

2.5.1 Defects in diamond

The impurities take the forms of the substitutional defect and the interstitial defect. If a carbon atom in the lattice is replaced by other types of atoms or a vacancy, where a carbon atom is missing, the replaced site is called a substitutional defect. If the impurity atom is added to the lattice without replacing the original atom, the site is called an interstitial defect.

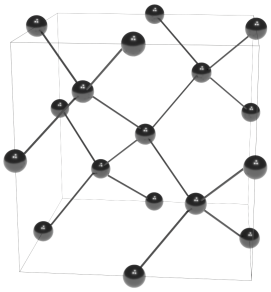
The impurity atoms might be different in size; they have a different number of outer electrons, resulting in additional optical and electronic properties. Furthermore, different impurity atoms possess different defect symmetries, for example, the NV centre has a C_{3v} symmetry, whereas the SiV centre has a D_{3d} symmetry, resulting in changes in the physical properties of the original crystal such as the energy levels and local strain. For example, the type IIa diamonds do not have one-phonon absorption, at 7-13 μm, due to the crystal's inversion symmetry. The other types of diamonds break the local symmetry and result in one-phonon absorption [77].

The most common point defect is the nitrogen defect, where nitrogen atoms replace carbon atoms, the nitrogen defects consist of up to 1% of the total mass [78]. If there is a substitutional nitrogen atom replacing a carbon atom, the defect is called a C-centre. The natural form of the C-centre is neutral. High-pressure high-temperature synthesis diamonds contain a substantial amount of C-centres. The extra electron from the nitrogen acts as a donor electron and forms an energy level within the 5.47 eV band gap of the diamond that can be excited by 2.2 eV photons.

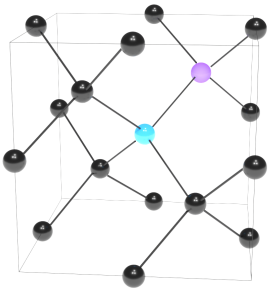
The NV centre consists of a nitrogen atom replacing a carbon atom in a diamond lattice, and a vacancy adjacent to the nitrogen. The NV^- was first reported in 1965 by Du Preez, who studied the spectral properties of nitrogen-rich diamond[79]. The electronic properties and the structural properties are investigated later [80] [81].

There are two charged states of the NV spin centre, NV^0 and NV^-. The zero phonon line of the NV^0 is at 575 nm, and the lifetime is 19±2 ns. The zero phonon line of the NV^- is at 637 nm, and both centres have an extensive phonon sideband.

In this thesis, only the negatively charged NV^- is primarily considered as only the negatively charged state contributes to masing, so the NV centres refer to the NV^- centres in the rest of the text and the NV^0 will be stated specifically. However, the presence of NV^0 is significant,



(a) Diamond lattice.



(b) Diamond lattice with NV centre.

Figure 2.2: (a) The diamond lattice unit cell. The carbon atoms are represented by the black sphere. (b)The NV centre in a diamond lattice unit cell. The carbon atoms are represented by the black spheres, the vacancy is in purple and the nitrogen atom is in cyan.

thus, it is useful for characterising the diamonds and the NV centres as a whole.

Figure 2.2 shows the diamond lattice structure and the NV centres lattice structure. Silicon vacancies (SiV) consist of a substitutional silicon atom that replaces two carbon atoms and two adjacent vacancies shown in Figure 2.3. Similar to the NV centre, the SiV centre also has two charged states, SiV^- and SiV^0. Figure 2.4 depicts the conduction band, the valance band and the energy levels of NV^- and NV^0 centres and the photoconversion between the two.

The zero-phonon line is at 737 nm and a phonon sideband at 760 nm and the lifetime is 1.28 $\pm$ 0.06 ns [82]. The zero-phonon line of the SiV^0 is at 946 nm and a phonon sideband at 976 nm and the lifetime is 1.8 ns [83]. One of the most prominent features is that the Debye-Waller factors, 0.7 [84], is much higher than the NV centre, which is 0.04 [85], resulting in more emission from the zero-phonon line, and a narrow linewidth of 1 nm, the inhomogenous broadening is much less than the NV centres [86]. The SiV centre is a D_{3d} point group, which results in an inversion symmetry and no permanent electric dipole. This will allow the SiV centre to be immune to an inhomogeneous lattice field that results in Stark shift to the first order. The SiV centre is referred to as the SiV^- centre in the rest of this thesis. The SiV centre has a spin 1/2. The ground and the excited states are double due to the spin-orbit interaction. The silicon atom can be implanted into the diamond via ion implantation.

[86] The germanium-vacancy centre is another optically active defect centre similar to the SiV

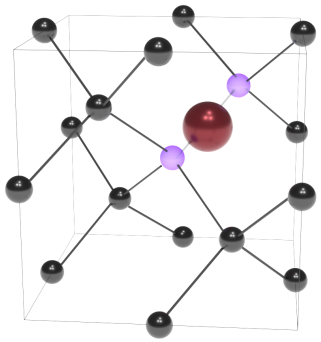


Figure 2.3: The SiV centre in a diamond lattice unit cell. The carbon atoms are represented by the black spheres, the vacancy is in purple and the silicon atom is in brown.

centre. It has a narrow zero-phonon line at 602 nm, and the lifetime is 1.4-5.5 ns [87]. Apart from GeV, there are other centres that have a similarer D_{3d} symmetry as the SiV such as the lead-vacancy and nickel-vacancy.

2.5.2 Diamond synthesis process

There are two main methods to synthesise bulk diamonds: the chemical vapour deposition (CVD) method and the high-pressure high-temperature (HPHT) method. The HPHT method mimics the natural environment for diamond formation in the Earth's mantle. This provides a thermodynamically favoured environment for diamond formation rather than graphite formation. It was first shown in 1955 [88]. The diamond is grown on a seed diamond in a chamber where graphite is used as the carbon source and metallic catalysts, such as Iron and Nickel, are used to transport the carbon atoms to the seed from the graphite. The temperature reaches 1400°C, the pressure reaches 5 GPa [89]. The CVD method involves growing diamond layers, where the carbon atoms are from a gas mixed with carbon and hydrogen, usually methane, on a diamond substrate. The gas is heated via filament or microwave to form plasma above the substrate, and the carbon atoms deposit on the substrate in the form of radicals. The role of the hydrogen radicals is to prevent the formation of the graphite bonding, sp^2 hybridisation [90]. In this case, no high temperature and high pressure are required. The internal strain is larger than the HPHT diamond due to the delocalisation during the growing process. The diamond formation is favoured as the chemically kinetic condition is favoured.

HPHT diamonds are nitrogen-rich, and the concentration is usually above 100 ppm [91]. Whereas, CVD diamonds have only a few ppm or down to 1 ppb nitrogen concentration [92]. The nitrogen is incorporated into the diamond from many sources during the process such as residual air.

The composites of NV centres are vacancies and nitrogen centres. The amount of nitrogen centres can be controlled during the diamond synthesis process and nitrogen ion implantation. Ion implantation is a more controllable way to control the nitrogen concentration than the synthesis process. However, the ion implantation will damage the diamond lattice and cause a detrimental effect on the coherence time [93]. The vacancies are created via high-energy particle irradiation. High energy electrons are favoured as the electrons are light and less destructive to the diamond lattice compared to other heavier particles such as neutrons and protons [94]. The electrons are also easy to control. After the creation of the vacancies, the next process is annealing, which drifts the vacancies in the lattice. The annealing temperature is about 600°C. Higher temperature will result in over-annealing and the conversion to graphite [77]. An NV centre will form when the vacancy is captured by a nitrogen centre, and an additional electron is required to form an NV^- centre. The additional electrons are usually provided by adjacent charge donors [92].

The formation of NV centres is complicated as it involves estimating the formation energy and the energy levels of the charge transition of different possible defects. Diamonds are good insulators with a large bandgap, so it is difficult to use deep-level transient spectroscopy to determine their energy levels [91].

Early studies investigated the spectrum of natural and synthetic diamonds and deduced the properties of the vacancy such as charged states and the substitutional nitrogen atom in radiation-damaged diamonds by high energy electrons or neutron irradiation [95, 96, 97] as well as electron spin resonance studies and hyperfine interactions between ^{14}N and ^{13}C in diamonds [98].

2.5.3 NV centre properties

In this thesis, only the room-temperature electronic structure of the NV centre is considered. An NV centre has six electrons, five of them are from the carbon dangling bands and one of

them is from a nearby donor. It has a C_{3v} symmetry. For simplicity, in the electronic structure, two holes are considered instead of six electrons. The two holes form singlet, $^1A_1$ and ^1E, and a triplet spin states, such as the ground triplet state $^3A_2$ and the excited triplet state ^{3}E.

The NV centre has $S = 1$ electronic spin, which corresponds to a triplet state, m_S= +1, 0, -1. The energy of these three states is lifted due to the spin-spin interaction between the unpaired electrons. The splitting is called the zero-field splitting. This arises in non-cubic symmetric systems with S greater than 1/2. Both spin-spin interactions and spin-orbital interaction will contribute. The zero-field splitting of the ground triplet state is 2.87 GHz, which breaks the degeneracy of the triplet state into $m_s = 0$ and $m_s = \pm 1$. The m = ±1 degeneracy can be split by temperature, strain and magnetic field. When an external magnetic field is applied, the spin states will shift by the amount of f/B = 28 GHz/T. Thus, the m_S = -1 states will go lower than the $m_S = 0$ state when the external magnetic field is at 102.5 mT.

The excited triplet state has a zero-field splitting of 1.42 GHz at room temperature. At low temperatures, the excited triplet states are split into orbital doublet due to the non-axial strain, at room temperature, the averaging of the doublet decouples the spin and the orbit [99]. The fine structure of the excited triplet state dependent on strain and temperature is more than the ground triplet state at low-temperature [100][99][101].

The energy gap between the ground triplet state and the excited triplet state is 637 nm corresponding to the zero-phonon line. The transitions that involve phonons are known as phonon sideband transitions. The zero phonon line is sharp and it does not involve phonons, the lifetime of the excited state determines the linewidth of the zero-phonon line, and crystal strains will broaden the linewidth. At room temperature, the phonon sideband is the preferred emission band.

The excited electrons decay back to the ground states and emit light into the zero phonon line or the phonon side band, or undergo intersystem crossing that converts the triplet state to the singlet state, then decay back to the triplet ground state with an equal probability to m_s = 0 and $m_s = \pm$ 1. The intersystem crossing is primarily due to the spin-orbit coupling states, resulting from the magnetic field from the orbiting electrons and the spins. When the spin-orbit coupling is weak, the spin-spin interaction of the electrons and hyperfine interaction between the electrons and the nucleus will contribute to the intersystem crossing [102]. The m = ±1 states are more likely to undergo intersystem crossing. Thus, after a few optical excitation

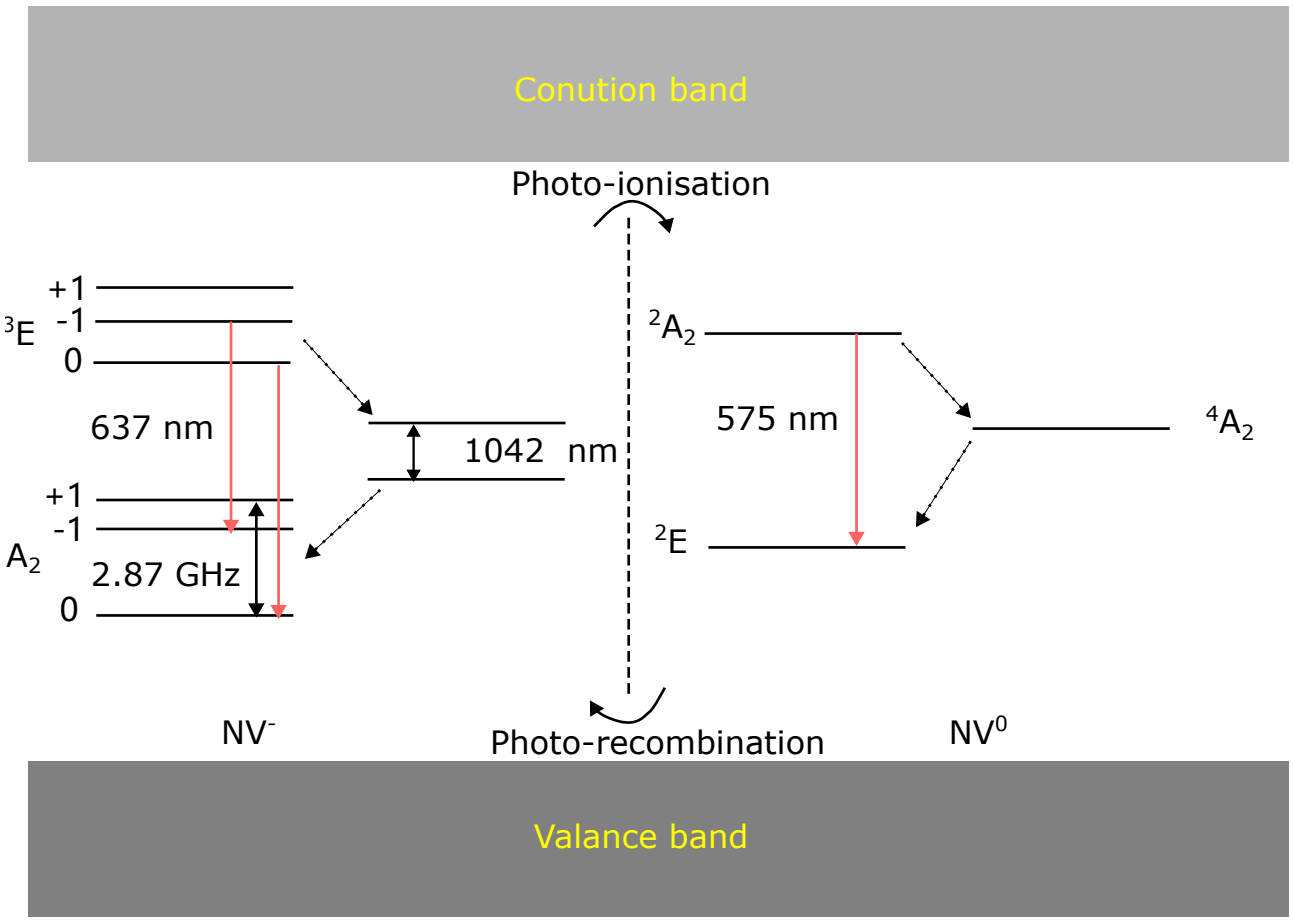


Figure 2.4: The energy levels of the NV centre. NV^-: The triplet states are on the left, showing the 532 nm excitation and the 637 nm zero-phonon line. The spin-conserving intersystem crossing to the singlet states on the right, shown in the dotted lines. NV^0: The doublet ground state, the excited state and the metastable state.

cycles, the NV is polarised to the $m_s = 0$ state.

The triplet excited states have a lifetime of approximately 10 ns [103] while the singlet excited state has a lifetime of approximately equal or less than 1 ns [104] and the singlet ground state has a metastable state lifetime of 150 ns.

At room temperature, the excited vibrational state has a lifetime of approximately 1 ps [105]. The optical transitions between energy levels are spin-preserved, as the NV centres only have a weak spin-orbit interaction. Due to the interaction with ^{13}C nuclear spins, the zero-phonon line is shifted by 2.1 meV. Importantly, the spin-orbit interaction can be neglected due to thermal averaging [103]. However, the Frank-Condon effect and the wide absorption band make the 532 nm laser a suitable light source for excitation. In another report, it is shown that the optimal

excitation ranges from 510 nm to 540 nm [106]. The energy gap between the two singlet levels is 1042 nm.

Similarly, the nitrogen nuclear spin, ^{14}N, has a triplet ground state as the electron has both $|0\rangle_n$ and $|\pm1\rangle_n$ that are split by 4.95 MHz due to the nuclear quadruple coupling [107]. It is important to note that the interaction between the electronic spin and the spin bath affects the dephasing of the nitrogen nuclear spin. For a m = 0 electronic state, dephasing is primarily due to the nuclear magnetic dipole-dipole interaction of the surrounding spin bath, whereas, dephasing of the m = ±1 electronic state is due to the electron-induced gradient magnetic field on the spin bath [108].

The emission intensity of NV centres with a magnetic field along the $< 111 >$ axis is temperature dependent and it becomes stress-dependent at low temperature [103]. The Hamiltonian of an NV centre is expressed in the following equation [109]:

$$H = \hbar D(S_z^2 - \frac{2}{3}) + \hbar\gamma \mathbf{B}\cdot\mathbf{S} + g_z E_z(S_z^2 - \frac{2}{3}) + g_{xy}\{E_x(S_xS_y + S_yS_x) + E_y(S_x^2 + S_y^2)\} \quad (2.40)$$

where the z-axis is the $< 111 >$ axis, $\mathbf{B}$ is the magnetic field, $E_{x,y,z}$ are the electric field components along x, y and z directions, $g_{z,xy}$ are coupling constants along and perpendicular to the z axis, D is the zero-field splitting, S_z is the spin operator projected on the z-axis and γ is the electron gyromagnetic ratio, $\gamma = 2\pi\times$ 28 GHz/T. The Zeeman interaction breaks the degeneracy of the $m_s = \pm1$ states. Hyperfine interactions split the $m_s = 0$ and $m_s = \pm1$ states further into sublevels, separating by a few MHz. In addition, the hyperfine coupling Hamiltonian is expressed as follows:

$$H = \Omega S_x + \omega_I I_z + AS_zI_z + BS_zI_x \quad (2.41)$$

where I is the spin of the nucleus, and the first term is contributed from the microwave Rabi field. A is the hyperfine constant, A = 60 MHz for ^{15}N in the excited state [110]. It is important to note that the I_z component exchange between two nuclei occurs when the magnetic field is applied along the z-axis, which will lead to spin dephasing [111]. In general, the hyperfine interaction has an isotropic part due to the Fermi contact and an anisotropic part.

A typical diamond contains more than 98.9% of spin-free ^{12}C nuclei and a decoherence time of NV centres more than 1.8 ms at room temperature [111]. Decoherence time is limited by the spin-spin dipolar interaction for dense NV centres. The main source of decoherence is the nuclear spin bath due to ^{13}C nuclei. The stable fluorescence property of the NV centre is observed [112].

As mentioned earlier, the NV^0 can play a role in characterising the diamonds and the NV centres as a whole. The electronic structures and their characteristics are introduced. In a simple picture, NV^0 has only 5 electrons and it is modeled as a S = 1/2 ground state, ^2E, an S = 3/2 excited state, $^2A_1$, and a metastable state, $^4A_2$ [113]. In contrast to NV^-, the NV^0 does not have a magnetic resonance signal from its ground state due to strain broadening [114], however, it exhibits an EPR signal from the ground state if a CW optical excitation is applied [115].

Chapter 3

Experimental Methods and Apparatus

3.1 Optical characterisation methods

One of the aims of this thesis is to characterise point defects in diamonds, primarily NV^- and NV^0 spin defects in diamonds. These spin defects all have a magnetic moment that is suitable for magnetic resonance experiments and fluorescence emission when they are excited by light, NV^- defects in particular are suitable to be optically read and polarise the spin state. The defects have many important parameters such as the lattice relaxation time, T_1, the coherence time, T_2, the spin dephasing time, T_2^*, fluorescence lifetime imaging and the polarisation spin state down to a small region or even a single point defect which reveals the local environment around the spin defects and the crystalline structure.

To achieve this aim, a multi-functional fluorescence microscope that is capable of measuring spectral, fluorescence lifetime, and spin relaxation time information, was built. The fluorescence microscope is integrated with a microwave antenna and magnets to perform optically detected magnetic resonance (ODMR) experiments. The fluorescence microscope is based on a confocal scanning laser microscope. The spectral information is measured by a spectrometer connected to the microscope. A filter wheel is used to switch between filters for both spectral measurements. The laser and the microwave are modulated using a Pulse Streamer 8/2 from Swabian instruments.

3.1.1 Scanning laser confocal microscope

In a conventional fluorescence microscope, a wide field illumination excites a large volume of the sample, the fluorescent light from the sample through a filter that only allows the fluorescent light to pass to the camera and filter out the excitation light. The camera will pick up the fluorescence from the focal plane and a lot of background fluorescence, which contributes to Poisson noise and degrades the signal-to-noise ratio.

The idea of a confocal scanning laser microscope is to use a focused laser spot with a pinhole to only excite a small spot on the focal plane without exciting other parts of the sample. The advantage of using a laser is that it is monochromatic and it is well focused. Even though the laser spot is small, it still excites samples above and below the focal planes. The light from the focused spot is collected using a pinhole at the image point in front of a photodetector to block the majority of the out-of-focus fluorescence from above or below the focal plane while passing the in-focus light from the focal plane. As a result, the image quality and the resolution increase, as the pinhole will collect the central part of the Airy disk and less intensity from the side rings [116]. The size of the focused spot is diffraction limited, the image is known as the Airy disk, which is the point spread function of a point source. The size of the Airy disk is 1 Airy unit (AU). If the size of the pinhole is the same as the size of the in-focus spot, which equals 1 AU, the effect of blocking the out-of-focus fluorescence is maximised [117]. The larger the pinhole size, the more out-of-focused fluorescence is collected. However, if the pinhole size is smaller, the fluorescence intensity reduces. The actual optimal size of the pinhole is determined by the magnification of the objective, the typical size is between 0.6 AU to 0.8 AU [118]. The diameter of the focused spot in the image plane is expressed, according to the Rayleigh criterion:

$$D = 2\frac{0.61\lambda}{NA}M \tag{3.1}$$

where λ is the optical wavelength, NA is the numerical aperture and M is the magnification. When the magnification is one, the diameter of the spot in the image plane is the same as the spot in the focal plane.

The signal is collected using a photomultiplier tube (PMT), which is a high gain, fast response, single-photon avalanche photodiode or Charge-coupled device (CCD) camera.

The full image of the sample is built by scanning over the sample plane similar to an analogue television. Either the laser excitation light or the sample stage can be moved. In the first case, a set of oscillating galvanometer mirrors is used to scan across the field of view. Usually, one of the mirrors is the fast mirror that scans across a row horizontally, and the other mirror is the slow mirror that moves vertically after the fast mirror scans across one row.

In this thesis, the moving part is the sample stage, this is beneficial for reducing the off-axis aberrations of the objective [118]. However, the total acquisition time might be longer, and it requires a high precision stage. The total acquisition time is limited by the minimum dwell time of the camera.

When the thickness of the sample is very thin, there is no particular need for the confocal setup, which is time-consuming. In this thesis, the thickness of the samples varies around 500 μm which is well above the optical section, z, of the microscope which is estimated to be about 17 μm if the NA is 0.4, the wavelength is 532 nm and the magnification is 10. The diameter of the focused spot under the same condition is about 1.6 μ m.

$$z = 2\frac{n\lambda}{NA^2} \tag{3.2}$$

where n is the refractive index of the sample.

The larger the size of the pinhole the higher the light transmission and lower the resolution. At 1 AU, 85% of light is going through the pinhole, at 0.5 AU, only 60% light goes through [119].

A laser is used as the light source, as it can provide a monochromatic and collimated excitation to the defects. The excitation light passes through a set of two steering mirrors that can move the light along both the X and Y directions on the sample plane. The excitation light is focused to a spot on the sample plane by an achromatic microscope objective. An achromatic microscope objective is corrected for axial chromatic aberration, which occurs when light with different wavelengths is focused on different focal planes. Another benefit of achromatic lenses is that they are also corrected for spherical aberration. Spherical aberration occurs when the rays incident at the edge of the lens are refracted more and focused on a focal plane that is close to the lens than the rays incident at the lens close to the centre. They are usually made of a doublet consisting of two pieces of material with different dispersions such as a concave flint glass, which has a high dispersion, and a convex crown glass, which has a low dispersion. An

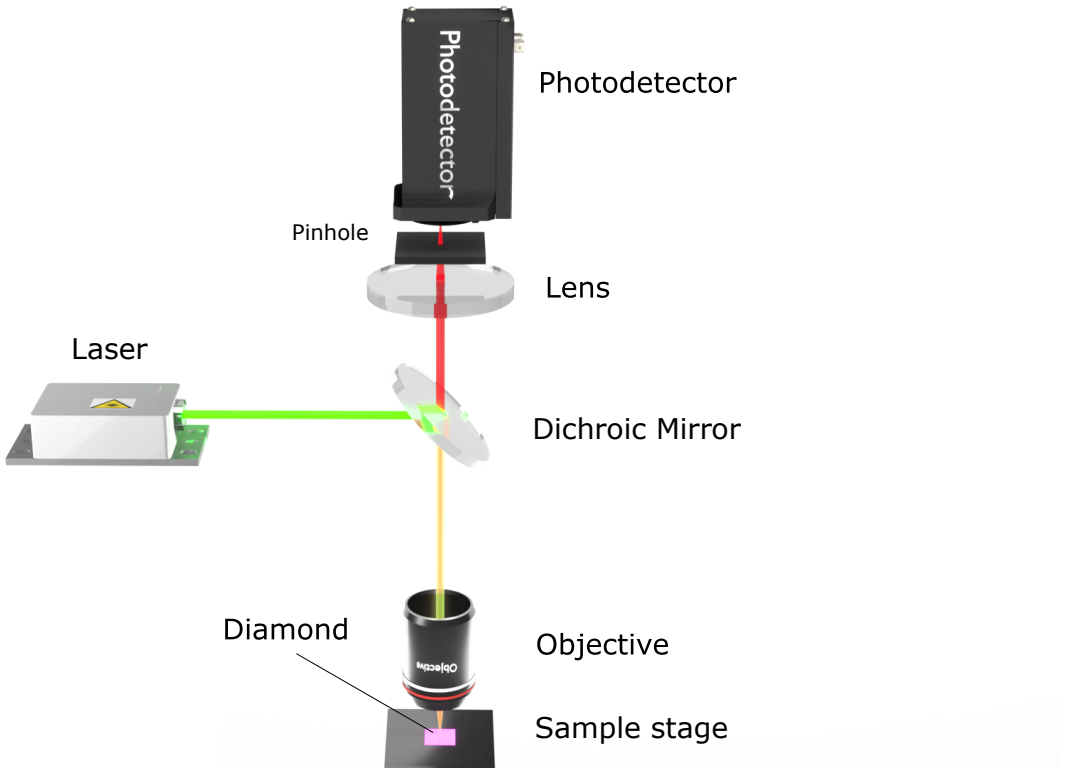


Figure 3.1: This diagram shows the confocal microscope setup.

achromatic doublet corrects for only two wavelengths, which means that only two wavelengths are brought to a single focal plane.

The fluorescent light from a focal spot is collimated by the same objective and passes through a dichroic mirror that separates the excitation light and the fluorescent light. Then, the fluorescent light is focused by a tube lens onto a detector sensitive to the light intensity. PMT is a type of high gain, high dynamic range and responsive photon single point detector. It consists of a photocathode which converts an incoming photon to an electron and multiple dynodes accelerating and multiplying the electron. The electrons are attracted to the anode which collects most of the electrons and turns the electrons into a current. The sensitivity can be controlled by the driving voltage. However, the quantum efficiency is low, the quantum efficiency is usually peaks at 25 %, and the quantum efficiency is higher in the blue and the green spectrum. The quantum efficiency is low at the red and the infrared part of the spectrum as the photon energy decreases.

Figure 3.1 shows a simplified setup of a fluorescence confocal microscope. The dichroic mirror reflects the excitation and transmits the fluorescence. A pinhole is used to select the in-focus

light.

3.1.2 Fluorescence lifetime imaging

The fluorescence lifetime is the time an excited electron stays in the excited state before it emits a photon and returns to the ground state. The transition only happens between either triplet excited state to triplet ground state or singlet excited state to singlet ground state. The time scale is generally in nanoseconds. In contrast, phosphorescence takes a much longer time to decay, as this occurs at the forbidden transitions between different spin multiplicities, such as from triplet to singlet states or vice versa.

In reality, the electron is affected by the environment and undergoes non-radiative decay, such as intersystem crossing between singlet and triplet states, turning into heat, and the fluorescence lifetime is not the same as the natural fluorescence lifetime when it is not affected. The ratio of the fluorescence lifetime to the natural fluorescence lifetime determines the quantum efficiency. The fluorescence intensity decays exponentially. It takes lifetime, τ, to decay to 1/e of its initial intensity.

The excitation source is a pulsed laser with a short pulse duration. During the data acquisition, the fluorescence lifetime measurements are recorded across the sample to form a lifetime image. It is important that the convolution effect is taken into account. The intensity profile is the convolution of the instrument response function (IRF), which determines how the instrument responds to a delta signal, with the optical signal. Ideally, the IRF is an infinitely narrow sharp peak. There are many factors causing the broadening of the IRF. The detector response function and the excitation source, which set the timing reference, can broaden the IRF. The uncertainty in timing during the conversion from the photon pulse to the electrical signal is a dominant broadening factor. Furthermore, the jitter of the TCSPC causes broadening of the IRF. The total IRF broadening is the root-mean-square of the uncertainties from each component. Thus, the components with the highest uncertainty dominate the IRF broadening. It is necessary to measure the IRF before or after a measurement. This can be conducted by placing a non-emissive scattering sample at the sample plane. The IRF is a decaying curve with a certain decay rate. The fluorescent lifetime measurement is meaningful if the lifetime is much longer than the IRF. However, a deconvolution with the IRF can be used to improve the

experimental results.

Time correlated single photon counter (TCSPC) is used for counting the photons in the time domain. The TSCPC has two inputs from the excitation source and the single photon detector. The time starts when the laser excitation pulse is applied as a reference. The detector records the arrival time of a single photon with respect to the start time. The laser is applied multiple times to record a sufficient amount of photons. The result is a histogram of photons arrival times. It is important that only a single photon is recorded.

Photon detectors have a parameter called dead time when the detector does not respond to the following photon arrival event after detecting a photon. In the case of high count rates, the detector only records the first arrival photon and does not respond to the following photon during its dead time. This will result in an incorrect histogram. This effect can be reduced by decreasing the count rate.

Apart from the dead time, photon detectors have other errors, such as the time delay between the photon incident and outputting an electrical signal and the quantum efficiency, which determines the efficiency of detecting a photon. PMTs are normally used as the single photon detector due to its fast respond time. The PMT has a high count rate ranging from a few to a few million counts per second. The timing resolution and the electron transit time spread, which determine the IRF, is also low enough to resolve the fluorescent decay. Other detectors like single photon avalanche diode and superconducting nanowire, are also capable of counting photons at low counting errors.

There is an electronic discriminator used for further reducing the noise by rejecting pulses with low power levels.

There are two types of measurement: frequency domain and time domain. The time domain measurement requires a pulsed excitation source, a single photon detector and a TCSPC that records the photon arrival time at each pixel. The resulting intensity profile will be a multi-exponential decay that is characterised by the fluorescence lifetime. In the frequency domain, the excitation source is modulated, usually sinusoidal. The fluorescence response will be phase shifted as the time delay is present between the excitation and the fluorescent emission. The amplitude of the fluorescence response is smaller than the amplitude of the excitation modulation. The phase shift and the decrease in amplitude are characterised by the fluorescent

lifetime. The shorter the lifetime the smaller the phase shift. The time delay between the excitation and the fluorescent emission causes demodulation, which is characterised by the demodulation lifetime. The detector is modulated at the same frequency as the excitation source, and collects the fluorescent emission. The detector modulation is phase shift by a small step to measure the fluorescent emission at a different phase with respect to the excitation source. Multi-exponential decay lifetime can be measured using different modulation frequencies.

A Time Tagger Ultra from Swabian instruments, which has a dead time of 2 ns and a RMS jitter of 8 ps, is used for the TSCPC. The time tagger assigns a stamp for each event detected from the single photon detector.

3.1.3 ODMR

Optically detected magnetic resonance (ODMR) is a powerful magnetic resonance technique used for fluorescent defects such as NV centres in diamonds. ODMR combines photofluorescence technique and magnetic resonance techniques that detect the fluorescence intensity and sweep the microwave to find the resonances [120].

The spins in the ground singlet state of the NV centre can be excited using a green laser to the excited singlet state.

By illuminating the NV centres, the population of the m = 0 state increases. A MW pump at the zero-field splitting at 2.87 GHz pumps the spins to the m = ±1 state from the m = 0 state, which results in a reduction of fluorescent light intensity. An external magnetic field parallel to the NV axis splits the m = ±1 state into m = -1 and m = +1 states by $g_e \mu_B B$, where g_e is the g-factor of the electron, μ_B is the Bohr magneton and B is the external magnetic field. Any transverse magnetic field causes the spin states to be mixed. The reduction of the fluorescent light intensity occurs at the two separate resonant frequencies. ODMR can be either continuous wave (CW) or pulsed. In a CW ODMR setup, the laser and the MW are applied continuously to initialise and pump the defects simultaneously; and readout the fluorescence intensity throughout the measurement. In a pulsed ODMR, the laser is applied at the beginning to initialise the spins and at the end to readout spins, the MW is applied for a period that flips the spins after the laser initialisation. It was introduced in studying NV centres in 2011 [121]. The linewidth at the resonance frequency of the fluorescence spectrum is power-bordered in the

CW ODMR induced by the MW. It is a trade of getting more power to pump the spins and the narrow linewidth to resolve subtle features.

3.1.4 Spin lattice relaxation time imaging

Spin lattice relaxation time imaging is a useful tool to map the relaxation time of a sample and determine the distribution of the inhomogeneity in the relaxation time. The relaxation time is an important factor in determining the masing threshold. The spin-lattice relaxation time of NV centres can be measured using all-optical methods that is using an excitation pulse to initialise the NV centres and an optical readout pulse after a time period τ, where τ is a range from microseconds to milliseconds in a step of microseconds.

3.2 Optical characterisation setup

The optical characterisation uses a multi-dimensional scanning laser confocal microscope which is able to examine a sample with various optical methods such as ODMR, pulse sequences and fluorescence lifetime. The optical setup can be divided into three sections: CW laser section, supercontinuum laser section and sample stage section.

The optical characterisation setup consists of three laser sources, CW 532 nm laser, laser quantum Ventus 532, which is used as the excitation source for the ODMR and the fluorescent microscope.

A 457 nm blue CW laser, MLL-U-457nm-100mW from CNI Laser, is used as the excitation source for the Raman spectroscopy. The maximum output power is 126.5 mW. The diameter of the beam is 0.58 $\times$ 0.768 mm, and an NKT FIU-15 supercontinuum laser, which has a total power of 5.5 W and and visible power of 1.5 W. The repetition rate is from 0.15 MHz to 78 MHz. The total output spectrum can range from 400 nm to 2400 nm. In this thesis, only the visible spectrum is used. The output of the supercontinuum laser is fibre coupled to an IR filter that cuts off the IR spectrum. The beam size varies with the wavelength. It is roughly 1 mm at 532 nm. A 5x beam expander is used to expand the beam. For simplicity, the setup is divided into two parts, where the first part is associated with the 532 nm laser and the 457 nm laser, while the second part is associated with the supercontinuum laser.

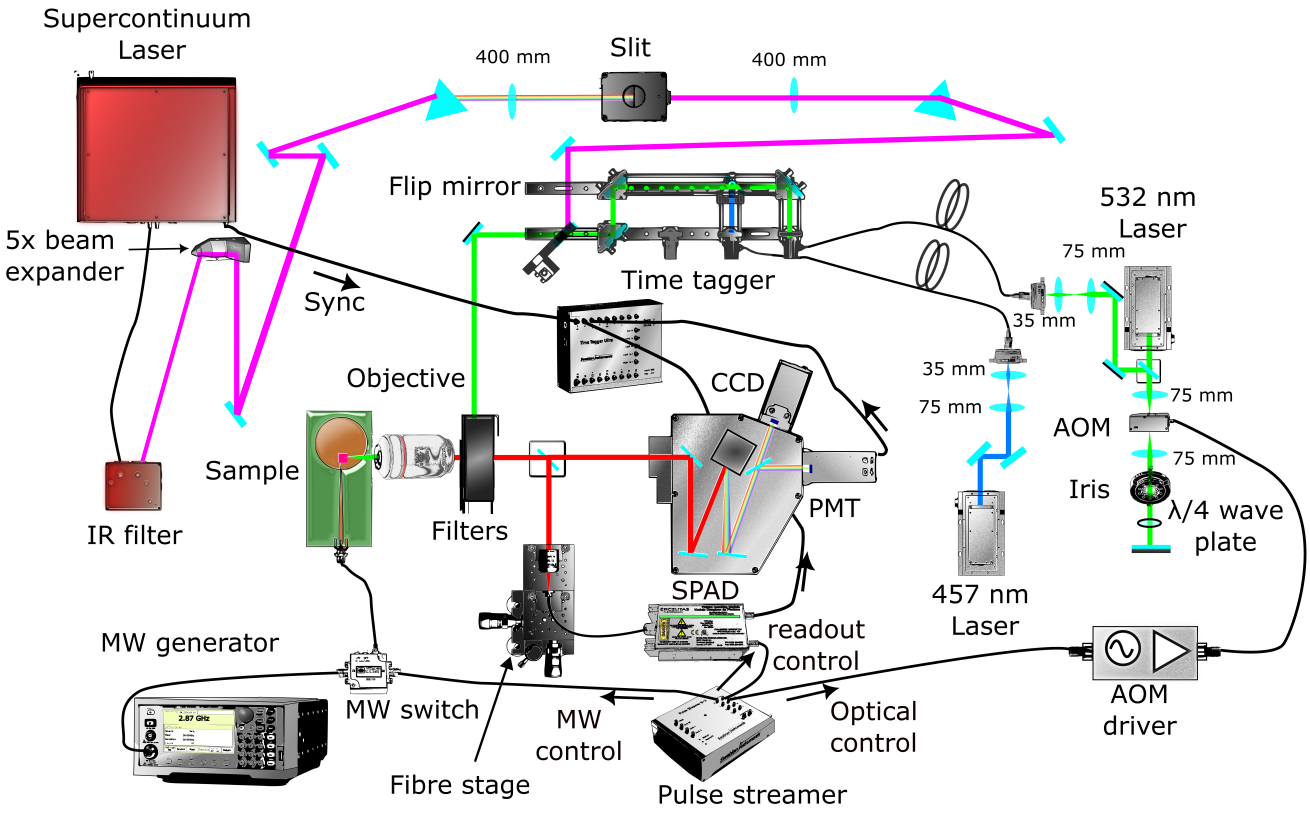


Figure 3.2: A schematic diagram of the optical confocal microscope with MW, pulse control using the pulse streamer and the time tagger for counting signal from the detectors.

Figure 3.2 shows the schematic diagram of the confocal microscope for the optical characterisation. The red box on the upper left corner is the supercontinuum laser source, and there are a 532 nm laser and a 457 nm laser on the right. The purple light shows the light path of the supercontinuum laser and the green and the blue light show the light path for the 532 nm laser and the 457 nm laser. All light paths meet at the "Optical junction" that consists of two fibre ports for the 532 nm laser and the 457 nm laser and the corresponding dichroic mirrors. There is a flip mirror that selects either the supercontinuum path or the 532/457 nm path. The red path shows the fluorescence path from the sample to either the single photon avalanche diode (SPAD) or the spectrogram consisting of a CCD and a PMT. At the bottom, there is a MW generator and a pulse streamer that is used to generate MW signal to the sample and the pulse sequences to the sample, the AOM driver to modulate the laser and the SPAD for time-gated measurement. The time tagger at the centre of the diagram collects all the signal from the SPAD, PMT and the supercontinuum laser synchronised trigger to generate data for the optical characterisation.

3.2.1 CW-laser section

Starting from the 532 nm laser, the excitation beam first goes through a polarising beam splitter (PBS) cube, which splits the incoming beam into two by their orthogonal polarisation. The incoming excitation beam is polarised to perpendicular to the direction of the traveling beam and the beam with a polarisation horizontal to the plane of the table fully passes through the PBS. The vertically polarised light will be reflected to a beam block. After passing the PBS cube, the beam is focused down to an acousto-optic modulator (AOM) by a 100 mm lens. The AOM is made of a crystal attached to a Piezo-electric transducer that generates an acoustic wave in the crystal to diffract the incoming light beam from an RF signal from the driver. The AOM used is ISOMET M1250-T200L-0.5, which consists of a tellurium dioxide (TeO_2) as the interaction medium. The AOM driver is custom-built according to [122], which mainly consists of a Voltage-controlled oscillator, an RF switch, and a variable voltage attenuator to generate a 200 MHz RF signal with an external RF amplifier that drives the AOM. The AOM can be treated as a diffraction grating in a good approximation, but, if the beam size is large, any changes in the form of acoustic waves take time to travel across the beam waist. This is determined by the optical rise time or the modulation speed $t_r = 0.65d/v$, where d is the

diameter of the beam and v is the acoustic velocity which is 4.21 mm/μs for TeO_2 [123]. The modulation bandwidth of the AOM is $BW_{AOM} = 0.7/t_r$. The intensity of the diffracted light beam is determined by the intensity of the sound wave. The deflection efficiency is defined as the ratio of the intensity of the first-order deflected light to the zero-order light. The deflection efficiency of the AOM at 633 nm is above 80%. The light beam after the double passing configuration will have above 64% of its original intensity. The deflection efficiency is maximised if the incoming beam is at the Bragg angle. The optimal RF drive power is $P_d = kh_e\lambda/(2lM)$, where k is the transducer conversion loss, h_e is the height of the electrode, l is the length of the electrode and M is the figure of merit. The diffraction angle between the first and the zeroth order beams, $\theta = \lambda f_c/v$, is determined by the modulation frequency, where f_c is the centre frequency and v is the acoustic velocity [124]. The Bragg angle, θ_B, is $\theta_B = \theta/2$. The beam size is crucial in AOM. The smaller the beam size, the faster the modulation speed and the broader the modulation bandwidth. However, if the beam is focused down to a small spot, the rays from the beam will have a range of incident angles, and not all the rays meet the Bragg angle condition. The overall deflection efficiency is decreased. In this setup, a lens is used to focus down the beam for a higher modulation speed.

The AOM can either be turned on constantly to allow the excitation beam to pass continuously or can be modulated using the pulse streamer, Swabian instruments, allowing the excitation to be pulsed. The light beam will then be collimated by another 100 mm lens before passing through an iris that only allows the first order to pass, a quarter wave plate and is reflected by a mirror back to the lens and the AOM. After the second pass of the AOM, the beam is reflected by the PBS cube, as it has a different polarisation than the first pass. The benefit of the double-pass AOM configuration is that it deflects the first-pass beam back to the optical path with a 90° shift of polarisation, thus it follows the same path as the first-pass beam and is reflected by the PBS. A set of beam expanders, 75 mm and 35 mm lenses, expands the beam by a factor of 2.14 before being coupled into a single-mode optical fibre. The fibre joins a fibre junction at the centre of the optical table, where all the fibres meet and the beams are collimated and directed to the sample stage. There are two fibre collimator for the 532 nm beam and the 457 nm beam. A dichroic mirror is used at the 457 nm port to reflect the 457 nm beam while transmitting the 532 nm beam. At the end of the junction, there is a flip mirror that can either reflect the 532 nm beam and the 457 nm beam to the sample stage or transmit the supercontinuum laser beam to the sample stage while blocking the 532 nm beam and the

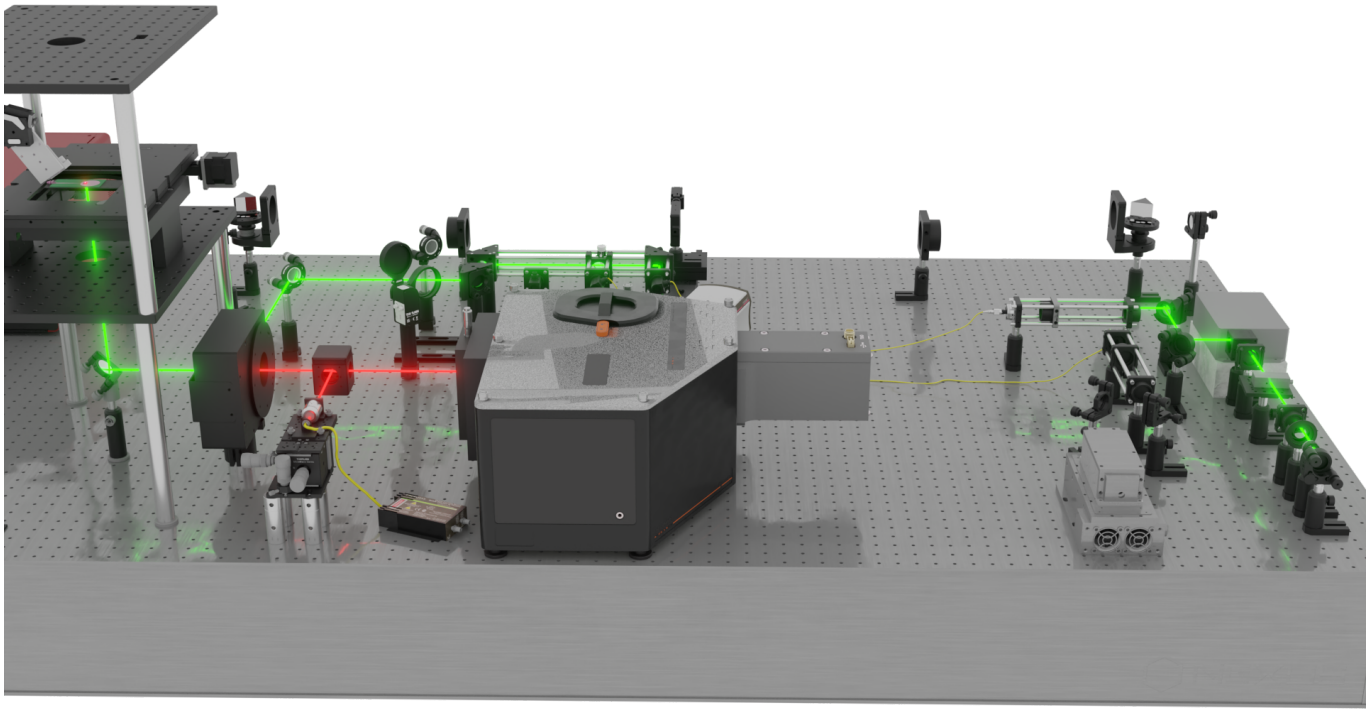


Figure 3.3: This diagram shows the experimental setup with the 532 nm laser in operation.

457 nm beam.

The confocal microscope is designed using computer-aided design (CAD) software. All the components are placed at the precise location and the optical ray tracing can be done from the laser source through multiple mirrors, lenses and other components. This is a helpful way to design complicated optical systems that require accuracy. The construction of the confocal microscope follows the CAD design and achieves a high level of accuracy. The final design of the optical setup is rendered in Figure 3.3 and Figure 3.4.

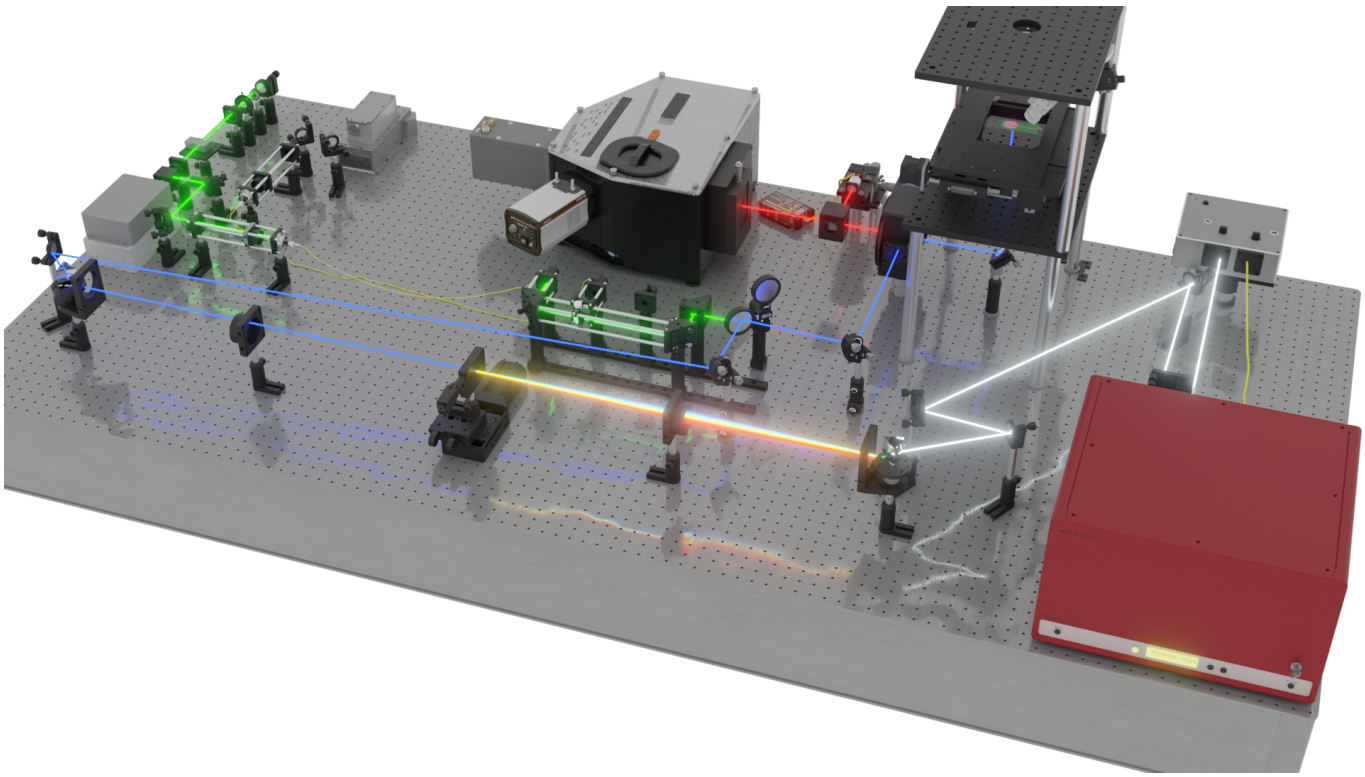


Figure 3.4: This diagram shows the experimental setup with the supercontinuum laser in operation.

3.2.2 Supercontinuum laser section

The second part consists of a supercontinuum laser and a prism-based monochromator. The output of the supercontinuum laser is fibre-coupled and is connected to an IR filter that only allows the visible wavelength from 400 nm up to 700 nm to transmit. The beam then travels in free space after the IR filter. A set of steering mirrors is used to direct the beam to the first prism, which is made of BK4. The beam is diffracted by the prisms and dispersed to a range of wavelengths, which is collimated by a 400 mm lens. A motorised slit is used to select the wavelength. The selected beam is collimated by another 400 mm lens and dispersed by the second prism. Another set of mirrors is used to direct the beam to the flip mirror.

3.2.3 Sample stage and detection section

The third part consists of a Zaber dichroic wheel, the sample stage and the detection system. After the flip mirror, the beam goes through the Zaber dichroic wheel, which consists of different dichroic filters. The beam is then reflected upward by a mirror to the objective that focuses the beam on the sample. The fluorescence travels back from the sample through the objective to the Zaber dichroic filters and to the detection system. The detection system consists of two parts. The beam can either go to the SPAD or the Andor monochromator, which has an EMCCD and a hybrid PMT installed. The beam that goes to the SPAD is reflected by a right-angle prism mirror. When the mirror is removed, the beam will go to the Andor monochromator, which has an internal mirror to select either the EMCCD or the hybrid PMT to detect the signal. On the sample stage, there is the Pior motorised stage which controls the x and y movements. The objective is installed on a linear motor that can move along the z-axis. The sample can either be stuck on the bottom side of a glass slice or a MW PCB that contains a MW antenna. In this thesis, the MW PCB has a resonance at 2.87 GHz and a wide bandwidth of around 300 MHz, which acts as the MW excitation for ODMR experiments. The rendered image of the sample stage is shown in Figure 3.5. The motors, consisting of a linear motor and two rotary motor, above the sample are used to control the position of the permanent magnet. The black curves and arrows indicate the movement of the motors. The white structures holding the motors and the magnet are designed using CAD and 3D printed using PLA materials. The magnet holder in the figure is for a single magnet, the two-magnet holder is designed that hold a stack of two

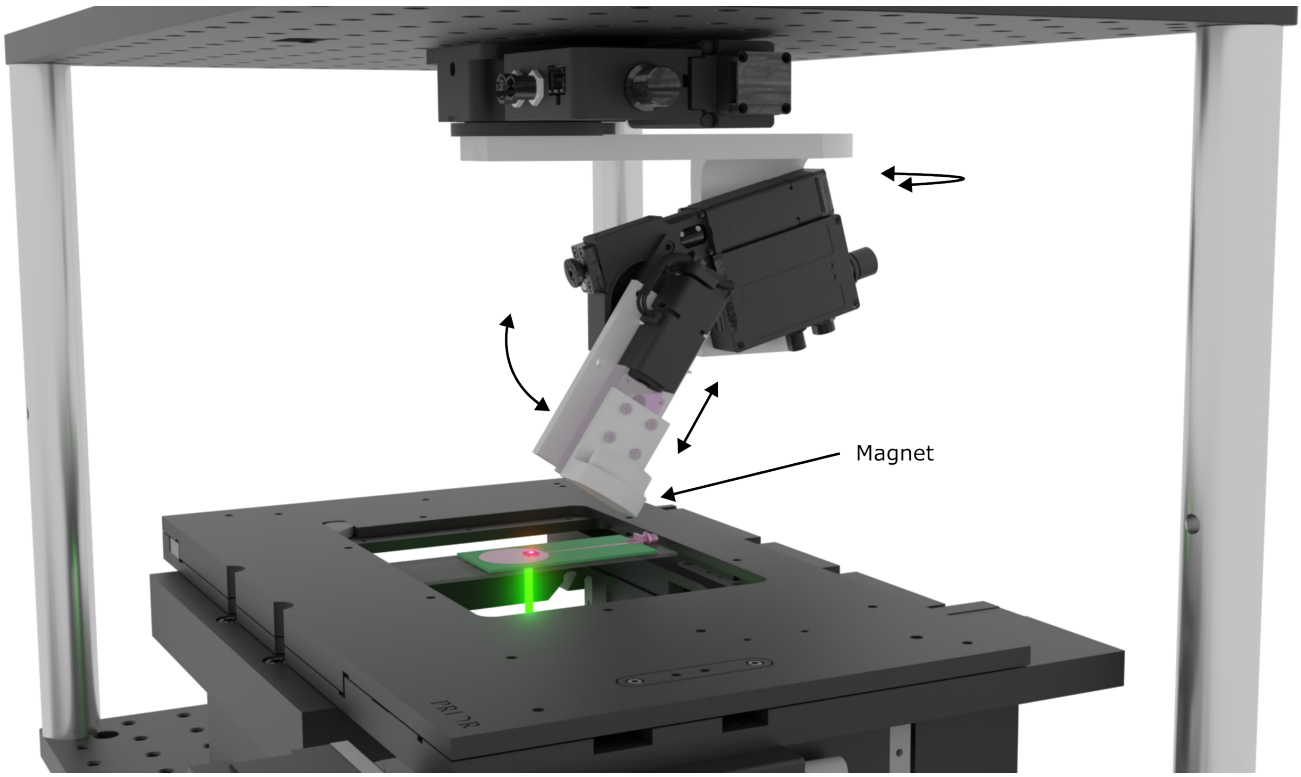


Figure 3.5: This diagram shows the ODMR experimental setup with a cylindrical permanent magnet container and three motorised stages. A magnet can be loaded on or off to do ODMR with or without a magnetic field. The black curves with arrows on both ends indicate the motion of the motors. The motorised states provide movements so that the magnet can align to the sample with the desired angles and radial distance.

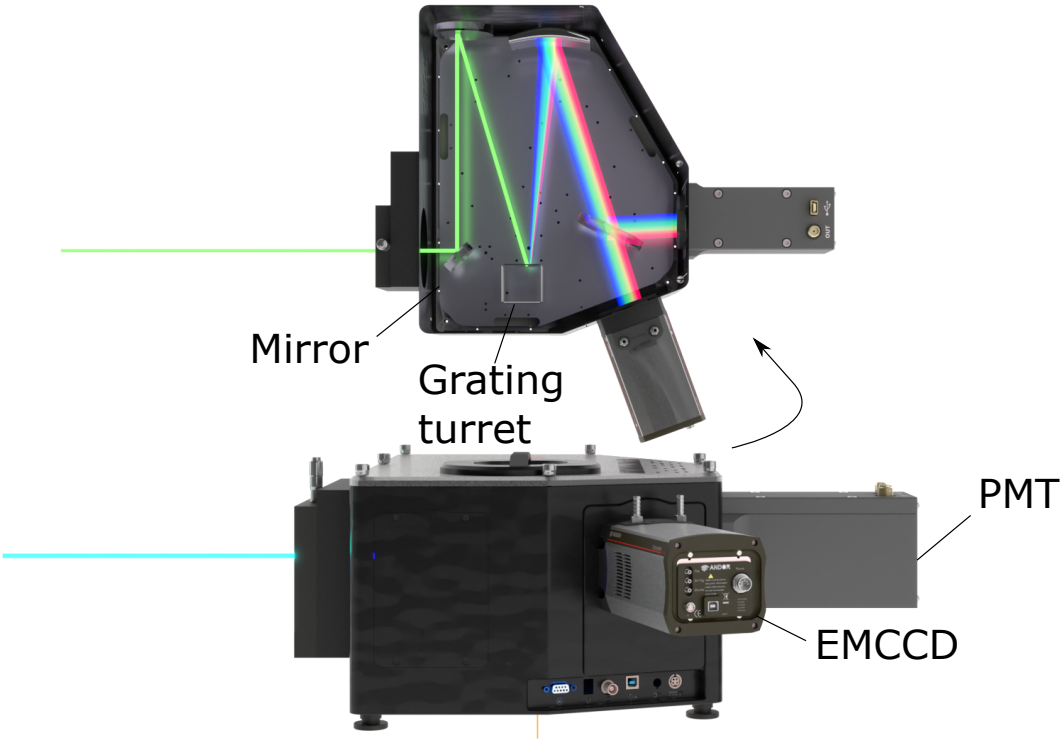


Figure 3.6: The spectral information of the output beam is obtained using the Andor Kymera 328i spectrometer.

magnets and can easily replace the magnet holder for a single magnet.

Figure 3.6 shows the internal structure of the Andor Kymera 328i spectrometer. There is a grating turret that diffracts the incoming beam to the detectors. There are two detector ports, which are currently occupied by an EM-CCD and a PMT. This home-built confocal microscope demonstrates robustness and it is modular, which can be easily extended or modified such as replacing the laser sources or adding more laser sources, or replacing filters or detectors for experiments using a different wavelength.

3.2.4 Apparatus specifications

Camera and Calibrations

CCD and complementary metal-oxide-semiconductor (CMOS) cameras are used for imaging in this thesis. Pixels on CCD are arranged in an array. Each pixel is made of a MOS capacitor that consists of a gate, a SiO_2 oxide layer and a doped silicon, usually p-type on a p^{++} substrate. A depletion region is formed when a positive biased voltage is applied at the gate. In this region, photons might convert to an electron-hole pair and the electron is separated and stored in the capacitor. After the exposure time, the charges are transported to the vertical shift register at the end of each line via controlled sequences of voltage, which is controlled by shift register clock control circuits, applied at the gate of each pixel so that the charges are shifted to the neighbouring pixel. The charges stored in the vertical shift registers then transferred the charges to a horizontal shift register where the charges are sent into processing units. The processing units will amplify the charges and converts to digital signals for further process. It is very similar to how memory works in PC.

The well depth, or the maximum number of electron can be stored in the capacitor, of CCDs are on the order of 10^5. It is important to note that overflow might occur if the capacitor is saturated, and causing blooming effect. So, an overflow drain channel is built in each pixel to prevent blooming in modern CCDs.

EMCCD stands for electron multiplying CCD. It has an additional step to multiply the charges before read out the data, which could increase the signal without increasing much read noise. The electrons are multiplied via impact ionisation, similar to an avalanche photo diode, in multiplication register after the horizontal shift register. EMCCD is only necessary in weak signal scenario. If the signal is strong, the additional electron multiplication process will introduce more noise than the conventional CCDs.

The conventional architecture of CCD is full-frame. It has two phases. In the first phase, all of the pixels are exposed to light and collecting signals. In the second phase, a shutter is used to block the light, the sensors are allowed to transfer the charged to the registers. This similar to the dead time in TSCPC, and this limits the efficiency and response.

There are other two more efficient architectures used in recent CCDs, which are frame-transfer

and interline. In the frame-transfer architecture, half of the sensor is active region for collecting data and the other half is a inactive region where the sensor stops collecting data to store and transfer the data. The interline architecture separates the imaging area into active columns for collecting data and an inactive columns next to it for storage and readout. In this case, the shifting time between the active and inactive region is much reduced compared to the frame-transfer architecture, but the fill factor is halved.

CMOS cameras also use semiconductor technologies. The sensors are arranged in an array. A typical unit cell contains a photo diode and three metal-oxide-semiconductor field effect transistors (MOSFETs), one for reset, one for amplification and the last one for selecting the address. Most of CMOS cameras work in the rolling-shutter mode, where the signals are read from the top row to the bottom row. This mode allows rapid acquisition but fast moving objects will distort the image vertically.

Data collected in both CCD and CMOS cameras have read noise and dark noise due to the readout process, such as the analogue to digital converter, and electronic noise from some random events that emits electrons, such as thermal fluctuation and surface states where electrons are trapped and released at some distributions, in each pixel. The thermal fluctuation might promote electrons formation via thermal energy. The lower the temperature, the lower the dark noise.

There are also artifacts from the optical system such as vignetting, which causes reduction of illumination at the edges of the image. The read noise can be quantified using the bias field calibration technique. This requires a dark field and zero exposure time to minimised the dark noise. The images taken under this condition are dominated by read noise. The intensity will be fluctuating around a mean value. The fluctuation is quantified as the standard deviation. If the exposure time increases, the dark noise will become dominant. The exposure time should be set to be the same as the experiment. The vignetting can be reduced via the flat field technique. The camera takes images of a uniformly illuminated flat plane. The quality of the final image can be improved using an algorithm to reduce the noise using the bias field, dark field and the flat field images.

Photomultiplier tube

A conventional PMT is a vacuum tube consisting of a photocathode that converts an incoming photon to an electron and multiple dynodes accelerating and multiplying the electrons via secondary emission. The materials used for dynodes are usually BeO and MgO. The materials used for photocathode can be Alkali metal, such as Bialkali, Multialkali and Sb-Cs, or semiconductor-based, such as GaAs. The Bialkali photocathode has a relatively high quantum efficiency at above 20% in the blue and green spectrum, whereas, the multialkali has a spectrum in the red, but with a lower quantum efficiency [125]. The electrons are attracted to the anode which collects most of the electrons and turns the electrons into a current signal. Typically, the photocathode is at a large negative potential, at each dynode, a positive potential is added, and the potential of the anode is about zero. The sensitivity can be controlled by the driving voltage. The photocathode has an efficiency of converting photons into electrons, the efficiency is defined as the ratio of the number of electrons generated to the number of incident photons, $QE = N_{eletron}/N_{photon}$. It is the so-called quantum efficiency. However, the quantum efficiency is low, usually peaking at 25 %, and the quantum efficiency is higher in the blue and the green spectrum. The quantum efficiency is low at the red and the infrared part of the spectrum as the photon energy decreases. There is another type of PMTs called microchannel PMTs. The microchannel PMTs replace the conventional dynodes with a continuous channel acting as dynodes. This modification will reduce the transit time of the electrons and increase the overall timing resolution [126].

In this thesis, a hybrid PMT is used. Hybrid PMTs combine the PMT and avalanche diode to detect the photos and amplify the signals. The incident photons are converted to electrons at the photocathode. A strong electric field is applied to accelerate the electrons until the electrons reach a silicon-based avalanche diode, the electrons generated in the diode are accelerated under a large reverse bias, which has enough energy to ionise other bound electrons in the diode. The electrons are multiplying by the diode. Unlike, the conventional PMTs, hybrid PMTs can use a strong electric field to accelerate the electrons to the diode instead of using a series of dynodes. This will reduce any errors and noise during the transit [126], and avoid losses when the electrons interact with the dynodes [127].

Time-correlated single-photon counting

Time-correlated single-photon counting (TCSPC) is a technique that measures a single photon at a time with respect to a reference signal such as a sync signal from a laser. It is used for fluorescent lifetime experiments, where repetitive laser pulses excite the sample and the fluorescent photon and the arrival time is recorded. The TCSPC consists of constant fraction discriminators (CFD), a time-to-amplitude converter (TAC), analogue to a digital converter (ADC). The input signals from the detector will be amplified by a preamplifier before the CFD. The optimal timing resolution is achieved when the rise time of the preamplifier is similar to the rise time of the detector. The CFD is a timing technique that reduces the jitters and the amplitude walk of the signal pulses from the detector and increases the timing resolution. It is considered to provide a higher timing resolution than the leading-edge discriminator, which uses a voltage comparator to only count the signals with an amplitude higher than a threshold. The jitter, which is the random fluctuation of the amplitude, will introduce an uncertainty in timing. The amplitude walk occurs when two pulses have the same shape but different amplitudes will cross the threshold at different times. The CFD will make a bipolar signal by preparing two identical signals, one is attenuated and the other is delayed and inverted. Then, the signals are added, the CFD counts at the zero-crossing time and generates a logic pulse for further process. The TAC converts the time to the amplitude by triggering a growing ramp signal when the time starts and terminates the growing signal when there is a single photon recorded. The ADC measures the height of the signal after the TAC output is amplified. The final data are quantised into time bins, forming the histogram. The maximum range of the time bins is determined by the bit depth of the ADC. The number of bins should be above the Nyquist frequency, which states that the sample rate should be at least twice the highest frequency in the analogue signal. During this counting process, the TCSPC is unable to count another photon before it finishes the process and resets the count. This period is known as dead time. If the photon detection rate is considerably higher, when the instrument is not able to count the photons, an error, known as pile up, will occur and increase the lifetime curve, as the instrument can only count the early photon, while missing the late photons. So, it is important to leave a relatively long time, such that, only 5% of the cycles have a photon detected.

The minimum lifetime that can be measured is limited by the signal jitter and the linewidth of the light source and the detector response function. The maximum lifetime is limited by

the dark noise from the detector and the excitation rate. If the excitation rate is high, there is a background fluorescence that reduces the dynamics range. If the repetition is too fast, a background signal will be present.

Spectrometer

A spectrometer is an instrument that separates incoming light into its spectral components. There are many types of spectrometers, such as prism-based and grating-based spectrometers.

A typical spectrometer consists of prisms or diffraction gratings and some mirrors to direct the light inside a box, where the incoming light travels through a slit. Cameras or other photodetectors are used to image the spectrum at the output port of the spectrometer.

The spectrometer used in this thesis is based on Czerny-Turner. The incoming light from the slit is collimated and directed to a diffraction grating by a concave mirror. If a light beam incident at an angle θ_i on the grating, the diffraction angle θ_m can be estimated as the expression below.

$$sin(\theta_m) = n\frac{\lambda}{d} + sin(\theta_i) \tag{3.3}$$

where n is the number an integer, $n = 1, 2, ...$, that represents the diffraction order, λ is the wavelength and d is the separation of the splits in the grating.

Another concave mirror is used to focus the diffracted light onto a PMT or a camera. The concave mirrors are typically made nonspherical to reduce spherical aberration and astigmatism.

Microwave Apparatus

The MW signal is generated using an RF signal generator, Tektronix TSG 4106A. An external 40 dB MW amplifier is connected to the output of the signal generator, which can amplify the power by 34 dB. The signal generator can generate a signal with a power of up to -5 dBm before the amplifier.

All the modulated signals, for the AOM, the SPAD and the MW signal, are generated and controlled using a pulse streamer, Swabian instruments. The pulse streamer has two types of outputs: digital and analogue. The digital output has a 1 GSa/s sampling rate, and it generates either 1, high, or 0, low, voltage levels that are useful for square waves. At a high state, the voltage is about 3 V. The analog output has a 125 MSa/s sampling rate, and it generates any numbers between 0 and 1 that are useful to construct any analogue signals. The pulse streamer can generate a sine wave at a frequency as high as 62.5 MHz from the analogue output with an amplitude of 1 V. The digital outputs are capable of generating a 100 MHz square wave. Whereas, the signal generator can only generate a square wave at 50 kHz, which is a 10 μs squared pulse, but the frequency of the sine wave is above 2 GHz. The amplitude of the sine wave generated is about 0.5 V.

The pulse streamer is connected to the laboratory network via an Ethernet cable and it is controlled via a custom MATLAB programme. Aside from the MW modulation, the programme also controls the optical modulation and the detection modulation that uses the other ports of the pulse streamer. The pulses from the pulse streamer are used to modulate the MW signal via a MW switch. The pulse shape is limited to a square pulse, using the digital output from the pulse streamer. The rise and fall time measure using an InfiniiVision MSO-X 3104 A mixed signal oscilloscope from the digital output is about 2.5 ns.

The type of MW antenna used is a microstrip antenna that consists of a metallic ground plate, a dielectric substrate and a metallic top plate. The signal is fed into the top plate via a feed-taped line. The input end of the feed line is impedance matched to 50 Ω. The metallic top plate is the main part of the antenna. The top plate forms patches that act as a feed-line, a capacitor and an impedance. The design is based on [73] and it is redesigned and optimised to better fit the purpose of the experiments conducted in this thesis. The thickness of the substrate, FR-4, is 1.6 mm. At 2.87 GHz, the skin depth is estimated to be 1.2 μm. The thickness of the copper

layer is kept above 6 μm to avoid additional resistive loss. In PCB fabrication, the standard 1 oz finished copper is used, which corresponds to 34.8 μm of thickness.

CST microwave studio is used for the simulations. Multiple simulations with slightly different parameters of the antenna are simulated until it finds the optimal design that resonates at 2.87 GHz and has a broad bandwidth, ideally a few hundred MHz. The parameters are the radius of the large circular patch, R, the width of the gap, g, the deviation of the small hole from the centre of the large circular patch, s and the radius of the small hole, r. The S_{11} parameters are simulated and shown in Figure 3.7, which is suitable for the application. The antenna has a broad resonance at around 2.87 GHz. The bandwidth is about 200 MHz.

The H field profile of the antenna is shown in Figure 3.8, which demonstrates a high field concentrates slightly above the hole, where the sample is placed. Figure 3.9 shows a vector field plot where the H field is pointing vertically. The sample will be experiencing a field normal to the <100> plane. The field quickly deviates to the horizontal direction moving toward the far edge of the circular patch, whereas the field remains in the normal direction moving along the gap. The final design of the antenna is rendered in Figure 3.10 (a) and the photo of the antenna for this thesis is shown in (b).

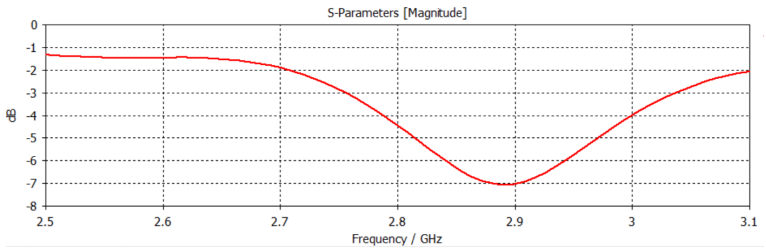
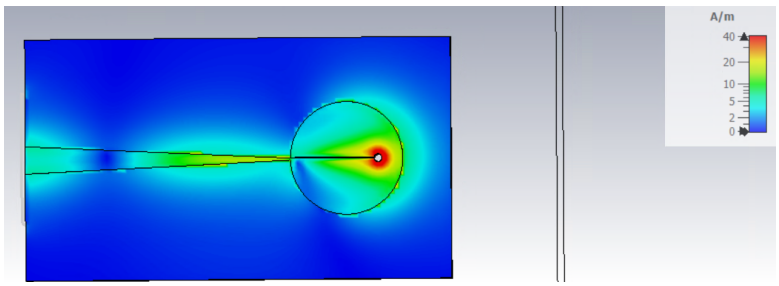
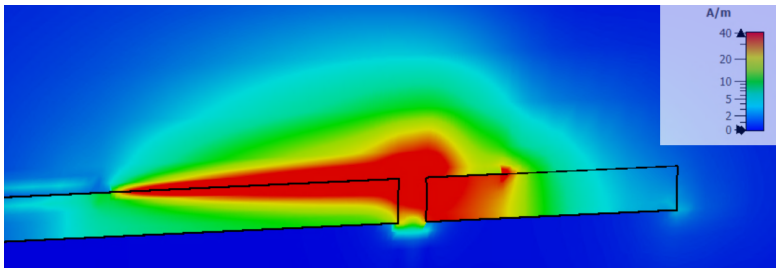


Figure 3.7: The S_{11} of the microstrip antenna, where R = 7 mm, g = 0.1 mm, s = 3.9 mm and r = 0.5 mm.

The first batch of designs was sent to JLCPCB for manufacture. The microstrip antennas are about 100 MHz lower than the designed frequency, and the bandwidth is about 100 MHz. It is suspected that the designs are limited by the manufacturing tolerance and the limits. The manufacturing error in the diameter of the hole is +0.13 mm and -0.09 mm. The limit of the width of the gap is 0.127 mm. The design is pushing the limit of the manufacturing process. Additionally, in the PCB design, the trace-pad connection is not smooth, as the trace has a rounded end whereas the pad has a flat end, and the resolution of the antenna, which is



(a) Field profile



(b) Cross-sectional field profile

Figure 3.8: (a)The tangential H field of the microstrip antenna at 2.87 GHz, where R = 7 mm, g = 0.1 mm, g = 3.9 mm and r = 0.5 mm. (b)The cross-sectional view of the tangential H field of the microstrip antenna at 2.87 GHz, where R = 7 mm, g= 0.1 mm, g = 3.9 mm and r = 0.5 mm. The colour scale indicates the strength of the magnetic field.

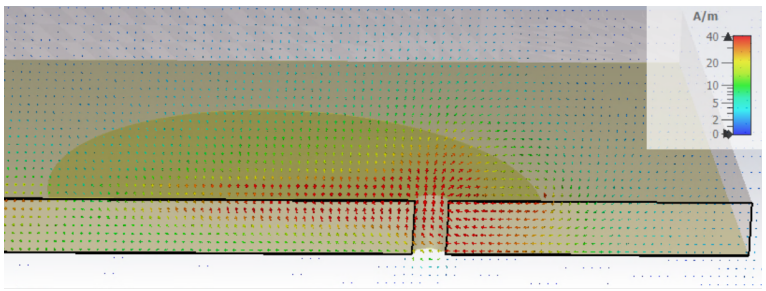
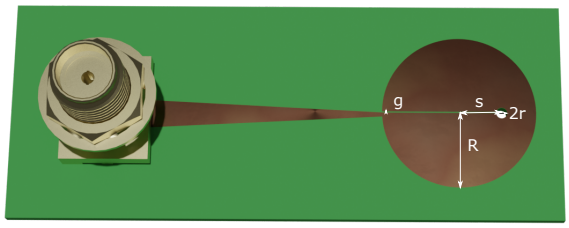


Figure 3.9: The cross-sectional view of the tangential H field of the microstrip antenna at 2.87 GHz, where R = 7 mm, g = 0.1 mm, g = 3.9 mm and r = 0.5 mm.

imported from a bitmap as a pad, is limited by the dpi.

To solve this issue, a matrix approach is used. This involves varying a parameter while keeping the other parameters constant in the form of a matrix. For example, the size of the small hole can be either increased or decreased, while the others fixed. By manufacturing a number of these, there is a better chance of finding an antenna that best matches the simulation and can be used in the experiment.

By decreasing the size of the antenna, R, the resonant frequency increases. Let's suppose s is 3.9 mm, r is 0.5 mm and g is 0.01 mm, if R is 6.75 mm, the frequency is 2.95 GHz and the



(a) Rendered image



(b) Photo

Figure 3.10: (a)The microstrip antenna has a resonant frequency of 2.87 GHz. The diameter of the circular antenna is R = 7 mm. The diameter, r, of the small hole, is 0.5 mm. The width of the gap, g, is 0.2 mm and the length, s, is 3.9 mm. (b)The manufactured microstrip antenna used in this thesis.

bandwidth is 241.9 MHz, of R is 7 mm, the frequency is 2.89 GHz the bandwidth is 221.3 MHz if R is 7.25 mm, the frequency is 2.82 GHz the bandwidth is 215.9 MHz. If R is kept constant, the larger the s, the lower the frequency and the narrower the bandwidth. If s decreases, the frequency increases and the bandwidth decreases. The radius of the hole, r, is kept constant in the designs, as the dimension is very small, the manufacturing error might shift the frequency a lot. For R = 7 mm, s = 3.9 mm, g = 0.1 mm, the frequency will be 2.89 GHz when r = 0.5 mm, 3.02 GHz when r = 0.4 mm and 2.77 GHz when r = 0.6 mm. The width of the gap plays an important role. Increasing the gap width, g, the frequency increases and the bandwidth increases.

The matrix of designs covers a range from 2.69 GHz to 3.09 GHz, the bandwidth covers from 200 MHz to 338 MHz.

3.3 Maser

3.3.1 Dielectric resonator and cavity

The cavity designed for the small GMW electromagnet, which is the smaller electromagnet, has an inner radius of the copper cavity of 13 mm, and an outer radius of 15 mm. The dimension of the sapphire resonator has an inner radius of 2.5 mm and an outer radius of 5 mm. The resonant frequency estimated using CST is 9.74 GHz, and the unloaded Q factor is 49,623. The mode volume is 0.2857 cm^3 and the filling factor is 0.0137.

The characterisation of the cavity involves measuring the loaded and unloaded Q factor and the resonant frequency with the use of a vector network analyzer (VNA). VNA is a type of network analyzer that measures both the phase and the amplitude of high frequency signals at the same time. It is used to characterise the S parameters of microwave systems in a range of frequencies. The VNA used is a 2-port M5180 VNA, Copper Mountain Technologies. The loaded Q factor is simply calculated by measuring the 3 dB width of S_{21} and the resonant frequency, using the resonant frequency divided by the -3 dB bandwidth. The unloaded Q is estimated using both the insertion loss method and the coupling coefficient method. The VNA is first calibrated using the ACM 2520 auto calibration kit, to reduce some systematic errors and errors related to the environment such as cables. The calibration process is essentially measuring the known impedance of the kit terminating the ports with short-circuits, open-circuits, through lines and matched loads and evaluates the error paths and error models to minimise the errors at a wide frequency range [128].

The insertion loss method is based on the insertion loss equation and only requires transmission measurements, such as S_{21} and S_{12}. The parameters are the loaded Q factor, Q_L, and the insertion loss, IL, at resonance measured using the VNA. The two coupling loops are both under-coupled to obtain a high Q factor. The relationship between Q_L and Q_U is gien by [62].

$$Q_U = \frac{Q_L}{1 - 10^{IL/20}} \tag{3.4}$$

Knowing that the unloaded Q factor, Q_U is about 35,000, and the insertion loss is -20.8 dB. The unloaded Q factor is about 38,512. This implies that the coupling is weak since the coupling loops are very small and placed near the wall of the copper cavity and the small insertion loss.

The loaded Q factor is only slightly lower than the unloaded Q factor. The other method requires the S_{11} and S_{22} parameters to estimate how much the coupling loops couple to the cavity at resonance [62].

$$\beta_1 = \frac{1 - S_{11}}{S_{11} + S_{22}} \tag{3.5}$$

$$\beta_2 = \frac{1 - S_{22}}{S_{11} + S_{22}} \tag{3.6}$$

$$Q_U = Q_L(1 + \beta_1 + \beta_2) \tag{3.7}$$

where β_1 and β_2 are the input and output coupling coefficients. Knowing all of the S parameters, the unloaded Q is estimated to be 39,313. This implies that the system is only weakly coupled. The loaded Q factor is very similar to the unloaded Q factor, the unloaded Q factor is about 1.27 times higher than the loaded Q. Whereas, the unloaded Q factor predicted in CST is about 49,000. It is concluded that apart from the losses during the measurement, a lossy post, tarnished copper cavity and any other errors introduced during machining, the conductivity of the copper might be lower than the default value in CST, which is $5.87 \cdot 10^7$ S/m. To estimate the actual conductivity, an equation is derived by assuming that the conducting loss is dominant over the dielectric loss.

$$\sigma = \frac{Q_U^2 A^2}{2\mu\omega V^2} \tag{3.8}$$

where A is the surface area of the cavity, V is the volume of the cavity, μ is the permeability inside the cavity and ω is the frequency. The conductivity is estimated to be $2.66 \cdot 10^7$ S/m. To double-check with CST, the actual conductivity is used in the CST simulation, and the simulation gives an unloaded Q of 38,772.

Figure 3.11 shows the image captured from the VNA measurement of the S_{12} of the maser resonator inside a cavity. The VNA software estimates the loaded Q factor to be around 35,576 at 9.57 GHz. The insertion loss is estimated to be -26.8 dB. Using the insertion loss, and assuming the two ports are equally coupled. The coupling coefficient is about 0.024 and suggests the resonator is under-coupled. This gives a very rough estimate of the coupling of this setup. Using equation (3.4), the unloaded Q factor is about 37,280.

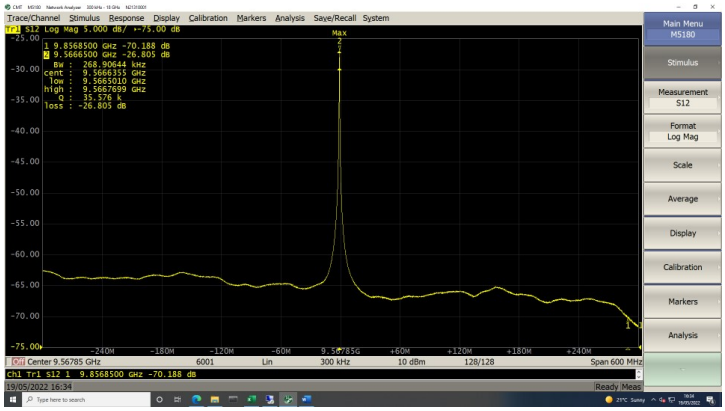


Figure 3.11: The S12 of the design cavity and resonator, the results are averaged based on 128 measurements. The loaded Q is above 35,576.

Cavity simulations

The cavity design for the GMW magnet is based on the previous parameters in Chapter 3.3.1.

The copper cavity and the dielectric resonators are simulated using the eigenmode frequency domain simulation in CST microwave studio. The mode considered is the $TE_{01\delta}$.

The dielectric resonator is made of sapphire, $\epsilon_d = 11.5$ parallel to the C-axis and $\epsilon_d = 9.3$ perpendicular to the C-axis, in the microwave spectrum. Sapphire is used as it has a relatively low dielectric loss at room temperature.

The simulation of the resonator is calculated using the Frequency domain eigenmode solver. This solver finds the eigenmodes within a metal-enclosed space. In the simulation the model consists of a quartz post, outer radius is 3 mm, inner radius is 1 mm, height is 3.15 mm, dielectric constant is 3.75 and the dielectric loss $\delta = 0.0004$; a sapphire resonator, outer radius is 7.2 mm, inner radius 2.55 mm, height of 2 mm, the dielectric loss $\delta = 8.6 \cdot 10^{-6}$. The bottom part of the cavity has an outer radius of 13 mm and a thickness of 4 mm. The top plate has an outer radius of 12 mm and a thickness of 1 mm. The body has an outer radius of 12 mm and an inner radius of 11 mm and a height of 25 mm. The movable top plate is at a height of 10.3 mm.

Figure 3.12 shows the rendered view of the $TEM_{01\delta}$ 3D field configuration inside the cavity. Figure 3.13 shows the heatmap of the $TEM_{01\delta}$ mode of the resonator. The H field is concentrated at the center whereas the E field is inside the resonator, shown as the bottom subfigure and the

top subfigure respectively. In the top and the middle subfigures of Figure 3.14, the relationship between the Q factor and the inner radius of the resonator and the mode volume and the inner radius of the resonator is shown. The smaller the inner radius of the resonator, the Q factor approaches to a maximum Q factor and the smaller the mode volume. Figure 3.14 shows the relation between the Q factor, the mode volume and the inner diameter of the copper cavity. It is found that the Q factor is optimal when the inner diameter is at 31 mm. Figure 3.15 is the version 2 resonator which is used in the Bruker electromagnet-based maser. Figure 3.16 is the version 3 resonator which is used in the GMW maser.

Given that the sapphire resonator is fixed in size, which is 10 mm in outer diameter and 5 mm in inner diameter, the optimal inner diameter of the copper cavity is found using CST. There is an optimal inner diameter that gives the highest Q factor, which is about 31 mm. If the cavity is smaller, the Q factor will drop as the cavity wall introduces excess conduction loss. If the cavity is larger, the Q factor will reduce as the radiation loss is dominant, shown in Figure 3.14.

The effect of varying the inner diameter of the resonator while keeping everything else constant is also interesting. The smaller the inner diameter of the resonator, the better the Q factor and the smaller the mode volume. In this thesis, the inner diameter is designed to be 5 mm so that samples can be fixed and rotated inside.

The cavity consists of a bottom plate, a cylindrical body and a movable top plate.

In the first design, the bottom plate is separated from the body and the top plate. The bottom plate has to be screwed onto the body. There are two holes on the wall for laser excitation and the coupling loops. The design is not very convenient as it is impossible to freely move the resonator and the coupling loops at the same time, and the coupling loops have to be removed every time the cavity is open.

The second design is similar to a "Coffee cup", where the body and the bottom plate are fixed, and the top plate is separated and can be screwed onto the body, which is like a lid for a cup. The position of the resonator and the coupling loops can be easily adjusted when the top plate is not on. The cavity based on this design is made of oxygen-free copper, and it is used for the diamond maser with the Bruker EPR electromagnet. A third cavity for the GMW electromagnet is made, which is similar to the EPR cavity design, but the outer diameter of

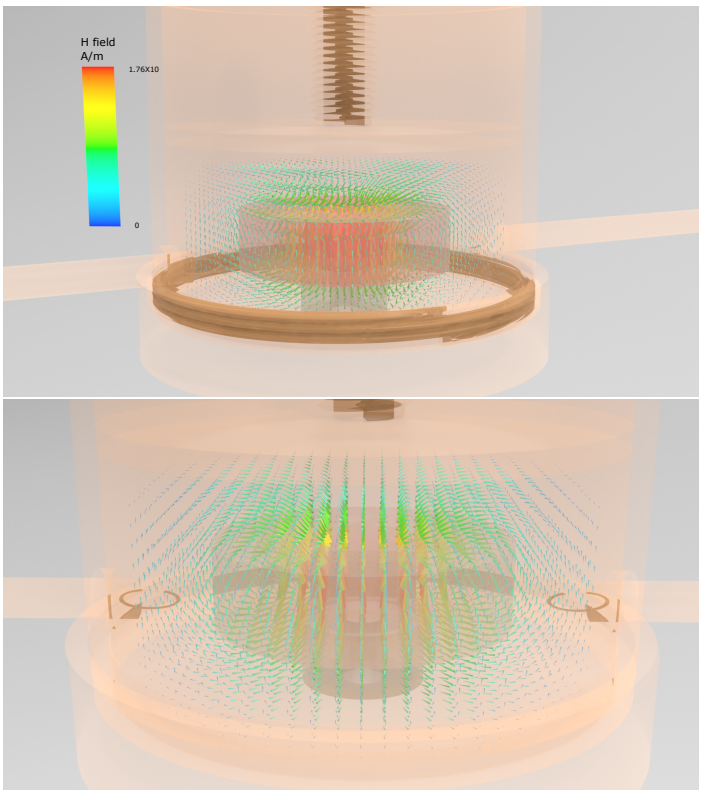


Figure 3.12: The 3D H field the E field of the $TE_{01\delta}$ mode, which is computed using the eigenmode method in CST, in a sapphire cylindrical dielectric resonator, inner diameter of 5 mm, outer diameter of 10 mm, height of 6 mm, on a quartz post in a copper cavity, inner diameter of 31 mm.

the cavity is reduced to 29 mm to fit in the space between the pole of the GMW electromagnet. The inner diameter is 23 mm. The Bruker EPR electromagnet has a much wider space between the two poles, 62 mm, and the inner diameter can be 31 mm to research the optimal size.

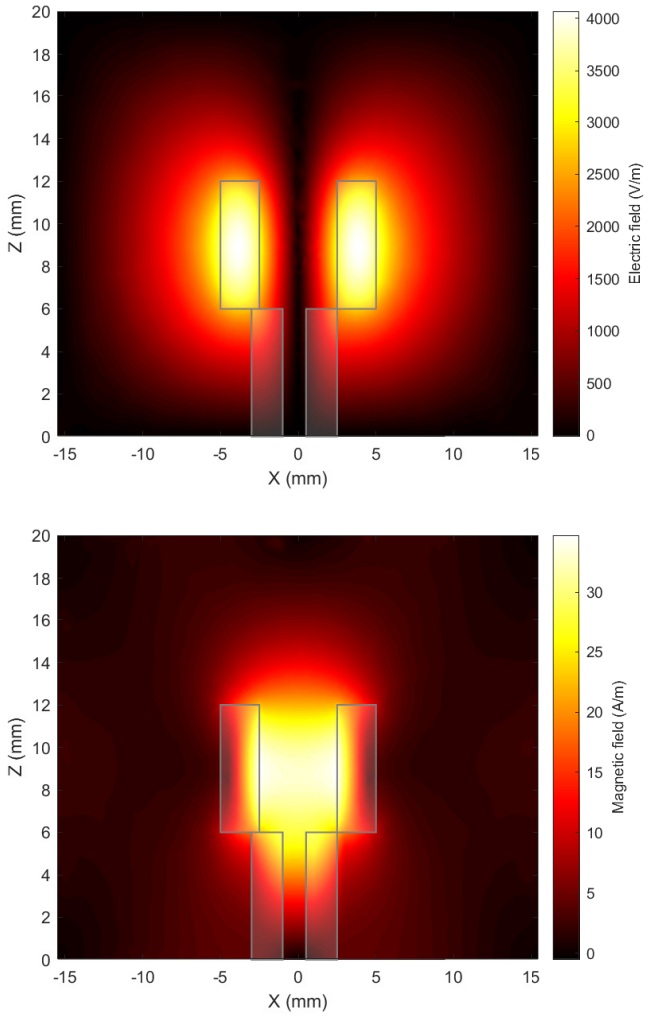


Figure 3.13: Top: The E field. Bottom: the H field of the $TE_{01\delta}$ mode, which is computed using the eigenmode method in CST, in a sapphire cylindrical dielectric resonator, inner diameter of 5 mm, outer diameter of 10 mm, height of 6 mm, on a quartz post in a copper cavity, inner diameter of 31 mm.

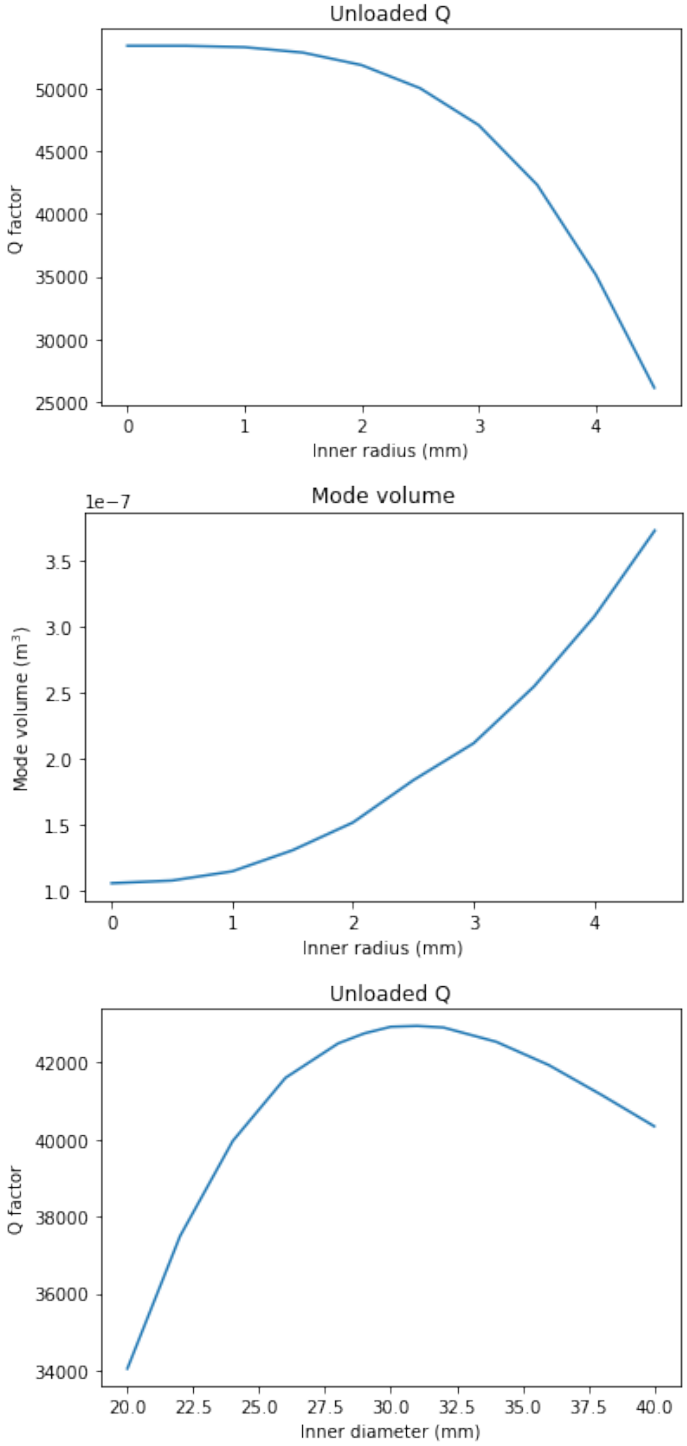


Figure 3.14: These figures show the relation of the inner radius of the sapphire resonator and the Q factor and the mode volume. The last subfigure shows the plot of the inner diameter of the copper cavity against the unloaded Q factor. It is shown that at 31 mm, the Q factor is optimised, provided that the outer diameter of the sapphire resonator is 10 mm.

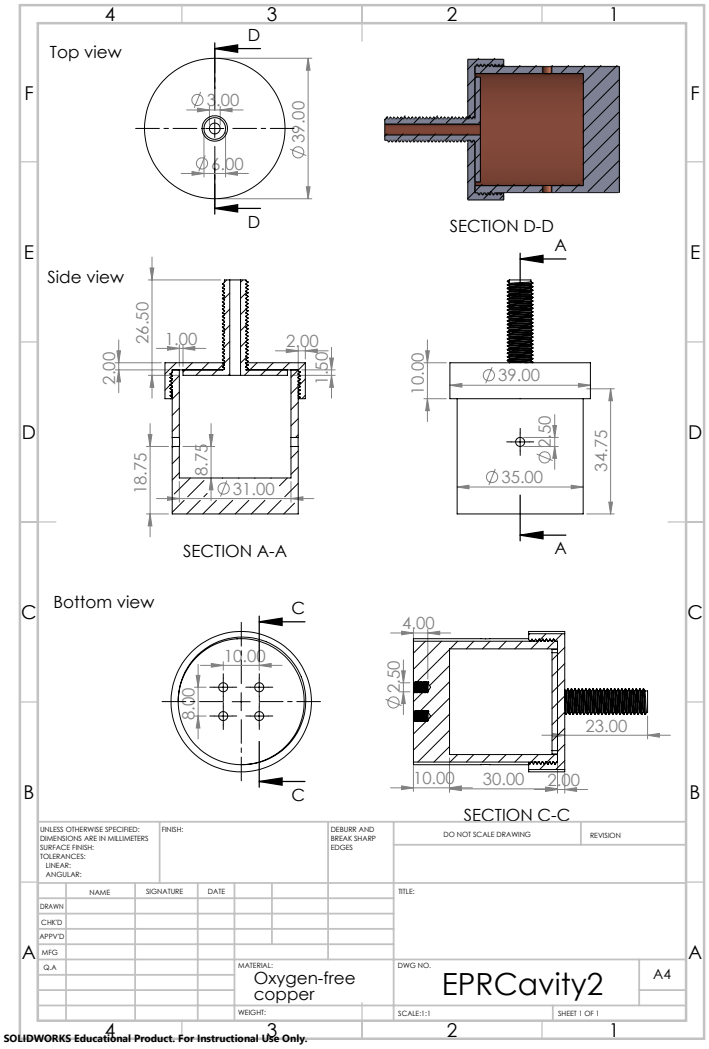


Figure 3.15: The drawings for the "coffee cup" design. This is designed for diamond maser using the EPR electromagnet.

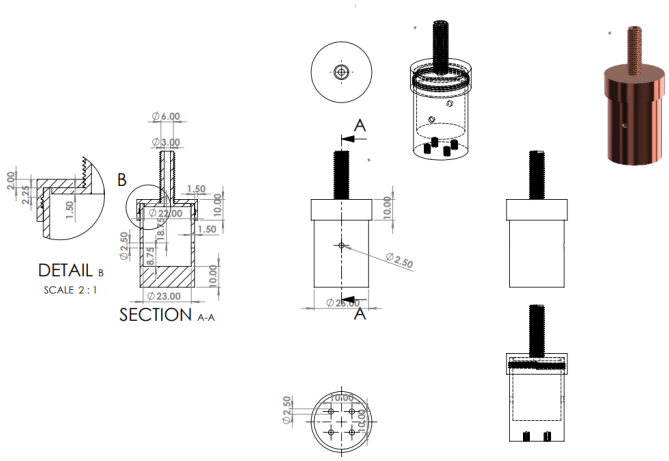


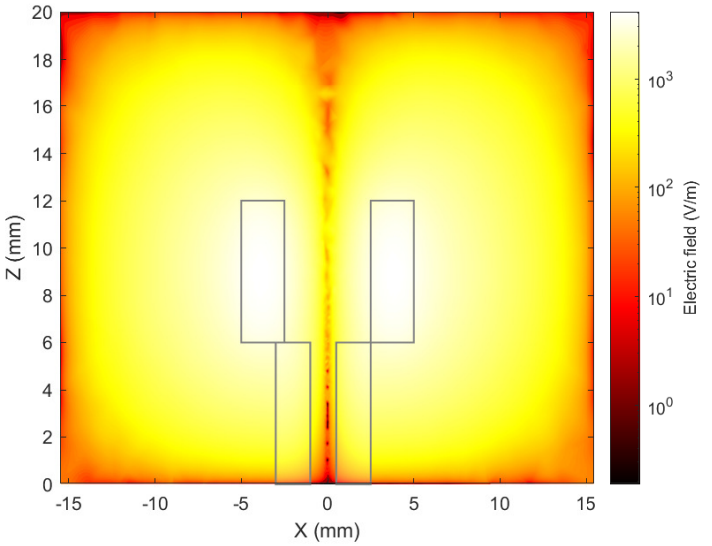
Figure 3.16: The drawings for the GMW cavity design. This is designed for diamond maser using the GMW electromagnet.

Figure 3.17 shows the magnetic field and the electric field profile of the $TEM_{01\delta}$ mode of the sapphire resonator at 9.54 GHz on the logarithm scale. The magnetic field profile is relevant in the maser application. Ideally, the centre of the resonator should have the maximum and uniform magnetic field. From Figure 3.17, the magnetic field is uniform across the centre, where the maximum points are on the edge of the resonator.

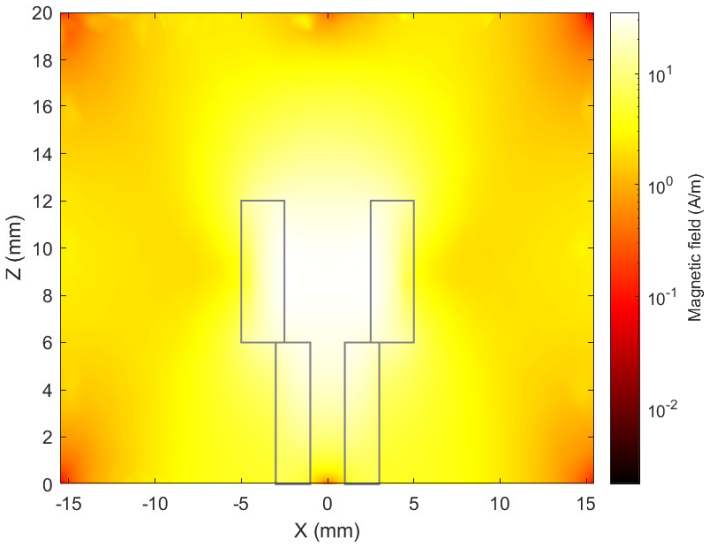
On the other hand, the electric field is mostly confined to the resonator wall. The logarithm scale shows the detailed field profile far away from the resonator. This gives information about the field profile near the wall. From Figure 3.17 (b), the magnetic field has six dark spots, which represent a weak magnetic field at the centre of the top cavity wall, the bottom of the cavity wall and the top corner and the bottom corner of the cavity. There is a bright spot around the equator of the cavity wall, where the coupling loops are placed.

Figure 3.18 (a) shows the magnetic field profile of the rutile resonator at 9.26 GHz. The dimension of the resonator is reduced to an outer radius of 2.55 mm and an inner radius of 2.1 mm, the wall thickness is 0.45 mm, and a height of 3 mm to resonate at a similar frequency as the sapphire resonator. It is clear that the maximum field is located on the inner edge of the resonator, while the field at the center is not as uniform and strong. This might be the reason for the thin wall of the resonator. Similarly, in Figure 3.18 (b), the magnetic field profile of the BMT at 9.54 GHz has relatively less uniformity and field magnitude at the centre than the sapphire resonator but more than the rutile resonator. However, the dimension of the resonator of the outer radius is 3.6mm, the wall thickness is 1.1 mm, the inner radius is 2.55 mm and the height is 5 mm. Figure 3.18 (d) shows the magnetic field profile of the BZT at 9.36 GHz. To further investigate the impact of the wall thickness, the same rutile resonator is simulated but with a smaller inner radius, 1.5 mm, thus the wall thickness increases to 1.05 mm, almost double, as shown in Figure 3.18 (c). The resonant frequency is dropped to 6.99 GHz, however, the mode volume is reduced to 0.019 cm^{-3} due to the smaller inner radius, and the cooperativity is 8.5, which is higher than the thin wall resonator. The centre region of the resonant has a higher uniformity and field strength as expected for a thicker wall. Overall, the smaller inner radius can help increase the cooperativity, but the space for the sample is reduced. This requires a more careful fit. In addition, the resonant frequency will be reduced. If the same frequency has to be kept, the outer radius has to be reduced with the inner radius. The thinner the wall, the more the field gradient from the inner edge of the wall to the centre.

Furthermore, in the thin resonators, the electric field maximum is located in the wall, but there is a significant amount of electric field penetrating out the wall and overlapping the magnetic field maximum. The electric field will cause unwanted off-resonance absorption that might reduce the energy stored in the cavity and degrade the efficiency of the maser. Table 3.1 shows the dielectric properties of the different dielectric materials and Table 3.2 shows the calculated frequency, Q factor, mode volume and the cooperativity.

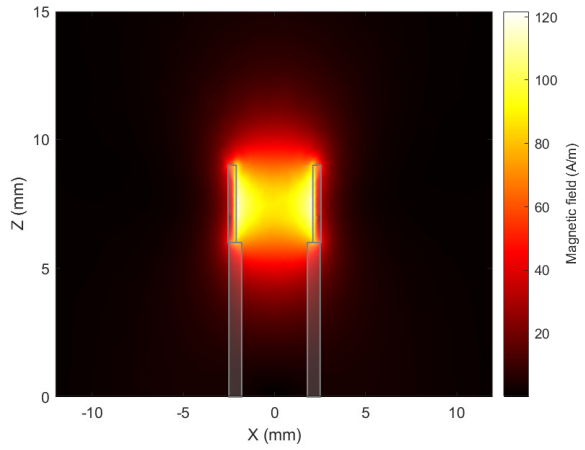


(a) H-field

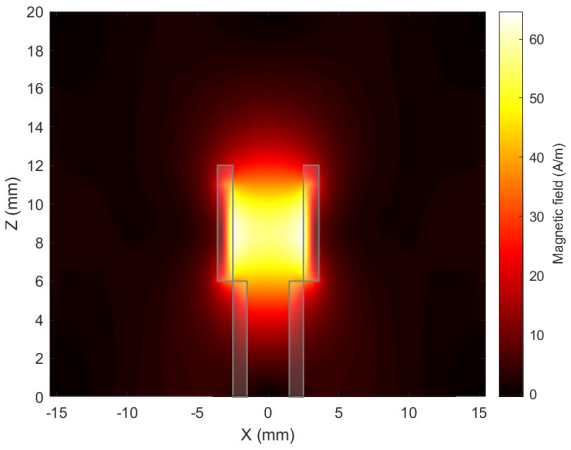


(b) E-field

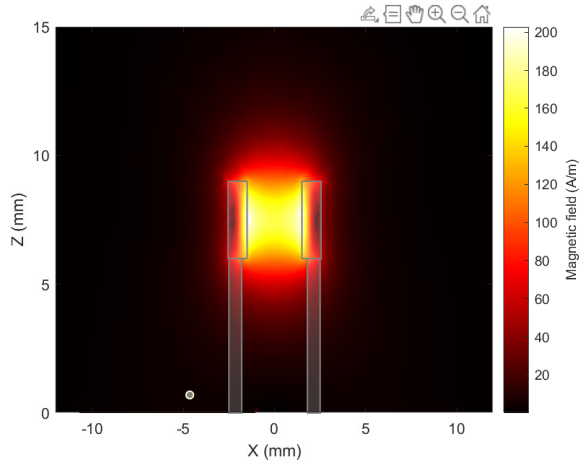
Figure 3.17: (a) The electric field profile of the $TEM_{01\delta}$ of the sapphire resonator shown in logarithmic scale. (b) The magnetic field profile of the $TEM_{01\delta}$ of the sapphire resonator shown in logarithmic scale.



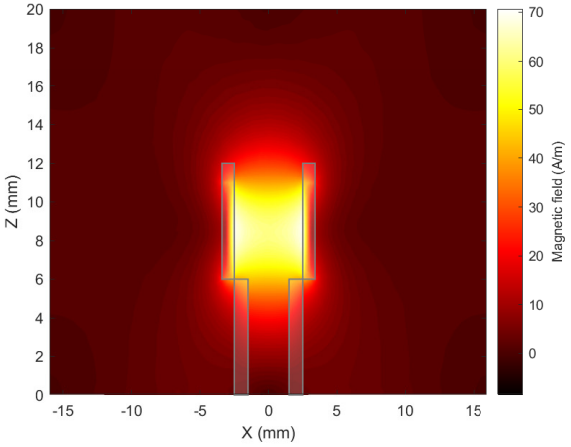
(a) Rutile



(b) BMT



(c) Rutile with thick wall



(d) BZT

Figure 3.18: The magnetic field profile of the $TEM_{01\delta}$ of the (a) Rutile (b) BMT (c) Rutile with a thicker wall (d) BZT.

Dielectric parameters at room temperature (10 GHz)		
Dielectric name	Dielectric constant	Dielectric loss
Sapphire (Al_2O_3)	9.4	$1.2{\cdot}10^{-6}$
Lanthanum aluminate ($LaAlO_3$)	19.6	$4.3{\cdot}10^{-5}$
Barium Magnesium Tantalate	24	$4.5{\cdot}10^{-5}$
Barium Zirconate Titanate	30	$5.55{\cdot}10^{-5}$
Rutile (TiO_2)	86	$1.8{\cdot}10^{-4}$

Table 3.1: A list of dielectric constant and dielectric loss of various dielectric materials.

Dielectric resonators					
Dielectric name	Outer radius (mm)	Frequency (GHz)	Q factor (Unloaded)	Mode Volume (cm^3)	Cooperativity
Sapphire (Al_2O_3)	5	9.54	50,832	0.290	13.3
Lanthanum aluminate ($LaAlO_3$)	3.7	9.15	20,839	0.137	7.5
Barium Magnesium Tantalate	3.6	9.45	22,908	0.09	12.8
Barium Zirconate Titanate	3.4	9.36	19,116	0.08	11.1
Rutile (TiO_2)	2.55	9.26	6,220	0.023	6.6

Table 3.2: A summary of the performance of different dielectric resonators.

Cavity pulling

Cavity pulling is an important effect that shifts the masing frequency due to the interaction between the spin defects and the cavity due to a mismatch of resonant frequency between the cavity and the spins. The masing frequency, μ_m is [25]:

$$\mu_m = \mu_0 + \frac{Q_c(\mu_c - \mu_0)}{Q_0} \tag{3.9}$$

where μ_c is the cavity frequency, μ_0 is the frequency of the NV centre, Q_c is the Q factor of the cavity and Q_0 is the Q factor of the NV centre transition, $\mu_0/\Delta\mu$, where $\Delta\mu$ is the linewidth of the NV centre transition [129].

3.3.2 DC magnetic field characterisations

The magnetic field plays an important role in this thesis. Especially in the maser, the magnetic field is used to tune the frequency of the NV^- via the Zeeman effect. More importantly, a sufficiently large magnetic field, 102.5 mT, can shift one of the triplet ground states, m = -1, lower than the m = 0 ground state, which leads to population inversion. There are two types of magnets used in this thesis for masing: A Bruker electromagnetic paramagnetic resonance (EPR) electromagnet and a GMW electromagnet. A commercial Halbach array is discussed in the conclusion of this chapter. The detailed field characterisation is shown in the Appendix A.4. The GMW electromagnet is characterised but not the Bruker electromagnet.

The GMW 3480 electromagnet is capable of generating a magnetic field above 2 T. The gap between the edge of the poles, which is the narrowest part, used in this thesis is 29 mm. There is a water cooling system used for this electromagnet.

The magnetic field is characterised by scanning the field at the centre using a Group3 DTM 151 digital teslameter with two Zaber X-LSM100A linear motorised stages, scanning in the vertical and the horizontal plane, namely X and Y. There is another manual stage that can scan the Z axis. The control software is custom-built in LabView and Python. The teslameter has a reading uncertainty of ± 1 μT. The minimum step size of the stage is 0.0476 μm. The region of interest is 2 x 2 mm. In principle, the smaller the step, the more accurate the mapping will be. However, the total sampling time will be very long. In addition, any perturbation of the environment such as the mechanical instability of the teslameter will affect the measurements during the scanning. As the teslameter's probe is long and heavy, gravity has a tendency to pull it down. The probe is fixed on a 3D-printed polylactide (PLA) holder screwed onto the X stage. Multiple layers of packaging tape are wrapped around the holder and the probe. The teslameter scans across a small square at the centre, the size is 2 x 2 mm. The step size is 10 μm. The proof is first moved to the top left, and starts scanning across x, then returns to the x = 0 position before it steps down one step in z. At each step, the teslameter reads 5 times and takes the average. The sampling frequency is 10 Hz. There is a delay introduced after each step to ensure the probe will have time to the time it responds to the field at the latest position and measure 5 measurements. The total acquisition time is over 5 hours.

Figure 3.19 shows the teslameter reading at a stationary position in a 3D-printed Halbach array,

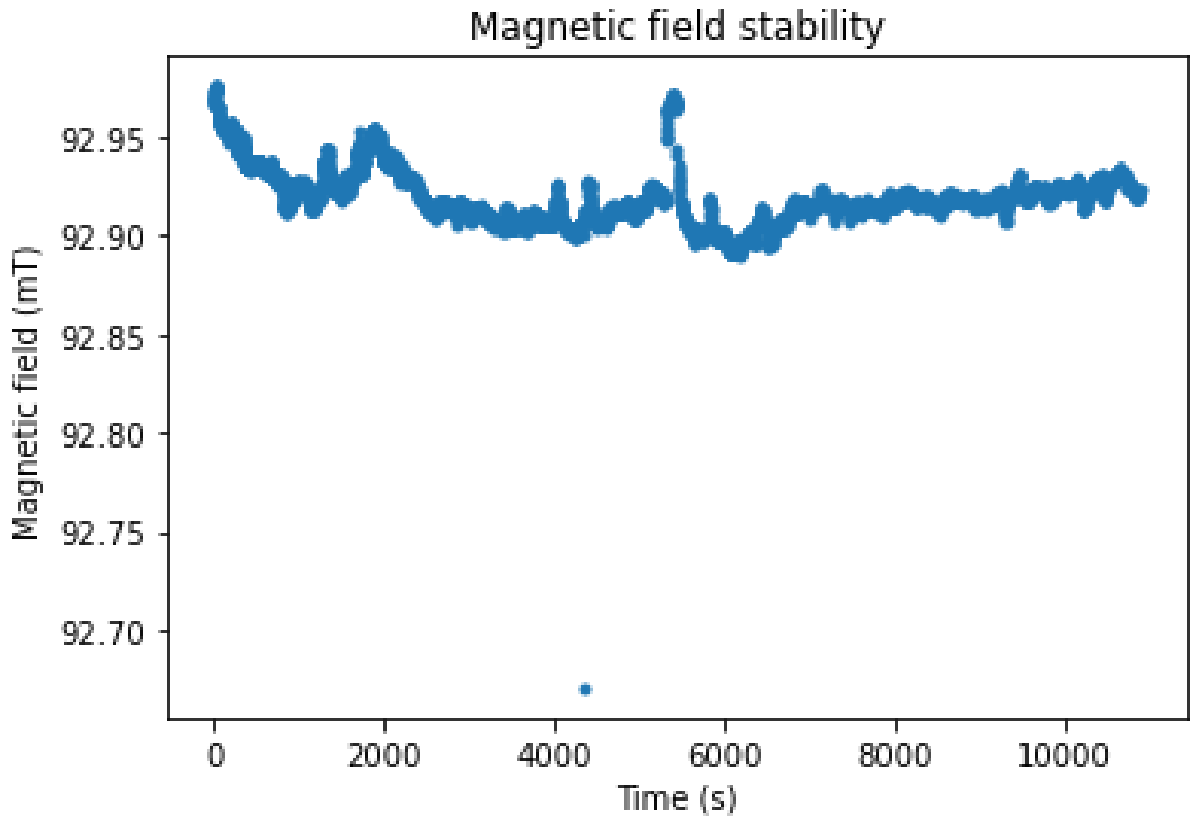


Figure 3.19: The field reading of the teslameter at a stationary point in a magnetic field.

which is shown in the Appendix A.4. to estimate the stability of the setup. It is shown that the maximum change in field reading is about 0.05 mT for a period of 12000 seconds. Overall, the field reading is stable. Figure 3.20 shows the magnetic mapping of the GMW electromagnet. The field is uniform, as the reading varies within a range of 0.02 mT, which is comparable to the reading error and the reading instability of the teslameter.

Conclusion

A three-axe motorised stage with a teslameter is constructed to characterise the 3D magnetic field of the commercial Halbach array and the GMW electromagnet. The commercial Halbach array has a central field of about 345 mT, which does not reach the desired field for an X-band maser. It might be useful for a maser at a lower frequency, at 6.79 GHz, which might be beneficial for qubits control and readout. However, the homogeneity is also poor, which is about 896.6 ppm. The number of emitters is reduced by a factor of 40 due to the field inhomogeneity and leads to no maser regime. A new Halbach design with a higher field and

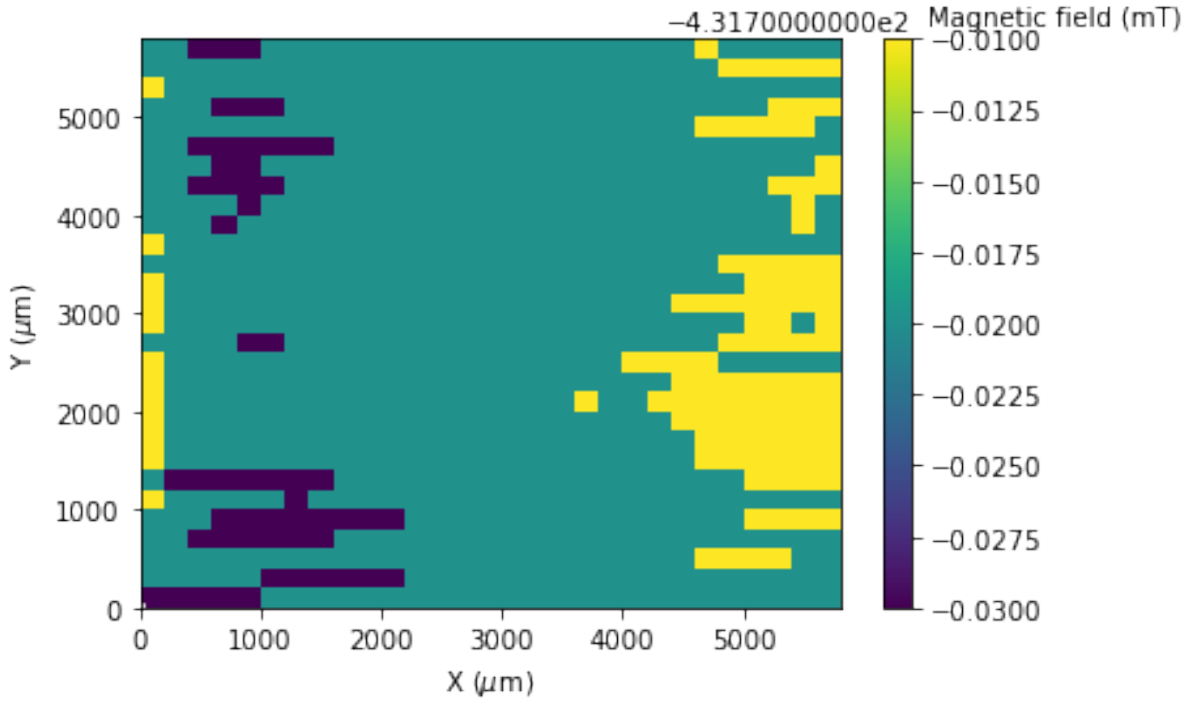


Figure 3.20: The magnetic field map of the GMW electromagnet, the field difference is too small to be detected by the teslameter.

higher field homogeneity is required to construct a maser using permanent magnets. The optimal and adaptive design of Halbach arrays with significant high field and high homogeneity are simulated in the later chapter. On the other hand, the GMW electromagnet has a very high field homogeneity, such that the variations in the field profile are comparable to the reading fluctuation of the teslameter. Therefore, a lower limit of the homogeneity is estimated to be 46.3 ppm when the field is operating at 431.7 mT.

3.3.3 Diamond maser

The excitation laser is a laser Finesses Pure 532 nm 10 W laser from Laser Quantum. The beam diameter is 2.25 mm. A laser diode at 520 nm is an alternative excitation source that has a Peltier cooling instead of water cooling, is smaller in size and is a cheaper option.

The diamond is placed inside a cylindrical sapphire resonator. The resonator is placed in a copper cavity that shields the resonator and reduces the radiation loss. The resonator is placed on top of a sapphire post to separate the resonator from the copper cavity. The laser beam illuminates the sample from the top or from the side through the hole on the wall, where it can be steered by a set of mirrors and through the hole of the top plate of the cavity that has a 3 mm hole. There is a coupling loop inserted in the cavity from the side to out-couple the MW output. The MW output is measured by a real-time spectrum analyser, ThinkRF R5550, and a vector signal analyser (VNA), Copper Mountain Technologies M5180. A switch is used to select if VNA or the spectrum analyser is in operation. In addition, the VNA is used for checking the resonances of the resonator, by finding the reflection dips and the wiggle of the dips when the magnetic field scan passes. The MW output can also be measured using a real-time spectrum analyzer. A PC is used to display the spectrum of the MW output. There are two configurations for the static magnetic field. The static magnetic field is generated by the Buker electromagnet. Or, the static magnetic field is generated by an electromagnet, GMW 3480 dipole electromagnet, which is controlled by a programmable DC power supply, Sorensen DLM 80-37e. The benefit of the GMW electromagnet is that it is much smaller and more compact than the Bruker electromagnet, on the other hand, the GMW electromagnet has a poorer homogeneity than the Bruker electromagnet.

For GMW setup, a pair of modulation coils, which is controlled by a Kepco power supply, is used to fine-tune the magnetic field to match the maser transition. The GMW electromagnet only provides a rough field control. Figure 3.21 shows the schematic diagram of the GMW maser setup, and Figure 3.22 shows the rendered image of the setup.

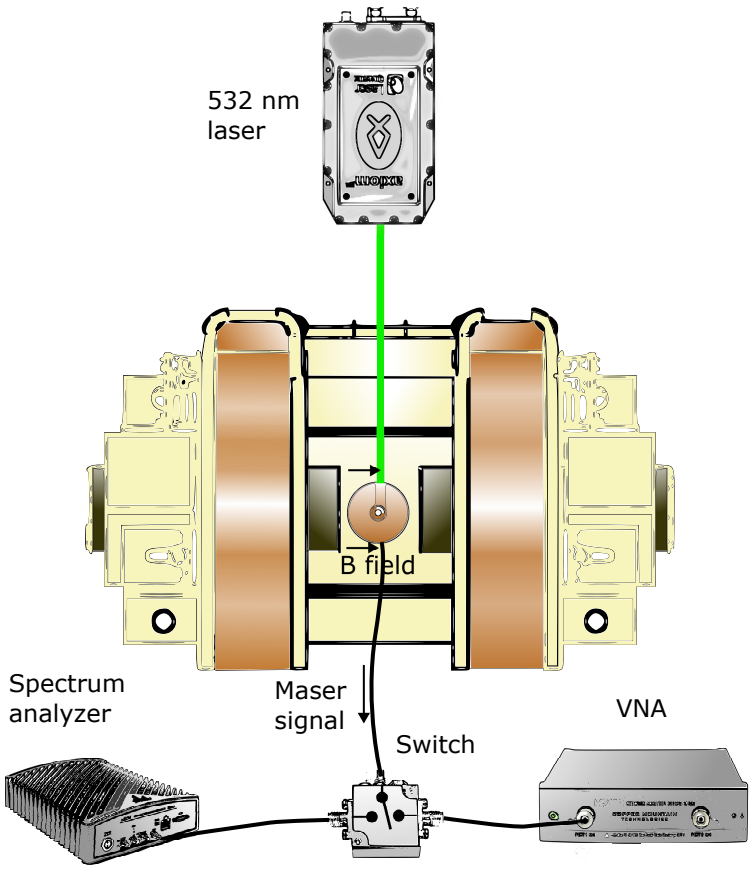


Figure 3.21: A schematic diagram of the diamond maser with the GMW electromagnet. The diamond inside a dielectric resonator and a copper cavity are fitted inside the pole pieces of the electromagnet. The output signal is detected by the spectrum analyser and the VNA, which can be used to check the resonance of the resonator before masing. The switch is used to select which detector to be used.

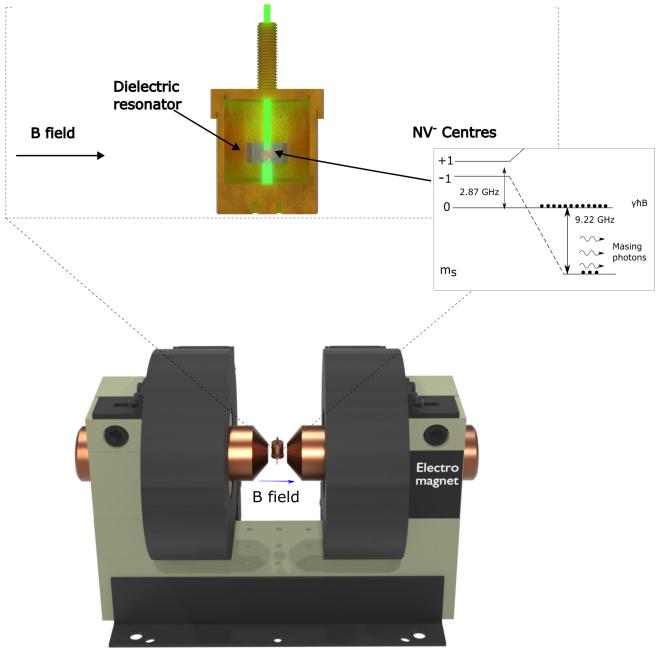


Figure 3.22: A schematic diagram of the diamond maser with the GMW electromagnet. The diamond inside a dielectric resonator and a copper cavity are fitted inside the pole pieces of the electromagnet. The output signal is detected by the spectrum analyser and the VNA, which can be used to check the resonance of the resonator before masing. The switch is used to select which detector to be used.

Chapter 4

Optical Characterisation Results

This chapter presents the three different methods, the least square method, the phasor method, including the global binning method and the random search method, and the deep learning method, and the results of the optical characterisation. Ground truth evaluation is introduced and the three methods are compared. The deep learning method demonstrated exceptional accuracy and precision within the training intervals and outperformed the others. By comparing the deep learning method results with the others and the ground truth, the lifetime results are validated. Based on the three methods, the ratio of the lifetime components varying with the excitation wavelength. The longer the wavelength, the more fluorescence from NV^- relative to NV^0. The lifetime values tau_1 and τ_2 is lower when the excitation wavelength is at 492 nm and 502 nm compared with the lifetime values above 532 nm. The distribution of the lifetime values is similar to a normal distribution on D09, 10BA and 10BB. The D09 sample has the narrowest distribution. The NID_{02} shows a bimodal distribution on tau_1. This is suspected to be the influence of the singlet transition that splits the lifetime of different spins, $m_s = 0$ or $m_s = \pm 1$. The lifetime amplitudes result indicates that the NV^-/NV^0 ratio is the highest for the D09 sample and the lowest for NID_{02}.

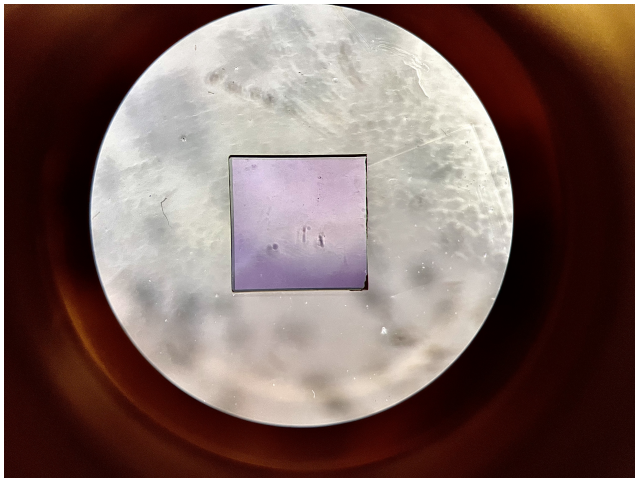
4.1 Samples

The diamond samples are all from Element Six, which are all made using the CVD method. The first diamond is labeled D09, it is an isotopically high purity diamond that consists of 99.999%

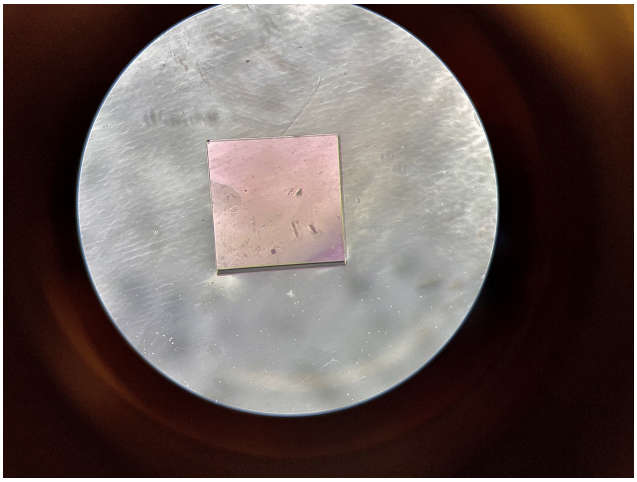
Sample	Dimension (mm)	NV concentration (ppb)
NID_{02}	2.5 ×2.5 × 2	1350
D09	2.89 ×2.83 × 0.504	4500
10BB	2.8 ×2.8 × 0.32	369
10BA	2.8 ×2.8 × 0.449	429

Table 4.1: A table of the four-diamond samples used in this thesis. The [NV^-] concentration is not rigorously determined in this thesis, the concentration of the NID_{02} and D09 are quantified by EPR measurements, not included in this thesis.

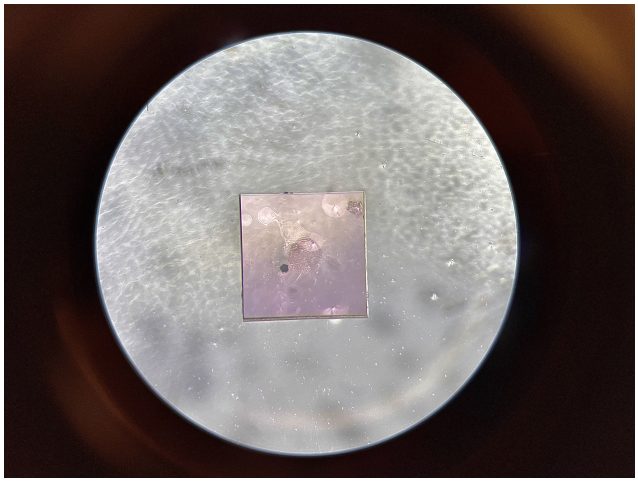
^{12}C, with zero spin S = 0, to reduce any undesirable effect from the ^{13}C, S = 1/2, which occurs naturally at 1.1%. The nitrogen concentration is 16000 ppb, and the NV concentration is 4500 ppb The size is 2.83 x 2.89 mm and the thickness is 504 μm, shown in Figure 4.1 (a). The second diamond sample is labelled 10BA, the carbon is natural abundance, which means the ^{12}C is about 98.9%. The NV concentration is 429 ppb, the size is 2.8 x 2.8 mm and the thickness is 449 μm, as shown in Figure 4.1 (b). The third diamond sample is labelled 10BB, it has natural abundance carbons, the NV concentration is 369 ppb, the size is 2.8 x 2.8 mm and the thickness is 320 μm, shown in Figure 4.1 (c). It is the thinnest and the least NV concentrated diamond sample. The images of each diamond sample are taken by a mobile phone through a WF10X/20 eyepiece and a 0.5X Barlow lens on an Amscope stereo microscope. There is an additional sample labeled NID_{02}, which is a cubic CVD diamond. The dimension is 2.5 mm x 2.5 mm x 2.0 mm, as shown in Figure 4.1 (d). The concentration of NV centres is 1350 ppb, with an NV^- concentration of 620 ppb, quantified by EPR measurement [130]. The dimensions and the NV concentration are listed in Table 4.1. The four edges of the three thin samples, 10BB, 10BA and D09, were black. The Q factor measured with the samples was very poor on the order of a few hundred instead of around 30000. It was believed that the black sustain was graphitic carbon residual after laser cutting. The samples were then treated by Element Six with chemicals. The samples were immersed in boiling sulfuric acid, nitric acid and perchloric acid mixture that selectively etched any graphitic carbon from the surface of the samples. However, the Q factor was still poor. It was believed that graphitic carbon may be included within the crystal. A further treatment was carried out by Element Six using the "Scaife polishing", which removed the black edges and the Q factor no longer dropped.



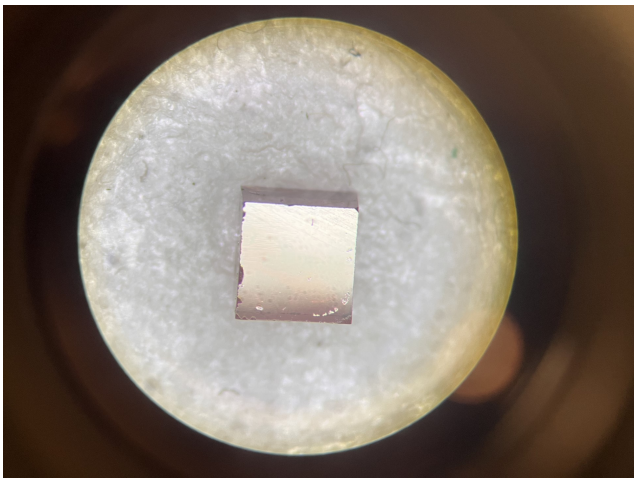
(a) D09



(b) 10BA



(c) 10BB



(d) NID_{02}

Figure 4.1: The image of the samples (a) D09 (b) 10BA (c) 10BB (d) NID_{02}.

4.2 Fluorescence lifetime imaging of diamond samples for maser

Fluorescence lifetime is a method to characterise fluorescent defects in diamonds. NV^-, NV^0, and SiV^- are defects that exhibit fluorescence. It is a robust method to identify defects, as it is associated with the lifetime of an excited state of a particular defect. It is also robust against crosstalk of different spectral components.

Mapping a diamond sample using fluorescence lifetime can in principle map the distribution of different fluorescent defects and it is useful for checking the homogeneity of NV centres in a diamond sample.

A supercontinuum laser is used to provide a variable excitation wavelength from 400 nm up to 700 nm. A set of filters in the Zaber wheel and the Andor spectrometer is used as a long-pass filter to block the excitation wavelength. The fluorescence light is collected using a hybrid PMT. A time tagger is used to count the arrival of a fluorescence photon after the laser excitation, by setting the start channel as the laser-synchronised signal and the trigger channel as the PMT. The time tagger, which is a TCSPC instrument, constructs a histogram of the delay of the arrival time of single-photon counts from the excitation laser after a long acquisition period to record a sufficient amount of photon counts. The typical exposure time for this setup is between 3 to 15 seconds. A shorter exposure time means fewer averaging so that the noise is more significant. On the other hand, a longer exposure time requires a long time to complete the experiment. The time bins of the histogram are evenly spaced with a small bin width, of 100 ps, that can sample the decay profile. The number of data points is 1150. In total, there is a 115 ns long period to capture the lifetime decay profile. This setup has a very small instrument response function (IRF) which is estimated to be about 30 ps, which is smaller than the binwidth. The time scale of the decay of NV centres is much greater than the IRF. The IRF is ignored during the analysis. In order to map the sample, this process is repeated for every pixel. The data collected is a 2-dimensional map where each pixel contains a time-resolved histogram. There are three methods employed to estimate the fluorescence lifetime across the sample. The first method is a standard method used in lifetime estimation. The other two methods are proposed as novel methods that have less human bias on the initial guesses and act as references to validate the results. The second method uses a graphical analysis of the

lifetime components. The third method is introduced to reduce human bias and efficiently analyse complicated lifetime decay such as multi-lifetime decay.

Least square method The first method uses the nonlinear least-square method to fit the histogram with a bi-exponential function with initial guesses. This method minimises the sum of squares of the difference between the data and the fitting. The Levenberg-Marquardt algorithm is used to optimise the fitting, which is ideal for nonlinear fitting problems with constraints and bounds. The goodness of the fitting is determined by the reduced chi-square, which is the chi-square per degree of freedom. Usually, the smaller the reduced chi-square the better the fit. However, a more complicated model will lead to overfitting and unphysical issues. The bi-exponential function is used as it improves the chi-square and it is reasonable as the two-lifetime components might be associated with the NV^-, around 11 ns, and NV^0, around 19 ns [115]. The lifetime values vary between NV centres in bulk diamonds and nanodiamonds. The fitting is performed pixel-wise, an alternative approach is to average all the pixels and perform one fit, which is the global binning method. This approach assumes that the lifetime components are the same across the sample. The benefit is the speed of this method, the downside is to sacrifice the spatial information. This can be used to get a rough estimation of the sample. This shows the nonlinear least-square equation:

$$min \sum_i (f - y)^2 \tag{4.1}$$

where f is the predicted data from the fit and y is the measured data. However, the initial guesses are important as they will determine the lifetime and might be biased. The fitting process is long for a 2-dimensional map as the calculation iterations increase. The formula for the reduced chi-square is.

$$\chi_r^2 = \frac{\sum (I_r - I_f)^2}{I_r(n-p)} \tag{4.2}$$

where I_r is the raw intensity, I_f is the fitted intensity, p is the free parameters and n is the number of data. For simplicity, chi-square refers to reduced chi-square. The multi-exponential function $F(x)$ is shown:

$$F(t) = \sum_i A_i e^{-\frac{t}{\tau_i}} \tag{4.3}$$

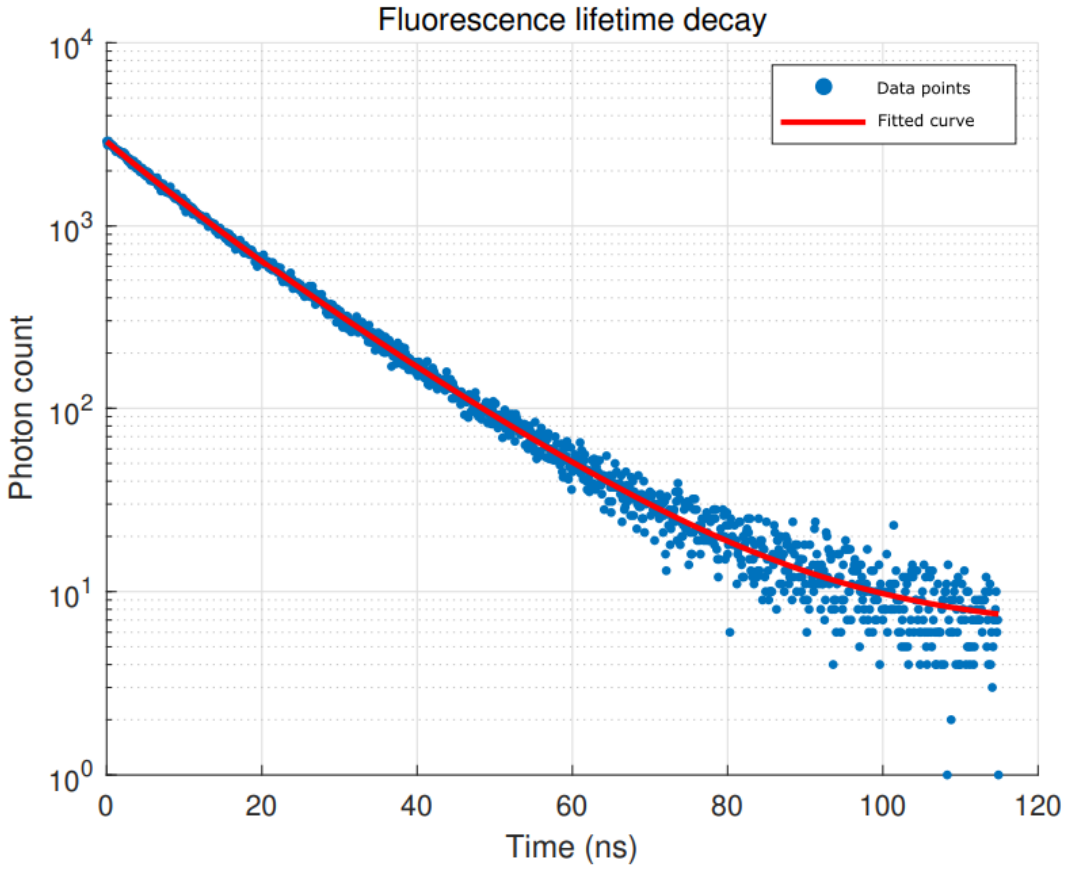


Figure 4.2: The fluorescence lifetime decay profile using the least square method to analyse the sample D09 at 532 nm excitation. The dots are the data and the red curve is the fit.

where A_i is the amplitude of the i^{th} exponential component, τ_i is the lifetimes of the i^{th} exponential component. For bi exponential, the sum is over i = 1, 2. Figure 4.2 shows the exponential decay of a single point on the upper surface of the D09 sample, exited with 532 nm. The points are the experimental data and the red line is the fitted line. The exposure time is 7 s and the resolution is 75 μm.

Figures 4.3, Figure 4.4, Figure 4.5 and Figure 4.6 show, starting from the top left, the map of the fluorescence intensity as the integral of the decay profile, the top right, the map of the decay time of the first-lifetime component, the middle left, the map of the decay time of the second-lifetime component, the middle right, the map of the χ^2, the bottom left, the map of the amplitude of the first-lifetime component, the bottom right, the amplitude of the second-lifetime component, shows the results of excitation of 532 nm, 502 nm, 592 nm and 402 nm. Each plot is the average of 100 fittings with random initial guesses. The integrated decay intensity reveals some patches of high intensity, on the right edge and the bottom edge of the sample. In the

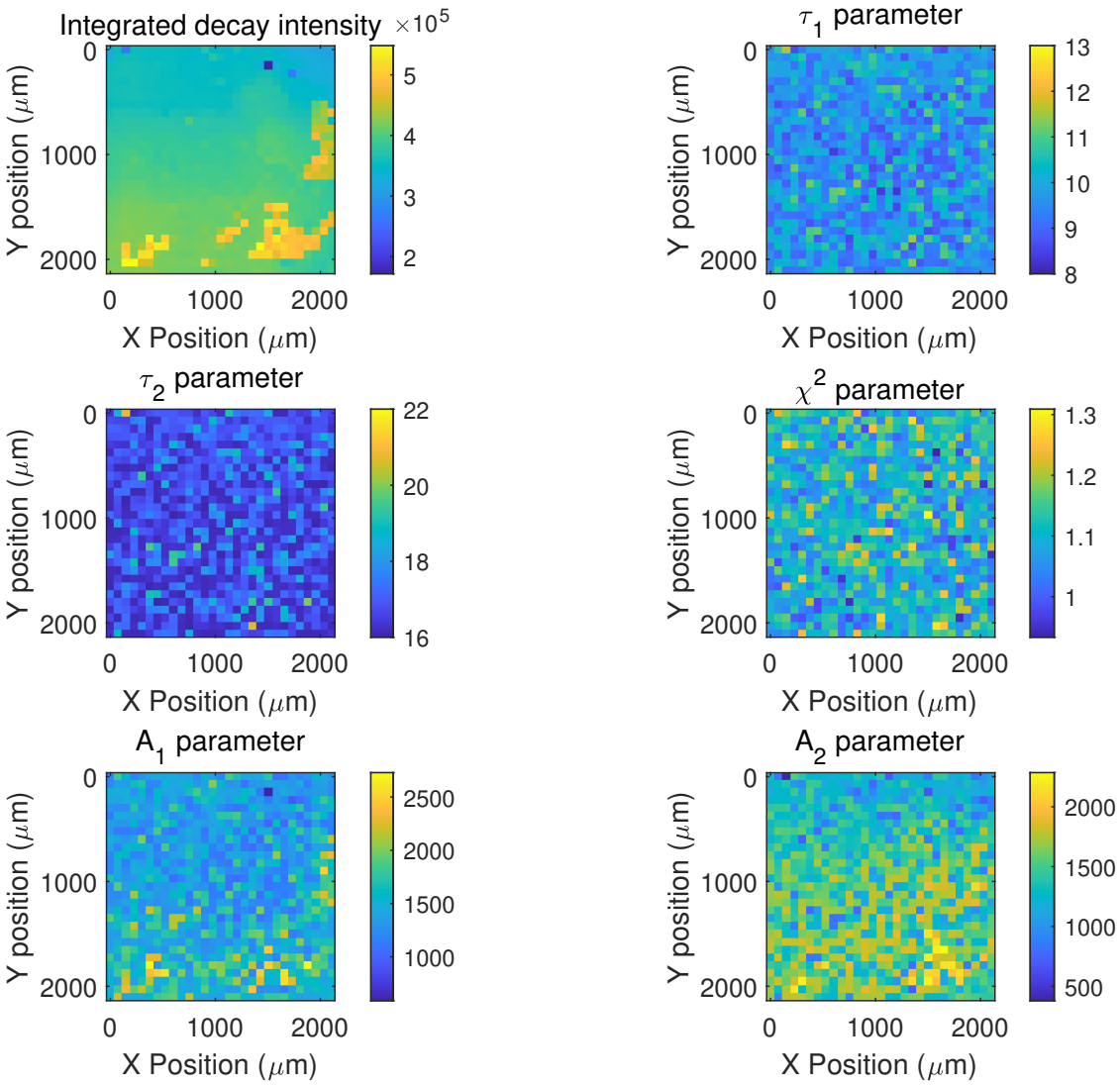


Figure 4.3: The fluorescence lifetime map using the least square method to analyse the sample D09 at 532 nm excitation. The subfigures show the integrated decay intensity which is the fluorescence mapping. The first and the second-lifetime components, τ_1 and τ_2, and the reduced χ^2 mapping and the amplitude, A_1 and A_2, of the first and the second components respectively.

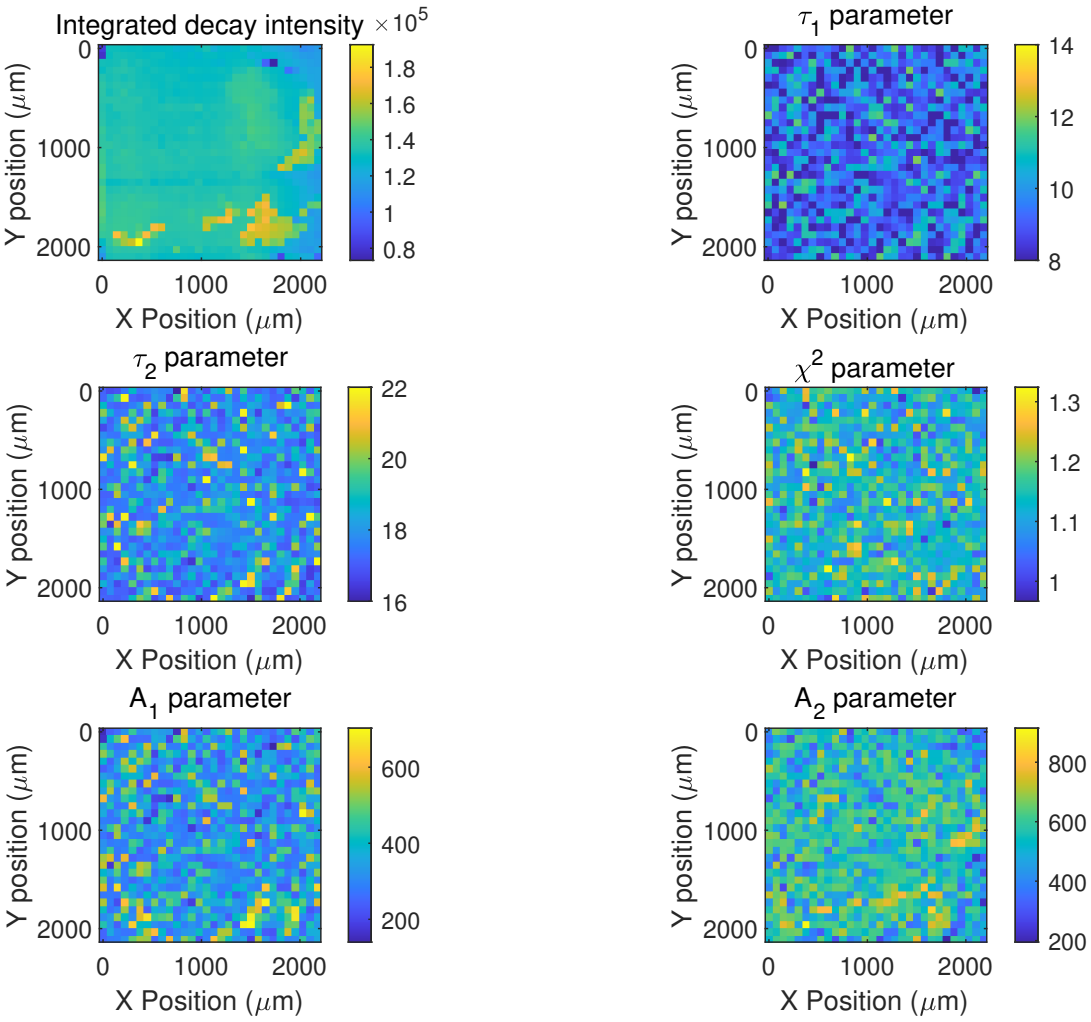


Figure 4.4: The fluorescence lifetime map using the least square method to analyse the sample D09 at 502 nm excitation. The subfigures show the integrated decay intensity which is the fluorescence mapping. The first and the second-lifetime components, τ_1 and τ_2, and the reduced χ^2 mapping and the amplitude, A_1 and A_2, of the first and the second components respectively.

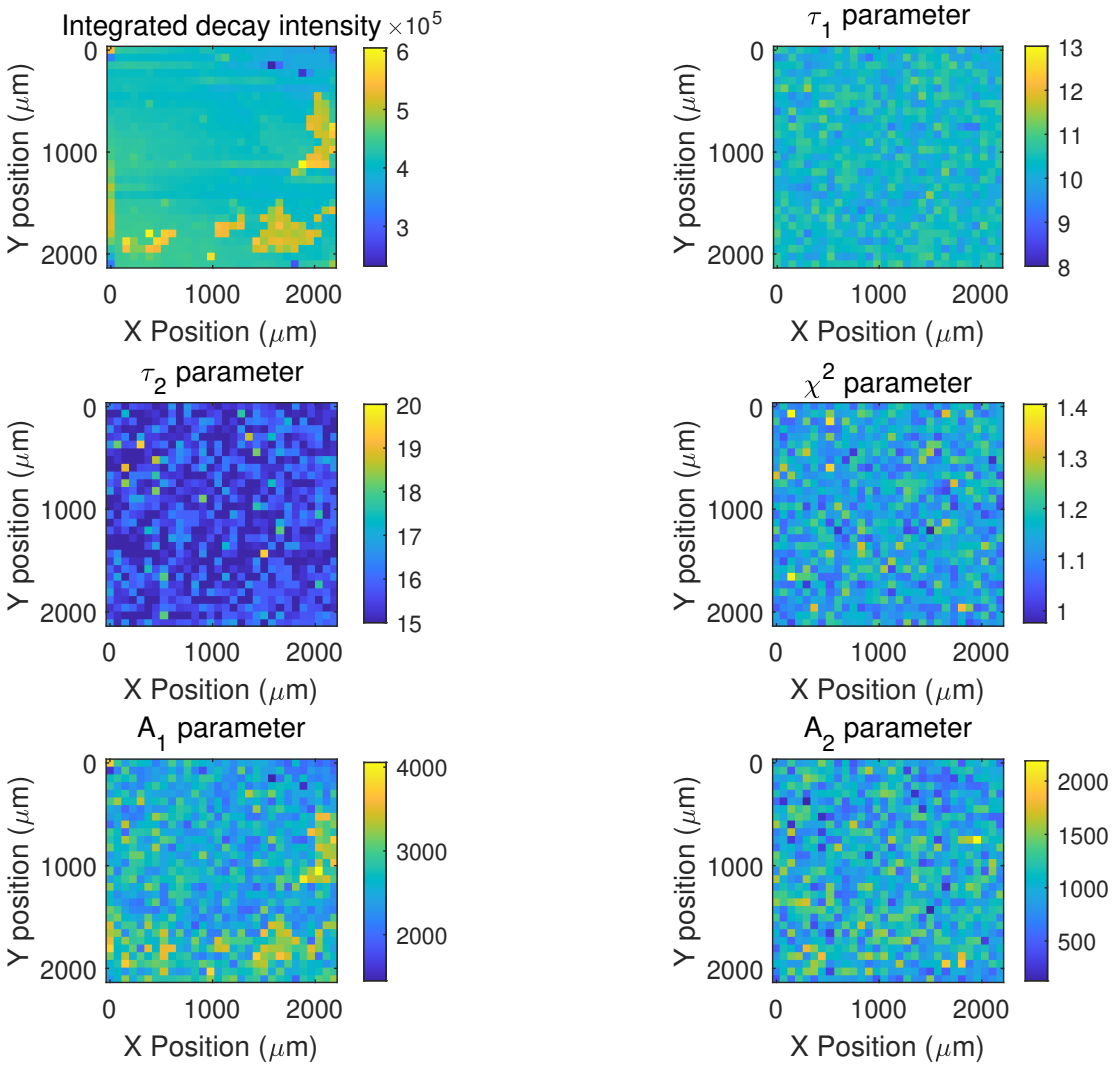


Figure 4.5: The fluorescence lifetime map using the least square method to analyse the sample D09 at 592 nm excitation. The subfigures show the integrated decay intensity which is the fluorescence mapping. The first and the second lifetime components, τ_1 and τ_2, and the reduced χ^2 mapping and the amplitude, A_1 and A_2, of the first and the second components respectively.

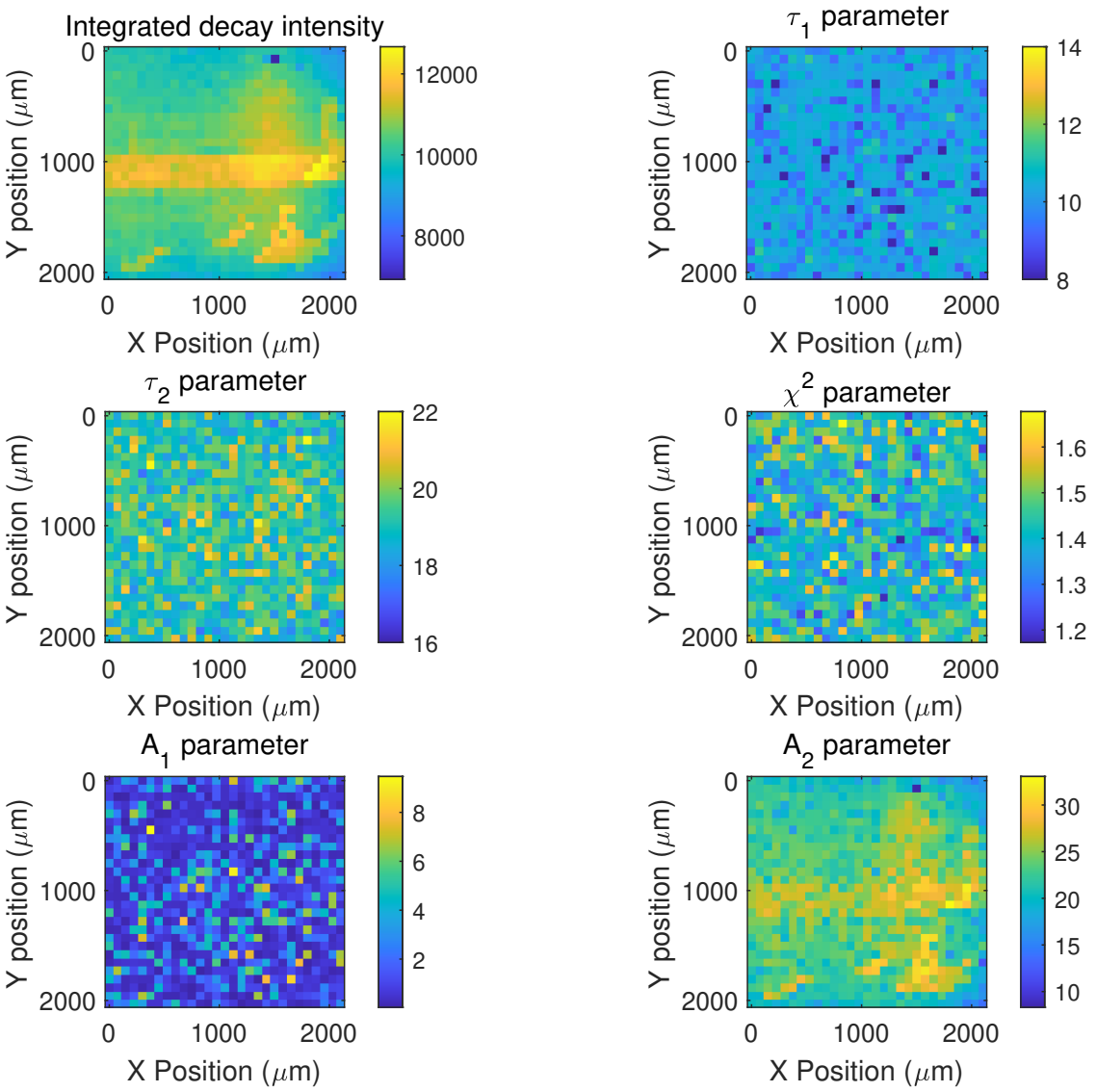


Figure 4.6: The fluorescence lifetime map using the least square method to analyse the sample D09 at 402 nm excitation. The subfigures show the integrated decay intensity which is the fluorescence mapping. The first and the second-lifetime components, τ_1 and τ_2, and the reduced χ^2 mapping and the amplitude, A_1 and A_2, of the first and the second components respectively.

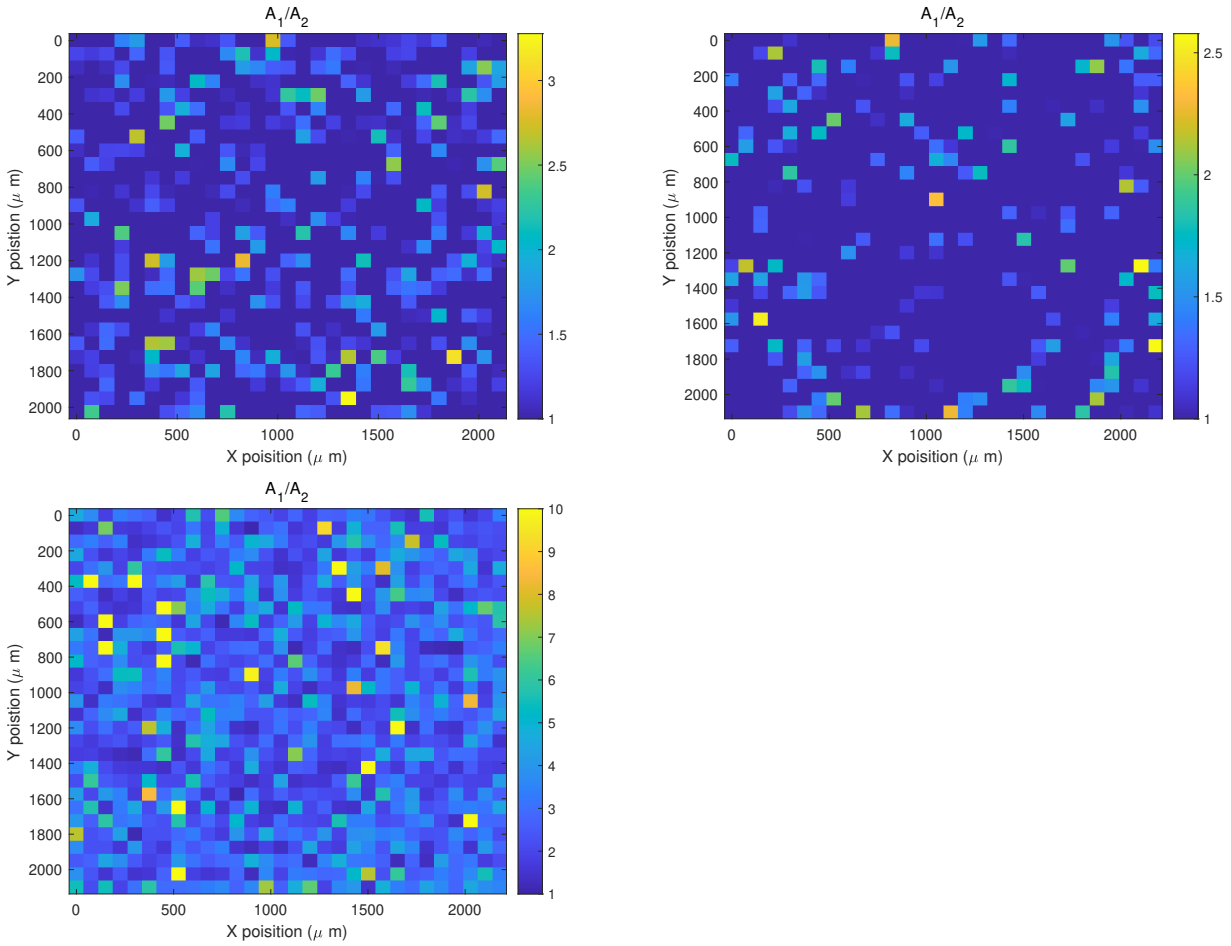


Figure 4.7: The image shows the pixel where NV^- is dominant over NV^0 under (a) 532 nm, (b) 502 nm and (c) 592 nm excitation.

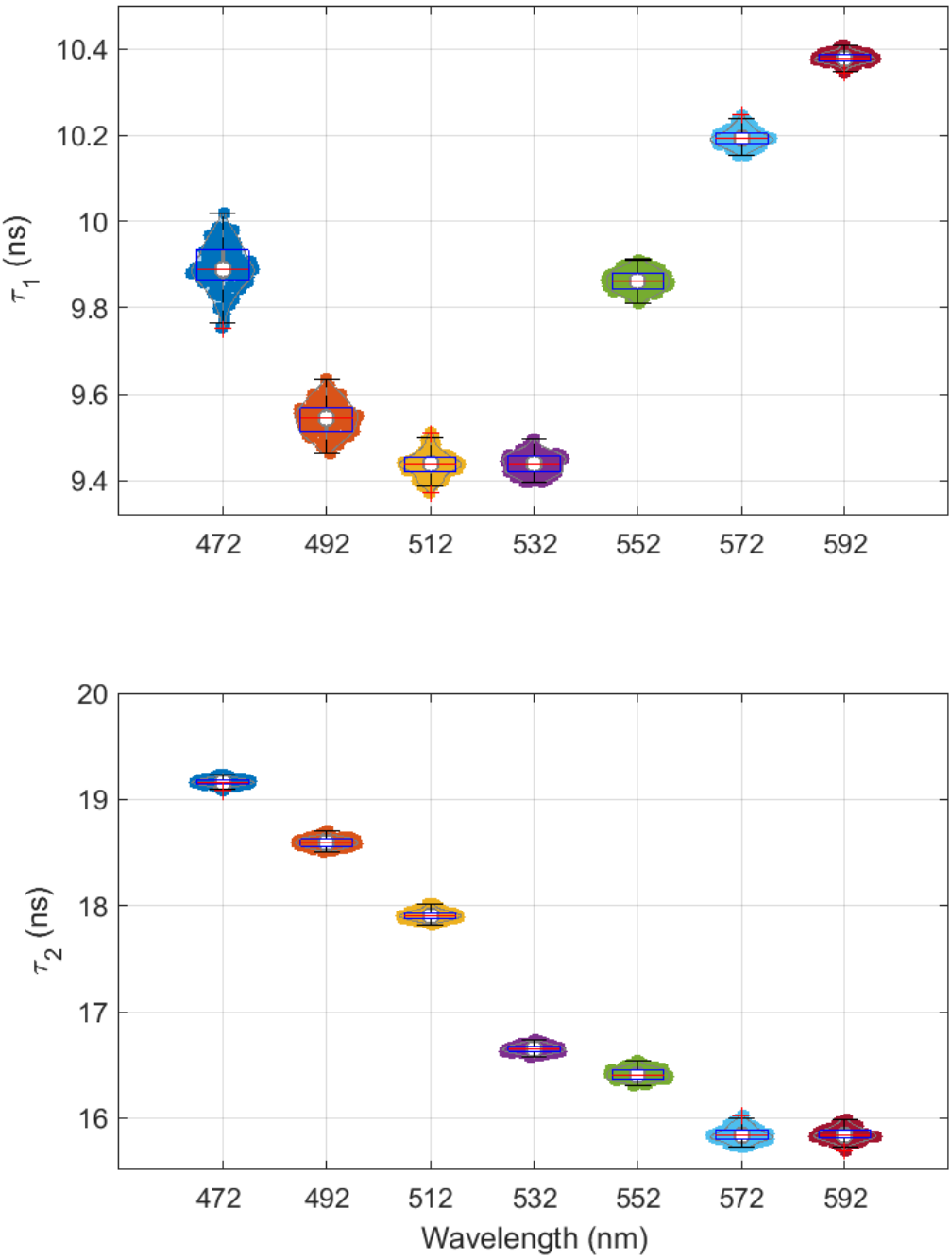


Figure 4.8: The plots show the mean and the dispersion of τ_1 and τ_2 of D09 sample with various excitation wavelengths.

lifetime fitting maps, the patches disappear, suggesting the lifetime is not correlated with the fluorescence intensity. However, the A_1 and A_1 have a similar pattern at those locations, but the bright regions of A_1 and A_2 do not coexist exactly at the same location. The bright patches might have different origins. The higher A_1 values in the pattern indicate a potentially high concentration region from the NV^- in the high-intensity patches in the integrated intensity map. The lifetime maps are more uniform, the high fluorescent patches have no impact on the fluorescence lifetime. For the following analysis, the mean is the mean of all the pixels from the 100 images of different fittings with random initial guesses. The standard deviation is the standard deviation of all the pixel values from 100 images. For example, the pixel values could be τ_1, and the image size could be 40 by 40, so the total number of pixels is 160000. The mean and the standard deviation are estimated based on the 160000 pixels. To further study the statistical features and significance of the results, the standard deviation of each pixel, which is the standard deviation of the mean of each pixel across all the images, and the standard deviation of each image, which is the standard deviation of the mean of each image across all the images, is used. They are referred to as pixel level and global level respectively. These will give valuable information about the fittings, initial guesses, pixels, and the image as a whole.

The mean values of the fitting are τ_1 is 9.44 ns, τ_2 is 16.65 ns, A_1 is 1414.27 and A_2 is 1539.02. The mean reduced chi-square is 1.12 ± 0.06. The standard deviation of τ_1 is 0.89 ns, τ_2 is 0.95 ns, A_1 is 362.61 and A_2 is 359.34. The large standard deviation of the amplitudes, 19.8% and 20.1% indicates the distribution of the amplitudes across the pixel is not uniform. The standard deviation of at the global level, is 0.023 ns and 0.037 ns for τ_1 and τ_2 and 10.18 and 10.24 for A_1 and A_2. The difference between different initial guesses is insignificant to the distribution of the fluorescence and the defects, which concluded that the fitting is stable and convergent. The pixel level standard deviation of the amplitude is 267.33 and 268.69 and the pixel level standard deviation of the lifetime is 0.59 ns and 1 ns. There is statistical significance in the map, except for τ_2, which has a comparable standard deviation in the mean of individual pixels as the standard deviation as a whole.

To show the effect of excitation wavelength, the same sample and mapping are conducted at 592 nm and 502 nm, with an exposure time of 7 s and a resolution of 75 μm.

Figure 4.7 shows the ratio of A_1 to A_2 under a different excitation wavelength. The results agree that the ratio is correlated to the length. The longer the excitation wavelength, the

higher the ratio and more pixels have a higher ratio. When the excitation is at 502 nm, the mean values of the fitting are τ_1 is 9.49 $\pm$ 1.22 ns, τ_2 is 18.17 $\pm$ 1.17 ns, A_1 is 362.80 $\pm$ 104.28 and A_2 is 552.22 $\pm$ 112.68. The uncertainty is the standard deviation across the pixels. The mean reduced chi-square is 1.14 $\pm$ 0.06. The integrated intensity was reduced by a factor of 2.8. The standard deviation of the amplitudes across all the pixels increases to 28.7% and 20.4%. It shows that the NV^- is more inhomogeneous across the sample. The A_2/A_2 ratio is more uniform across the sample. The amplitudes standard deviation of the fittings are 2.08 and 2.10, which shows the fittings using random initial guesses that agree with each other. The lifetime standard deviation at the global level is 0.021 ns and 0.024 ns. When looking at the standard deviation of each pixel across the 100 fittings, the standard deviation of the amplitudes is 63.97 and 64.66 and the standard deviation of the lifetime is 0.659 ns and 0.767 ns. The results suggest that the amplitudes and the lifetime variations across the samples are statistically significant, as the standard deviation of the whole map is significantly greater than the standard deviation of the mean of individual pixels.

When the excitation is at 592 nm. The mean values of the fitting are τ_1 is 10.32 ns, τ_2 is 15.59 ns, A_1 is 2628.37 and A_2 is 1008.99. The mean reduced chi-square is 1.15. The standard deviation of τ_1 is 0.39 ns, τ_2 is 0.74 ns, A_1 is 393.8 and A_2 is 311.16. The standard deviation of the amplitude at a global level is 14.22 and 14.27, and 0.012 ns and 0.062 ns for the lifetimes. The lifetime standard deviation of the mean of the individual pixel is 0.344 ns and 1.695 ns and the amplitude standard deviation of the mean of the individual pixel is 405.2 and 406.4. Further investigation of the histogram of the lifetimes and the amplitude shows that there are two peaks instead of one peak in the lower wavelength. For the histogram of τ_2, the distribution is cut off by the lower bound at 14 ns. This suggests the presence of the fluorescence from the NV^0 is minuscule. It is concluded that the NV^0 is not sufficiently pumped due to the long wavelength. The fluorescence collected is mostly from NV^-.

To investigate the fluorescence lifetime under a short wavelength, 402 nm is used to excite the sample. At this wavelength, the fluorescence intensity is very weak and noisy. To increase the intensity, the exposure time is set up to 60 seconds. However, the reduced chi-square of the fitting is 1.42, which indicates the fitting is not optimal. The mean values of the fitting are τ_1 is 10.15 ns, τ_2 is 19.29 ns, A_1 is 1.73 and A_2 is 23.4. The standard deviation of τ_1 is 0.79 ns, τ_2 is 0.66 ns, A_1 is 1.88 and A_2 is 3.04. The fluorescence light of the NV^0 is dominant in this

case. The standard deviation of the fittings for the amplitude at a global level is 0.0658 and 0.062 and 0.073 ns and 0.038 ns. The amplitude standard deviation of the pixels is 1.736 and 1.650 and the standard deviation of the lifetimes is 2.065 ns and 0.984 ns. From the results, the fluorescence is mostly from NV^0. This can be the result of photoionisation from NV^- to NV^0. Notice that there is a bright band in both the integrated intensity map and the A_2 map. The band is believed to be NV^0 abundant region. This band is only induced by short-wavelength excitation. It is believed to be a strong photoionisation region, where photorecombination back to NV^- is prohibited. From the integrated decay intensity map, there is a wide rectangular patch across the sample, which is not present in a longer wavelength. This feature might be associated with NV^0. The least-square method shows that at the pixel level, the fitting parameters significantly impact the results, as the results show large variability with different initial guesses. However, at the global level, which averages all the pixels, the influence from the initial guesses is minimised.

The results show that at 532 nm excitation, the proportion of NV^- and NV^0 is similar. At a longer excitation wavelength, the NV^- will have a higher proportion, whereas, at a short excitation wavelength, the NV^0 will be dominant. At 592 nm excitation, the energy is less than the zero phonon line of the NV^0. In principle, there might be no NV^0 centres excited. From the results, the τ_2 is the lowest and it is way below the expected lifetime of NV^0 and the chi-squared is higher. This suggests that the presence of NV^0 is low. Figure 4.8 shows the pixel distribution and the mean of the lifetime τ_1 and τ_2 under various excitation wavelengths. The τ_1 exhibits lower values between 492 nm and 532 nm and exhibits higher values above 572 nm. The τ_2 is anticorrelated to the excitation wavelength. Figure 4.9 shows the pixel distribution and mean of the lifetime τ_1 and τ_2 of the four samples under a 532 nm excitation. The D09 sample has the lowest τ_1 and τ_2. Whereas, NID_{02} has the highest τ_1 and τ_2. These values are related to the amplitudes, as a lower tau_2 is related to a lower A_2.

For the sake of brevity, the detailed results of the sample 10BA, 10BB and NID_{02} are shown in Appendix A.2. The summary of the results is shown in Table 4.2. The global level standard deviation is used as the uncertainty in Table 4.2. Table 4.3 shows the mean difference and the 95% confidence interval (CI) of the upper and the lower bound and the P value.

In conclusion, the A_1 and A_2 contributions are similar for D09 under a 532 nm excitation. As the means of different fittings are within the standard deviation. The fluorescence intensity

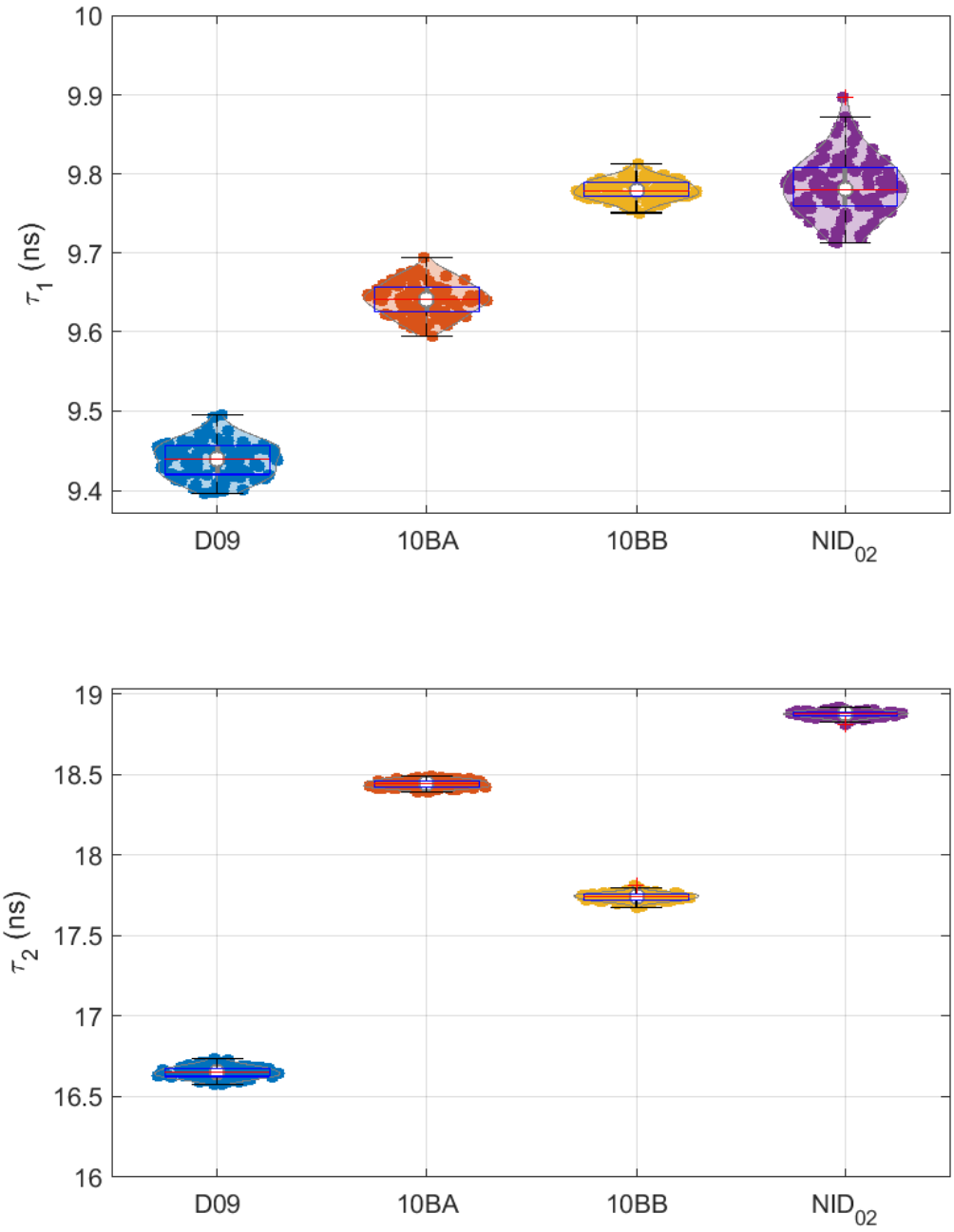


Figure 4.9: The plots show the mean and the dispersion of τ_1 and τ_2 of the four samples. From the upper plot, there is a positive correlation with the concentration and the τ_1 among the thin samples.

Sample	A_1	A_2	$\tau_1(ns)$	$\tau_2(ns)$
D09	1414 ± 267	1539 ± 269	9.44 ± 0.02	16.65 ± 0.04
10BA	314.08 ± 79	521.92 ± 80	9.64 ± 0.93	18.50 ± 0.99
10BB	141.97 ± 43.23	151.62 ± 43.76	9.82 ± 1.13	17.77 ± 1.69
NID_{02}	58.65 ± 26.58	208.57 ± 26.82	9.81 ± 1.65	18.94 ± 0.80

Table 4.2: A summary of lifetime measurement at 532 nm based on the least square method.

Sample 1	Sample 2	Mean difference	Lower bound	Upper bound	P value
D09	10BA	-0.2124	-0.2033	-0.1942	0
D09	10BB	-0.3508	-0.3417	-0.3326	0
D09	NID_{02}	-0.3544	-0.3453	-0.3362	0
10BA	10BB	-0.1476	-0.1385	-0.1294	0
10BA	NID_{02}	-0.1511	-0.1420	-0.1330	0
10BB	NID_{02}	-0.0127	-0.0036	-0.0055	0.7437

Table 4.3: A Tukey's Honestly Significant Difference test of the four samples. It shows the difference in mean between any two samples and the upper bound and lower bound of the 95% CI and the P value. It shows that there is statistical significance of the τ_1 values between the samples except for the 10BB and NID_{02}. It confirms that there is a positive correlation among the thin sample.

is the most intense. Similarly, the 10BB sample shows a similar amount of A_1 and A_2, but the fluorescence intensity is much lower due to the lower concentration of NV centres. In the 10BA sample, it is clear that the average A_2 over the sample is higher than A_1, which is not an optimal condition as the NV^-/NV^0 ratio is smaller than one. NID_{02} has a high A_2 and a low A_1. However, the volume of the NID_{02} is much larger than 10BA, and the filling factor and the number of spins are much higher than 10BA. It is predicted to be more likely to mase than 10BA. The four samples have similar τ_1 lifetime, but the τ_2 values vary among the samples. The tau_1 lifetimeseems to have a positive correlation with the NV concentration in the thin samples. The D09 is the most concentrated sample and has the shortest τ_1, whereas the 10BB sample is the least concentrated sample and has the longest τ_1. The NID_{02} is a cubic sample that has a moderate concentration. Both the τ_1 and τ_2 is long compare to the thin samples. By doing the T-test, there is a statistical significance of τ_1 of d09 to the 10BB and 10BA.

In a shorter excitation wavelength such as 402 nm, the fluorescence is significantly reduced and the noise increases. This may be caused by the low intensity in the blue end of the laser and lower quantum efficiency of the detector. However, the lifetime component is dominated by NV^0. In a longer excitation wavelength, the NV^- dominates the exponential fitting.

4.2.1 Random search for lifetime components and phasor method for diamond

The least square method provides a way of estimating the lifetime and the amplitude of each component. However, the lifetime model used in the least square method has to be defined. Usually, the more exponential terms, the better the fit. This will lead to an unphysical model. The phasor method is one of the methods that help find the number of lifetime components [131]. This method is introduced as a graphical method that will distinguish the number of exponential terms presented in the histogram. The histogram is phasor transformed and the result is a point on a complex plane with a coordinate of (G, S) [131].

For a mono-exponential decay, the transformed points are on the perimeter of an upper half of a circle, centre at (0,0.5) with a radius of 0.5. For a bi-exponential decay, the points are on the chord that links two mono-exponential decay points on the perimeter. For a tri-exponential decay, the points are located within a triangle that the vertices are on the perimeter of the circle corresponding to three mono-exponential decays. Similarly, more exponential decay components will contribute and form a polygon with vertices attached to the circle, where the phasor transformed points are inside.

The following diagrams show the phasor diagram for mono-exponential, bi-exponential, tri-exponential, and tetra-exponential lifetime components.

$$G = \frac{\int_0^I (t) cos(\omega t) dt}{\int_0^I (t) dt} \tag{4.4}$$

$$S = \frac{\int_0^I (t) sin(\omega t) dt}{\int_0^I (t) dt} \tag{4.5}$$

where $I(t)$ is the data and ω is the frequency of the measurement. The lifetime, τ, is estimated using the following equation that applies to the (G, S) coordinate of a component on the perimeter of the circle. For a multi-exponential decay, the lifetime components are traced out from the data and then the lifetime is estimated using the same method. The relative distance from the data to the components can be worked out and find the relative contribution from

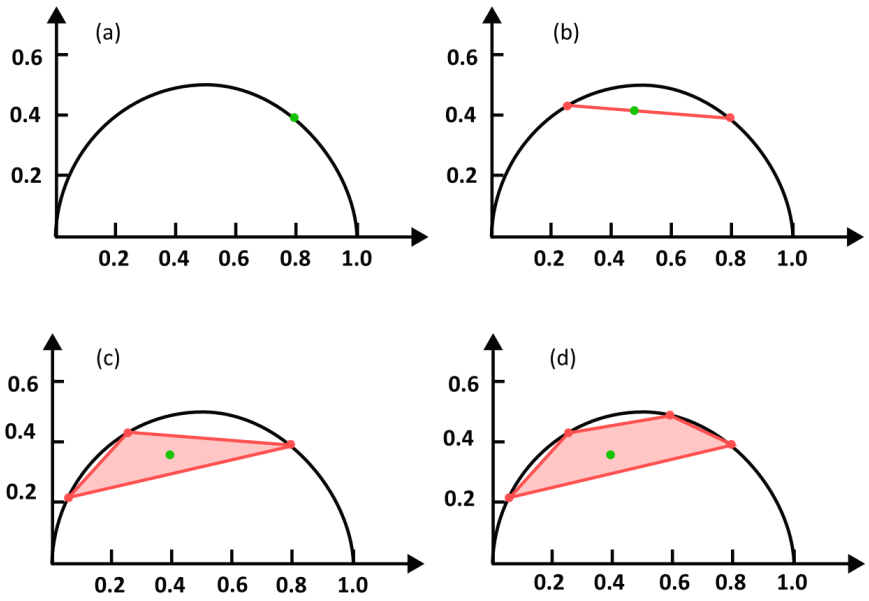


Figure 4.10: The plots show the phasor-transformed data point as a green dot and the red dots show the corresponding lifetime components on the circle. (a) Mono-exponential. (b) Bi-exponential (c) Tri-exponential. (d) Tetra-exponential.

each component.

$$\tau = \frac{1}{\omega}\sqrt{\frac{1}{G^2 + S^2} - 1} \tag{4.6}$$

The larger the G value (x-axis), the shorter the lifetime of the component, whereas the smaller the G value, the longer the lifetime of the component. For a multi-exponential component, the relative position of the data point indicates the relative contribution from the components. For example, if the data point is on the midpoint of a chord linking two lifetime components, the data point has an equal contribution from both lifetime components. On the other hand, the closer the data point is to a point, the higher the contribution from that point. Until it is at that point, where other components are negligible, and become a mono-exponential decay.

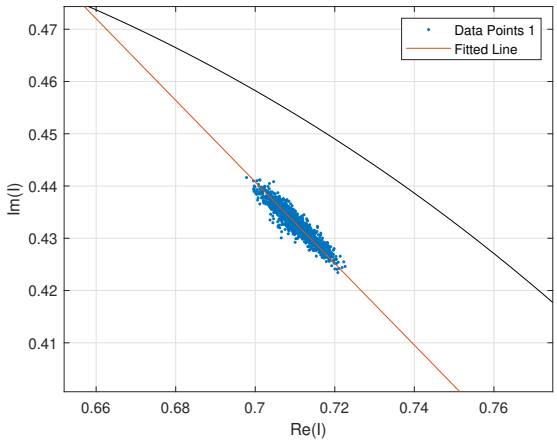
For a simple estimation of the averaged lifetime of the samples. It is assumed that all the data points across the sample have the same bi-exponential components, namely the NV^- and the NV^0. It is expected that the points should lie along the chord connecting the two lifetime components.

However, this method can only find an averaged lifetime. In order to find the lifetime of each pixel. The full harmonics analysis is adapted with a custom optimisation algorithm [132].

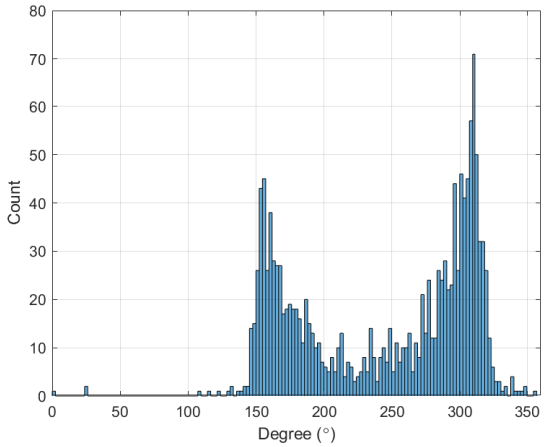
The optimisation employed here is the random search which is a lightweight optimisation and does not require the computation of gradient and might be more efficient for this algorithm. A classifier can be used to classify lifetime data into various lifetime components. This will eliminate the need for estimating the lifetime time for various lifetime models and comparing them to select the best model. Appendix A.1 demonstrates the details of a hybrid classical-quantum classifier to classify the data for the samples.

The first method is to phasor transform all the pixels to the phasor space and then linearly fit the data points, assuming it is bi-exponential. The fitted line intersects at two points on the circle, which is used to estimate the two-lifetime components. The situations for all one, two, three and four components are illustrated in Figure 4.10 (a), (b), (c) and (d) respectively. It is assumed that the distribution of the NV centres is uniform, the pixels after phasor-transformed will be binned and it is expected to lie along the chord connecting τ_1 and τ_2. To show the variance and the geometrical shape of the distribution of the data in the phasor space, shown in Figure 4.11 (a), (c) and (d) for different excitation wavelengths, a histogram of the data at angles from 0° to 360° at the middle of the data points is shown in Figure 4.11 (b), (d) and (f). This method is effective in estimating the number of lifetime components as a bi-exponential decay will give two peaks in the histogram, and a tri-exponential decay will give three peaks. From the phasor plot in Figure 4.11 (a), the pixels are distributed along a line with a small deviation from the line, which suggests it can be modeled by the bi-exponential model. Knowing the coordinates of the interception points, the midpoint of the fitted line is estimated, and the relative proportion, A_1/A_2, of the two-lifetime components is found to be 20.2 %. This indicates that the longer lifetime component is dominant. This method agrees that the A_2 is dominant, but the least square estimates the ratio to be 47.6 %. The black curve in the figure is the circle that bounds the phasor plot. From the angular histogram, in Figure 4.11 (b), most of the pixels are along the 155 ° and the 310 ° directions. The two lifetimes extracted from the fitting are 9.065 ± 0.119 ns 19.785 ± 0.146 ns. The errors are estimated by propagating the errors of the linear fit with the standard deviation of the residuals of the fitting. Compared to the least square method, the long lifetime component is longer, whereas the shorter lifetime component is much shorter. This discrepancy might arise from global binning, which suggests that global binning might introduce some errors.

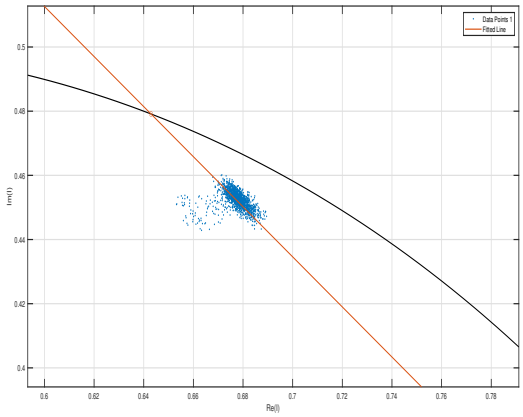
At 502 nm, the two lifetimes extracted are 11.645 ± 0.282 ns and 21.107 ± 0.347 ns. The



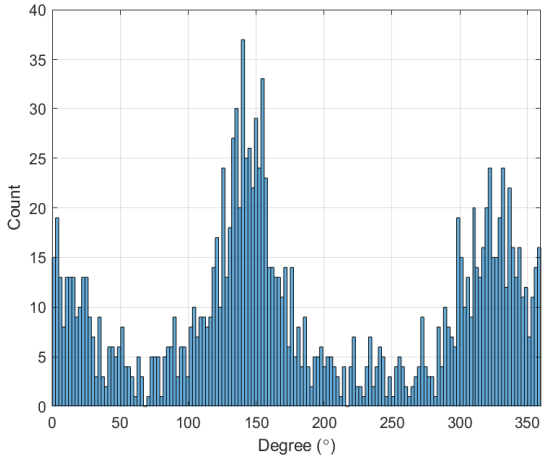
(a) 532 nm



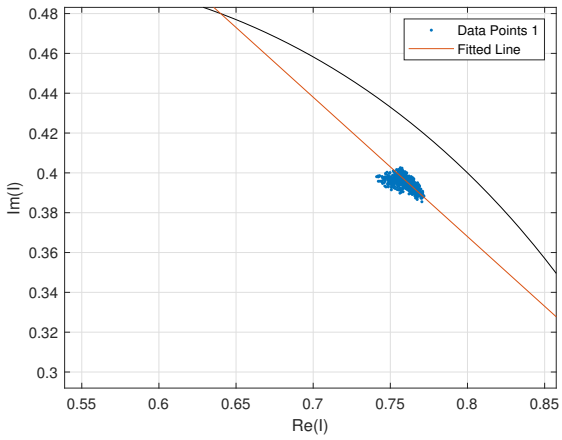
(b) 532 nm



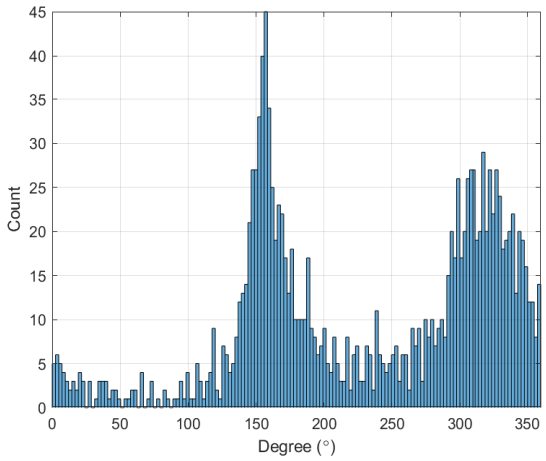
(c) 502 nm



(d) 502 nm



(e) 562 nm



(f) 562 nm

Figure 4.11: The phasor diagram of the 10BA sample, (a) for 532 nm, (c) for 502 nm, (e) for 562 nm and the angular histograms of the 10BA sample (b) for the 532 nm, (d) for the 502 nm and (f) for the 562 nm.

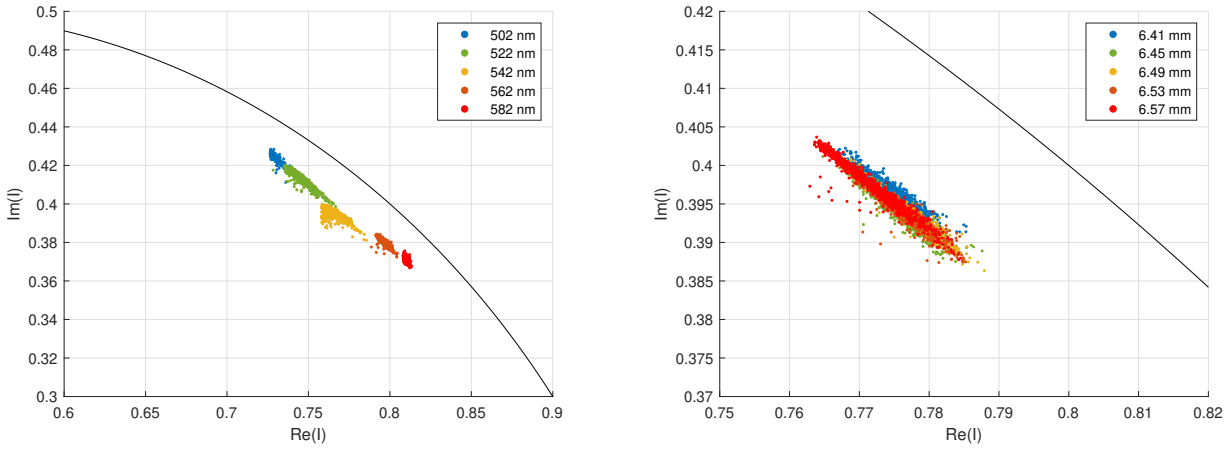
results of the phasor plot and the histogram. In the phasor plot, there is a side branch, which has a horizontal distribution with a large variance, and it is believed to be noise. The lifetimes are extracted by removing the horizontal distribution. If the horizontal distribution is fitted with a line, it will have lifetimes of 17.54 ns and 83.172 ns, which has no fluorescence defects that match the lifetime.

The relative proportion of the two lifetime components is 13.0%. The longer lifetime component becomes even more dominant at 502 nm. This can be seen in the histogram plot, where the two peaks at 141° and 330° are the main branch and the small peak at 0° is believed to be noise. Notice that the separation between the two peaks is smaller compared to the 532 nm peaks. At 562 nm, the two lifetimes extracted are 10.740 ± 0.197 ns and 24.259 ± 0.268 ns. The relative proportion is 46.2 %, meaning that the long lifetime component and the short lifetime component have a similar contribution but the longer lifetime component is slightly more dominant. The detailed results of the other samples are shown in Appendix A.3.

Figure 4.12 (a) shows the phasor plot of multiple excitation wavelengths of the fluorescence lifetime data of the D09 sample. It implies that the longer the excitation wavelength, the greater the contribution from the shorter lifetime component, as the clusters approach the lower right along a line. The shape of the phasor points becomes more concentrated at a point instead of along the chord as the excitation wavelength increases. This suggests the proportion of the amplitudes at various pixels is more similar.

In Figure 4.12 (b), the clusters are all excited with 532 nm with the sample D09 but with a different depth, meaning the data is from a different focal plane within the sample from the top. The clusters all overlay each other, suggesting the depth information is very similar and no difference in lifetime components. Table 4.4 shows the summary of the lifetime components using the phasor method. The larger uncertainty of NID_{02} is due to the wider spread of the points in the phasor plot.

The global binning technique provides a fast and robust method for estimating the lifetime components. However, it can not determine the lifetime component of each pixel. For 10BB and 10BA, the shorter lifetime component deviates from the literature values. The relative proportion shows that the D09 sample has more NV^- than NV^0, and 10BB has slightly fewer NV^-, but the overall NV concentration in 10BB is much less than the D09 sample. On the other hand, NID_{02} has relatively fewer NV^- and 10BA has the least amount of NV^-. The



(a) Wavelength (b) Depth

Figure 4.12: (a) The plots show the phasor-transformed data point from sample D09, with an excitation of a range of excitation wavelengths. (b) The plots show the phasor-transformed data point from sample D09, with an excitation of a range of depths from the top surface from 6.57 mm at 532 nm excitation.

Sample	$\tau_1(ns)$	$\tau_2(ns)$
D09	10.289 ± 0.151	20.366 ± 0.186
10BA	9.065 ± 0.119	19.785 ± 0.146
10BB	10.707 ± 0.210	19.892 ± 0.254
NID_{02}	14.335 ± 0.350	22.063 ± 0.421

Table 4.4: A summary of lifetime measurement at 532 nm based on the phasor method using global binning.

global binning might average the error from each pixel, and give one estimation and error. A pixel-wise method might be more accurate, as each pixel is examined separately. Here, the blind determination method is adapted to estimate the lifetime component of diamonds, and a random search method is applied to extract the lifetime component from each pixel. The random search method developed is significantly faster than the least square method. The original blind determination can be found from [133], which was used to estimate the lifetime components in live cells. The main idea is to use the higher harmonics in the phasor transform. In the previous global binning techniques, only the first harmonics are used. The bi-exponential blind determination required only the first and the second harmonics. For more lifetime components, higher harmonics are needed. For example, the tri-exponential blind determination requires the first, the second and the third harmonics are required. However, the blind determination lacks the ability to learn the number of fluorescence lifetime components beforehand. Thus, similar to the conventional method, the results from all mono, bi, tri, or even more components

models have to be used and compare the results and the fitting errors to decide which model fits the best. In Appendix A.1, a new algorithm is introduced to classify the number of lifetime components in the phasor plots. This is vital as it determines whether the bi-exponential or the tri-exponential blind determination should be used and eases the need for the computation of different lifetime components. In addition, the classified model is based on a quantum-classical hybrid transfer learning architecture, which showcases the capability of quantum computing in classification and the research of the optical characterisation of diamonds. In this thesis, the diamond samples are limited to uniform and high concentrations of NV for maser application. Thus, the lifetime components are limited to NV^- and NV^0, only the bi-exponential blind determination is used.

The working principle of the random search blind determination for the bi-exponential model is to randomly select two lifetime components, which are two points on the circle. Draw a line between the points, with a constraint that the line must pass through the data point. This step ensures that the data point results from the two lifetime components. Calculate the second harmonics of the two lifetime components and obtain another set of points on the circle and draw a line connecting them. Calculate the second harmonics of the data and obtain the distance between it and the line joining the two second harmonics points on the circle. If the distance is 0, the two second harmonics lifetime components are the exact solution. A random search algorithm is designed to search for the two lifetime components that minimise the distance with a random step that improves the result. Figure 4.13 shows the first and the second harmonics and the corresponding lines and data points, where d is the distance between the second harmonics data point to the line.

By performing the random search on each pixel for every sample, D09, NID_{02}, 10BA, 10BB, at 532 nm, the results are shown in Figures 4.14 to 4.17. Within each figure, there are four sub-plots, starting from the top left is the amplitude of the normalised shorter lifetime component, A_1, and on the right is the normalised amplitude of the longer lifetime component, A_2. Starting from the bottom left is the lifetime of the shorter lifetime component, t_1 and on the right is the lifetime of the longer lifetime component, t_2. The figure of merit, which is the residual distance, is defined as the minimum distance between the data and the line. The mean τ_1 cross all the pixels for D09 is 11.04 ns. The mean τ_2 is estimated to be 22.31 ns. The amplitude of the shorter lifetime component, A_1, is 64.15 %, and 35.85% for the longer lifetime component,

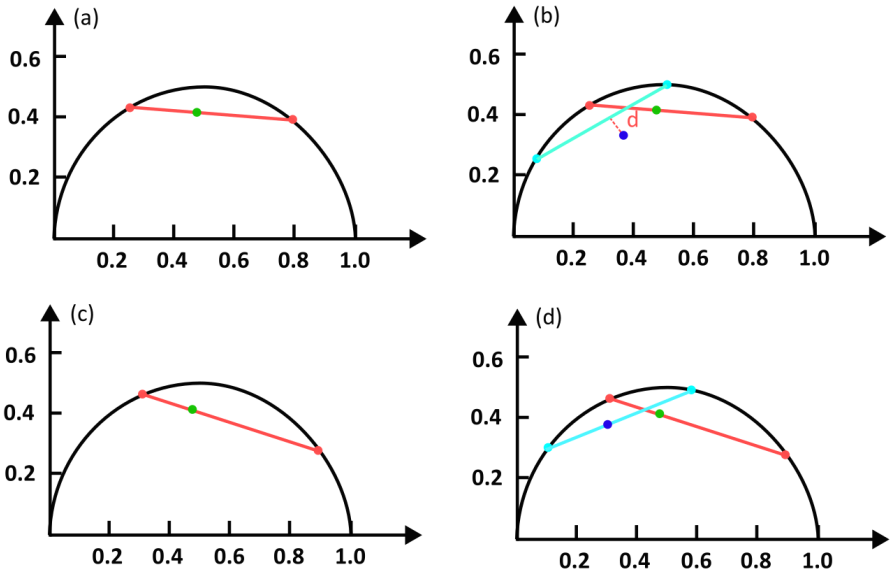


Figure 4.13: The plots show the blind determination in phasor space data point as a green dot and the red dots show the corresponding lifetime components on the circle. The cyan line and the cyan dots are the second harmonics of the corresponding lifetime components. The dark blue dot is the second harmonic of the data point. d is the distance between the second harmonics of the line and the data point. (a) Initial guess of the lifetime components (b) Second harmonic of the initial guess (c) The ideal lifetime components (d) Second harmonic of the ideal lifetime components that the line perfectly intercepts the data point.

A_2. The mean residual distance is 0.0044.

The mean τ_1 cross all the pixel for NID_{02} is 11.02 ns. The mean τ_2 is estimated to be 20.02 ns. The amplitude of the shorter lifetime component, A_1, is 19.88 %, and 80.12% for the longer lifetime component, A_2. The mean residual distance is 0.0025.

The mean τ_1 cross all the pixels for 10BA is 11.03 ns. The mean τ_2 is estimated to be 21.60 ns. The amplitude of the shorter lifetime component, A_1, is 41.42 %, and 58.58% for the longer lifetime component, A_2. The mean residual distance is 0.0051.

The mean τ_1 cross all the pixels for 10BB is 10.98 ns. The mean τ_2 is estimated to be 21.88 ns. The amplitude of the shorter lifetime component, A_1, is 50.80 %, and 50.02% for the longer lifetime component, A_2. The mean residual distance is 0.0047.

In the τ_1 distribution plot, it is clear that there are two modes, one is around 12 ns and one is around 7 ns. This can be the result of a lifetime from the $m_s = 0$ and $m_s = \pm 1$ the exited levels [134].

Sample	$\tau_1(ns)$	$\tau_2(ns)$	A_1	A_2
D09	10.9937 ± 0.7838	24.0707 ± 8.2397	0.6326 ± 0.1351	0.3719 ± 0.1547
10BA	10.9936 ± 0.7829	21.4834 ± 2.0332	0.4151 ± 0.2215	0.5849 ± ± 0.2215
10BB	10.9844 ± 0.7848	20.2467 ± 1.3453	0.5174 ± 0.0779	0.4826 ± 0.0779
NID_{02}	10.9928 ± 0.7879	19.9872 ± 0.4724	0.1963 ± 0.0474	0.8037 ± 0.0474

Table 4.5: A summary of lifetime measurement at 532 nm based on the random search method.

The standard deviation of pixels across the 100 fittings is similar to the standard deviation of the mean of the fittings. This suggests a more robust pixel-level fitting than the least square method and is potentially more useful in looking at individual pixels. Figure 4.18 shows the distribution and the mean of the lifetimes τ_1 and τ_2 of the fittings of 7 different excitation wavelengths. (a) is the distribution of the pixel level and (b) is the values averaged every 900 pixels to reduce the noise. Figure 4.19 shows the distribution and the mean for the four samples. Table 4.5 shows the mean values and the standard deviation of the lifetimes and the amplitudes.

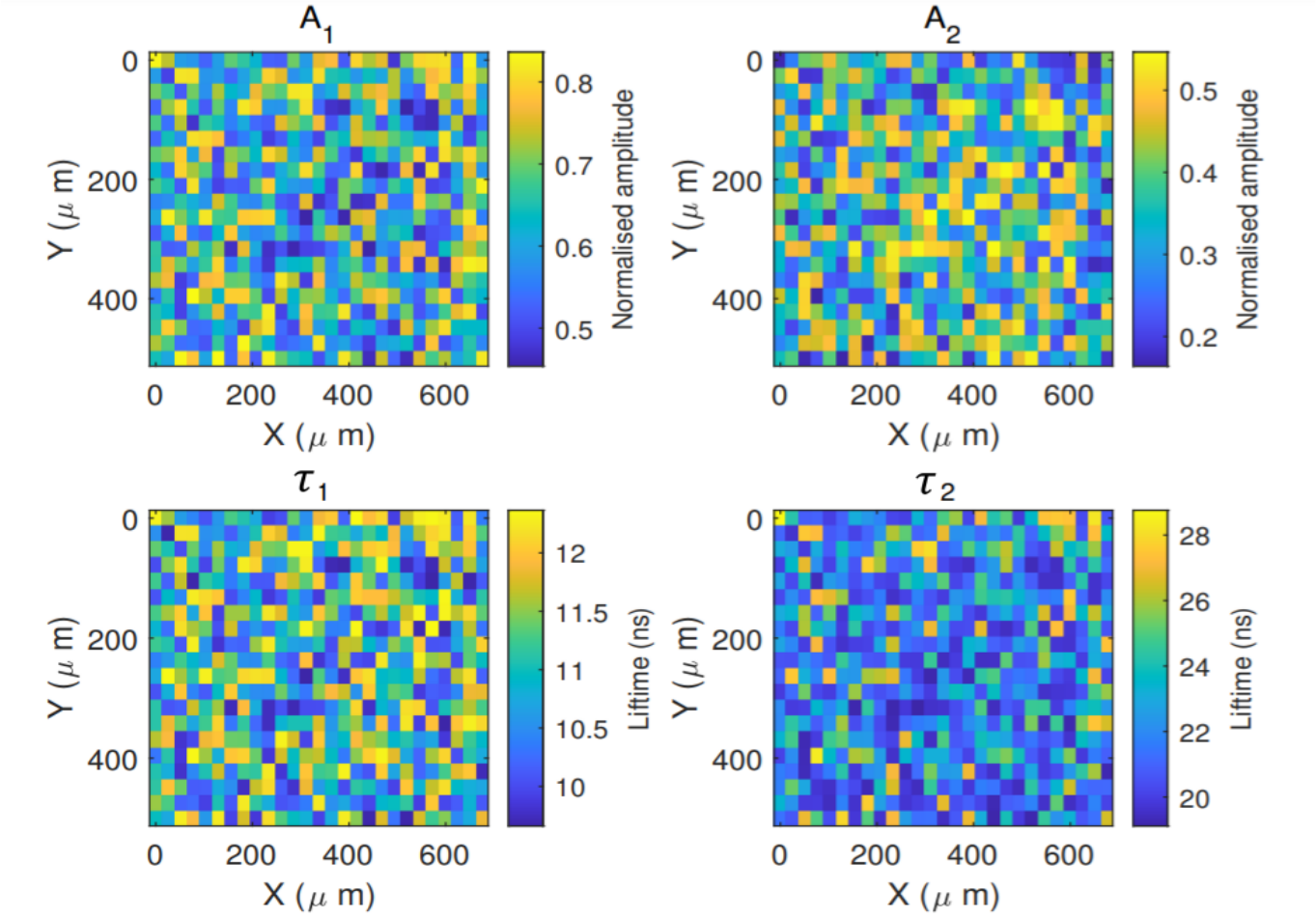


Figure 4.14: The plots show the lifetime component imaging of the D09 sample using the random search method.

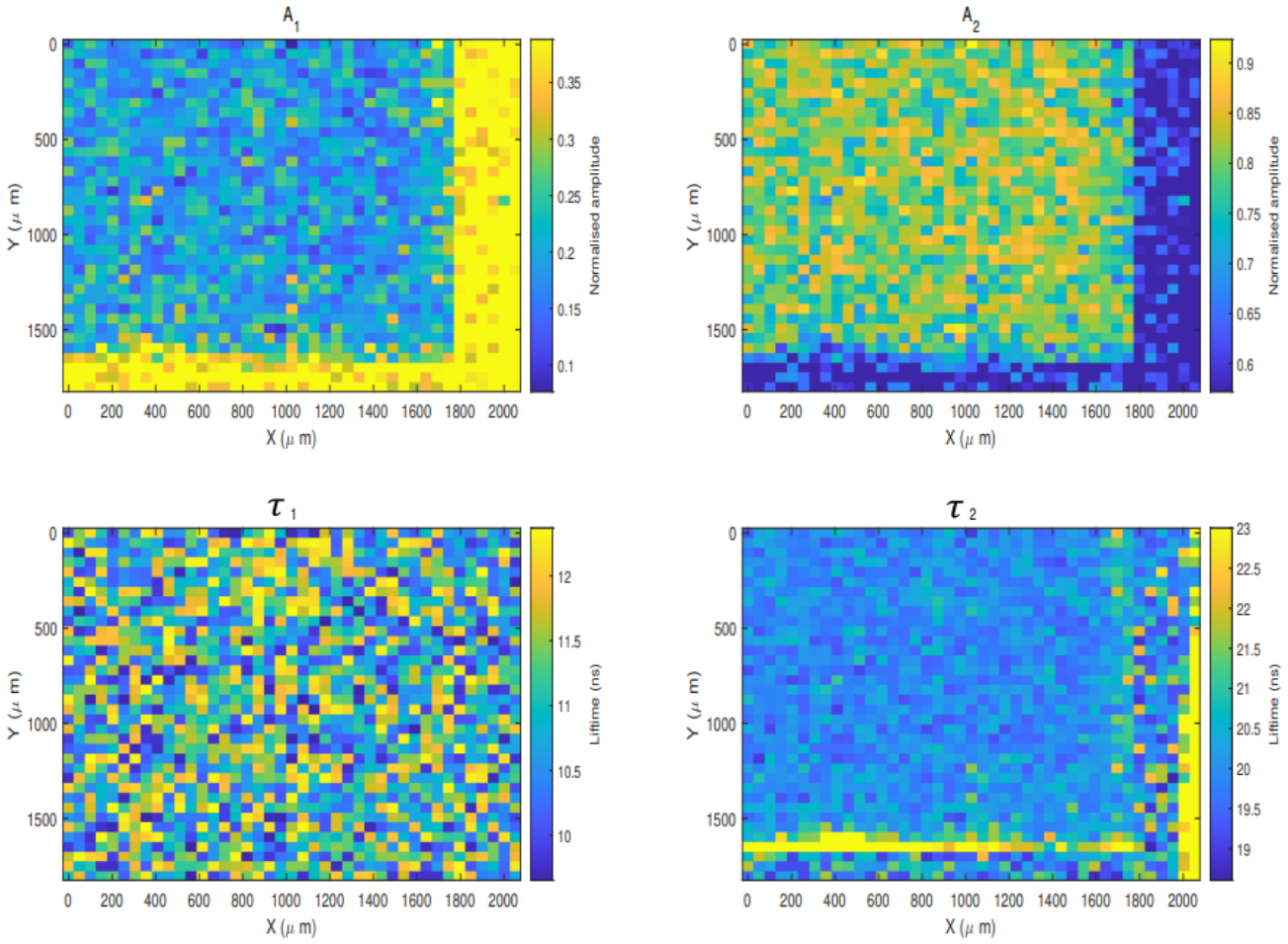


Figure 4.15: The plots show the lifetime component imaging of the NID_{02} sample using the random search method.

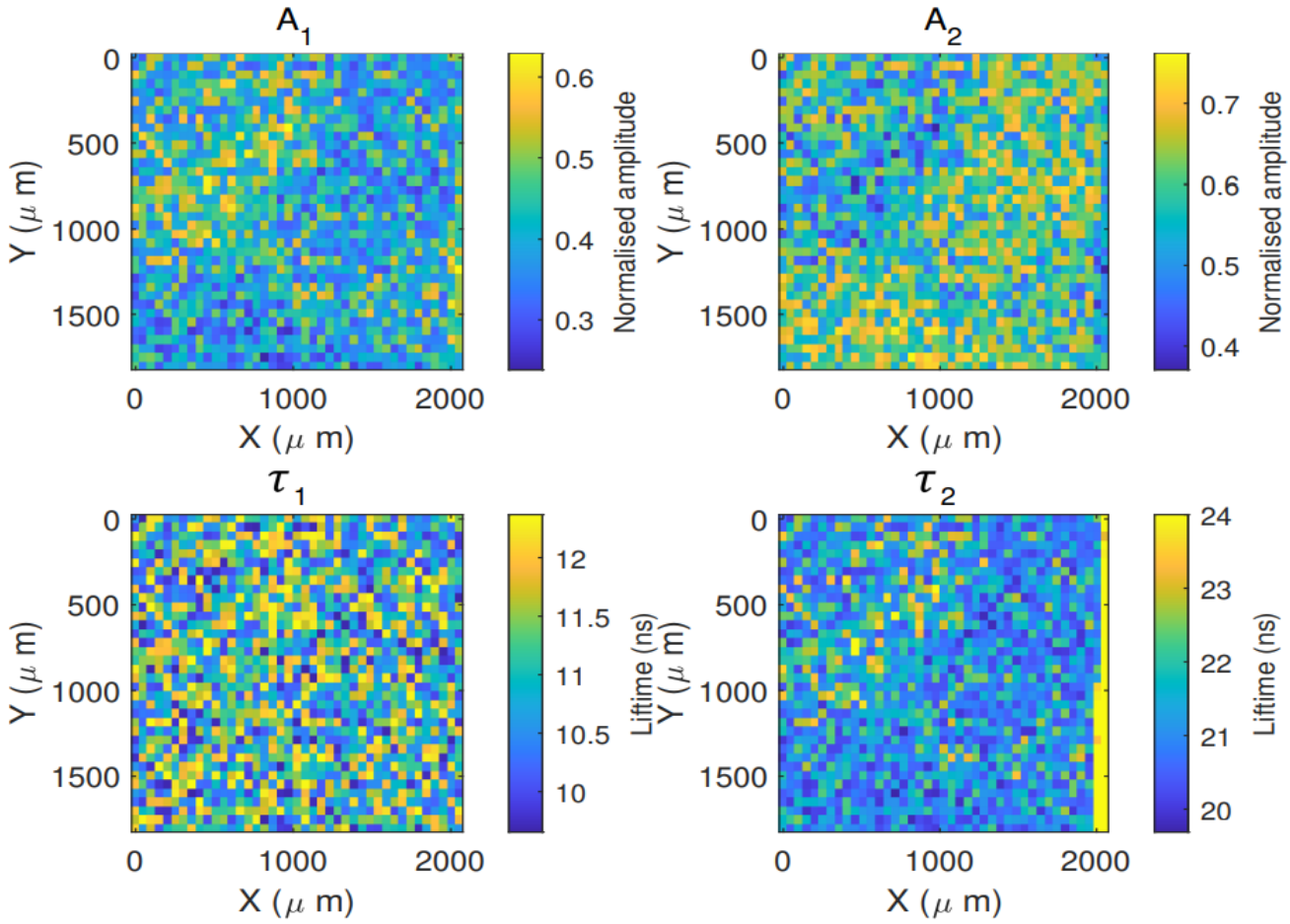


Figure 4.16: The plots show the lifetime component imaging of the 10BA sample using the random search method.

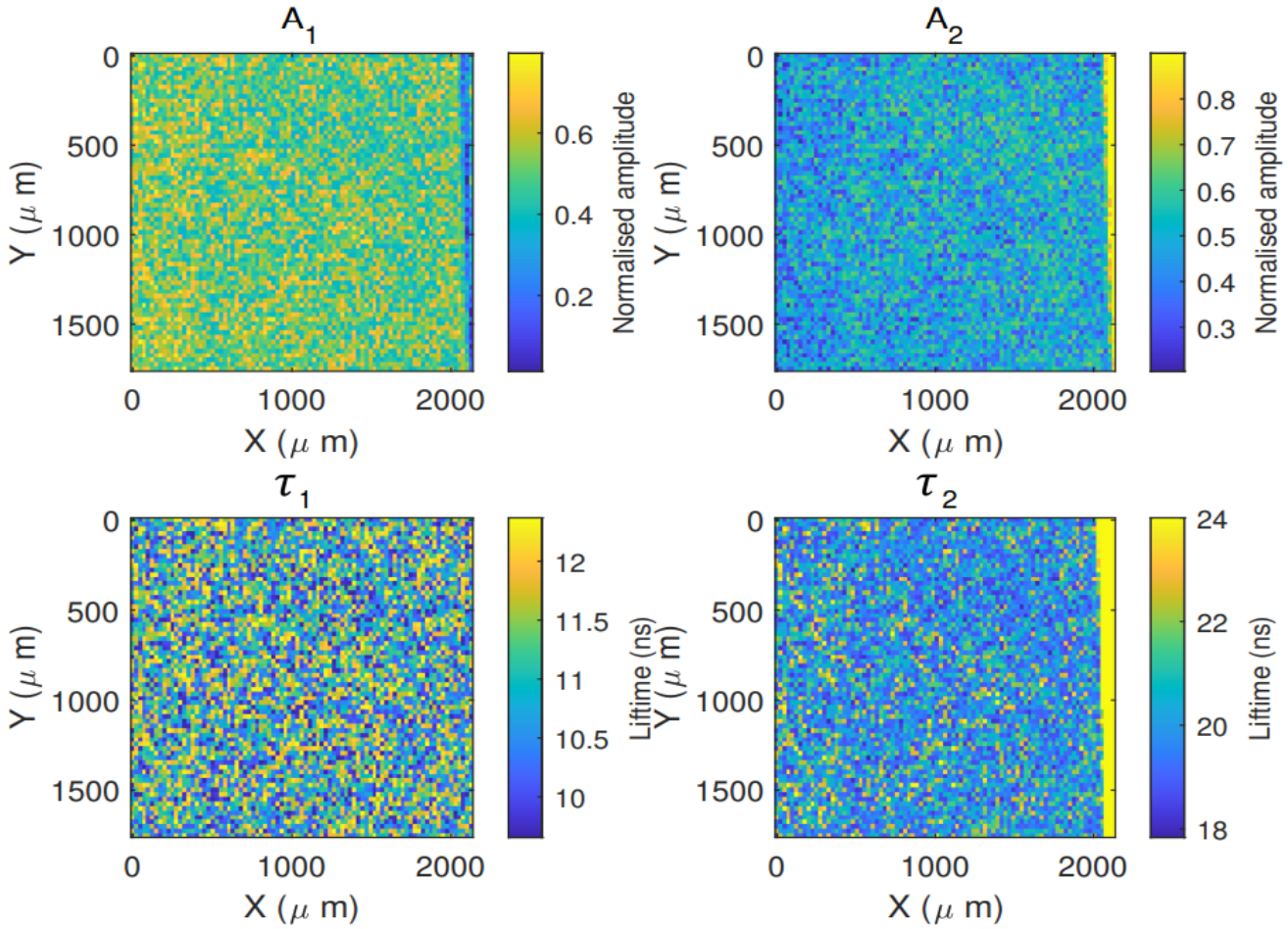
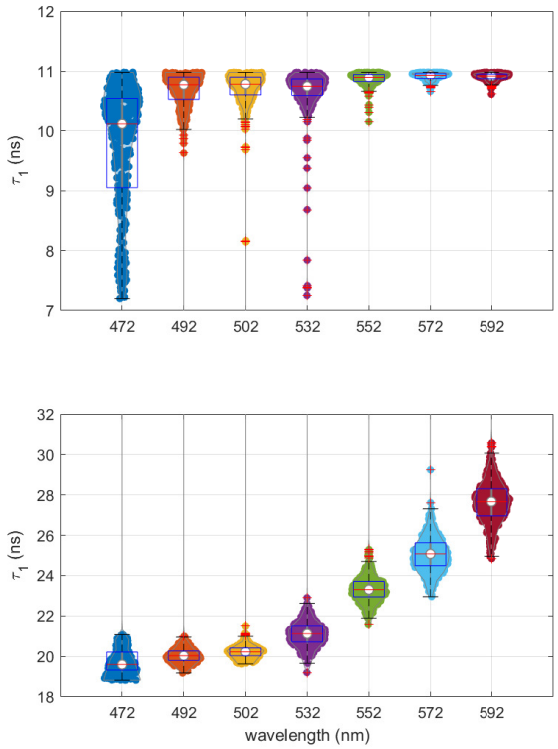
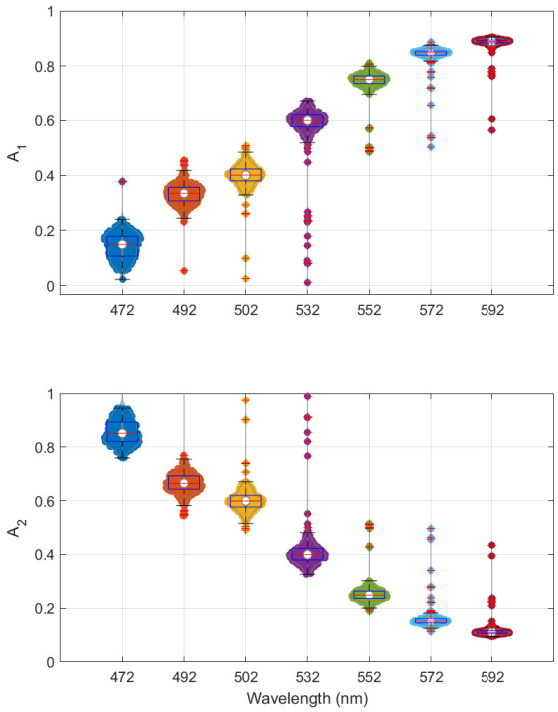


Figure 4.17: The plots show the lifetime component imaging of the 10BB sample using the random search method.

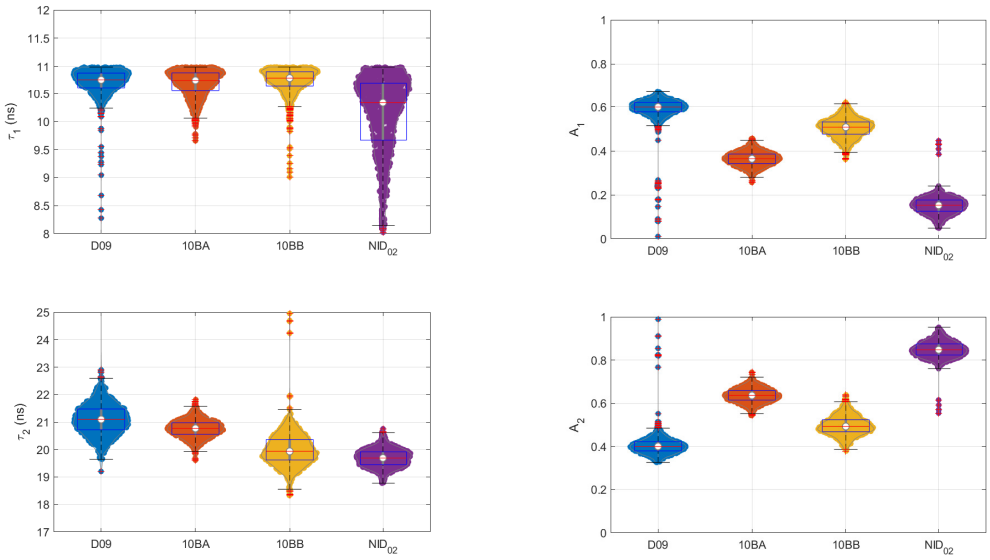


(a) Lifetime



(b) Amplitude

Figure 4.18: The plots show the mean and the dispersion of τ_1 and τ_2 of the D09 sample using the random search method. By varying the wavelength, the distribution varies from a uniform distribution to a transition, where it is similar to a normal distribution with a long tail at one end to a bimodal distribution. The distribution is opposite in direction between the τ_1 and τ_2.



(a) Lifetime (b) Amplitude

Figure 4.19: The plots show the lifetime components distribution in the pixel level of the 4 samples using the random search method.

Conclusion

In conclusion, based on the global binning and the blind determination technique the NV^- and NV^0 contribution, A_1 and A_2, in every sample is roughly similar to the least square method. The global binning method can only estimate an overall lifetime, which is not ideal for studying the distribution of the lifetime components. The pixel-wise lifetime data is analysed using the random search blind determination method. The random search method

For the previous least square method, the short lifetime component, $_1$ appears to be dominant at longer excitation wavelengths and it is the opposite for the long lifetime component. The uniform distributions of the lifetime correspond to the case that it is not dominant and the calculation is not accurate. When the component is more dominant, the distribution changes from a uniform distribution to a bimodal distribution. A possible case is that the sample has two distinct regions, showing a minority of pixels shift their lifetime above from the majority when the excitation is above 552 nm for τ_1 and it is the opposite for τ_2 when the wavelength is below 512 nm. It might be the case of the environmental changes due to the photo-conversion that a change in the NV^- and NV^0 ratio changes the charge and spin environment. The effect is more significant on NV^- above 552 nm excitation wavelengths.

In general, the longer the excitation wavelength the more A_2 contribution, the shorter the excitation wavelength the more A_1 contribution. It might be favourable to excite the diamond sample using a longer wavelength. The results partially agree with the NV centre ionisation and recombination measurement from [106], which reports having more fluorescence from NV^0 at blue excitation light caused by the one-photon ionisation and reduced fluorescence at red excitation light caused by the dark state, and theoretical calculations of two-photon photoionisation [135], where the NV^- fluorescence peaks at around 590 nm. The recombination rate peaks at 575 nm. The NV^- population states at a high level between 480 nm to 570 nm. Part of the reason for the disagreement is that the NV^0 has a zero-phonon line at 575 nm, and the excitation wavelength longer than that might not efficiently excite the NV^0 centre. The ionisation rate and the recombination rate are also power dependent, the power used in this thesis is different from the paper [106] [136].

4.2.2 Deep learning for defects in diamonds

Machine learning has been widely used for data analysis in many areas including both industry and academia. It can discover hidden data structures by learning from a large set of data and optimise the data processing process. A convolutional neural network is a popular method for imaging processing, such as image segmentation, image classification and regression. In particular, the use of machine learning in fluorescence lifetime is an emerging method that can perform better in the computational time it uses per image analysis and accuracy than its counterpart. It introduces a new fitting strategy as opposed to the traditional model-fit that optimises the fitting parameters for a predefined model and phasor analysis that optimise the phasor parameters for the barycenter of the lifetime components in the phasor space. There are numerous reports on using machine learning in fluorescence lifetime analysis [137] [138][139], as well as in optical readout [140]. This data-driven approach with an appropriate physical model, can thus, reduce the level of human bias while obtaining a fast speed of lifetime imaging.

For fluorescence lifetime mapping, the data is a 3-dimensional cube consisting of a 2D map and a decay in time, as the z-axis. A combination of convolutional neural networks and residual networks is adapted to the model. The model is trained using synthetic data from a tri-exponential function, corresponding to NV^-, NV^0, and SiV. This model can be extended to learn more fluorescent defects in diamonds and become a robust model for diamond fluorescence lifetime mapping in a multiple fluorescent defects situation.

The advantages of using neural networks are the speed of lifetime estimation and free of initial guesses, such as the lifetime, amplitude, and the number of lifetime components, which have a large impact on the fitting. For multi-exponential decays, which involve more dimensions, as well as a large number of pixels, the nonlinear least square method, which adopted the Hessian matrix method, might become inefficient and expansive. Furthermore, the performance of the least square method can be poor in low light conditions[141]. Another problem of fluorescence lifetime mapping is that the number of lifetime components is usually assumed and biased. The phasor analysis performed well when there are a few components, as the number of lifetime components increases it becomes harder to extract the number of components and their lifetime. The neural network on the other hand can provide an ensemble estimation, using multiple networks of different numbers of lifetime components and give statistical measurements of the number of lifetime components. This provides a way to decrease the bias in selecting the

number of lifetime components.

The results from the neural networks can be processed further with other methods such as the least square to achieve accurate results. The model used for fluorescence lifetime mapping for multi-defects in diamond is based on the 3D convolutions neural network and residual network used in [137]. The deep neural network proposed has also been adapted for various tasks in fluorescence lifetime such as in low dimensional deep learning for biomedical imaging [142]. Therefore, it is an important task to construct a deep learning method for diamond optical characterisation. The training data is generated by a tri-exponential function based on the fluorescent defects in diamonds. The model consists of 74 layers and 865,935 parameters.

A total 150,000 number of trainable data are trained with a batch size of 32. The training data is generated in MATLAB by defining a tri-exponential model, where the parameters are set so that the generated data is similar to the exponential data. The dataset contains three lifetime components, where the lifetimes are from 0.5 ns to 4.5 ns, τ_3, 8.5 ns to 12.5 ns, τ_1, and 17 ns to 21 ns, τ_2. The amplitudes are normalised to 1. Poisson noise is added to the training data to consider the photon noise. The level of noise is added so that the training data is very similar to the experimental data. The validation set is 20% of the total data, which is 30,000. The actual number of training data is 120,000.

The performance of the model is presented as percentage errors between the predicted values from the model and the data generated for the test which are similar to the training data.

Firstly, the model is tested with a bi-exponential function. The non-existent third is found to be at 0.78 %. The null hypothesis, giving a p-value smaller than 0.05, suggests that the third component is not present. The tri-exponential nature of the deep learning model works in a bi-exponential situation.

The trained model is used to predict and reconstruct the fluorescence lifetime imaging with lifetime components such as the amplitudes and the lifetimes. By comparing the fluorescence lifetime imaging of the NID_{02} sample, the deep learning techniques developed have a clear outline of the sample in all the amplitudes and lifetime components. The background is mostly zero. The contrast of the fluorescence lifetime imaging is high. The model effectively learns to distinguish the samples and the background. Whereas the outline of the sample is not clear or vanishes, giving irrelevant values, the background has very close values to the samples in both

the least square method and the random search method, making the imaging hard to analyse.

The deep learning model developed has drastically improved the fitting processes for fluorescence lifetime imaging in diamonds. It does not require any fitting reduces human bias, and produces very high-contrast images that can not be achieved using the least square method and the random search method. Later in this section, ground truth evaluations are performed and provide a benchmark for the three methods used in this thesis.

Figure 4.20 shows the architecture of the neural network and the flowchart of the training and inference process. The architecture of the model is divided into a main branch and side branches for each parameter. The convolutional layers are the building blocks of this model. The test results are shown in Figure 4.21. In Figure 4.21, the model reconstructs the third component of a bi-exponential synthetic image, in which the non-existent third component represents the noise. Figure 4.21 (b) is the histogram of the non-existent third component. The error is about 1%. If the third component is much higher than 1% in future optical imaging data, it indicates the presence of the third component. On the other hand, if the third component is about 1%, the third component is unlikely to be present as it is below the p-value threshold. From Figure 4.22 to 4.25, the reconstructed images of D09, NID_{02}, 10BA and 10BB are shown. In the 10BA data, the mean value of A_1 is (45.44 ± 3.7)%, the mean value of t_1 is 9.9507 ± 0.3413 ns and the mean value of t_2 is 19.8365 ± 0.2092 ns. In the 10BB data, the mean value of A_1 is (55.09 ± 4.81)%, the mean value of t_1 is 10.1054 ± 0.5218 ns and the mean value of t_2 is 18.6982 ± 0.4266 ns. The detailed results for the four samples are listed in Table 4.6. The distribution plots of the lifetimes and the amplitudes at 532 nm excitation but with four different samples and D09 under various excitation powers are shown in Figures 4.26 and 4.27.

Sample	$\tau_1(ns)$	$\tau_2(ns)$	A_1	A_2
D09	10.3367 ± 0.1828	19.9663 ± 0.2252	0.6955 ± 0.0220	0.3011 ± 0.0251
10BA	9.9507 ± 0.3413	19.8365 ± 0.2092	0.4544 ± 0.037	0.5394 ± ± 0.0361
10BB	10.1054 ± 0.5218	18.6983 ± 0.4266	0.5509 ± 0.0481	0.4481 ± 0.0493
NID_{02}	10.0821 ± 0.8461	19.1072 ± 0.3910	0.2205 ± 0.0547	0.7866 ± 0.0660

Table 4.6: A summary of lifetime measurement at 532 nm based on the deep learning method.

To better compare the performance of the deep learning method against the least square method and the random search method, as well as finding the range of τ_1 that the deep learning is optimal. Ground truth (GT) images are generated so that the predictions from each method

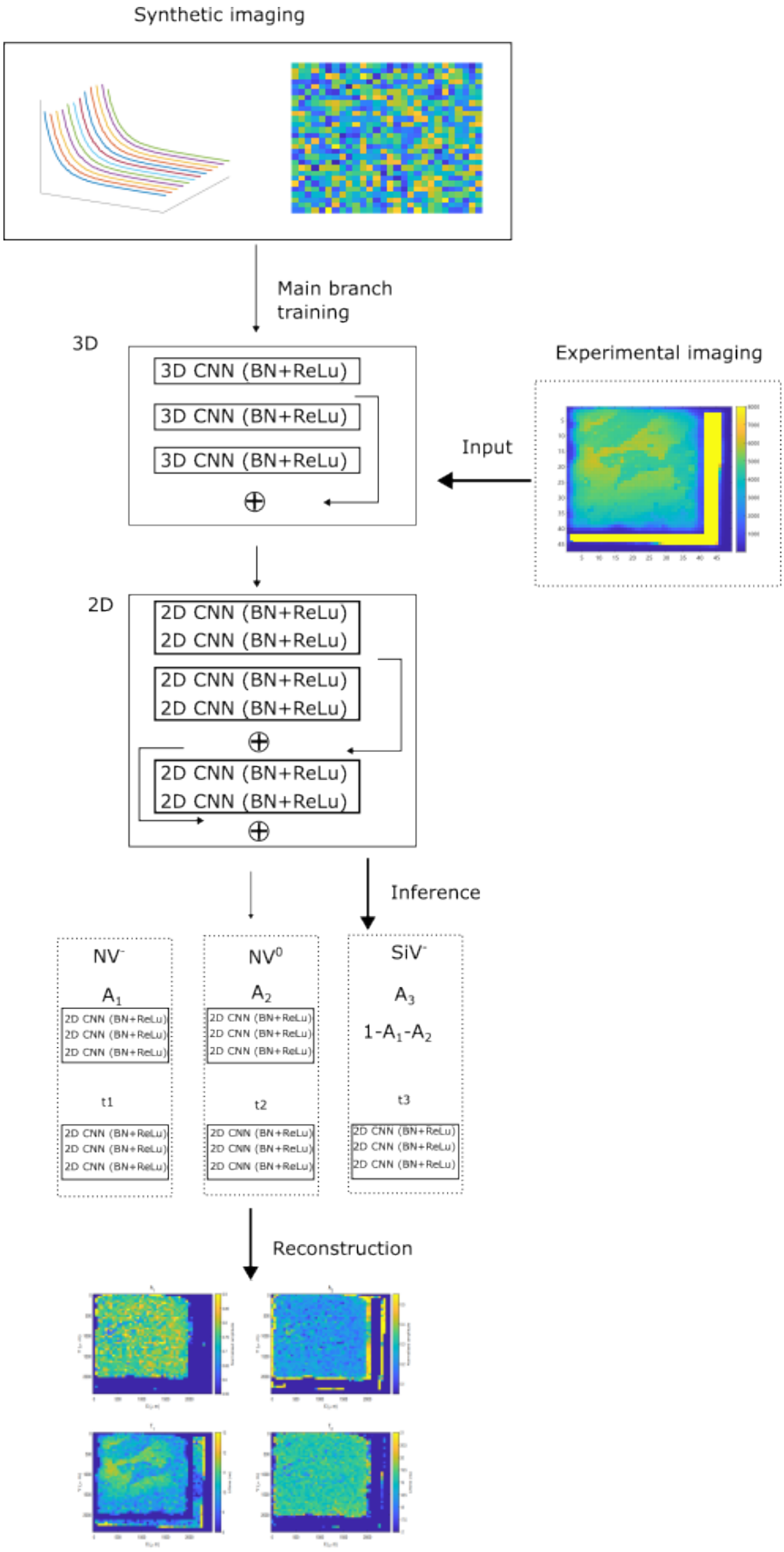
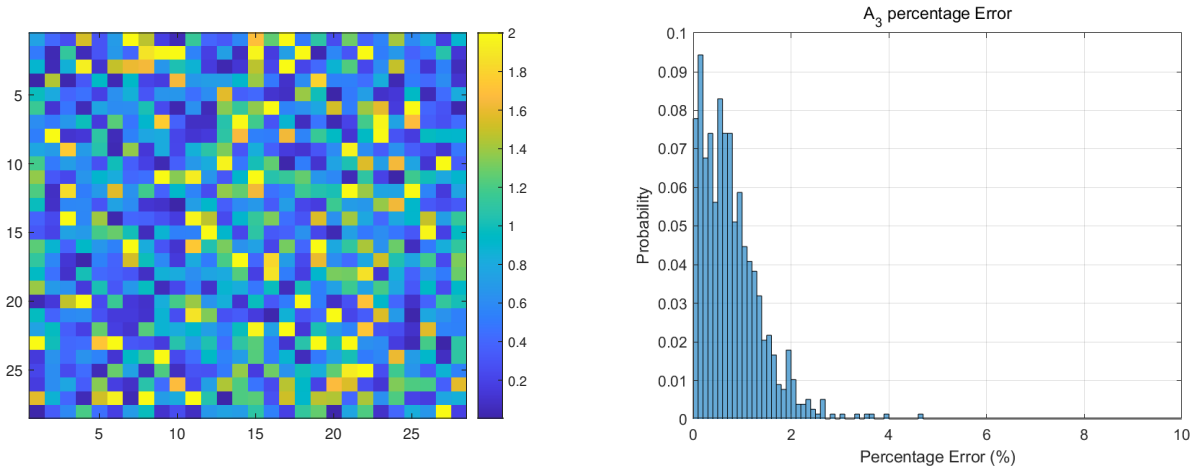


Figure 4.20: The image shows the flow chart of training and inferring the fluorescence lifetime imaging data. The architecture of the model is made of a main branch that consists of 3D CNN layers that extract the features on both the spatial and the temporal domain and 2D CNN layers. The main branch is separated into small branches for each parameter.



(a) (b)

Figure 4.21: (a) The image shows the percentage errors of the trained model for a non-existent lifetime component. (b) The histogram shows the percentage errors of the trained model for a non-existent lifetime component.

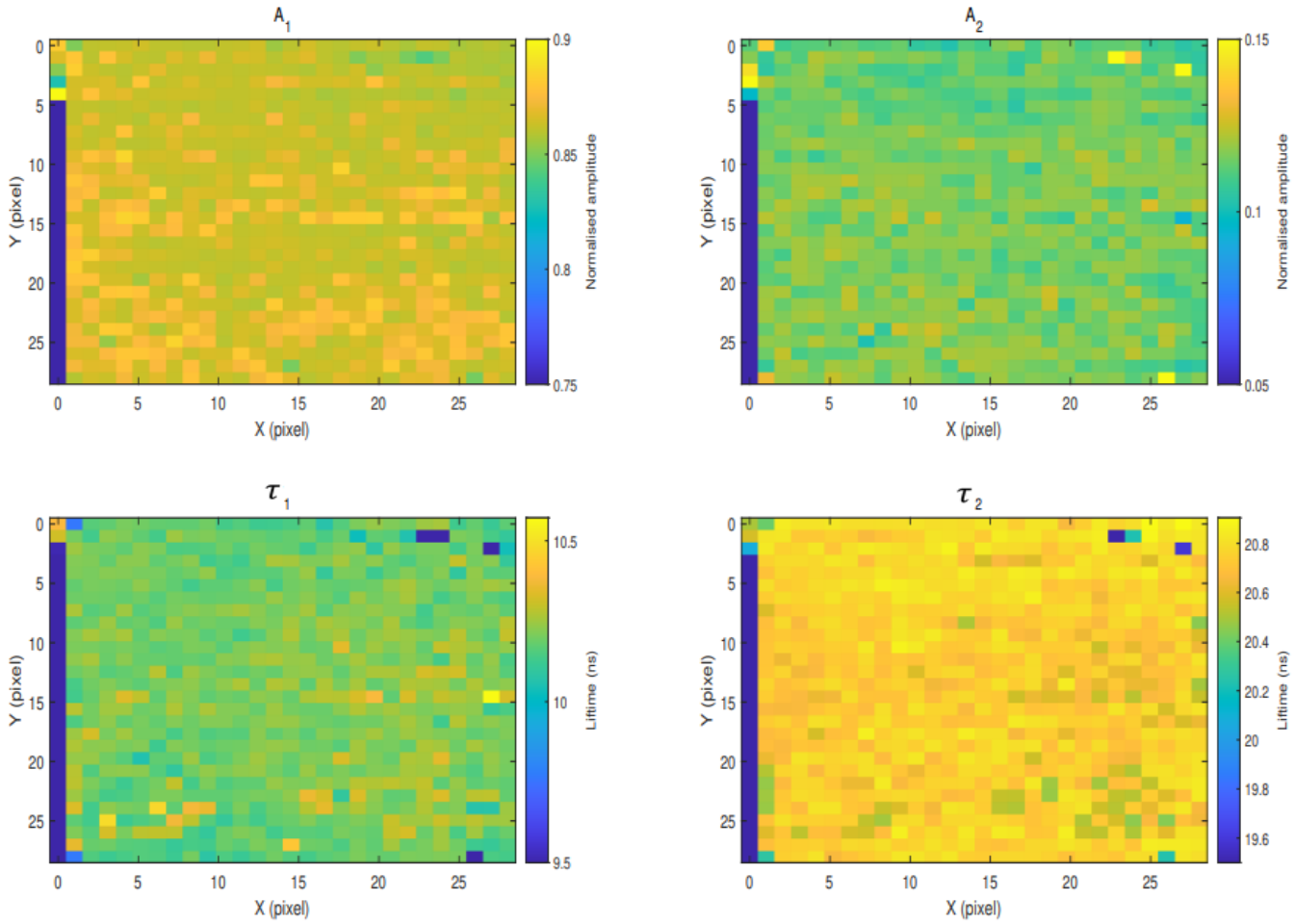


Figure 4.22: The images show the lifetime components of the trained model for D09 sample at 592 nm.

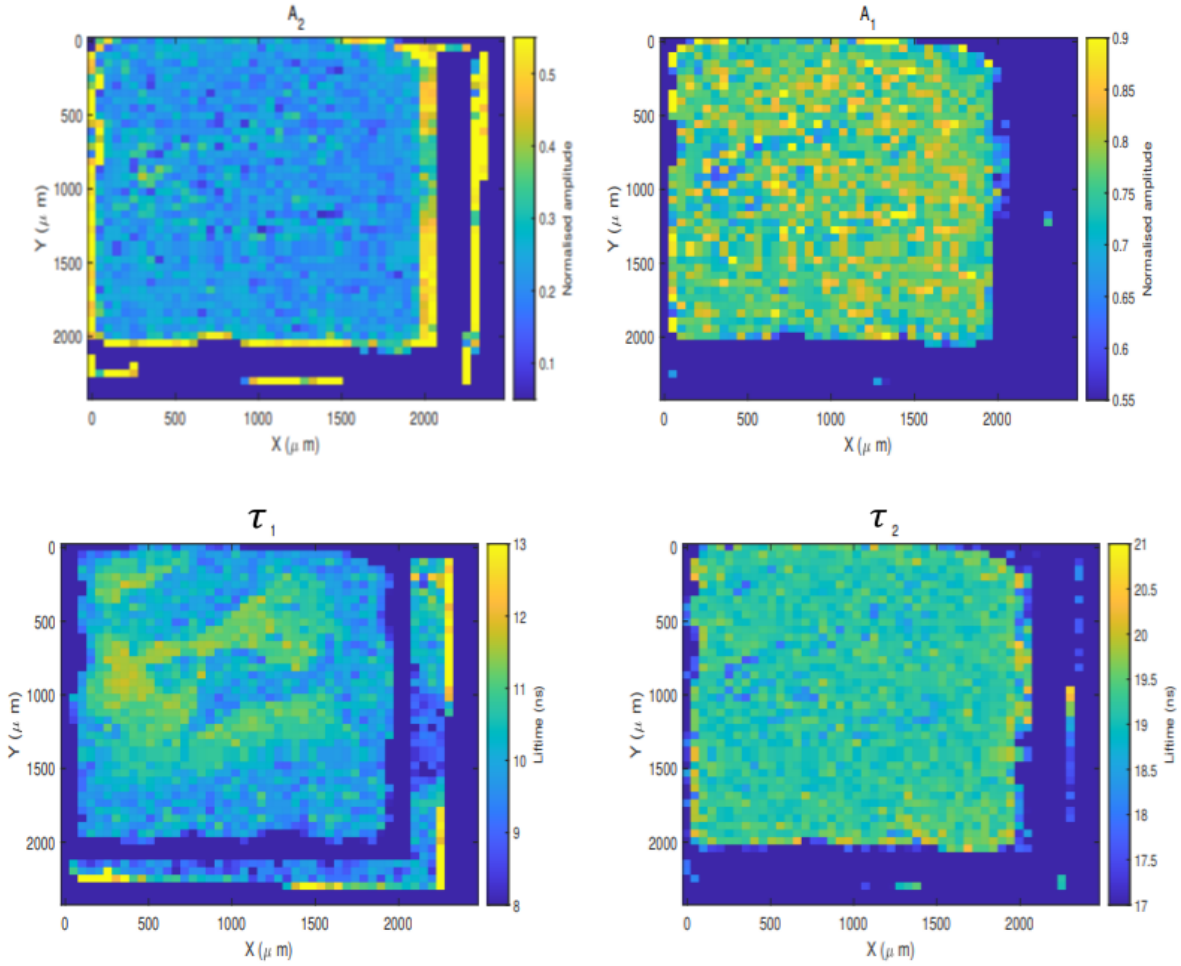


Figure 4.23: The images show the lifetime components predicted and reconstructed using the trained model for NID_{02} sample at 532 nm.

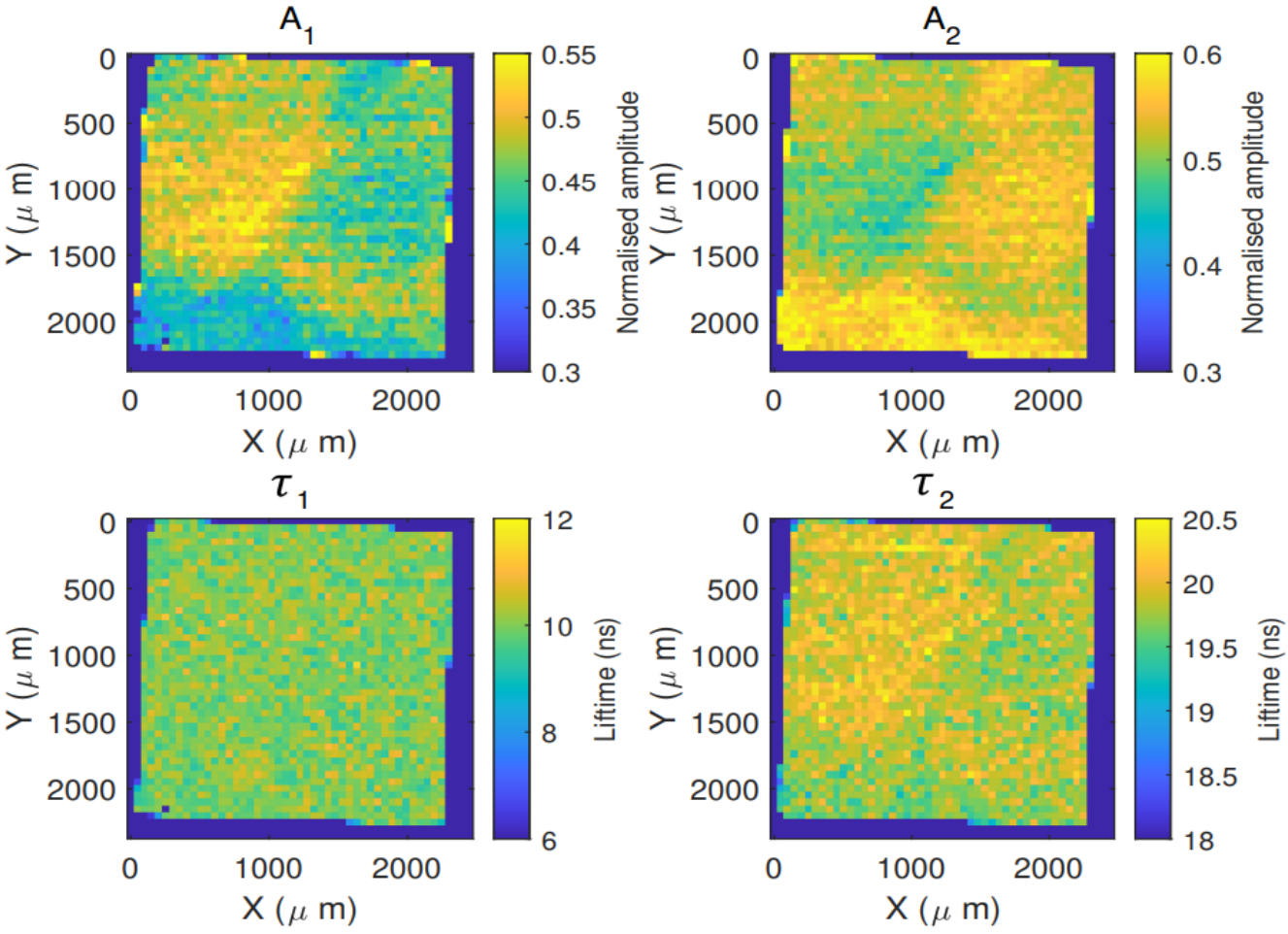


Figure 4.24: The images show the lifetime components predicted and reconstructed using the trained model for 10BA sample at 532 nm.

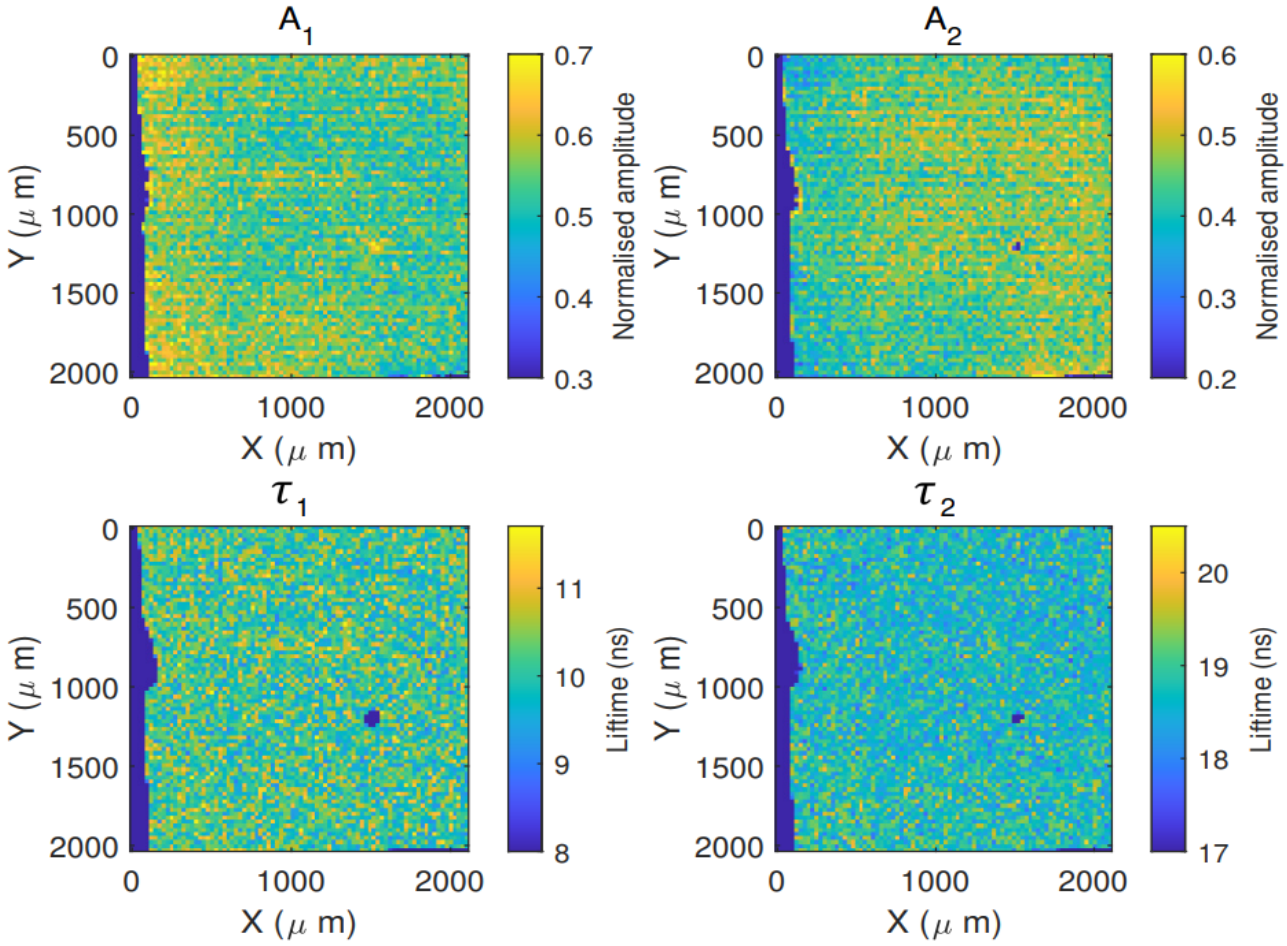
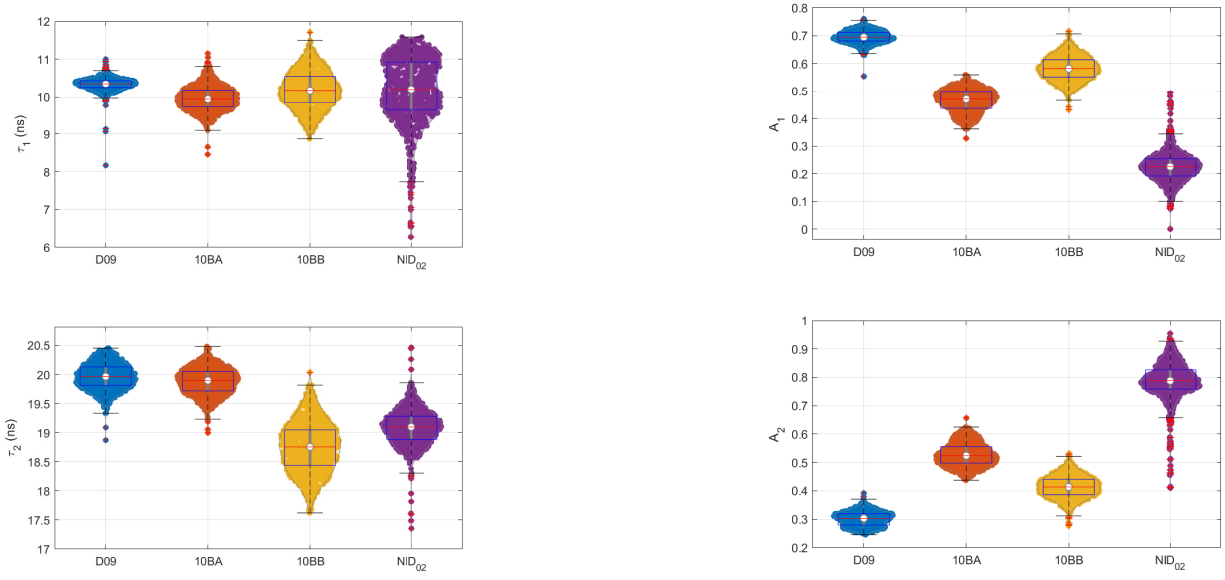
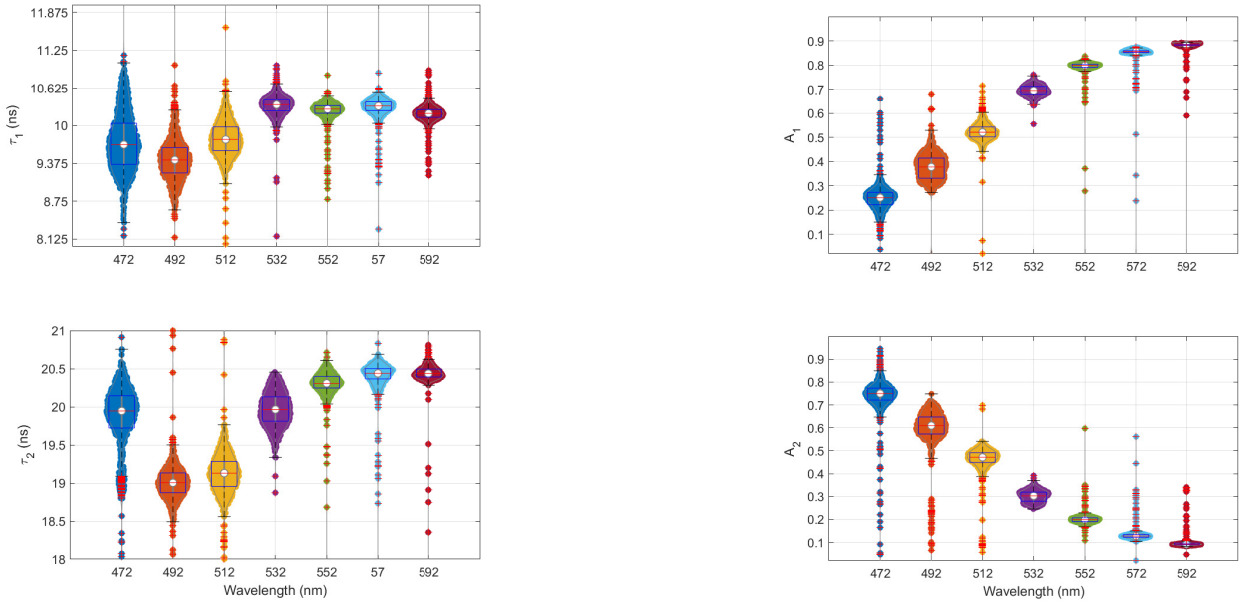


Figure 4.25: The images show the lifetime components predicted and reconstructed using the trained model for 10BB sample at 532 nm.



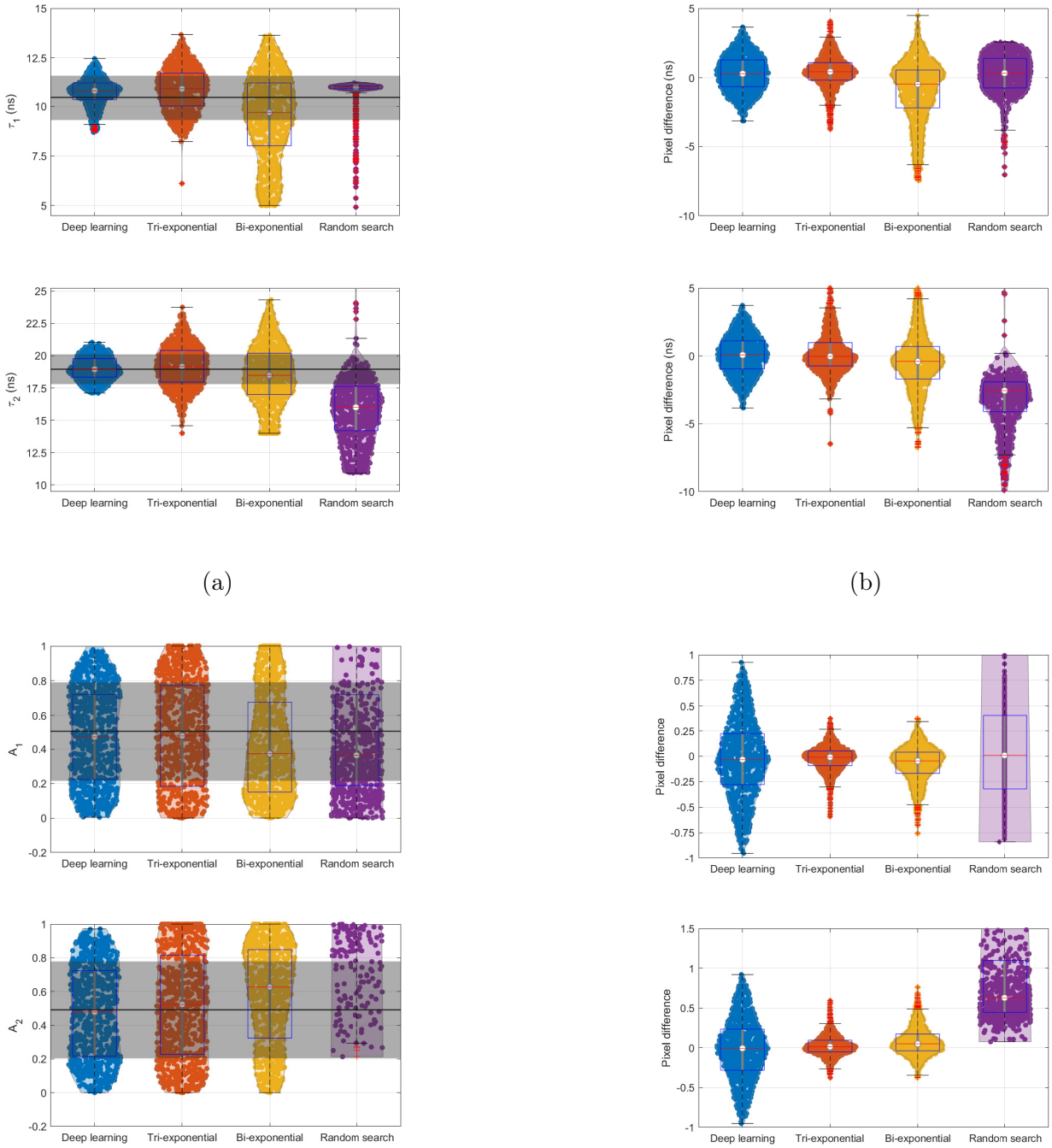
(a) (b)

Figure 4.26: The distribution of the lifetimes and the amplitudes: (a) τ_1 and τ_2 and (b) A_1 and A_2, of the four samples using the deep learning method.



(a) (b)

Figure 4.27: The distribution of the lifetimes and the amplitudes: (a) τ_1 and τ_2 and (b) A_1 and A_2, of the d09 sample excited with 7 difference excitation wavelengths using the deep learning method.



(a) (b)

(c) (d)

Figure 4.28: GT1. The image shows the predicted values of τ_1 and τ_2 (a), A_1 and A_2 (c), using four different analyses and the ground truth value as a black line and the shaded area represents the standard deviation. The pixel difference between the predicted values and the ground truth values,(b)τ_1 and τ_2 (d) A_1 and A_2.

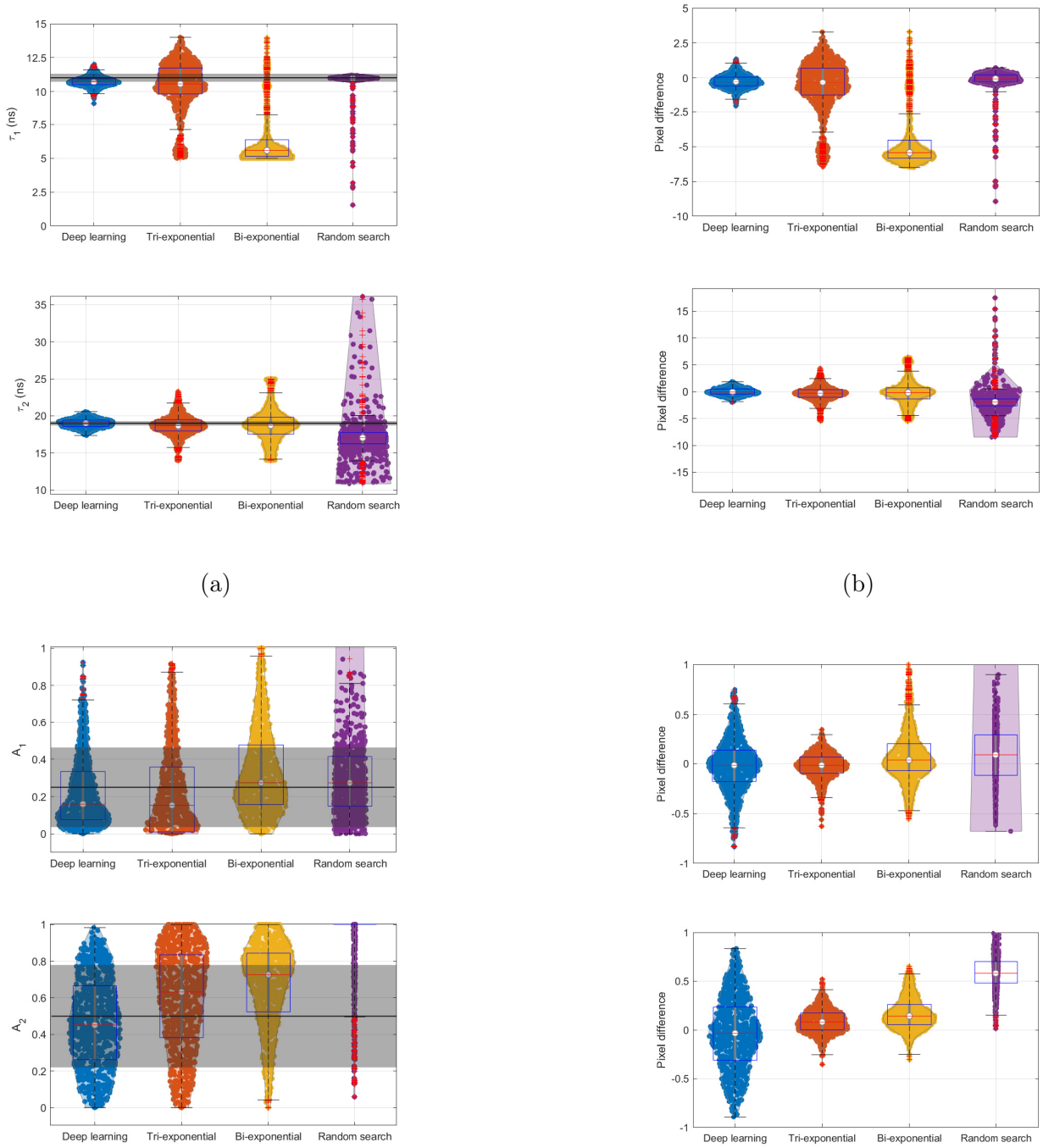


Figure 4.29: GT2. The image shows the predicted values of τ_1 and τ_2 (a), A_1 and A_2 (c), using four different analyses and the ground truth value as a black line and the shaded area represents the standard deviation. The pixel difference between the predicted values and the ground truth values,(b)τ_1 and τ_2 (d) A_1 and A_2.

can be directly compared with the ground truth images. Mean square error (MSE) is used to show the goodness of fit of each method.

The GT images have a size of 28 by 28 and a mean intensity of 300, a mean τ_1 is 11 ns and τ_2 is 19 ns and a τ_3 at 1.5 ns.

The first GT, named GT1, the image has an amplitude of 0.4975, 0.4975 and 0.005. This represents a bi-exponential model. The results from GT1 are shown in Figure 4.28.

The next GT, named GT2, has amplitudes of 0.25, 0.5 and 0.25. These GT images can test both the bi-exponential model, which gives the level of deviation from the GD, and the tri-exponential model of the least square method. The results from FT2 are shown in Figure 4.29. In the results, the deep learning model gives a τ_2 mean of 19.9932 ns and the GD mean is 19.9966 ns, whereas the bi-exponential least square, averaging over 100 runs, gives 18.846 ns, which has a 1.1506 ns deviation. If the tri-exponential least square, averaging over 100 runs, is used, the τ_2 mean is 18.666 ns. The MSE of the deep learning model is 0.3343 for τ_1, whereas it is 4.4041 for the tri-exponential least square and is 25.0958 and 0.9974 for the bi-exponential least square and the random search method. The MSE of the deep learning model is 0.4625 for τ_2, whereas it is 2.2830 for the tri-exponential least square and is 5.8489 and 2475.8 for the bi-exponential least square and the random search method. The third component deviates the bi-exponential model to a lower τ_1 and causes a significant error. The MSE of A_1 and A_2 are 0.1954 and 0.1598 for the deep learning model, 0.2872 and 0.3131 for the tri-exponential model, 0.2791 and 0.3010 for the bi-exponential model and 147.6426 and 149.1719 for the random search method. From the MSE values, the deep learning method has a significantly smaller MSE than the others. The tri-exponential least square comes second, the bi-exponential is worse. The MSE of the random search is small for τ_1 and it is very large for τ_2.

The following GT image is generated by changing the τ_1 to various values such as 9 ns and 13 ns while keeping the other parameter unchanged to find the optimal τ_1 range of the deep learning model. The summary of the performance of both GT1 and GT2 are shown in Table 4.7 and Table 4.8.

For the bi-exponential model, the amplitude of the third lifetime is set to zero.

If the GT has an unseen parameter, such as 8 ns, the training set contains only 8.5 ns to 12.5 ns. The accuracy of the deep learning model is reduced. The distribution of the predicted

Method	$\tau_1(ns)$	$\tau_2(ns)$	$\tau_3(ns)$
GT1			
Deep learning	10.7261 ± 0.7505	19.0137 ± 0.9381	2.4238 ± 0.3810
Tri-exponential least square	10.8610 ± 1.1198	19.1780 ± 1.6079	3.3249 ± 1.0333
Bi-exponential least square	9.4491 ± 2.2034	18.512 ± 2.3672	0
Random search	10.6644 ± 0.9398	17.3025 ± 11.2737	0
GT2			
Deep learning	10.7288 ± 0.4108	19.9932 ± 0.6117	1.3084 ± 0.4930
Tri-exponential least square	10.344 ± 2.3918	18.669 ± 2.0747	2.2748 ± 1.5088
Bi-exponential least square	6.4968 ± 2.5452	18.817 ± 2.5584	0
Random search	10.8064 ± 1.3432	20.2311 ± 477.7955	0

Table 4.7: A summary of lifetime measurement at 532 nm based on the phasor method.

Method	A_1	A_2	A_3
GT1			
Deep learning	0.4766 ± 0.2776	0.4741 ± 0.2805	0.0492 ± 0.0311
Tri-exponential least square	0.4830 ± 0.3229	0.5170 ± 0.3229	0.0317 ± 0.0405
Bi-exponential least square	0.4271 ± 0.3015	0.5729 ± 0.3015	0
Random search	0.3644 ± 35.4531	1.2891± 35.4570	0
GT2			
Deep learning	0.2304 ± 0.1987	0.4607 ± 0.2510	0.3089 ± 0.2112
Tri-exponential least square	0.2265 ± 0.2388	0.5895 ± 0.2807	0.1841± 0.1753
Bi-exponential least square	0.3334± 0.2388	0.6666 ± 0.2807	0
Random search	0.2434 ± 0.0795	1.1767 ± 118.8622	0

Table 4.8: A summary of lifetime measurement at 532 nm based on the phasor method.

values exhibits bimodal distribution, showing a lower peak at 8.7 ns and a higher peak at 10.5 ns. The lowest 5% will reach below 8 ns. The MSE of the deep learning model is 2.2914, the MSE of the tri-exponential model is 1.8585 and the bi-exponential model is 0.6096. Whereas, the random search model gives an MSE of 8.5253.

If the GT is at 9 ns. The MSE is 0.8913 ns, 0.9247 ns, 0.9039 ns and 3.6891 ns for the deep learning, tri-exponential, bi-exponential and random search models. If the GT is at 12 ns, the MSE is 0.7237 ns, 0.9272 ns, 2.8533 ns and 3.4616 ns. At 13 ns, the MSE is 2.9672 ns, 2.7159 ns, 5.2930 ns and 5.0001 ns for the deep learning, tri-exponential, bi-exponential and random search models. Below 9 ns, both the tri-exponential and the bi-exponential least square method outperform the deep learning model and the random search model by MSE. The deep learning model performs the best between 9 ns to 13 ns. This results from the training data being

between 9 ns to 13 ns.

Due to the limitation of the training data and the model, the performance of the deep learning model is reduced below 9 ns, The results of the least square method can be used to check if the lifetime is out of the range. If the lifetime is lower than 9 ns or higher than 13 ns, the least square method is used, otherwise, the deep learning model provides an exceptionally good accuracy than the others. The current performance is satisfactory as it is sufficient for NV^-.

By observing the distribution plots of the predicted values from the four methods and compare, it is possible to map the experimental data to GT data that has certainty. In conclusion, the high dimensional convolutional neural network reconstructs the fluorescence lifetime imaging for all the diamond samples. The model infers the parameters such as the lifetime and the amplitude for each lifetime component without any fitting and initial guess. The model confirms that the bi-exponential model is sufficient. From the deep learning method, it is concluded that the D09 sample has the highest τ_1 and τ_2, 10BA has the lowest τ_1, 10BB has the lowest τ_2. By comparing with the GT1 and the least square method used, the least square gives a τ_1 of 9.449 ns, which is lower than the GT1, whereas the deep learning method gives a much closer prediction. It is concluded that deep learning is the most accurate method to analysis lifetime images. The isotopically-enriched samples have a statistical significance in both the lifetimes τ_1 and τ_2 compare with the other three. The lifetimes of the NID_{02} sample is very similar to the 10BB.

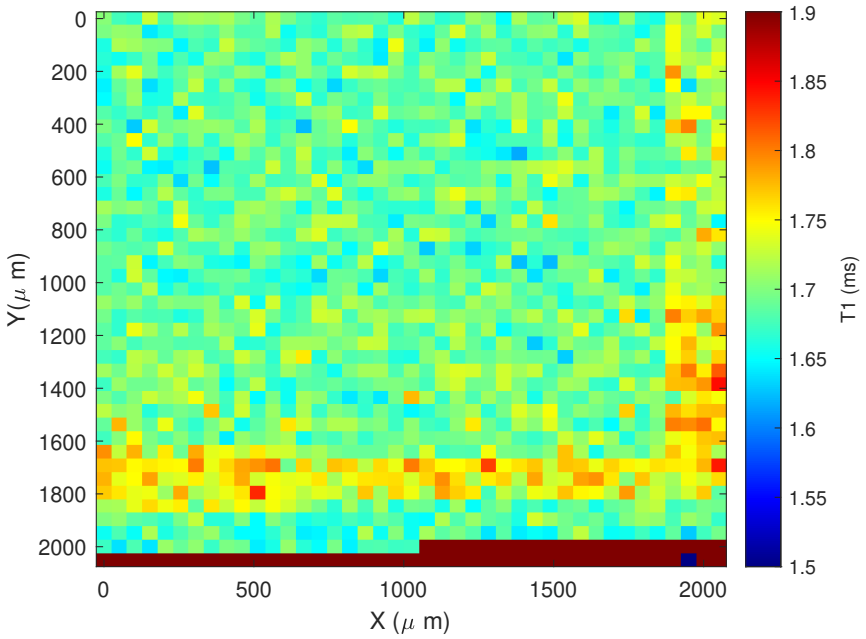


Figure 4.30: The plots show the T_1 lifetime imaging of NID_{02} sample. The step size is 50 μm.

4.3 Spin-lattice relaxation time imaging of diamond samples

Spin-lattice relaxation time or T_1 time is one of the critical parameters in the maser threshold calculation. The T_1 time determines the threshold condition by limiting the time for maintaining population inversion. The figure shows the T_1 mapping of the NID_{02} sample, with a step size of 50 μm. The mean T_1 from the 10BA map is 1.4306 ms and it is 1.6895 ms for the NID_{02}. The standard deviation is 0.0241 ms. Whereas the standard deviation is 0.0613 ms for the 10BA sample. The 10BB samples have more inhomogeneity in spin-lattice relaxation, which might hint at the lattice structure and the local environment might not be as uniform as the NID_{02} sample.

The images show that the mean T_1 of the NID_{02} is much higher than the T_1 in sample 10BA. This result shows a positive correlation, that states that the higher T_1 the easier to breach the masing threshold, between the T_1 and the maser threshold. The T_1 map of the NID_{02} is shown in Figure 4.30, and the T_1 map of the 10BA is shown in Figure 4.31.

From the mapping, the 10BA samples have a lower T_1 time compared to the NID_{02},

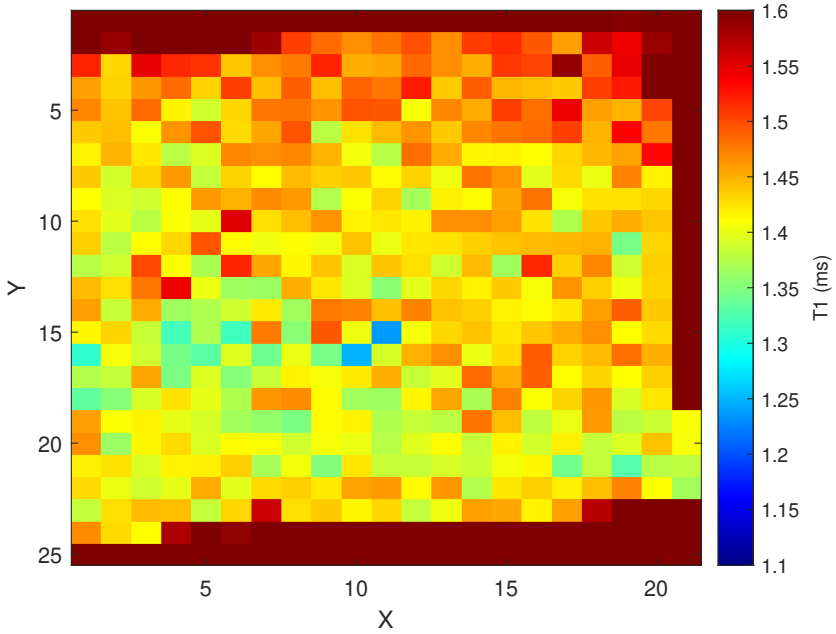


Figure 4.31: The plots show the T_1 lifetime imaging of 10BA sample. The X and Y are the steps. The step size is 100 μm.

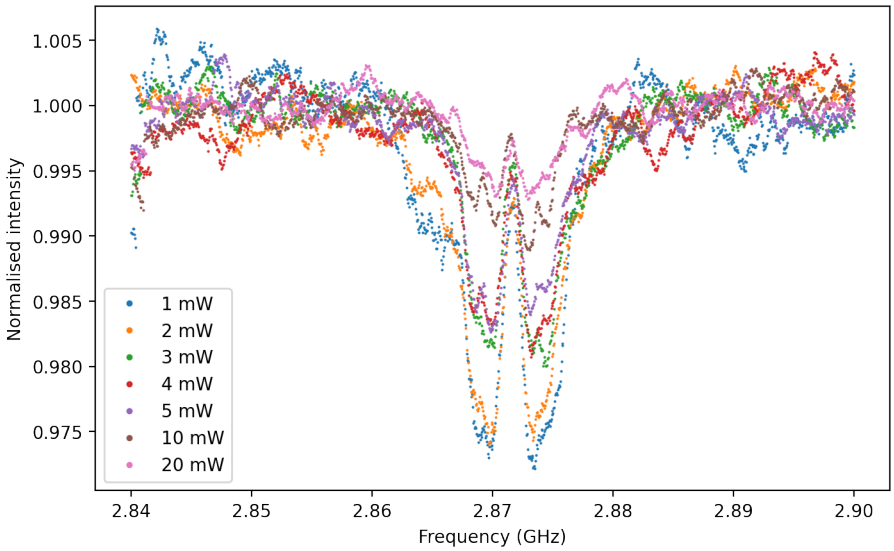


Figure 4.32: The plots show the CW-ODMR of the sample 10BB at 532 nm excitation and with various optical power.

4.4 ODMR

ODMR experiments are conducted for each diamond sample to study the fine structure interaction between the transverse spins that are related to local stresses and strains [143] [144]. For a zero-field ODMR of NV^- centre in a diamond, there should be a dip at 2.87 GHZ, corresponding to the zero-field splitting due to the resonant absorption. The zero-field ODMR results shown all exhibit two dips split around 2.87 GHZ. This might be caused by the local strain. In the 10BB and 10BA samples, the peaks are separated by about 2.95 MHz and 4.32 MHz respectively. This suggests that the 10BB sample has lower interaction. Figure 4.32 shows the CW-ODMR spectrum of various optical pump powers on sample 10BB. The contrast of the dips depends on the pump power, but the linewidth does not change significantly. A higher optical pump power leads to a lower contrast of the resonant dips. By inspecting the shape of the dip, there are two sub-dips that can just be resolved. According to the NV^- Hamiltonian, these sub-dips might be due to the nuclear hyperfine interaction of I=1 nuclear, such as N^{14}.

Figure 4.33 shows the CW-ODMR with a magnetic field aligned to the <111> axis, where there are four dips with a 1:3:3:1 intensity ratio at 4 mW. Figure 4.34 demonstrates the pulsed-ODMR spectrum of 10BB at 4 mW, it is clear that the linewidth is much narrower than the CW-ODMR as expected.

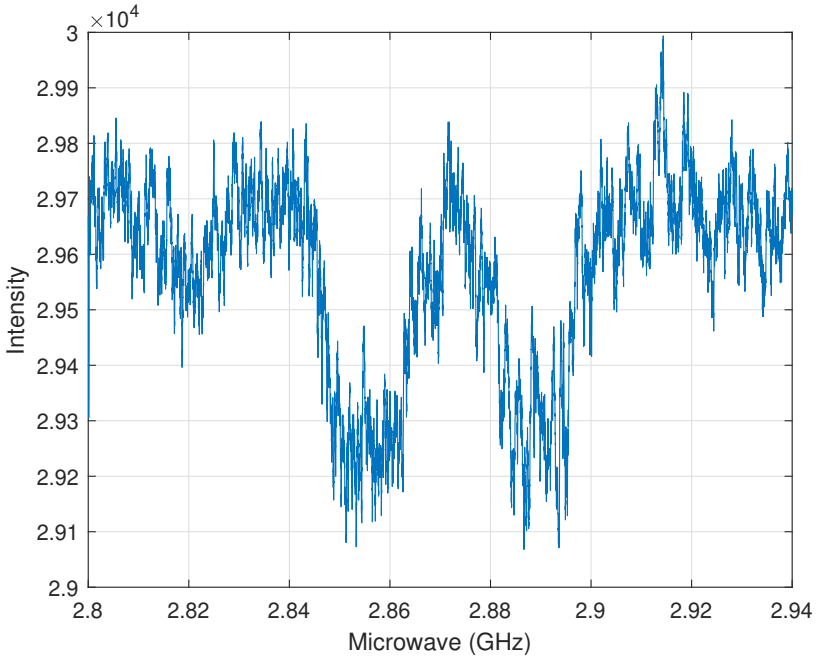


Figure 4.33: The plots show the CW-ODMR of the sample 10BB at 532 nm excitation and with a magnetic field aligned to one of the NV axes.

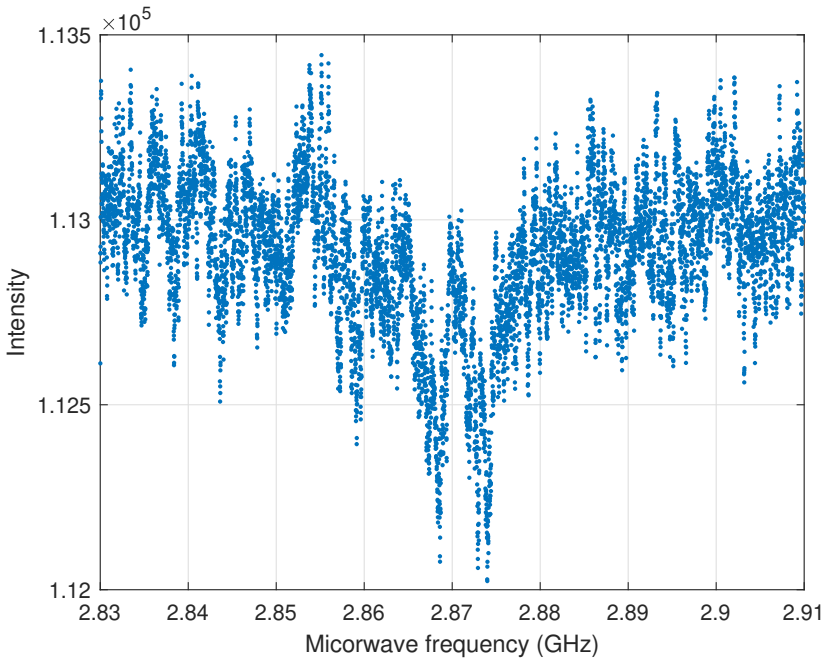


Figure 4.34: The plots show the pulsed-ODMR of the sample 10BA at 532 nm excitation.

4.5 Conclusion

Using various techniques and analytical methods for the optical characterisation of the diamond samples and combining the maser results, the conclusion is that two samples that can mase: the D09 diamond has a high NV concentration, as well as a high proportion of NV^-, which is more than the NV^0. Furthermore, the D09 sample is isotopically pure, thus the T_2 decoherence time is minimised. This is the key for it to mase. The NID_{02} can also mase, owing to a large volume, despite the low NV^- proportion.

The main feature here is that the diamond sample is a cube, so it has more NV centre inside the volume that is optically excited. In addition, the T_1 measurements are longer than the counterpart. The key parameters are the filling factor and the total number of NV centre. On the other hand, both 10BB and 10BA fail to mase. The key issues are the NV concentration and the size. The two samples are similar in shape and size to the D09 sample but the NV concentration is much lower. Needless to say, the coherence time should be much lower than D09, and the NV^- proportion is also lower than D09. The thesis predicts that the optimal diamond sample will take advantage of both the isotopically pure and high NV concentration and high NV^- proportion in D09, and the large cubic shape of the NID_{02}.

The thesis demonstrates the blind determination of lifetime components in diamonds, based on a random search method and phasor transformation. The method extracts the lifetime components that are similar to the least-square method for each pixel. This method can be used with the least-square method to ensure the results.

Applying deep learning to reconstruct fluorescence imaging of diamonds have been demonstrated as a fitless method that produces high-contrast images that show the relative proportion and the distribution of defects in diamonds without the need for a model and the predefined number of lifetime components. Each reconstruction and inference is fast compared to the least-square and the blind determination methods. In addition, this will lower the difficulty and human bias, as it is trained using a large amount of data containing various defects to discover the data pattern without a human predefined fitting model, such as the bi-exponential used in the least-square method. More importantly, the deep learning method has a higher accuracy and more reliable than the other methods.

Chapter 5

Modelling Methods and Simulations

This chapter presents the modelling of threshold conditions of room-temperature diamond masers, as well as ODMR and the spin dynamics of NV^- using 7-level extended rate equations. The results agree with recent experimental results.

5.1 Extended rate equations simulation of spin dynamics and ODMR of NV^-

The results of this chapter formed the basis of an article published in the Journal of Applied Physics [3]. The populations of the electronic energy levels of the NV^- can be described by a 7-level model. The spin dynamics of different states under an optical pumping and a MW pumping on NV spin defects are described by the rate equations based on the 7-level model and the semi-classical optical Bloch equations describing the spin dynamics of the 7-level model interacting with the laser and the MW fields [145].

A laser pumps the population from level 1, level 2, and level 3 to level 4, level 5, and level 6 with the same rate, Ω_l. Level 1 corresponds to the m = 0 state, and level 2 and level 3 correspond to the m = -1 and m = +1 respectively. The population then decays back to the corresponding levels with decay rates, κ_{41}, κ_{52}, and κ_{63}. The population in the excited levels also decays to the singlet state, level 7 with a rate, κ_{47}, κ_{57}, and κ_{67}. The population of level 5 and level 6 is much more likely to cross to the singlet state, level 7. Figure 5.1 shows the

energy level diagram. The population in level 7 decays back to level 1 with a rate, κ_{71}, and to level 2 and level 3 with a rate, κ_{72} and κ_{73}. Furthermore, the population in level 1, level 2, and level 3 are roughly equal at room temperature in thermal equilibrium, due to the small energy differences between each level. Any polarisation will be depolarised at the longitudinal relaxation rate, κ_{21}. The MW pumping is determined by the MW Rabi frequency Ω_m. The rate equations are expressed in terms of density matrices.

$$\dot{\rho} = \mathbf{M}\rho$$

$$\rho = \begin{pmatrix} \rho_1 \\ \rho_2 \\ \rho_3 \\ \rho_4 \\ \rho_5 \\ \rho_6 \\ \rho_7 \\ \rho_{12} \\ \rho_{21} \\ \rho_{13} \\ \rho_{31} \\ \rho_{14} \\ \rho_{41} \\ \rho_{25} \\ \rho_{52} \\ \rho_{63} \\ \rho_{36} \end{pmatrix}$$

$$\mathbf{M} = \begin{bmatrix} \mathbf{M_{11}} & \mathbf{M_{12}} \\ \mathbf{M_{21}} & \mathbf{M_{22}} \end{bmatrix}$$

where $\mathbf{M_{ij}}$ is the sub-matrix of M. The $\mathbf{M_{11}}$ is the 7x7 population sub-matrix, describing the spin dynamics of the 7-level model. The $\mathbf{M_{12}}$ and $\mathbf{M_{21}}$ are the population-coupling, 7x10 and 10x7, sub-matrices that describe the coupling of the laser field and the MW field with the 7-level model. The $\mathbf{M_{22}}$ is the coherence sub-matrix that describes the coherence of the coupled

fields.

$$\mathbf{M_{11}} = \begin{bmatrix} -2\kappa_{21} & \kappa_{21} & \kappa_{21} & \kappa_{41} & 0 & 0 & \kappa_{71} \\ \kappa_{21} & -2\kappa_{21} & \kappa_{21} & 0 & \kappa_{52} & 0 & 0 \\ \kappa_{21} & \kappa_{21} & -2\kappa_{21} & 0 & 0 & \kappa_{63} & \kappa_{73} \\ 0 & 0 & 0 & -(\kappa_{41}+\kappa_{47}) & 0 & 0 & 0 \\ 0 & 0 & 0 & 0 & -(\kappa_{52}+\kappa_{57}) & 0 & 0 \\ 0 & 0 & 0 & 0 & 0 & -(\kappa_{63}+\kappa_{67}) & 0 \\ 0 & 0 & 0 & \kappa_{47} & \kappa_{57} & \kappa_{67} & -(\kappa_{71}+\kappa_{72}+\kappa_{73}) \end{bmatrix}$$

$$\mathbf{M_{12}} = \begin{bmatrix} -\frac{\Omega_m}{2}i & \frac{\Omega_m}{2}i & -\frac{\Omega_m}{2}i & \frac{\Omega_m}{2}i & -\frac{\Omega_l}{2}i & \frac{\Omega_l}{2}i & 0 & 0 & 0 & 0 \\ \frac{\Omega_m}{2}i & -\frac{\Omega_m}{2}i & 0 & 0 & 0 & 0 & -\frac{\Omega_l}{2}i & \frac{\Omega_l}{2}i & 0 & 0 \\ 0 & 0 & \frac{\Omega_m}{2}i & -\frac{\Omega_m}{2}i & 0 & 0 & 0 & 0 & -\frac{\Omega_l}{2}i & \frac{\Omega_l}{2}i \\ 0 & 0 & 0 & 0 & \frac{\Omega_l}{2}i & -\frac{\Omega_l}{2}i & 0 & 0 & 0 & 0 \\ 0 & 0 & 0 & 0 & 0 & 0 & \frac{\Omega_l}{2}i & -\frac{\Omega_l}{2}i & 0 & 0 \\ 0 & 0 & 0 & 0 & 0 & 0 & 0 & 0 & \frac{\Omega_l}{2}i & -\frac{\Omega_l}{2}i \\ 0 & 0 & 0 & 0 & 0 & 0 & 0 & 0 & 0 & 0 \end{bmatrix}$$

$$\mathbf{M_{21}} = \begin{bmatrix} -\frac{\Omega_m}{2}i & \frac{\Omega_m}{2}i & 0 & 0 & 0 & 0 & 0 \\ \frac{\Omega_m}{2}i & -\frac{\Omega_m}{2}i & 0 & 0 & 0 & 0 & 0 \\ -\frac{\Omega_m}{2}i & 0 & \frac{\Omega_m}{2}i & 0 & 0 & 0 & 0 \\ \frac{\Omega_m}{2}i & 0 & -\frac{\Omega_m}{2}i & 0 & 0 & 0 & 0 \\ -\frac{\Omega_m}{2}i & 0 & 0 & \frac{\Omega_m}{2}i & 0 & 0 & 0 \\ \frac{\Omega_m}{2}i & 0 & 0 & -\frac{\Omega_m}{2}i & 0 & 0 & 0 \\ -\frac{\Omega_l}{2}i & 0 & 0 & 0 & \frac{\Omega_l}{2}i & 0 & 0 \\ \frac{\Omega_l}{2}i & 0 & 0 & 0 & -\frac{\Omega_l}{2}i & 0 & 0 \\ 0 & -\frac{\Omega_l}{2}i & 0 & 0 & 0 & \frac{\Omega_l}{2}i & 0 \\ 0 & \frac{\Omega_l}{2}i & 0 & 0 & 0 & -\frac{\Omega_l}{2}i & 0 \\ 0 & 0 & -\frac{\Omega_l}{2}i & 0 & 0 & 0 & \frac{\Omega_l}{2}i \\ 0 & 0 & \frac{\Omega_l}{2}i & 0 & 0 & 0 & -\frac{\Omega_l}{2}i \end{bmatrix}$$

The $\mathbf{M_{22}}$ can be further split into $\mathbf{A}$ and $\mathbf{B}$.

$$\boldsymbol{M_{22}} = \begin{bmatrix} \boldsymbol{A} & \mathbf{0} \\ \mathbf{0} & \boldsymbol{B} \end{bmatrix}$$

$$\boldsymbol{A} = \begin{bmatrix} -\gamma_m + i\Delta_{-m} & 0 & 0 & 0 & 0 \\ 0 & -\gamma_m + i\Delta_{-m} & 0 & 0 & 0 \\ 0 & 0 & -\gamma_m + i\Delta_{+m} & 0 & 0 \\ 0 & 0 & 0 & -\gamma_m + i\Delta_{+m} & 0 \\ 0 & 0 & 0 & 0 & -\gamma_l + i\Delta_l \end{bmatrix}$$

$$\boldsymbol{B} = \begin{bmatrix} -\gamma_l + i\Delta_l & 0 & 0 & 0 & 0 \\ 0 & -\gamma_l + i\Delta_l & 0 & 0 & 0 \\ 0 & 0 & -\gamma_l + i\Delta_l & 0 & 0 \\ 0 & 0 & 0 & -\gamma_l + i\Delta_l & 0 \\ 0 & 0 & 0 & 0 & -\gamma_l + i\Delta_l \end{bmatrix}$$

where $\dot{\rho}$ is the time derivatives of the level matrix ρ and its elements ρ_i represents the population in level i. M is the rate matrix.

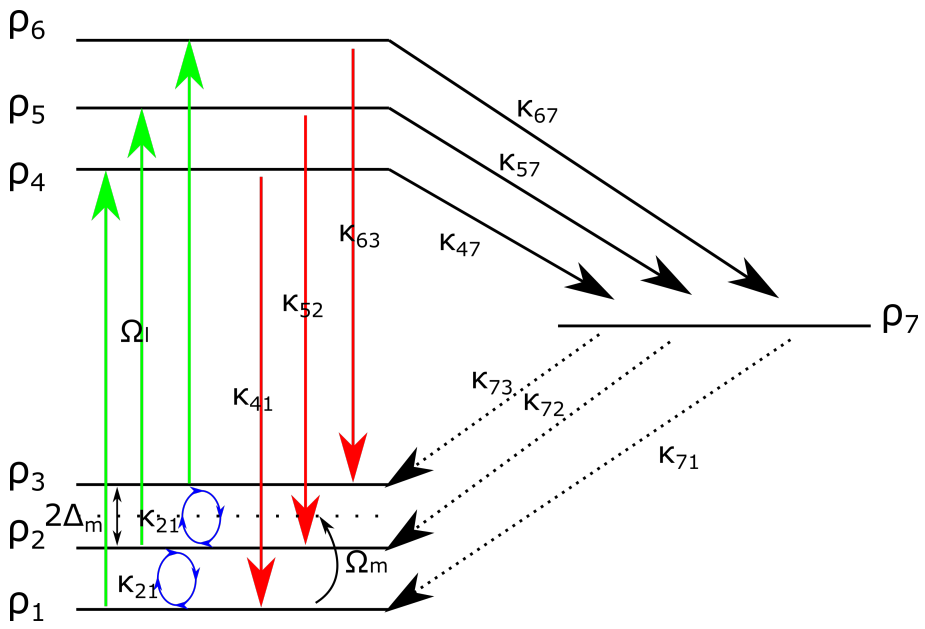
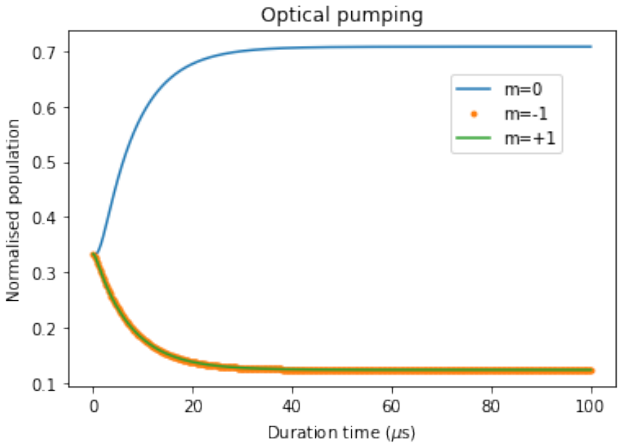


Figure 5.1: This diagram shows the energy levels, decay rate and pumping rate of the 7-level model.

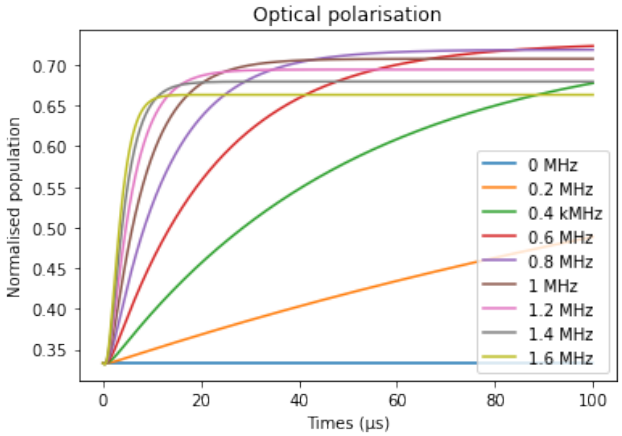
The assumption is that the coherences and the Rabi frequencies are all real. The rates are: κ_{41} = 65.9 MHz, κ_{52} = 65.9 MHz, κ_{63} = 65.9 MHz, κ_{57} = 53.3 MHz, κ_{67} = 53.3 MHz, κ_{47} = 7.9 MHz, κ_{71} = 0.98 MHz, κ_{72} = 0.73 MHz, κ_{73} = 0.73 MHz, κ_{21} = 0.17 kHz [1], γ_m is the dephasing of the MW coupled spin states, γ_l is the decoherence of the laser coupled states, $\Delta_{-m} = \omega_{-1} - \omega_m$ is the detuning of the MW pump from the m=-1 state, $\Delta_+ m = \omega_{+1} - \omega_m$ is the detuning of the MW pump from the m=+1 state and Δ_l is the detuning of the laser.

From Figure 5.2, the spin in the m=0 is preferably polarised under a laser excitation. It saturates at around 71%. The higher the pumping rate the quicker the saturation is reached. The saturation level is reduced as more population is pumped into the singlet state. Figure 5.2 (b) shows the spin dynamics and saturation at different pump powers.

MW pulse at 2.87 GHz can drive the population oscillation between the m=0 m=±1 states, shown in Figure 5.3. A π pulse pumps all the population from the polarised m=0 state to the m=±1 state. The duration of the π pulse is π/Ω_m. The intensity of fluorescence is $\kappa_{41}\rho_4 + \kappa_{52}\rho_5 + \kappa_{63}\rho_6$. The CW-ODMR spectrum is simulated under continuous MW and laser pumping, as shown in Figure 5.4 (a). The higher the MW power the broader the linewidth, shown in Figure 5.4 (b). On the other hand, high high-powered laser will reduce the linewidth, as shown in Figure 5.4 (c). The spectral profile of the CW-ODMR is predominantly Lorentzian. The laser-narrowed profile, Figure 5.4 (c), has the least narrow linewidth at around 1.22 MHz and it



(a) Optical pumping of the 7-level system



(b) Optical polarisation

Figure 5.2: (a) Optical pumping of the 7-level system.
This diagram showing that under a optical pumping at Ω_l=1 MHz, the m=0 is polarised to about 71% of the total population after 30 μs of laser excitation. (b) This diagram shows the optical polarisation under various laser rates. The higher the laser rate, the quicker the saturation is reached, and the long-lived singlet state is more populated.

is Lorenzian. In contrast, the inhomogeneous broadening spectral dip, which is the combination of 5 sub-species experiencing a range of different magnetic fields, is more Gaussian-like. When a magnetic field is applied, there are two dips observed. Figure 5.4 (d) shows the inhomogeneous broadening of the CW-ODMR spectrum. Figure 5.5 (a) shows the CW-ODMR under a static magnetic field. In Figure 5.5 (b), the MW power increases so that the spectrum is broadened. In pulsed ODMR, shown in Figure 5.5 (c) and 5.5 (d), a laser pulse is applied to polarise the m=0, then an MW π pulse pumps the population to the m = $\pm$1 states and a final optical readout by a short laser pulse. The pulsed ODMR almost eliminates the MW power-broadening effect. The linewidth, which is 3.06 MHz, is narrower than the CW-ODMR, which is 6.39 MHz. The oscillatory feature in the fluorescence intensity is due to the Rabi oscillation of the detuned MW pumping pulse.

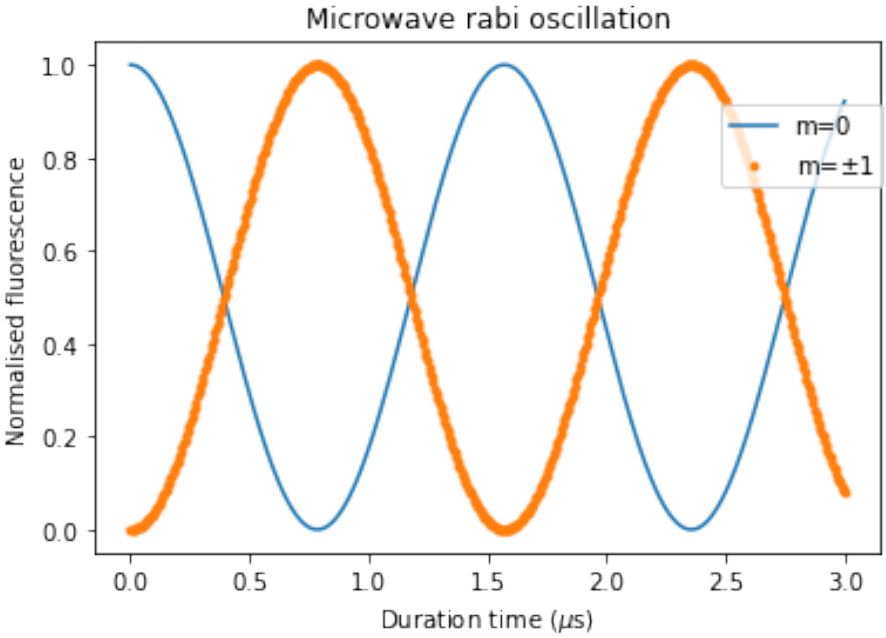
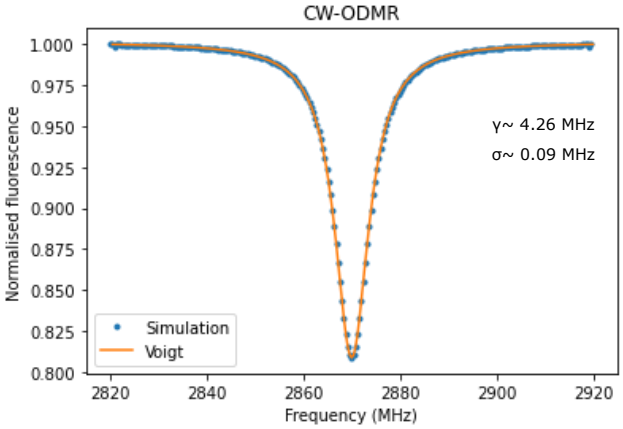
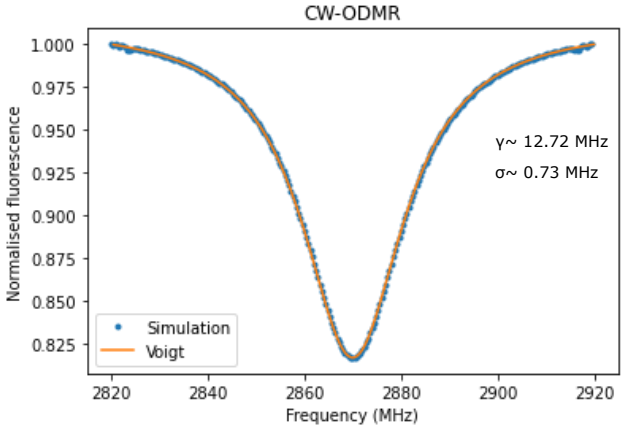


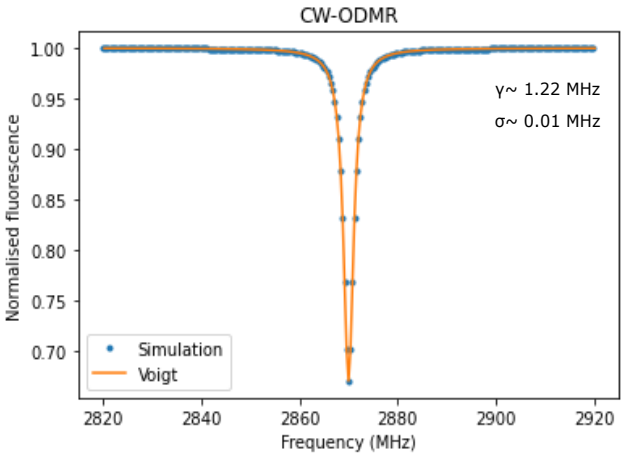
Figure 5.3: This diagram showing the population oscillates between the m=0 and m=±1 states when the Ω_m=4 MHz and the dephasing γ_m is zero. The π pulse has a duration, τ_π, of 786 ns which agrees with $\tau_\pi = \pi/\Omega_m$.



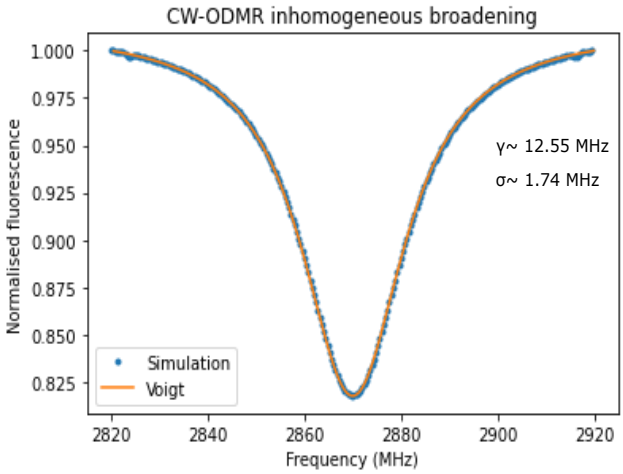
(a) Zero-field CW-ODMR



(b) MW power broadening

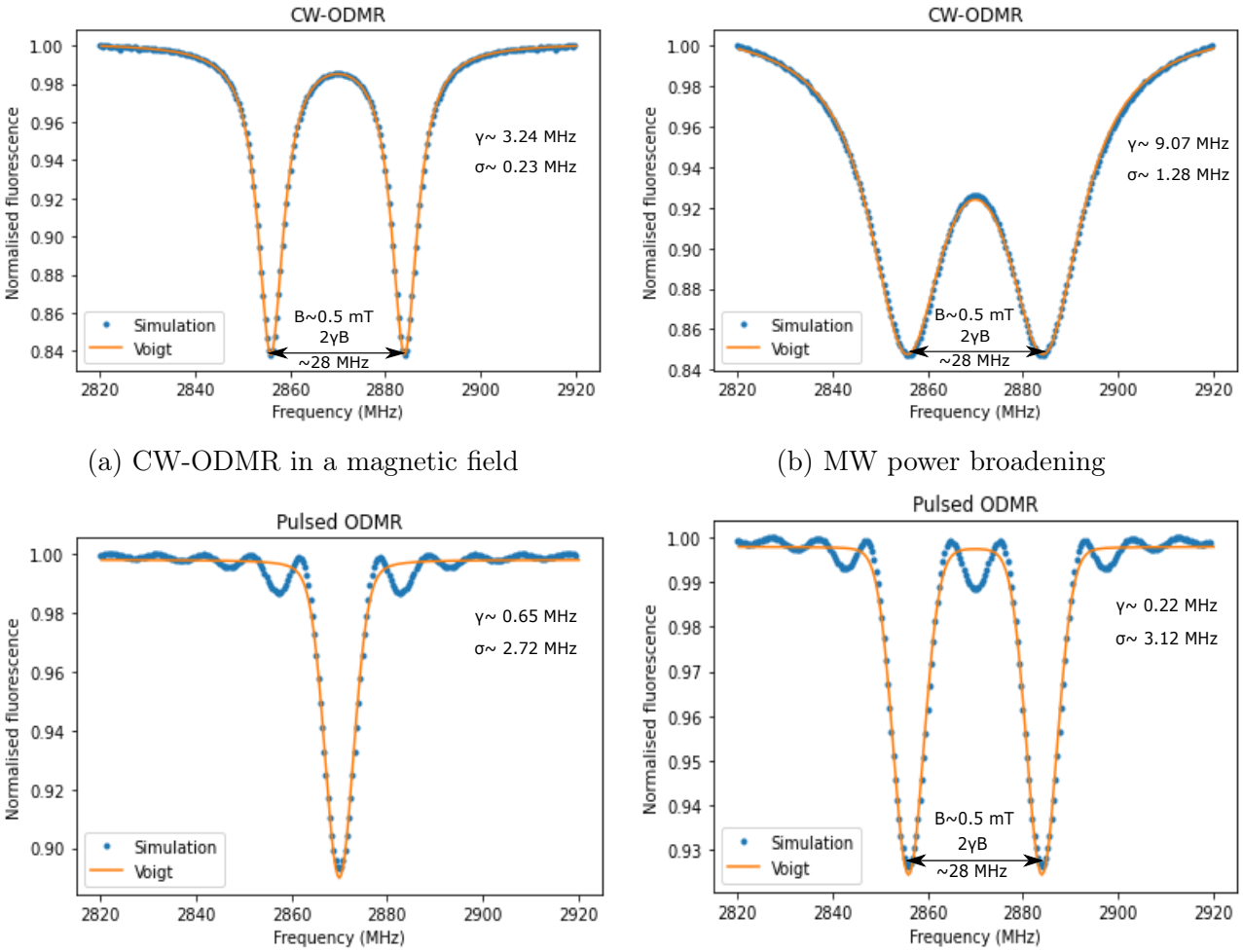


(c) Laser narrowing



(d) Inhomogeneous broadening

Figure 5.4: (a) This diagram showing the CW-ODMR spectrum when the Ω_m=4 MHz, Ω_l=1 MHz without any magnetic field. The spectrum is fitted using a Voigt function. The spectrum is almost a Lorentzian. The linewidth is about 6.39 MHz. (b) This diagram shows the MW power broadening of the CW-ODMR spectrum when the Ω_m=12 MHz, Ω_l=1 MHz without any magnetic field. The spectrum is fitted using a Voigt function. The broadened spectrum is more Gaussian. (c) This diagram showing the CW-ODMR spectrum when the Ω_m=4 MHz, Ω_l=4 MHz without any magnetic field. The spectrum is fitted using a Voigt function. The linewidth is narrower and the Lorentzian is more significant. (d) This diagram shows the inhomogeneous broadening of the power broadened CW-ODMR spectrum when the Ω_m=12 MHz, Ω_l=1 MHz. The spectrum is the combination of five NV centres sub-species that experience a slightly different magnetic field. The spectrum is fitted using a Voigt function. The broadened spectrum is more Gaussian.



(a) CW-ODMR in a magnetic field

(b) MW power broadening

(c) Zero-field pulsed ODMR

(d) Pulsed ODMR in a magnetic field

Figure 5.5: (a) This diagram showing the CW-ODMR spectrum when the Ω_m=4 MHz, Ω_l=1 MHz. The magnetic field is 0.5 mT. The spectrum is fitted using two Voigt functions. (b) This diagram shows the MW power broadening of the CW-ODMR spectrum when the Ω_m=12 MHz, Ω_l=1 MHz. The magnetic field is 0.5 mT. The spectrum is fitted using two Voigt functions. (c) This diagram showing the pulsed ODMR spectrum when the system is polaried by Ω_l=1 MHz laser for 100 μs, then a π pulse, Ω_m=4 MHz, for 0.786 μs, without any magnetic field, and a final readout by a Ω_l=1 MHz laser for 10 μs. The spectrum is fitted using a Voigt function. The spectrum is almost a Lorentzian. The linewidth is about 3.06 MHz. (d) This diagram shows the pulsed ODMR spectrum when the system is polarised by Ω_l=1 MHz laser for 100 μs, then a π pulse, Ω_m=4 MHz, for 0.786 μs, with a 0.5 mT magnetic field, and a final readout by a Ω_l=1 MHz laser for 10 μs. The spectrum is fitted using a Voigt function. The spectrum is almost a Lorentzian. The linewidth is about 3.06 MHz.

5.2 Exploring the Spin Dynamics of a Room-Temperature Diamond Maser using an Extended Rate Equation Model

This section was the basis of a recent publication [11].

5.2.1 Introduction

Due to their long spin relaxation times, negatively-charged nitrogen-vacancy defect centres (NV^-) in diamonds [146, 115] have been widely used as a room-temperature material for quantum metrology [147, 148, 149], communications [150] and quantum information processing [151, 152, 153]. Recently, their use has been extended to the microwave analogue of lasers, known as masers, by placing NV-enriched diamonds into dielectric resonators and enclosing the system in a copper cavity[2]. Although masers are unmatched for low-noise microwave amplification, their use has historically been limited to niche applications in deep space communications and radio astronomy due to the need for high vacuum and cryogenic temperatures required to allow them to operate. The demonstration of room-temperature masers based on organic [10, 154, 42] and inorganic [8, 2, 155, 156, 157] gain media thus opens up a path to the widespread use of masers as ultra-low noise microwave amplifiers, which in addition to existing applications in radio astronomy and communications technology are of increasing interest for the low-power microwave signal processing essential to many quantum technologies [158]. In this latter regard, masers may offer an advantage over Josephson parametric amplifiers, which have a limited dynamic range and are easily saturated compared to masers [159].

The NV^- defect is a $S = 1$ spin centre that can be described using a 7-level Hamiltonian consisting of a ground-state triplet, an excited-state triplet and an intermediate singlet state. NV^- defects can be photoexcited to the excited state triplet using laser pulses with wavelengths at or below 637 nm, from which they may relax either through a spin-conserving radiative decay or through a spin-selective non-radiative decay whose net effect is to preferentially transfer electrons from the excited $m_s = \pm 1$ states to the $m_s = 0$ ground state via the intermediate singlet state, as seen in Fig. 5.6. These spin-selective transitions mean that NV^- centres can be optically controlled and read out. The NV^- defect exhibits a long T_1 spin-lattice relaxation time (up to 6 ms [160]) and T_2 spin-spin relaxation time (0.6 ms for diamonds that with a

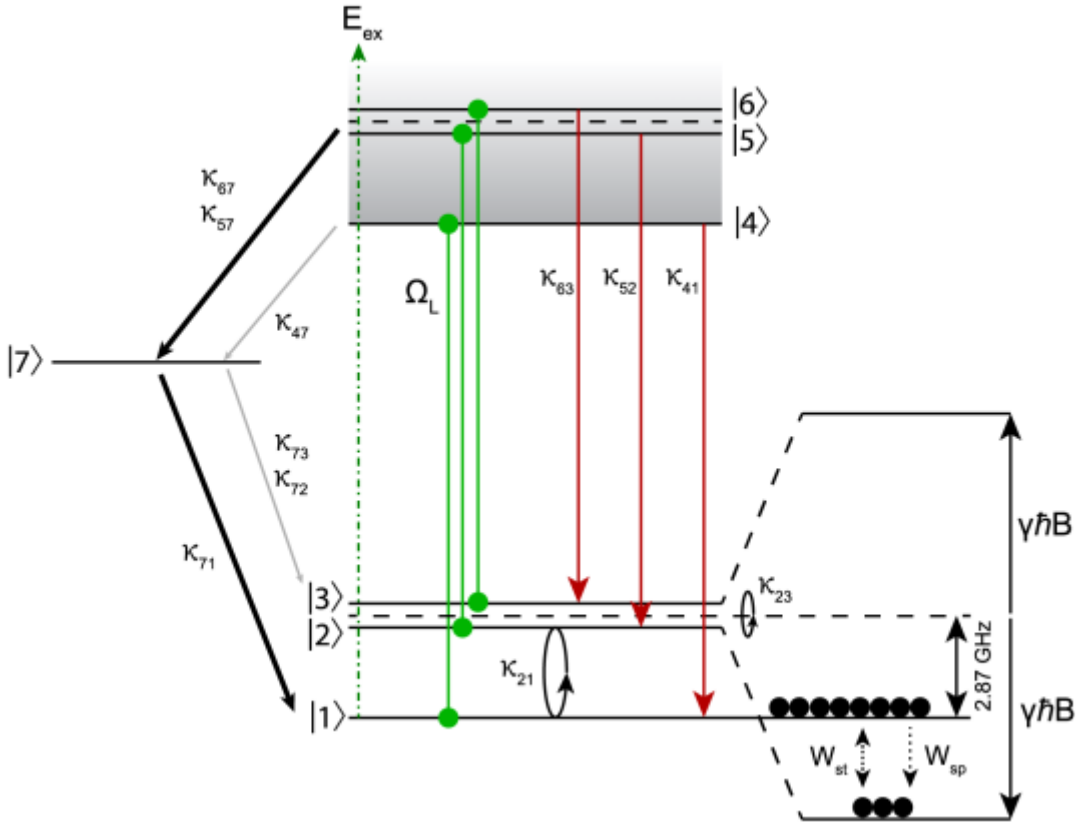


Figure 5.6: This NV^- energy level diagram indicating pumping and decay rates of the 7-level model with excited phonon bands shown by the grey area in levels $|4\rangle$, $|5\rangle$ and $|6\rangle$. Here, the green dashed line represents the energy of the excitation wavelength (532 nm, 2.33 eV) promoting population to the phonon bands, whereas the green solid line is the transition represented by the pump strength Ω_L. Decay rates are indicated by κ_{ij} (the values for these rates used to generate our results are provided in Table 1) for the decay from the initial electronic state i to the new state j, $\gamma\hbar B$ is the Zeeman splitting, W_{st} and W_{sp} is the stimulated emission rate and the spontaneous emission rate. Non-radiative decays are also shown to, and from, $|7\rangle$ where the bold line denotes the faster decay rate. Reproduced from AIP Publishing [3].

Table 5.1: Transition rates used to describe the time evolution of the ensemble of NV^- centres in a cavity to produce the results presented in Figures 3-8. The values are based on experimental results from Ref. [1].

Parameters	Values (MHz)
κ_{41}=κ_{52} =κ_{63}	65.9
κ_{57}=κ_{67}	53.3
κ_{47}	7.9
κ_{71}	0.98
κ_{72} =κ_{73}	0.73
κ_{21} =κ_{23}	4.4×10^{-4}

natural abundance of ^{13}C and an NV concentration of 3×10^{13} cm^{-3}, though this may be extended to 1.8 ms in isotopically purified ^{12}C diamond at lower NV concentrations [111][161]) at room temperature. It is these properties that allow an ensemble of NV^- defects placed in a dielectric resonator cavity in an applied magnetic field to be used as a gain medium for a room-temperature maser, as well as for lasers [162]. The threshold laser power with which an NV ensemble must be pumped to allow steady-state masing is proportional to $(T_1(C-1))^{-1}$, so that it depends on the spin-lattice relaxation time and a figure of merit known as the cooperativity C, defined as [2]:

$$C = 4g^2N/(\kappa_c\kappa_s) \tag{5.1}$$

where g is the spin-photon coupling strength between each active NV^- spin and the cavity field, N is the number of NV^- spins for which the masing transition between the $m_s = 0$ and $m_s = -1$ ground state sub-levels is resonant with the cavity (for a field aligned with one of the four possible directions of the NV axis, this corresponds to 1 in 12 NV spins, since in general only one of the three ^{14}N hyperfine transitions will be resonant with the cavity), $\kappa_c = \omega/Q$ is cavity loss rate, ω is the resonant frequency of the cavity, Q is the quality factor of the resonator, κ_s is the dephasing rate of the spins [2]. The cooperativity measures the ratio of the coupling effect of N spins and the combined decoherence rates and by inspecting the expression for the threshold laser pump power, it can be seen that masing requires the cooperativity to be larger than one. To achieve this, we can either increase the coupling by having a smaller mode volume or more NV^- spins or a higher Q factor to reduce the decoherence rate. The copper cavity in which the diamond and resonator are enclosed acts as a shield that reduces radiation losses, increasing the quality factor Q and hence the cooperativity.

Despite impressive experimental demonstrations and characterisation of room-temperature diamond masers [2, 156, 157], certain challenges for the widespread adoption of diamond masers have been identified spanning materials challenges such as making diamond gain medium with sufficient amount of photostable NV^- centres under optical excitation as well as engineering challenges such as applying a highly homogeneous external magnetic field in alignment with NV^- axes [149] and improving the cavity Q factor. This has led to efforts to better understand the material and device parameter space which diamond masers inhabit, typically through modelling of spin dynamics with semiclassical rate equations. Here we use rate equation simulations to investigate how maser performance depends on the properties of the diamond gain medium and the dielectric resonator.

The model is extended beyond the standard first-order rate equations sometimes used to model the photophysics of NV^- centres [155, 145] to a system of coupled equations that incorporate the number of photons in the cavity through second-order terms. The extended second-order rate equations incorporate the number of photons in the cavity and allow the time-evolution of the populations of NV^- centres in different energy states and the photon number to be simulated explicitly. The rate equations are employed to model the spin-dependent electronic population dynamics of the NV^- centres under optical pumping at a wavelength of 532 nm. The results show masing dynamics with various parameters such as the Q factor of the cavity and the mode volume of the resonator. Throughout this section, "Q factor" will be taken to refer to the loaded Q factor of the combined resonator-cavity system. As well as aiding the design of room-temperature diamond masers, the extended rate equations presented will be useful for describing microwave mode-cooling devices [163] and quantum heat engines based on NV^- centres in diamond [1].

5.2.2 Theoretical model

The population dynamics of the electronic energy levels of the NV^- are described using the 7-level model in Fig. 5.6, where levels $|1\rangle$ and $|4\rangle$ correspond to the $m_s = 0$ states, and levels $|2\rangle$, $|5\rangle$ and $|3\rangle$, $|6\rangle$ correspond to the $m_s = -1$ and $m_s = +1$ respectively. The spin dynamics of different states under an optical excitation on NV^- spin defects are described by rate equations based on a 7-level model and an extended Bloch equation formalism [145, 164]. We model the excitation of NVs with a laser to create a population inversion in diamond masers as an optical

pump from the ground-state sublevels $|1\rangle$, $|2\rangle$ and $|3\rangle$ respectively to the excited-state sublevels $|4\rangle$, $|5\rangle$ and $|6\rangle$ the rate at which NVs are excited by the laser is parametrised by the optical pump rate, defined as

$$\Omega_L = \mathcal{E}\mathbf{D_{ij}}/\hbar \tag{5.2}$$

where $\mathcal{E}$ is the electric field of the laser and $\mathbf{D_{ij}}$ is the dipole moment of the induced transition between level $|i\rangle$ and level $|j\rangle$, such as the ground triplet states and the excited triplets. In general, the transition dipole moment for the NV^- centres is sensitive to local strain in the diamond lattice and is, therefore, sample dependent. In this section, we use a dipole moment of 1.73×10^{-29} C·m, estimated from a fluorescence lifetime of 13 ns [165]. A shorter fluorescence lifetime will have a higher dipole moment. The electric field amplitude is determined by the laser pump power available at the NV^- centres with respect to the absorption dipole direction, laser polarisation and laser spot size. In diamond masers demonstrated to date, a laser of wavelength 532 nm is used to excite the NV^- spin defects from the ground state sub-levels ($|1\rangle$, $|2\rangle$ and $|3\rangle$) to an excited phonon band shown as a grey band in Figure 5.6. They subsequently relax nonradiatively to the excited sub-levels $|4\rangle$, $|5\rangle$ and $|6\rangle$. Since the phonon relaxation is generally fast compared to the optical pump rate, the off-resonant pumping is modelled using a common pump rate determined by the optical pump strength Ω_L for these transitions. From the excited states, the NV^- centres can either decay radiatively through spin-conserving fluorescence at a wavelength of 637 nm (indicated by red lines with respective decay rates) or non-radiatively via spin-selective intersystem crossing, passing through the spin singlet $|7\rangle$. The decays from excited states to lower energy states $|i\rangle \rightarrow |j\rangle$ have corresponding rates κ_{ij}.

Since κ_{57}, $\kappa_{67} \gg \kappa_{47}$, NVs in the $|5\rangle$ and $|6\rangle$ states are much more likely to decay to the intermediate singlet state $|7\rangle$ than those excited to the $|4\rangle$ state and the net result of optically pumping the system is to preferentially fill level $|1\rangle$. In a magnetic field applied along an NV axis whose magnitude exceeds the ground-state level anticrossing point at 102.5 mT, the $m_s = -1$ sub-level ($|2\rangle$) is shifted below $|1\rangle$ so that filling $|1\rangle$ entails a population inversion, as required for masing. For such a population inversion to be maintained the optical pumping must fill the $|1\rangle$ state faster than the longitudinal relaxation rate, κ_{21}, with which the NV ensemble tends towards thermal equilibrium (for which at room temperature the populations of levels $|1\rangle$, $|2\rangle$ and $|3\rangle$ are roughly equal).

The rate equations used to generate the results can be derived by taking the matrix elements

of the Hamiltonian and the density matrix and using them to form von Neumann equations of motion, which give the unitary evolution of the 7-level system. The decay rates between the levels are phenomenologically added in diagonal terms [164], representing the populations, whereas the dephasing terms are added in the non-diagonal terms, representing the coherences. The photon number is treated as a second-order rate equation that depends on the number of thermal photons, and the spontaneous and stimulated transition rates. The operating frequency of the maser is the same as the resonant frequency of the cavity. The rate equations thus form equations of motion for density matrix elements expressed with respect to a 7-level Hamiltonian of the form

$$\mathcal{H} = \sum_{i=1}^{7} E_i |i\rangle\langle i| + \hbar\Omega_L \sum_{i=1,2,3} (|i\rangle\langle i+3| + |i+3\rangle\langle i|) \tag{5.3}$$

where E_i is the energy of the ith level, h is the Planck constant, $|i\rangle$ denotes the ith state of the NV^- centres (as in Fig. 5.6). Photons are treated phenomenologically by the addition of a photon term included in the rate equations (see Appendix for further details). Using rates reported in Ref.[1], the equations of motion were solved numerically using an implicit Runge-Kutta method with a backward differentiation method [166, 167] to simulate the time evolution of a diamond maser.

5.2.3 Maser simulation

The 7-level rate equations can be used to predict masing operation when a magnetic field shifts the $m_s = -1$ state ($|2\rangle$) below the $m_s = 0$ state ($|1\rangle$). When optical pumping is employed to create a population inversion between states ($|1\rangle$) and ($|2\rangle$), the NVs will transition between these states to restore thermal equilibrium via spin-lattice relaxation (at a rate κ_{12}) and via the absorption and spontaneous and stimulated emission of MW photons. For microwave-frequency transitions, the spin-lattice relaxation rate, on the order of 10^2 Hz, is much higher than the spontaneous emission rate in free space, which is on the order of 10^{-13} Hz [168]. Hence the spins preferentially relax by transferring energy to the lattice. The spontaneous emission rate is described using Einstein coefficients **A** and **B**, which phenomenologically describe the rate of the spontaneous and stimulated emission processes and can be boosted through the Purcell effect depending on the cavity Q-factor.

The transition rate from one state i to another state j is determined[169] by the magnetic dipole matrix element of the corresponding two states, $\mathbf{D_{ij}} = \langle j|\mathbf{H}\cdot\mathbf{S}|i\rangle$, where $\mathbf{H}$ is the MW magnetic field and $\mathbf{S}$ is the spin vector, and the density of states of the electromagnetic field, $\rho(\omega)$ as $W \propto \frac{|\mathbf{D_{ij}}|^2\rho(\omega)}{\hbar}$. The magnetic field is approximated as a classical perturbation so that the matrix element is replaced by σ_{ij}, which denotes a matrix element for the spin transition, so its square-modulus is proportional to a transition probability, and the dipole matrix element is $(\mathbf{H}\langle j|\mathbf{S}|i\rangle)^2 = (\mathbf{H}\sigma_{ij})^2$. When the NV ensemble is placed in a cavity, the density of microwave photon states at the masing frequency is altered with respect to its free-space value, causing a proportionate shift in the spontaneous and stimulated emission rates for the maser transition. This change in these rates is equal to the Purcell factor, $F = \frac{3c^3}{2\pi\omega^3 n_{re}^3}\frac{Q}{V_m}$, where c is the speed of light, ω is the cavity resonance frequency, V_m is the mode volume and n_{re} is the refractive index in the cavity[168]. To enhance the spontaneous emission rate for a given frequency, a high Q factor and a small mode volume are thus required.

In the masing simulation, the initial photon number in the cavity is determined by the thermal photon number at thermal equilibrium, $n_{th} = (e^{\hbar\omega/k_BT} - 1)^{-1}$. There is no external microwave input. At 9.22 GHz and room temperature, $n_{th} \approx 635$ and these initial MW photons are able to be absorbed or trigger stimulated emission.

The stimulated emission rate per intracavity photon is given at resonance by [15, 163]:

$$W_{st} = \frac{\pi(g\mu_B)^2}{4\pi\hbar}\frac{\mu_0 T_2^* \omega\eta}{V_m} \tag{5.4}$$

where the filling factor η and the mode volume V_m are respectively defined by

$$\eta = \frac{\int_{Sample}|\mathbf{H}|^2 dV}{\int_{Mode}|\mathbf{H}|^2 dV} \tag{5.5}$$

$$V_m = \frac{\int_{Cavity}|\mathbf{H}|^2 dV}{|\mathbf{H}_{Max}|^2} \tag{5.6}$$

The higher the filling factor, the more strongly the sample interacts with the cavity mode. The numerator of the mode volume is integrated over the entire copper cavity volume, including the dielectric resonator.

For the results presented in the following section, the parameters from Table 5.1 and Table

Table 5.2: Variable parameters used in the rate equations to describe the time evolution of the ensemble of NV^- centres in a cavity. The number of available NV^-, the maser frequency, ω, the dephasing time, T_2^* and the Q factor is from [2]. The V_m and η are obtained in a CST MICROWAVE STUDIO simulation. The Δ_l is the detuning in frequency between the 532 nm excitation laser and the zero phonon line at 637 nm and Ω_L is the estimated pump strength at 400 mW of excitation power.

Parameters	Values
N	4×10^{13}
ω	$2\pi\times$ 9.22 GHz
T_2^*	0.5 μs
V_m	0.25 cm^3
Q	30,000
η	0.05
B	432 mT
Δ_l	92.89 THz
Ω_L	1150.7 MHz

5.2 are used. The finite-element software CST MICROWAVE STUDIO is used to estimate the mode volume and the filling factor, using equations (5) and (6). In the CST MICROWAVE STUDIO simulation, we model a system similar to that used to demonstrate masing from an NV-enriched diamond sample with a resonant frequency of 9.22 GHz, employing a sapphire resonator with an inner diameter of 5 mm, an outer diameter of 10 mm and a height of 6 mm on a sapphire post of 12 mm high and enclosed in a copper cavity with an inner diameter of 31 mm and a height of 30 mm. The dielectric constant of the sapphire was set to 9.4, the loss tangent to 8×10^{-6} [62]. The dielectric constant ϵ determines the size of the resonator and the mode volume (with $V_m \propto 1/\epsilon^{3/2}$, while the loss tangent affects the Q factor. Dielectric materials with a high dielectric constant and a small loss tangent are favorable, as this increases the Purcell factor. The energy density of the magnetic field of the $TE_{01\delta}$ mode of the cavity is shown in Figure 5.7. The W_{st} is approximately 1.98×10^{-6} s^{-1}. The spontaneous rate is given by [15]:

$$W_{sp} = \frac{\mu_0 \omega^3 (g\mu_B)^2}{6\pi\hbar c^3} \tag{5.7}$$

At 9.22 GHz, the spontaneous emission rate is about 1.57×10^{-12} s^{-1}, which is much slower than the stimulated transition rate and the spin relaxation rate.

The optical pumping strength, Ω_L, is 1150.7 MHz, which corresponds to 400 mW of optical power. The initial populations of the NV energy levels are set by the Boltzmann distribution,

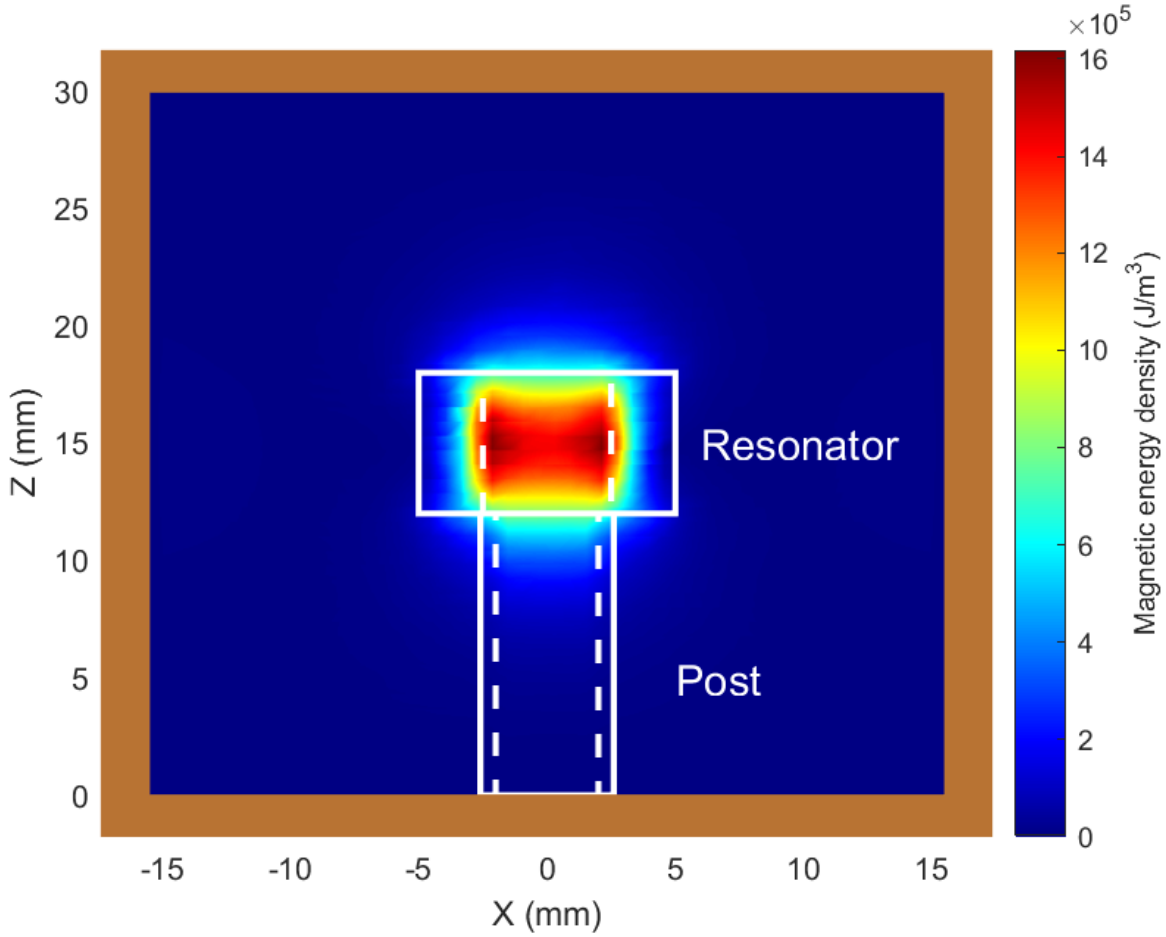


Figure 5.7: The energy density of the magnetic field of the $TE_{01\delta}$ mode of a cylindrical copper cavity simulated using CST MICROWAVE STUDIO. The solid white outlines show the boundaries of a sapphire resonator and post and the dashed white outlines the inner boundaries. The walls of the copper cavity are shown as the enclosure that bounds the image. Reproduced from AIP Publishing [3].

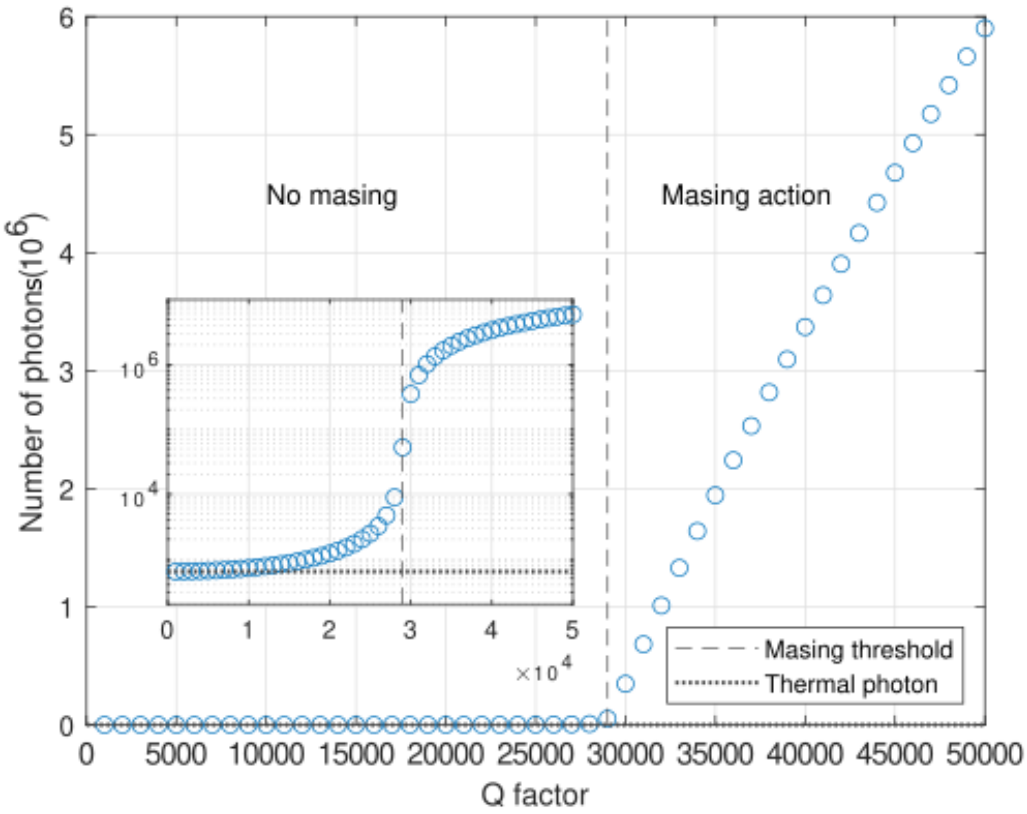


Figure 5.8: The steady-state number of photons as a function of the cavity Q factor. The photon number shows threshold behaviour with respect to the Q factor, with the onset of masing at around $Q = 29000$ for the parameters listed in Table 5.1. The inset shows the onset on a logarithmic scale. Reproduced from AIP Publishing [3]

with each state filled with a population proportional to e^{-E_i/k_BT}, where k_B is the Boltzmann constant, T is the temperature and E_i the energy of the $|i\rangle$ state. The initial number of MW photons is $(e^{\hbar\omega/k_BT} - 1)^{-1}$ with ω is the frequency of the cavity field and maser output, equal to the frequency of the transition between $|1\rangle$ and $|2\rangle$.

Looking at the intracavity photon number as a function of the cavity Q-factor (Figure 5.8), with other parameters fixed, it is possible to identify a masing threshold as the point where the number of photons in the cavity is an order of magnitude greater than the thermal population. The maser output power, in Watts, can be estimated using $n\hbar\omega^2/Q_m$, where ω is the operating maser frequency, n is the intracavity photon number (of order 10^5 when the maser is just above threshold) and $Q_m = 1/(1/Q_l - 1/Q_u)$, where Q_l and Q_u are the loaded and unloaded Q factors, is the contribution of the diamond to the loaded Q factor. For realistic values of $Q_l = 30,000$ and $Q_u = 50,000$ the maser output is thus around 0.5 pW, or -93 dBm. By incorporating the loaded and unloaded Q factors, the output coupling efficiency of the system

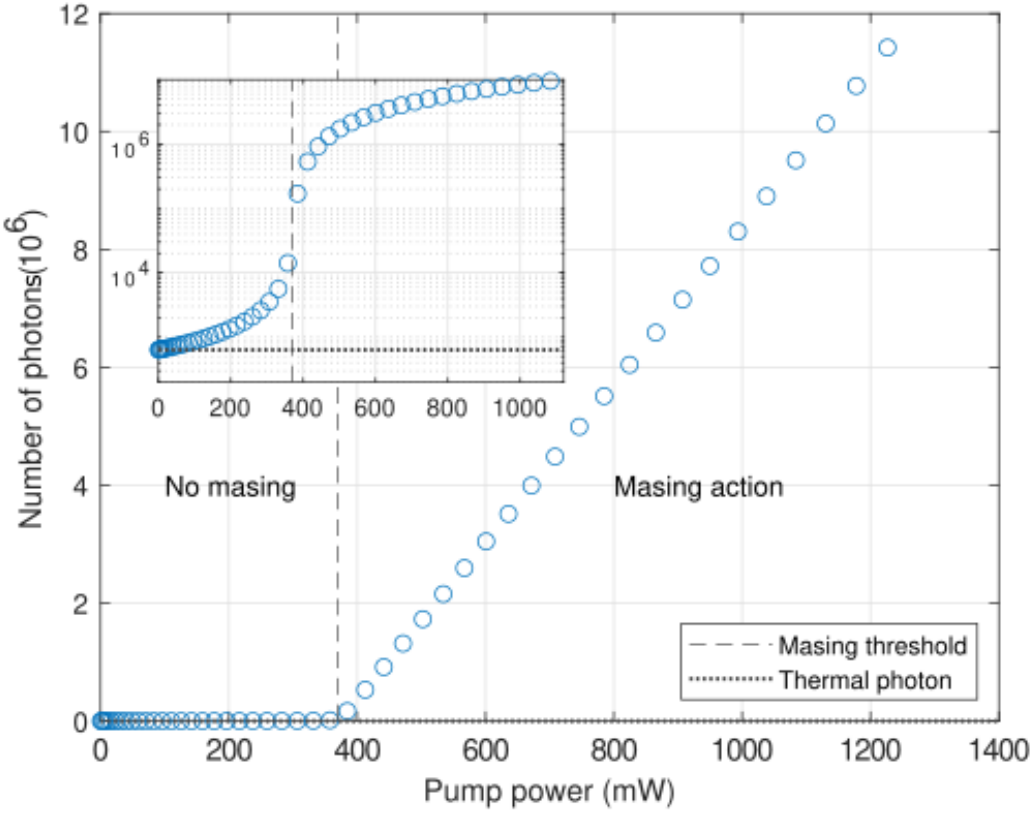


Figure 5.9: The steady-state number of photons as a function of the optical pump power. For the parameters listed in Table 5.1, the threshold pump power is about 370 mW. Reproduced from AIP Publishing [3].

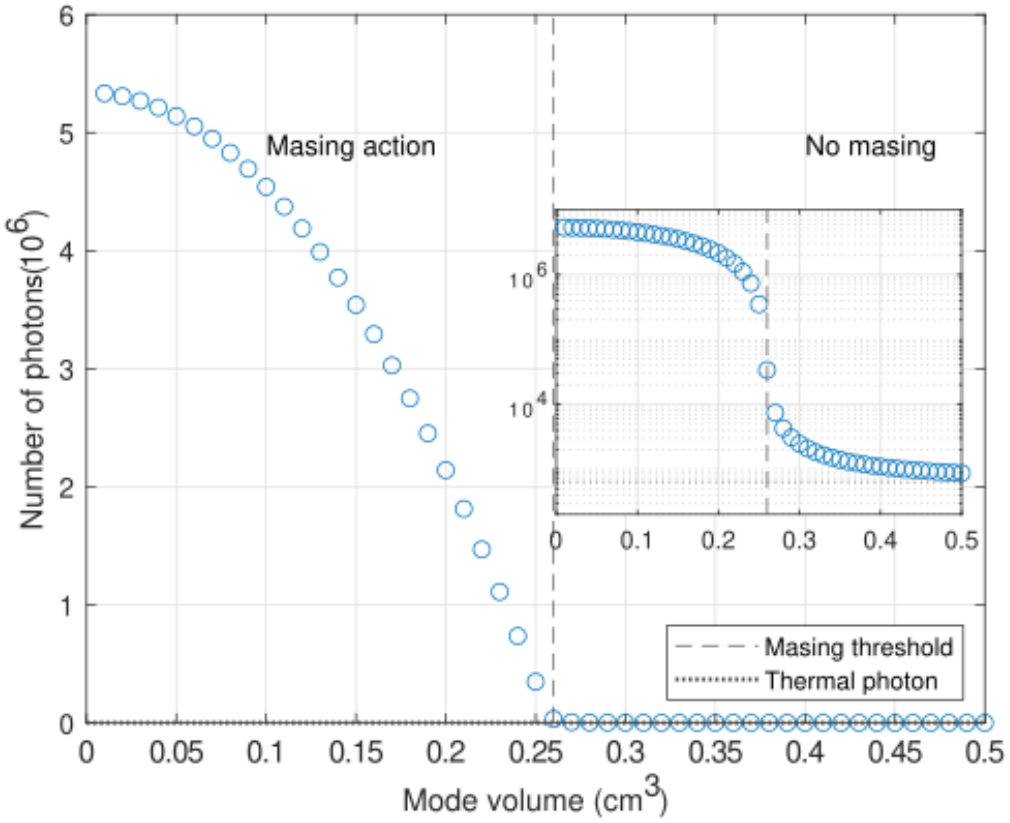


Figure 5.10: The steady-state number of microwave photons as a function of the cavity mode volume for the parameters listed in Table 5.1. The masing threshold occurs at a mode volume of about 0.26 cm^3. The inset shows the onset on a logarithmic scale. Reproduced from AIP Publishing [3]

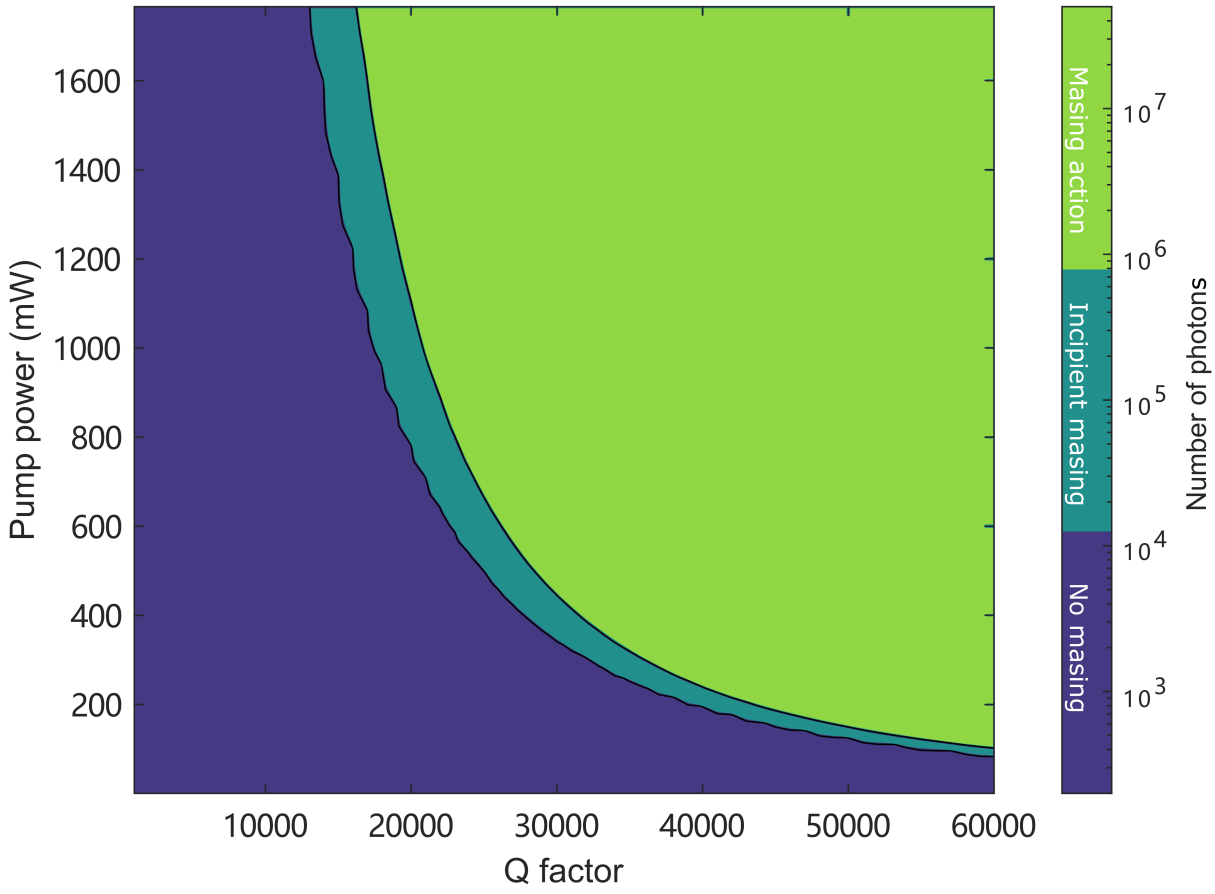


Figure 5.11: The steady-state microwave photon number as a function of the optical pump strength and the loaded cavity Q factor. It is possible to identify a masing action regime, a no masing regime and an intermediate "incipient masing" regime in which stimulated emission dominates spontaneous emission, but the maser cannot achieve self-sustaining oscillations. At all pump strengths, the photon number increases monotonically with the Q-factor as expected. Reproduced from AIP Publishing [3]

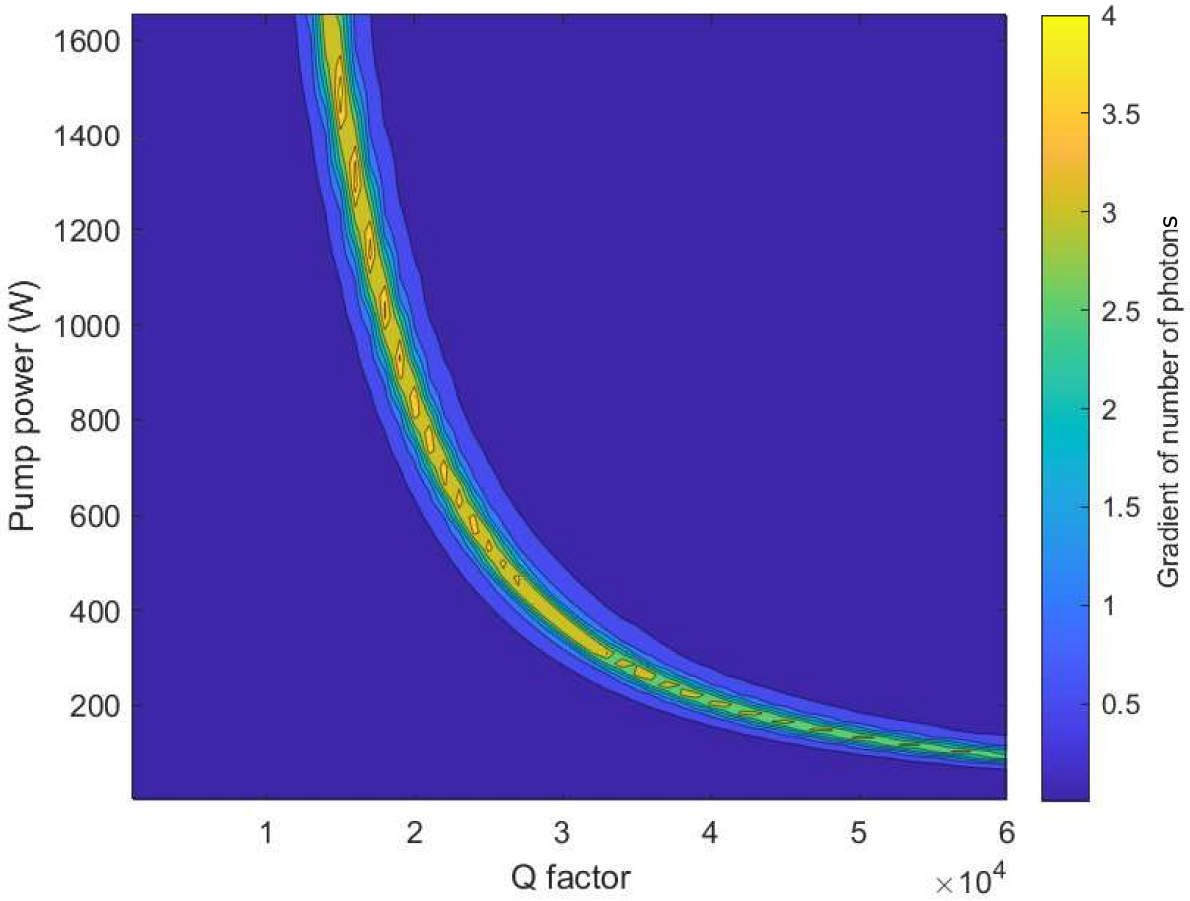


Figure 5.12: The log gradient map of Figure 5.11 shows the incipient masing regime, where the increase of number of photons with respect to the change in Q factor and the pump power is significant, on the order of 1 or more, the number of photons is moderate. In the no masing regime on the bottom and left, both the number of photons and the log gradient is low. In the masing regime on the top right, the number of photons is high but the log gradient is low.

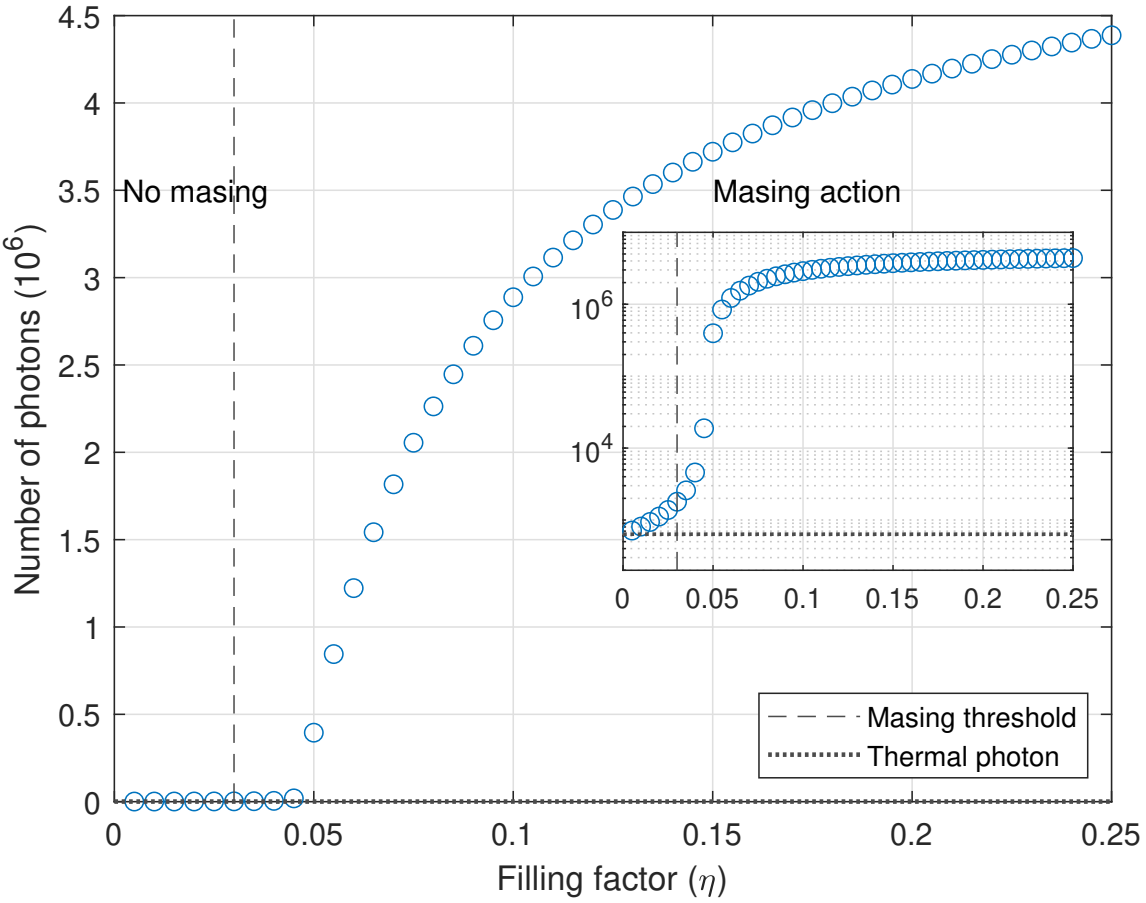


Figure 5.13: The number of microwave photons in the cavity as a function of the filling factor, defined by Eq. 4. The number of photons becomes saturated above $\eta = 0.3$. The inset shows the onset of masing at a filling factor of 0.03. Reproduced from AIP Publishing [3].

	No masing	Incipient masing	Masing action
Logarithm gradient	Low	High	Low
Number of photons	Low	Moderate	High

Table 5.3: Definition of the three masing regimes using the number of photons and the logarithm gradient.

is already taken into account so this can be directly compared to data from [2], which measured an output power of -90 dBm. With a lower Q factor, the number of photons will be closer to the thermal photon number, suppressing any maser action. As the Q factor increases, the number of cavity photons also increases until at a certain threshold Q factor, the number of photons increases significantly. Beyond this point, the photon emission rate is higher than the cavity decay rate, thus, the number of photons in the cavity is stable at a level significantly higher than the thermal photon background and will not decay away since in this case emission is predominantly stimulated and balanced by absorption at the same rate. In Figure 5.9, the performance of the maser at different optical pump powers is studied at a fixed Q factor of 30,000. For the parameters employed, the maser starts to operate above a threshold pump power of 370 mW. Despite using different diamond material parameters, the threshold Q factor and the threshold pump power are similar to those from recent experimental results reported in [157].

The threshold behaviour with respect to the mode volume, which is inversely proportional to the Purcell factor and the cooperativity, is shown in Figure 5.10. As expected, smaller mode volumes increase the number of masing photons in the cavity. For the parameters in Tables 1 and 2, the threshold is roughly at 0.27 cm^3, and for larger mode volumes masing cannot occur.

Figure 5.11 shows the contour map of the number of photons as a function of the optical pump power and the Q factor. The dark blue region shows that the masing effect does not occur due to the high losses and low pump power. The second region, in dark green, shows the "incipient masing" region, where stimulated emission starts to build up and the number of photons is higher than the number of thermal photons. In addition, the logarithm gradient is large, more than 1. In this region, an external MW signal fed into the maser would be amplified but the maser cannot be run as an oscillator. The maser is in operation in the light green region, where stimulated emission is maintained and the device can undergo self-sustaining maser oscillations.

Figure 5.12 shows the same map but shows the log gradient of the number of photons with respect to both the change in the Q factor and the pump power. It maps out the region that the number of photons change dramatically with respect to the change in both the Q factor and the pump power in the phase diagram. It outlines the masing threshold, which is defined as a significant increase in a number of photons, and the width of the region represents the incipient masing regime. In both the no masing and masing regime, the log gradient is small, but the number of photons is negligible in the no masing regime and is maintained at a high level in the masing regime. In the incipient masing regime, the increase is more significant towards the high pump power low Q factor end, whereas, the increase in photon is much smoother and smaller in the high Q factor low pump power end. This might suggest that a low Q factor maser with high enough pump power is beneficial for a maser amplifier.

The number of intracavity photons is shown as a function of the gain medium filling factor, defined in equation (5.5), in Figure 5.13, again displaying a clear threshold for masing. The results show that the threshold is about 0.03, beyond which the number of photons maintained in the cavity significantly increases beyond the thermal population. The number of cavity photons increases monotonically as the filling factor approaches unity.

It is assumed that the number of NV^- centres is constant during masing. This is reasonable for pump powers around the masing thresholds observed since these are low enough that the ionisation and recombination of NV centres due to laser excitation is expected to be weak [170, 162]. Similarly, all the rates are assumed to be constant, neglecting any heating which will lead to a reduction in T_1 time [157] as well as the T_2 time [171]. Both of these spin lifetimes vary with temperature as T^5, though the T_2^* lifetime caused by the field inhomogeneity is only very weakly dependent on temperature [171]. The zero-field splitting is also temperature dependent [172], but since this effect is weak (cooling from room temperature to 4 K, causes a change of less than 1% in the zero-field splitting) it is ignored in this model. All these temperature effects will tend to broaden the maser linewidth. Recent work has shown that the high power rate will significantly increase the temperature, especially the T_1 time, which makes maser action impossible [157] by affecting the ability of the gain medium to maintain a population inversion. It would be interesting to develop the rate equation approach presented here to include such effects, though they are expected to lead only to small changes in the predicted thresholds.

A further interesting extension to this rate equation model would be to explicitly model the effect of NV concentration on the spin lifetimes. To first order, changes in the NV^- concentration do not affect the cooperativity since the spin decay rate κ_s is proportional to the NV^- concentration[173] so that the factor of N/κ_s in the cooperativity is constant. However, the concentration of NV^- in diamond samples depends not just on the concentration of nitrogen impurities but on the efficiency with which such impurities can be converted to nitrogen-vacancy centres. The relative populations of the two possible charge states (NV^- and NV^0), each of which can have an independent effect on the spin decay rate, implies the cooperativity is not independent of the [NV^-] for real systems. The ratio of NV: NV^- is typically[2] around 14:1, but a ratio of 6.95:1 has been reported for an optimised system[174]. It is also important to note that the diamond sample can have spatially varying concentrations. Finally, we expect a higher concentration to lead to increased self-absorption [175], which is not taken into account in this model but will again tend to increase the threshold pump power by increasing the effective cavity decay rate.

Since the uniformity of applied magnetic fields is a key barrier to the miniaturisation of diamond masers, an important question is how field inhomogeneity affects the masing thresholds. The homogeneous linewidth of the NV^- resonance is about 1 MHz [176] and in these simulations, it is assumed that the spatial inhomogeneity of the applied magnetic field over the volume of the diamond is small enough that the resulting Zeeman shifts are within the homogeneous linewidths of the NV^- centres. For an intrinsic linewidth of 1 MHz, this means the field inhomogeneity should be < 0.03 mT. For experimental systems, smaller field inhomogeneity increases the number of NV spins in resonance with the cavity, increasing the cooperativity and reducing the pumping threshold.

5.2.4 Conclusion

Rate equations extended to second-order to incorporate the intracavity photon number and coherences between different NV energy states have been used to simulate the spin dynamics of an ensemble of NV^- centres in a diamond-based maser. The model predicts the behaviour of the maser as a function of material parameters of the gain medium and resonator in good agreement with recent experimental results [157].

Cooperativity (and the related Purcell factor) are identified as key quantities which, if increased, will reduce the threshold pump power for masing. On the one hand, this requires a high Q factor and a small mode volume, but intrinsic material parameters of the diamond gain media such as the concentration of NV^- and T_2^* play a significant role, where a long T_2^* and more excited spins, which are determined by the filling factor and the concentration of the sample, are favourable. Ever higher pump powers will eventually reduce the number of maser photons, as the populations end up in the singlet state and the population inversion is reduced due to a kinetic bottleneck leading to the accumulation of NV^- centres in the $|7\rangle$ state, so optimising the cooperativity to lower the threshold pump power will be important for developing scalable diamond masers. Alternatively, increasing the transition rate from the $|7\rangle$ state through Purcell enhancement of a 1042 nm transition between two sub-levels of $|7\rangle$ could thus be a pathway to higher maser power outputs, though this is beyond the scope of this model. Attention to these considerations will aid the design of diamond-based masers suitable for mass production.

Additionally, suggested further improvements in the modelling of NV^- ensembles for maser applications have been suggested. If the NV^- to NV^0 charge conversion and the effects of temperature and NV^- concentration on the spin lifetimes are considered, the trade-offs between maximising the coherence times and increasing output power and cooperativity by maximising the number of NV^- centres and the pump power will become clearer. Such improvements will require further experimental input, particularly on the relationship between charge-state ratios and spin lifetimes.

The method presented here, which computes the time evolution of the maser output explicitly, will be of particular use for describing the "incipient masing" regime where the stimulated emission is dominant over the spontaneous emission, but insufficient for self-sustaining maser oscillation and thus less amenable to solutions based on steady-state considerations. The full time-dependent response of diamond masers will also be useful for technological applications where masers are used to amplify arbitrary time-dependent microwave signals.

More broadly, it is anticipated that the model presented in this section will be of use for improved modelling of other quantum technologies based on ensembles of spin defects, such as diamond magnetometers [147] and room-temperature masers based on alternative gain media such as silicon-vacancy defects in SiC [36, 37, 177].

Chapter 6

Maser Results

This chapter presents the maser performance using the D09 sample and the NID_{02} sample on the Bruker EPR electromagnet and the D09 sample on the small GMW electromagnet. The results show promising performance on the small GMW electromagnet, which demonstrates the miniaturisation of room-temperature diamond maser.

6.1 Diamond based maser

6.1.1 Bruker magnet-based system

The author would like to thank Wern and Daan who helped set up the equipment and the data taken. The procedure of operating a diamond maser will be placing the diamond samples on a wedge, with an angle of 45 °, in the resonator and rotating it to meet the alignment along the <111> axis. The VNA is used to check the resonant frequency of the resonator. The alignment can be confirmed with EPR measurement, where the high-field and low-field of the NV centres, which correspond to the parallel components, of the $\Delta m_s = \pm 1$ are separated maximally about twice the zero-field splitting. These EPR signals can be detected in the VNA as a wiggle at different magnetic fields when the scanning the magnet field. The ^{14}N hyperfine peaks can be resolved using the VNA. Be aware that the laser excitation will heat up and the resonance will shift according to the excitation power. This will take 30 to 60 minutes from ambient temperature to warm up. Once, everything is ready, the output of the maser

cavity is connected to the spectral analyzer for the observation of the maser signals. Another important point of the laser is the reflection and transmission of the diamond sample and the sapphire post. In the experiment, the laser enters from the side so that the angle of incidence is assumed to be 54.75° which matches the angle of the <111> axis. The refractive index of the diamond is 2.42 and the refractive index of the sapphire is 1.76. Using Fresnel equations, an unpolarised light has a transmission of 0.804. Nearly 20% of the power is reflected off the diamond. For the P-polarised light, the transmission is 0.962 and for the S-poloarised light, the transmission is 0.645. By using P polarisation, the optical excitation efficiency can be improved. However, in the experiment, the diamond is roughly rotated to around 45°. In this case, the transmission is 0.818, which is slightly more transmissive. On the diamond/sapphire interface, the transmission of the unpolarised light is 0.974, suggesting that most of the excitation power will travel through the sapphire post. The secondary reflections of the 0.026 reflective power will be total internal reflections. For 45°, the transmission is 0.976. upon exiting the post to the air, the transmission is 0.911. The back-reflection transmission to the diamond is about 0.968, which will contribute to the subsequent reflection in the sample. The cavity is made of copper which has a low reflectance of 532 nm and will scatter almost half of the light.

To enhance the refractive light at the interface, a dielectric material with a lower reflective index might be used. For example, a quartz post will reflect 0.05 of the power which is double the reflectance of the sapphire, but the dielectric loss might be higher than sapphire. Overall, sapphire is preferred for masing action. The transmitted light may reflect at the copper cavity back to the sample which will contribute again to the masing process. On the other hand, if the optical excitation comes from the top, the transmission will be 0.825 for unpolarised light which might bring more light in the sample than the side excitation. The secondary reflection from the diamond/sapphire interface will be similar to the side excitation.

The maser is demonstrated in the custom design cavity in the Bruker electromagnet. The system operates at undercoupled due to the small coupling loops. In this thesis, only the NID_{02} sample and the D09 sample managed to mase. Firstly, the NID_{02} sample is used. At 350 mW, no masing occurred. At 380 mW, masing starts to occur. The accumulated traced over 10 s is shown in Figure 6.1 (a). The mean power is -95.44 ± 2.12 dBm and the frequency is 9296.09 ± 0.001 MHz. The mean 3 dB width is 0.89 ± 0.33 kHz. The 3 dB width is calculated by setting a threshold that is 3 dB less than the maximum power. Since the signal contains spikes and

noise that fluctuate more than 3 dB, the calculation of the width is estimating the difference in frequency between the first time it reaches the threshold and the last time it falls below the threshold.

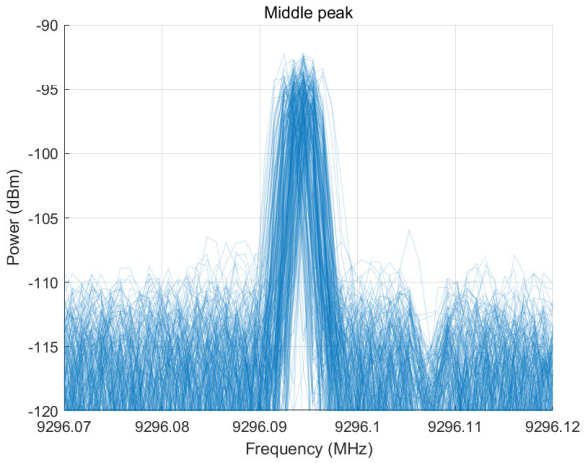
Autocorrelation is used to reveal the stability and periodicity of the signal in both the frequency and the amplitude. Figure 6.1 (b) shows that the amplitude autocorrelation decays rapidly with noise, while the frequency autocorrelation decays more slowly with a periodic oscillation, where the period is about 2400 ms.

At 800 mW optical power, the maximum of the middle peak signal is -90.5212 ± 0.6598 dBm. The three hyperfine peaks are clearly shown in the trace, where the separation is about 10 kHz, shown in Figure 6.1 (c). The 3 dB width is wider than the signal at 380 mW. From the Smith chart, the resonant frequency read from the S_{11} is 9.2863 GHz and the FWHM is about 30 kHz, the Q loaded Q factor estimated is about 15200. Figure 6.1 (d) shows the S_{11} taken from the VNA. Figure 6.2 shows the distribution plots of the maximum power, 3dB width and the frequency under various optical pump powers. Figure 6.2 (a) shows a linear relation of the optical pump power and the maser power up to 800 mW. Maser power is saturated at about -90 dBm for 800 mW, 1000 mW and 1200 mW. In addition, the saturated power has a smaller variance than the maser power in the linear regime, or under 800 mW. This behaviour is predicted by the extended rate equations in the previous chapter. Although the threshold power is between 350 mW and 380 mW, it takes about 800 mW to achieve a high and stable performance. The power and the stability will not increase when more excitation power is used. It is also noticeable that the 3 dB width is considerably wider in the saturation regime, and the width is very narrow at 380 mW and 400 mW. The masing frequency reduces as the optical pump power increases. There is a 15 MHz shift in frequency from 1200 mW to 380 mW. The results of Figure 6.2 are presented in mean values and standard deviations in Table 6.1.

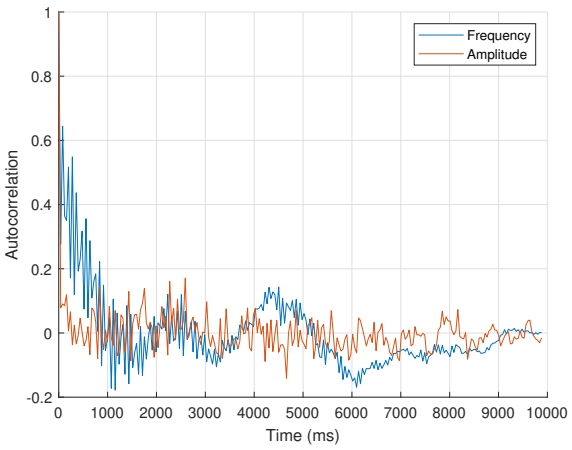
Optical power (mW)	Maximum power (dBm)	Frequency (MHz)	3 dB width (kHz)
380	-95.4442 ± 2.1151	9296.094 ± 0.001	0.89 ± 0.33
400	-92.9702 ± 2.7024	9295.924 ± 0.001	0.89 ± 0.30
600	-91.1732 ± 0.210	9290.711 ± 0.002	3.5 ± 2.8
800	-90.5212 ± 0.6598	9286.776 ± 0.006	18.2 ± 6.0
1000	-91.1109 ± 1.3983	9283.444 ± 0.003	7.3 ± 3.8
1200	-89.9938 ± 0.6071	9279.922 ± 0.008	23.7 ± 6.0

Table 6.1: A summary of maser performance of NID_{02} sample in the Bruker electromagnet.

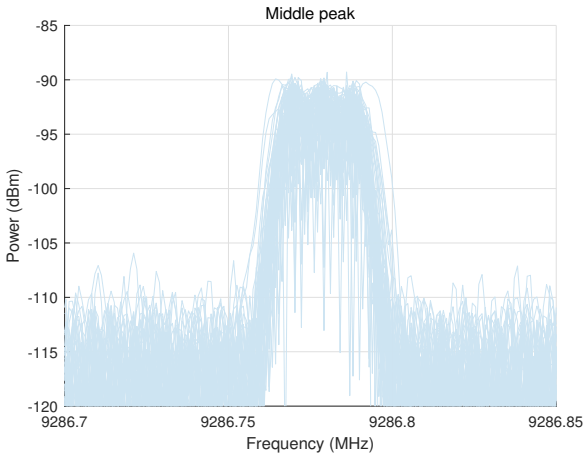
The D09 sample replaced the NID_02 in the Bruker electromagnet. The sample is excited at 1000 mW. The left peak trace is captured for 10 s and shows 191 traces, Figure 6.3 (a). The mean maximum power of the three hyperfine peaks are -83.81 ± 0.79 dBm,-83.42 ± 0.51 dBm and -83.37 ± 0.74 dBm and the mean frequency is 9657.48 ± 0.01 MHz, 9657.57 ± 0.03 MHz and 9657.64 ± 0.01 MHz. The three peaks are separated by about 80 kHz. This is slightly larger than the expected hyperfine splitting as in [2] due to the large amount of frequency jittering during the measurement that obscures the frequency spectrum's precious measurement. The 3 dB width of the signal is about 7.9 ± 3.2 kHz, which is similar to the 2 dB width of the NID_{02} maser. The higher masing frequency is the result of the smaller cavity used. Figure 6.3 (b) shows the 3D histogram in the frequency-maximum power space. It is shown that there are two peaks exist in the left peak traces that overlap and are separated by about 20 kHz it is believed to be the hyperfine splitting of the nitrogen atom similar to [2]. From Figure 6.3 (c), the frequency autocorrelation decays slowly and smoothly, indicating a steady signal in the frequency domain and small jittering. The frequency of the signal remains correlated for an extended period of time. On the other hand, amplitude autocorrelation decays rapidly with noisy fluctuations. Figure 6.3 (d) shows the frequency-maximum power distribution that illustrates the two peaks that are about 20 kHz apart. The higher frequency peak has a slightly higher power. At 1000 mW, the D09 diamond maser has higher masing power than the NID_{02} in the Bruker electromagnet. The D09 has almost 4 times the concentration of NV centre, and the NID_{02} is about three times larger in volume and has a higher filling factor. The D09 sample is isotopically pure and has a high T_2*.



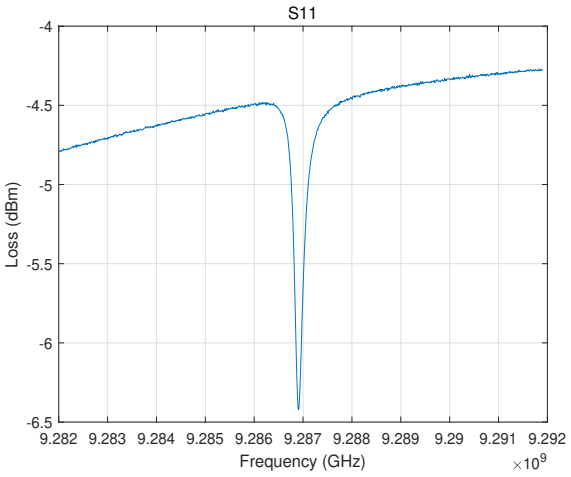
(a) 380 mW



(b) Autocorrelation at 380 mW



(c) 800 mW



(d) S_{11} at 800 mW

Figure 6.1: The maser signal of the left peak (a), middle peak (b) and the right peak(c) from the NID_{02} sample were measured in the spectrum analyser. (d) is the S_{11} of the maser resonator.

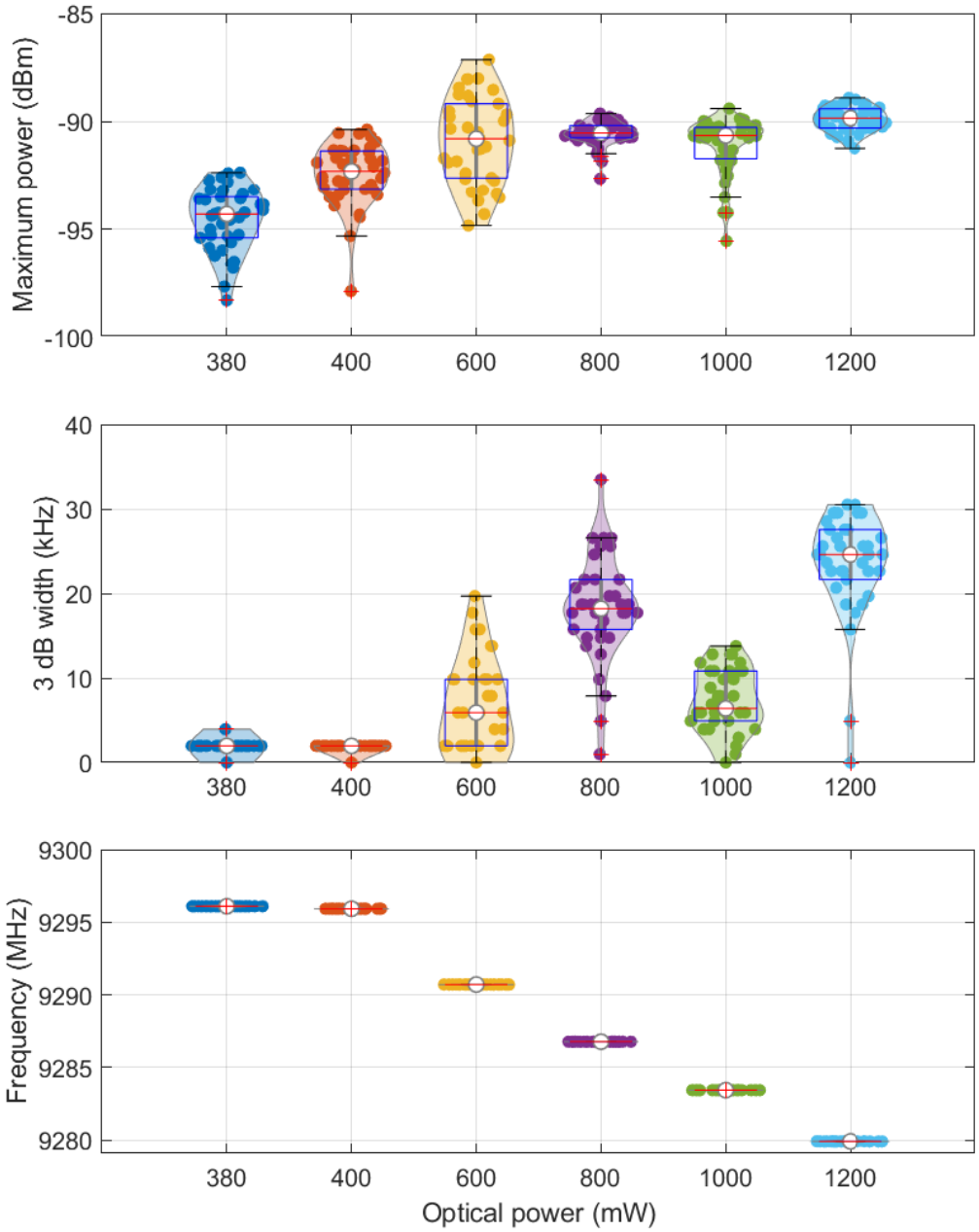
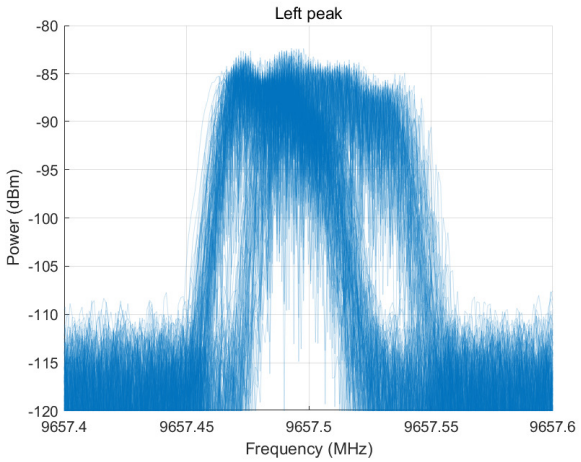
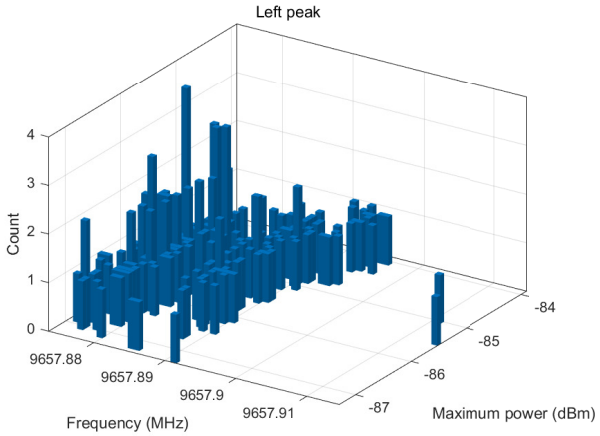


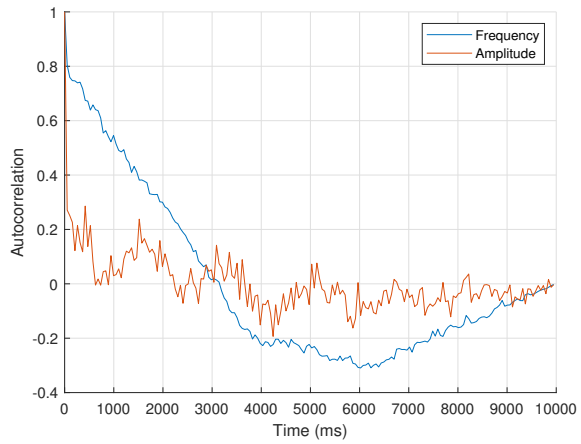
Figure 6.2: The distribution of (a) the maximum power, (b) the 3 dB width and (c) the frequency of data taken from the traces of the NID_{02} sample using the Bruker electromagnet with various optical pump powers.



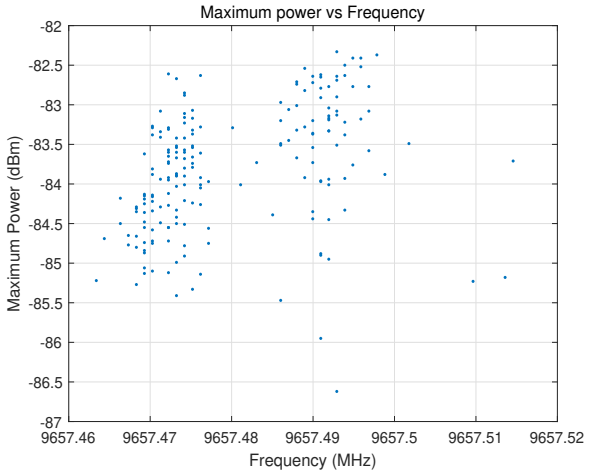
(a) Left peak accumulated traces



(b) 3D histogram



(c) Autocorrelation



(d) Frequency-maximum power distribution

Figure 6.3: The maser signal of the left peak (a) middle peak accumulated traces (b) the 3D histogram of the maximum power and the frequency (c) the autocorrelation of the frequency and the amplitude (maximum power) of the traces as a time series and (d) is the frequency against the maximum power from the D09 sample were measured in the spectrum analyser.

6.1.2 GMW based system

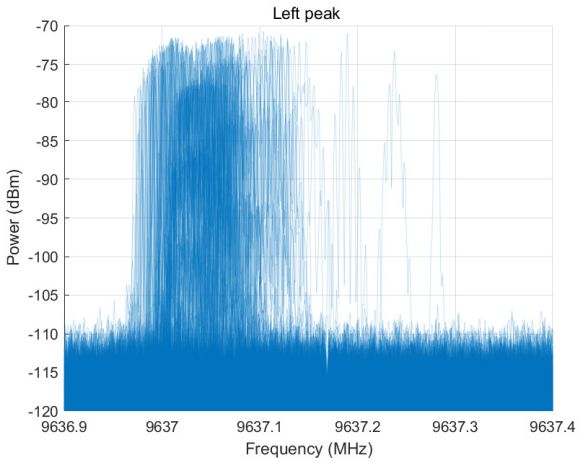
The author would like to thank Wern who had constructed and tuned the GMW magnet. The GMW electromagnet has a much smaller form factor than the Bruker electromagnet. By comparison, the GMW electromagnet has a weight of about 30 kg, whereas the Bruker electromagnet has a weight of about 1500 kg. Furthermore, the compact size of the GMW electromagnet allows it to be fixed on a breadboard no larger than 29 × 20 × 21 cm [178]. This significantly reduces the size and weight of the diamond-based maser. To fit the cavity in the GMW electromagnet, the size of the copper cavity is reduced from the Bruker cavity, 31 mm to 29 mm in diameter. The laser source is changed to a smaller 520 nm diode laser, which can provide up to 1.2 W at 5.0 V. In this section, the laser power is represented in Volt provided by the USB power port. The diode laser is assumed to be working at a linear regime of the power-voltage curve.

The smaller cavity will introduce more losses due to the cavity wall, and the small GMW electromagnet is less stable than the Bruker electromagnet. This led to a jittering signal, shown in Figure 6.4. The signal is captured at a fixed magnetic field as in the Bruker system. However, the maser signal jitters during the data acquisition that is shown in Figure 6.4 (a) which accumulates 329 acquisitions over 10 s, at 4.0 V excitation. The amplitude versus frequency of the maser signals gives information about the maximum amplitude variation and the frequency jitter among the signals captured. It shows that, at 4.0 V, there is a bandwidth of the accumulated traces of about 320 kHz, where the maser signal exists, and the maser signal quickly drops to the background level at -110 dBm outside the bandwidth. It is believed that the 330 kHz bandwidth is comparable to the bandwidth of the resonator at a Q factor of around 27000. The mean amplitude of the maser signal is -73.6 dBm and the standard deviation of 2.05 dBm. The low-frequency part of the maser is cut off by the resonator. Looking at the histogram of the maximum power, the distribution is asymmetric with a skewness of -1.79. The mean frequency is 9637.034 MHz and the standard deviation is 0.042 MHz and a skewness of 1.67. The magnitude of the skewness of the histogram of the amplitude and the frequency is similar, showing a non-Gaussian distribution. The sign difference indicates the shape of the distribution is opposite. The middle signals are at the centre of the resonance of the resonator, without any cutoff, so that the frequency jittering can be estimated to be 210 kHz. The right peaks have a mean of -73.8 dBm and a standard deviation of 1.97. The skewness is -1.74. The

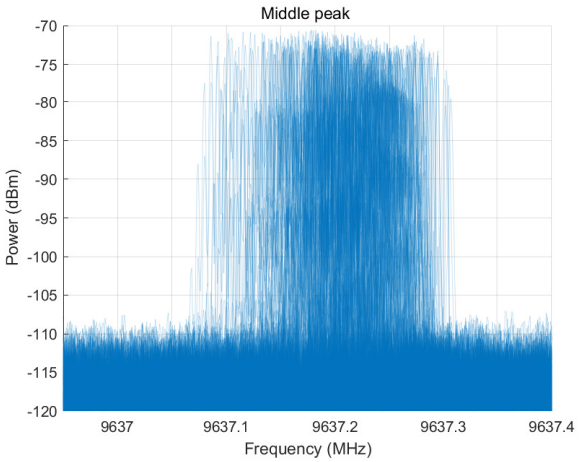
mean frequency is 9637.280 MHz and the standard deviation is 0.030 MHz and a skewness of -0.53. The middle peaks have a mean of -73.075 dBm and a standard deviation of 1.457. The skewness is -1.38. Focusing on the middle peak, the autocorrelation of the maximum power and the frequency is estimated. The maximum power autocorrelation quickly drops to 0, and randomly fluctuates between + 0.1 and - 0.1. The amplitude is gradually reduced to 0, and the amplitude is close to zero after 9 s. Whereas, in the frequency autocorrelation, the autocorrelation drops to 0 quickly and exhibits a periodic oscillation at a period of 2.1 s. Although the autocorrelation decreases the periodic oscillation is visible even at around 10 s. There are 4 oscillations that have an amplitude of no less than 0.05, suggesting a significant correlation. The mean frequency is 9637.219 MHz and the standard deviation is 0.043 MHz and a skewness of -0.45. The accumulated maser trace is shown in Figure 6.4 and 6.5.

Still, the maser signals jitter and shift constantly to other hyperfine peaks, where the span is 130 kHz, which is more than the span of the hyperfine maser signals in the Bruker system. It is unable to settle down into one of the hyperfine peaks, as the field is constantly jittering. However, the maser signal has a higher power at -72 dBm.

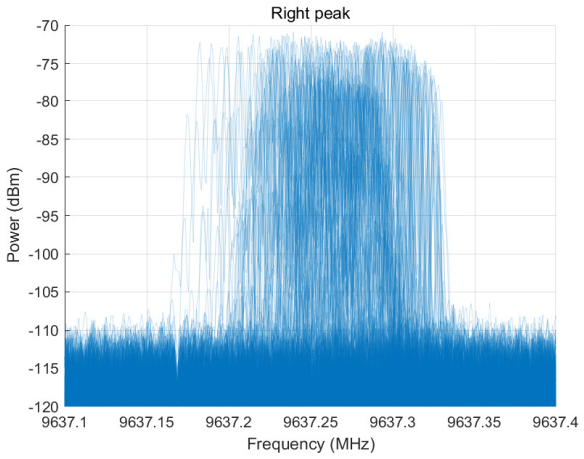
At 1.5 V, where the optical power is estimated to be 375 mW. The maser power is reduced to -77.216 $\pm$ 1.975 dBm. Further, by reducing the power down to 1.2 V, the spikes related to the chaotic behaviour disappear and the maser power is down to -85.057 $\pm$ 2.772 dBm. Figure 6.4 (d) shows the maser signal even at 1.2 V. Figure 6.6 shows the autocorrelation at three different optical excitation power. The autocorrelation is the most uncorrelated, whereas the other two have a slowly decaying frequency autocorrelation. Compared to the Bruker electromagnet, the maser on the GMW electromagnet is less stable in frequency. Comparing the frequency and amplitude instability, the amplitude seems more random and has more variance. Figure 6.7 shows the distribution of the traces in terms of (a) maximum power, (b) 3 dB width and (c) the frequency under various optical excitation powers. Similarly, it exhibits a linear regime and a saturated regime at about 2.0 V, which corresponds to about 480 mW. The 3 dB widths are similar under various excitation power and they are narrow compared to the maser using the Bruker electromagnet. The mean values and the standard deviations are shown in Table 6.2. The threshold pump power is between 1.1 V and 1.2 V, which is estimated to be 270 mW. The reduction in the threshold pump power is thought to be the high T_2^* due to the isotopically-enriched sample.



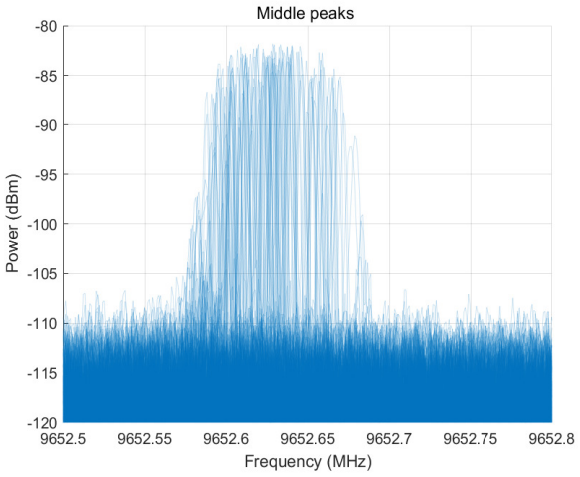
(a) Left peak at 4.0 v



(b) Middle peak at 4.0 v

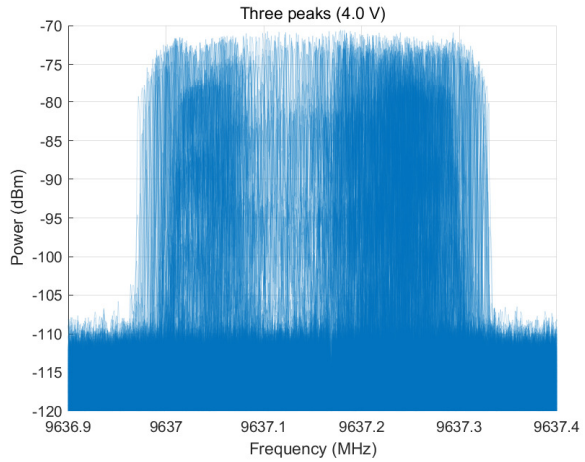


(c) Right peak at 4.0 V

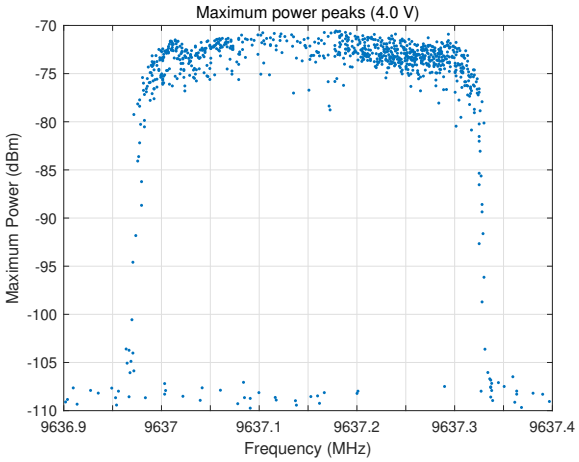


(d) 1.2 v

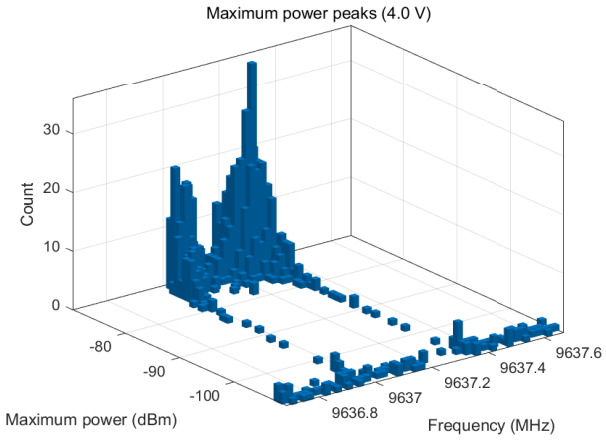
Figure 6.4: The accumulated maser signals were collected for 10 seconds, containing 325 traces, on a GMW electromagnet at 4.0 V laser power. (a) the left peak, (b) the middle peak, (c) the right peak. (d) The accumulated maser signals were collected for 10 seconds, containing 325 traces, on a GMW electromagnet at 1.2 V laser power of the middle peak.



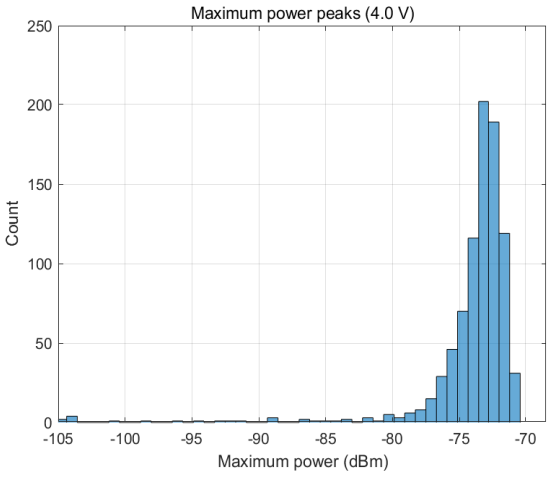
(a) Three peaks



(b) Three peaks

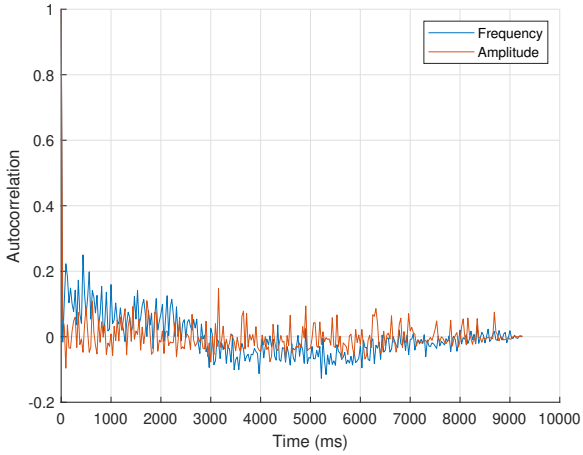


(c) Three peak

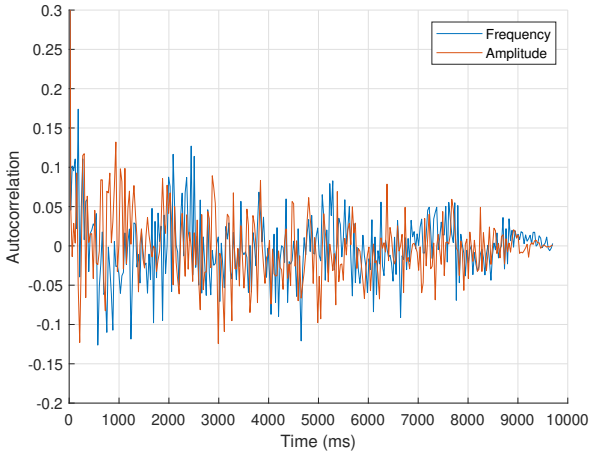


(d) Histogram

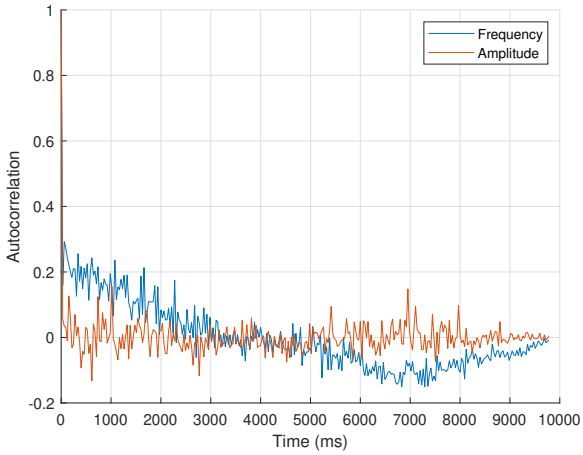
Figure 6.5: The maser signal of the left peak (a) the accumulated traces, showing the jitter during a 10 s measurement. (b) the positions of each peak in the frequency spectrum. (c) 3D histogram of the maximum power and the counts of the peak in the frequency spectrum. (d) the histogram of maximum power.



(a) 2.0 V



(b) 4.0 V



(c) 4.8 V

Figure 6.6: The autocorrelation of maser signals was collected for 10 seconds, containing 325 traces, on a GMW electromagnet at 4.0 V laser power.

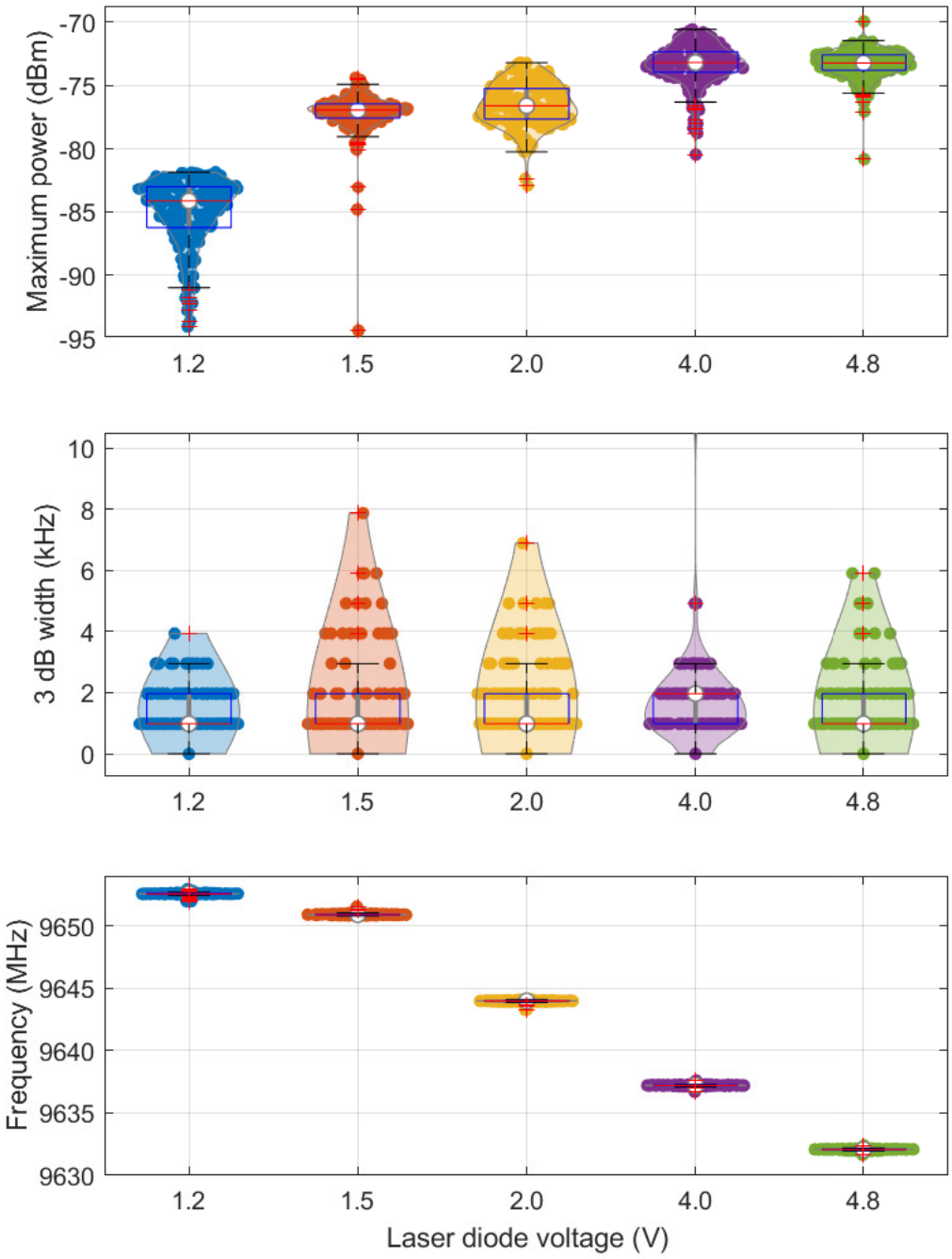


Figure 6.7: The distribution of (a) the maximum power, (b) the 3 dB width and (c) the frequency of data taken from the traces of the D09 sample using the GMW electromagnet with various optical pump powers.

Optical power (V)	Maximum power (dBm)	Frequency (MHz)	3 dB width (kHz)
1.2	-85.0567 ± 2.7721	9652.563 ± 0.1904	1.4 ± 0.77
1.5	-77.2159 ± 1.9748	9650.939 ± 0.072	1.6 ± 1.5
2.0	-76.9404 ± 2.7128	9643.960 ± 0.102	1.7 ± 1.1
4.0	-73.0751 ± 1.4568	9637.215 ± 0.071	1.7 ± 2.0
4.8	-73.4077± 1.4499	9632.050 ± 0.069	1.4 ± 1.1

Table 6.2: A summary of maser performance of NID_{02} sample in the Bruker electromagnet.

6.2 Conclusion

This chapter presents the maser results on both the Bruker system and the GMW system. A quantitative comparison is performed on the D09 sample on the two systems and the Bruker system using the D09 sample and the NID_{02} sample. The expectation is that the Bruker system will be more stable than the GMW system due to the higher stability of the electromagnet, the lower cavity loss and the slightly longer excitation wavelength at 532 nm. The result is that at 520 nm, the charge conversion rate from NV^- to NV^0 might be higher [106], in addition, the N^+ dopant will assist the charge conversion at a shorter wavelength, like 520 nm and 532 nm [136]. From the experimental results, the jitters are more in the GMW system as expected, but the maser signal is higher in the GMW system. The maser optical power threshold is below 1.2 V, and the maser chaotic threshold is at about 1.5 V.

Interestingly, by observing the jitter and the frequency shift, the temporal magnetic field stability can be estimated to be 5 μT which corresponds to a 140 kHz shift. This result provides an important hint on the field homogeneity requirement, as the teslameter is limited to around 20μT during the field characterisation. This gives a hint about the homogeneity requirement of a maser. Further experiments, such as reducing the homogeneity of the electromagnet by applying a gradient field, might need to be conducted to find the threshold homogeneity. The standard deviation of the frequency of the maser signal is below 10 kHz in the Bruker electromagnet, whereas it is around 100 kHz in the GMW electromagnet. The standard deviation in the maximum power of the maser signal is comparable, but the Bruker electromagnet is slightly lower than the GMW electromagnet. The standard deviation in the maximum power is smaller at higher optical excitation. Despite the fact that the GMW electromagnet is less stable, the D09 sample has a higher masing power in the GMW electromagnet than the Bruker electromagnet. There are a few reasons. The 520 nm laser might be better than the 532 nm under the same power. The alignment and the coupling of the Bruker electromagnet are difference, as the width of the maser peak is broader than the GMW electromagnet [178] and the coupling is in favour of higher power in the GMW electromagnet. It is believed that the maser is best to operate at the start of the saturation regime so that there is not much gain in masing power and energy waste when getting a higher power. Furthermore, the maximum power is more stable at the saturation regime. The linear and saturation regime is also shown in the maser simulations in Chapter 5, Figure 5.9 which shows a saturation above 800 mW.

Chapter 7

Conclusion

7.1 Summary of Thesis Achievements

The main goal of this work is to characterise diamond samples for masing and test the performance of the maser based on the diamond samples. This thesis applied various optical characterisation techniques, using a home-built confocal microscope, to study the samples, including fluorescence lifetime, spin-lattice relaxation, and spin-spin relaxation time map of the diamond samples to reveal the features of the diamonds. CW and Pulsed ODMR are constructed to study the spin dynamics and the internal stress of the diamonds. The confocal microscope is equipped with a continuous wavelength excitation source and detectors. With this powerful microscope, the important features of the diamonds for maser are identified.

The fluorescence lifetime imaging was applied to the diamond samples that identify the fluorescent defects to be NV^- and NV^0. The relative proportion of the defects is quantified and it is comparable to the EPR method. There are four methods are applied to the fluorescence lifetime imaging data. The least-square method is used as a conventional method. There are two methods based on the phasor transform, the first one is the global binning method, where all pixels follow the same distribution, this method shows some discrepancy with the least-square method. The second method is the random search method based on the blind determination. The blind determination method has a different model for a different number of lifetime components.

Lastly, this thesis introduces a deep learning model for fluorescence lifetime imaging of diamonds. To the best knowledge of the author, this is the first time to implement deep learning in fluorescence lifetime imaging in diamond and with multiple defects. This method successfully reconstructs fluorescence lifetime imaging of the samples that have a higher contrast than the other method. In addition, this method does not require any fitting and predetermined assumptions or models. As the deep learning model is trained with many defects and can determine which defect might be present. Spin-lattice relaxation time imaging of the diamond samples shows the T_1 relaxation time and its distribution. This shows that the NID_{02} used for masing has a longer relaxation time than the 10BB sample, which failed to mase. The ODMR provides a more complimentary picture of the optical characterisation, by showing the split between the two dips, which gives information about the lattice strain.

An extended rate-equation model is simulated and predicts the threshold of the maser which is verified by experiments. The model predicts the threshold Q factor, the threshold optical excitation power, the threshold filling factor and the threshold mode volume. In addition, the model also plots the map of the Q factor and the optical excitation power to show the region of no-masing, incipient-masing and the masing regimes. This extended rate-equation model is specifically used for NV centre maser, but the level and the rates can be redesigned for different defects that might achieve masing, such as the SiV defects in SiC.

Masers were built and tested using different magnetic field sources, from an EPR electromagnet to a small bench-top electromagnet, and different samples. The results show that only the NID_{02} and the D09 samples mase, the 10BB and the 10BA do not mase. The thesis also shows that both the EPR electromagnet and the GMW electromagnet can support the magnetic field for a maser. However, the GMW electromagnet has a higher threshold, which can be the result of low field homogeneity and stability.

Magnetic field mapping is performed to characterise the magnetic field of the GMW electromagnet, the commercial Halbach array and the in-house-built Halbach array. The mappings show that the GMW electromagnet has the highest homogeneity, having a teslameter-limited homogeneity of 46 ppm. As the field difference is similar to the field reading fluctuation in zero-field and stationary. The commercial Halbach array has a field of 345 mT and a homogeneity of 870 ppm. The DIY Halhbach, which is only to verify the simulation, has the lowest field at around 97.4 mT and homogeneity at 7187 ppm. To design a high-performance Halbach array

that satisfies the high field and high homogeneity, this thesis develops a PSO-based algorithm to simulate the 3D field profile of Halbach arrays. The algorithm finds a new optimised and adaptive structure that has a higher homogeneity than the conventional Halbach arrays and the teslameter-limited homogeneity.

If a Halbach array with a constant field is used and no temporal instability, the spatial field inhomogeneity should be smaller than 23 μT so that the change in the Zeeman shift is within the linewidth of the resonator. The corresponding field homogeneity is 53 ppm. It is known that the teslameter-limited homogeneity of the GMW electromagnet of 46 ppm can mase.

The major issue is the construction of such a Halbach array, as it might suffer from mechanical tolerance and more optimisations are required to assist in building the optimal designs in reality. The application of such a Halbach array is not limited to masers but can be used in magnetic resonance imaging and silicon-based quantum computing.

7.2 Future Work

Modelling chaotic masers and extended rate equations

For the simulations work, the author plans to add in more temperature-dependent effects, such as temperature-dependent T_1, from literature or experimental results. The extended rate equation model will be used as an amplifier instead of oscillator in this thesis. The extended rate equations can be modified and applied to different defects such as the silicon vacancies in SiC, which is a potential masing gain medium.

The chaotic dynamics are another interesting and crucial part of Maser. Future work will explore the theory and simulation of the chaotic dynamics, using chaotic models such as the Lorenz model, Vallis model, Chua's model, Rossler model and Rikitaki model [179] [180], that might agree with the experimental results. The model can be applied to a simple 2-level or 3-level maser model before extent it to multiple levels to represent the full NV centre.

Permanent magnet-based diamond masers

Future work will include validation of new optimised Halbach array, such as using different strength, different geometrical shapes and different structures with the aid of the optimisation.

Apart from the experiments with the Halbach system, there will be further work in the coding architecture, as the current code, utilises the vector extension support on CPUs in the magnetic field codes. Further improvement will be to ultilises GPUs parallel architecture, such as the tensor architecture and CUDA, to improve the efficiency of the codes. The demagnetisation method is grid meshing, which is not resource-efficient, adaptive meshing will be developed to ease the high memeory usage.

Diamond masers based on various dielectric resonantors

For the maser, future work will be on designing and operating the maser at a different frequency such as around 5 GHz for quantum computing applications. Furthermore, the discovery of alternative dielectric materials, such as BMT, for the resonator will be carried on. A high dielectric constant can decrease the size of the resonator and the mode volume, which might be beneficial to maser application. From the CST calculation, the LaAlO3, BMT, and BZT all have similar cooperativity as sapphire, rutile has only half of the cooperativity at 5.8, which might be unfavourable at masing.

Noise characterisation of diamond masers

Noise figure characteristics of masers are a critical feature that determines the performance of masers and it is a critical step to do so that the maser systems are well-understood before being applied to communication and other practical applications. When a maser is used as an amplifier, it will not only amplify the signal but also add extra noise. The noise figure is defined as the ratio of the signal-to-noise ratio at the input to the sign-to-noise ratio at the output, where the input noise is assumed to be at 290 K [181][182]. In the context of a low noise amplifier, the noise temperature is used. The noise temperature is defined as the temperature at which an ideal device will generate an equivalent noise power. For two-port masers, the noise characteristics can be modeled using four noise parameters, namely the mean

square fluctuations of the noisy voltage, the noisy current and the complex correlation between the noisy voltage and the noisy current and the corresponding minimum noise figure,F_{min}, and the optimised reflection coefficient, Γ_{opt},[183] [184].

Further work will focus on the noise figure measurement of masers based on different dielectric resonators. For example, the Y-factor technique, which is a conventional method for measuring the noise temperature for amplifiers [185]. This technique requires two noise powers at different temperatures known as the cold source and the hot source, generated by commercial noise sources, such as avalanche diodes [186]. Normally, the cold source corresponds to room temperature and the hot source corresponds to additional noise added to it. An additional noise calibration step is performed to estimate the noise figure of the maser. Other noise charaterisation methods such as the cold-source method and CW-signal-generator method can also be applied [187] [188].

In addition to noise, distortion from non-linear effects is another important parameter that determines the performance of a maser. An example of distortion is higher harmonics generation at a multiple of the fundamental frequencies. Harmonics generation is more prominent at high input power. The power of the harmonics might exceed the fundamental harmonics at some high input powers, this effect is known as second-order intercept for the second harmonics. In some situations, the harmonics might get saturated and never reach the intercept. Intermodulation is another example of non-linear distortion in microwave systems, formed by the sum and the difference of different frequency components. This is potentially more important, as the resultant intermodulation might end up close to the fundamental harmonics. The third-order intermodulation is the interesting effect that might affect the maser performance, as the frequency might be similar to the fundamental harmonics. To characterise the third-order intermodulation, the third-order intercept point can be estimated for the diamond maser system. This can be done by measuring the output power and the input power of the signal of interest. In oscillator mode, the phase noise is an important factor that determines the stability of the oscillatory signal. This can be measured using a phase noise measurement device or using a spectrum analyzer that measures the power at deviated frequencies from the masing signal. Leeson model can used to characterise the phase noise of the maser oscillator [189]. Based on the model, the performance of the maser oscillator can be optimised. Lastly, the Allen deviation or modified Allen deviation is a key parameter that estimates the frequency

stability in masers over a period of time.

Diamond maser amplifiers

Amplifier stability analysis will be performed to study the stability of the maser operating as an amplifier or an oscillator such as the mu stability factor. In a maser system, spontaneous emission may get amplified and reflect between the maser and the input or output matching circuit, resulting in instability.

Application-wise, the masers can be wired up to amplify a test signal that carries digital information and compare the performance with conventional amplifiers. One of the applications of maser amplifiers is in Radio astronomy and transmon qubit readout, which is typically at 5 GHz, in superconducting quantum computers. The transmon readout usually consists of JPA, which is beside the quantum processor, and HEMTs at different temperatures. Maser amplifiers can be used to replace HEMTs at low temperatures or even at room temperature to test the overall performance. However, the current design requires high laser power to breach the threshold, the optical energy will generate heat in the dielectric resonator and the diamond, which will impact the efficiency of the dilution refrigerator and lower temperature stages.

Travelling wave diamond maser

Traveling wave (TW) maser is another maser architecture that has a significantly higher bandwidth than the cavity maser reported in this thesis. In order to construct a room-temperature diamond TW maser, an efficient slow-wave structure, such as metamaterials and spoof plasmonic structure [190], is employed that has a high microwave index and low loss. Diamond gain media are placed in the slow-wave structure to interact with the microwave and amplify the signal.

Silicon Carbide maser

Apart from diamond, masing using homotypic Silicon vacancies (V_{si}) in 6H and 4H SiC will be investigated, as well as the optical characterisation of the V_{si} [36] [37][191]. SiC is a common semiconductor used in the industry, and it is cheaper to make on a large scale. It is shown that

the ground state of V_{si} has S=3/2. The zero-field splitting is found to have a range between tens of MHz to over 1 GHz, which is smaller than the NV centres. This potentially requires less magnetic field to achieve population inversion.

Optically excitation, readout at room temperature and EPR are realised [192]. In particular, the negatively charged V2 defects in 4H SiC, which has a zero-filed splitting at 70 MHz, are a potential maser gain medium. Similar to NV centre, it can be optically polarised and with a sufficient magnetic field a population inversion is created between the -3/2 and the -1/2 sub-levels. The zero-phonon line is around 917 nm. Thus, the optical setup has to be extended and optimised for Near IR.

Optical characterisation setup and methods

In the optical setup, there are more ports that allow more laser to be integrated into the system. One of the additional lasers is the 457 nm laser for Raman imaging. Raman imaging provides vital information of the lattice structure of diamonds. The shift of the first-order Raman peak will provide information about the compressive and tensile force along the diamond lattice and local lattice orientation [193] [194]. This can work together with ODMR mapping and the T_1 mapping to understand the lattice structure and its interaction with NV centres that might impact the masers.

At last, the neural network model will be further extended to more defects and optimised for diamond and SiC by improving the hyperparameters and architecture of the model. A transformer based architecture can be used instead of the current model. The use of the quantum neural network architecture for the phasor analysis can also be improved by tuning the parameters and improving the architecture. The network can be implemented on the histogram and compared to the cluster classifier in this thesis. Further benchmarking and comparison with classical codes and quantum hardware implementation can be conducted.

Appendix A

Appendix

A.1

Hybrid quantum transfer learning for phasor analysis

From the previous section, the random search method is applied which is a robust way to find the lifetime components. However, the set of equations that the random search method has to find the solution is different for different numbers of lifetime components. Therefore, one has make an assumption of how many lifetime components should there be, or apply different blind determinations, with different lifetime components, and choose the one that has the least error, as from [133]. For example, given a fluorescence lifetime image, the bi-exponential, the tri-exponential, and so on, are used to find the solutions and select the one with the least error. This method has to solve the models with different lifetime components every time. Thus, this approach is time-consuming in determining the number of lifetime components. A new approach that will release the effort in solving multiple models for selecting the number of lifetime components is introduced in this chapter.

This assumption is also applied in the global binning methods, as a bi-exponential lifetime function can use linear regression to extract the lifetime components and other fitting methods for different numbers of lifetime components. The determination of the number of lifetime components becomes a critical part of lifetime analysis.

Here, in the phasor space, the points are arranged to a certain geometry distribution that

correlates to the number of lifetime components, such as linear with bi-exponential distribution and triangular with tri-exponent distribution. One of the solutions to this task is to adopt novel image classification algorithms in computer vision for phasor analysis. The task is to train a classifier with distributions from different numbers of lifetime components with noise. The classifier can predict the number of lifetimes from the collected phasor plots.

One of the most important advantages of using this method is to predict unseen data, which might have a different amount of noise or lifetimes that result in changing shape and rotation of the points in the phasor space.

The training data is generated from a bi-exponential and a tri-exponential function, with Poisson noise, which mimics the experimental data and transformed to the phasor space. The model is constructed and trained using Pytorch 2.1 and with the Resnet18 architecture. The model is retrained for the purpose of phasor analysis. The author introduces quantum layers as the last layers of the classifier. This classical-quantum classifier takes advantage of the parallel architecture of quantum circuits [195]. The classifier can be trained on a quantum simulator or on quantum hardware. This method demonstrates the novel application of quantum algorithms in data analysis for fluorescence lifetime imaging and the field of diamond research. The quantum layers used are Hadamard layers for singlet qubits, RY layers for single qubits and entangling layers that apply a Hadamard gate to every two qubits. Figure A.1 shows the architecture of this hybrid classifier. Lifetime data with various decay times and components are transformed into the phasor data. A generic classical network is used to learn the data structure of the phasor diagrams. A specific network that consists of a trainable quantum layer is tuned to predict the results from diamond defects such as NV centres.

Below, the classifier successfully predicts the class of the experimental data of the D09 sample at 532 nm excitation. Even the trained data has more noise that looks more spread and shorter along the line, and the orientation is different. In Figure A.2, the four subplots are randomly selected images of the phasor data, which is labeled by either bi or tri for two exponential components or three exponential components, from the training set. Figure A.3 shows the predicted result of the experimental data from the NID_{02}, D09, 10BA and 10BB samples.

In conclusion, hybrid quantum transfer learning has been correctly predicting classes from two lifetime components and three lifetime components in the test and validation dataset. The accuracy of the test is 99.62 %. The classifier predicts the class for the diamond samples that

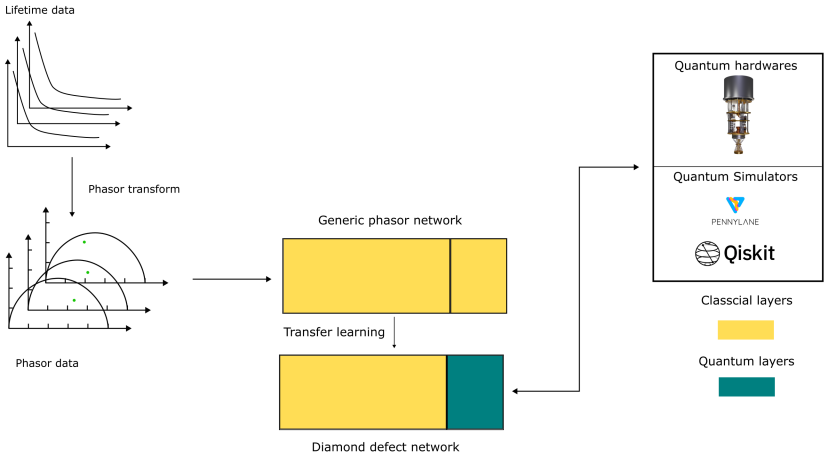


Figure A.1: The architecture of the hybrid classical-quantum classifier for phasor analysis. The knowledge of the generic phasor network can be transferred to a diamond defect network containing a trainable quantum layer at the end to predict the results. The generic phasor network has the knowledge of various lifetime components, whereas the diamond defects network only have the knowledge of the lifetime components specific to the diamond.

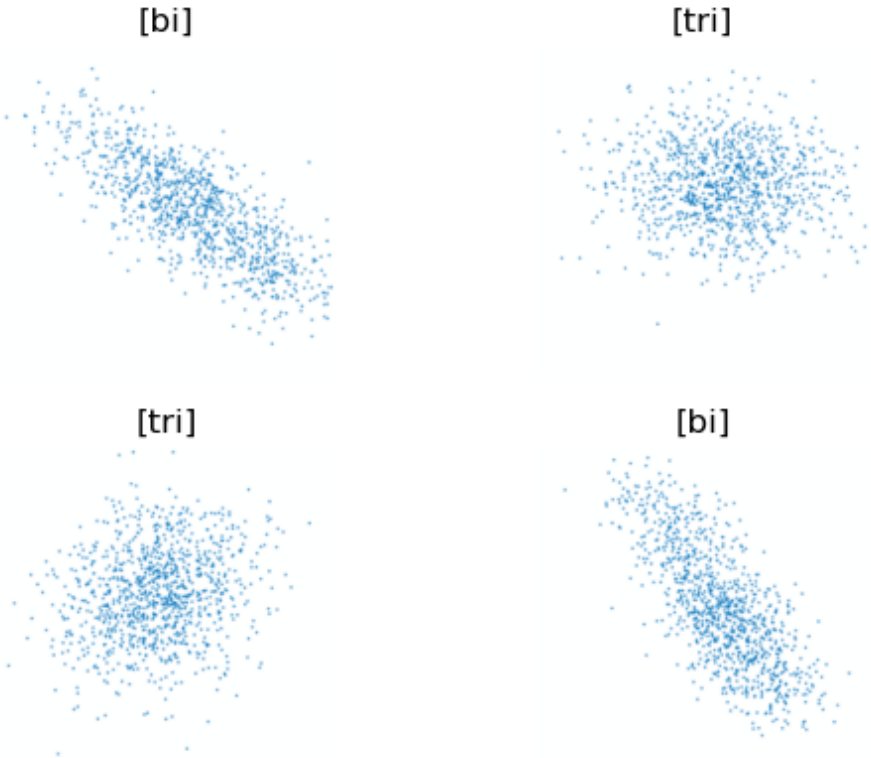
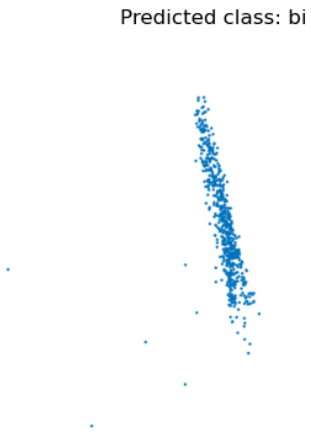


Figure A.2: The image shows the generated data from bi-exponential and tri-exponential functions with labels.



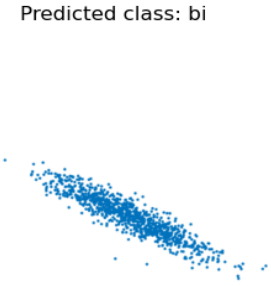
(a) NID_{02}



(b) D09



(c) 10BA



(d) 10BB

Figure A.3: (a) The image shows the predicted class for the NID_{02} diamond sample under 532 nm excitation. (b) The image shows the predicted class for the D09 diamond sample under 532 nm excitation. (c) The image shows the predicted class for the 10BA diamond sample under 532 nm excitation. (d) The image shows the predicted class for the 10BB diamond sample under 532 nm excitation.

agrees with the global binning and the random search results.

A.2

Fluorescence lifetime results

The figure has six subplots that show the integrated decay intensity that represents the total fluorescence intensity, the lifetime of the components, τ_1 and τ_2, the chi-square, χ^2, and the amplitudes of the two components, A_1 and A_2.

The set of results investigates the fluorescence mapping of the 10BA sample, shown in Figure A.4, Figure A.5 and Figure A.6. The resolution is 50 μm and the exposure time is 9 s. The excitation wavelengths are 532 nm, 502 nm and 562 nm. At 532 nm, the mean values of the fitting are τ_1 is 9.69 $\pm$ 0.02 ns, τ_2 is 18.50 $\pm$ 0.02 ns, A_1 is 314.08 $\pm$ 1.94 and A_2 is 521.92 $\pm$ 1.95. The mean reduced chi-square is 1.17. The standard deviation of τ_1 is 1.12 ns, τ_2 is 0.83 ns, A_1 is 72.66 and A_2 is 82.89. The noticeable difference is that the 10BA has a lower fluorescence intensity, even with a slightly longer exposure time, which is due to the lower NV concentration. The pixel level standard deviations of the lifetimes and the amplitudes are 0.93 ns, 0.99 ns, 79 and 80.

At 502 nm, the mean values of the fitting are τ_1 is 9.78 $\pm$ 0.03 ns, τ_2 is 19.07 $\pm$ 0.02 ns, A_1 is 76.2 $\pm$ 0.69 and A_2 is 222.8 $\pm$ 0.69 ns. The mean reduced chi-square is 1.07. The standard deviation of τ_1 is 1.29 ns, τ_2 is 0.55 ns, A_1 is 18.27 and A_2 is 25.14. The pixel level standard deviations of the lifetimes and the amplitudes are 1.64 ns, 0.93 ns, 32.01 and 32.45.

At 562 nm, the mean values of the fitting are τ_1 is 9.83 $\pm$ 0.02 ns, τ_2 is 17.37 $\pm$ 0.04 ns, A_1 is 445.47 $\pm$ 2.38 and A_2 is 321.83 $\pm$ 2.40 ns. The mean reduced chi-square is 1.17. The standard deviation of τ_1 is 0.91 ns, τ_2 is 1.09 ns, A_1 is 86.89 and A_2 is 91.48. The pixel level standard deviations of the lifetimes and the amplitudes are 0.80 ns, 1.75 ns, 105.08 and 105.81.

Similarly, the results of the sample 10BB are shown in Figure A.7, Figure A.8, Figure A.9, with excitation wavelengths of 532 nm, 482 nm and 592 nm. At 532 nm, the mean values of the fitting are τ_1 is 9.82 $\pm$ 0.01 ns, τ_2 is 17.77 $\pm$ 0.03 ns, A_1 is 141.97 $\pm$ 0.56 and A_2 is 151.62 $\pm$ 0.56. The mean reduced chi-square is 0.97. The standard deviation of τ_1 is 1.45 ns, τ_2 is 1.71

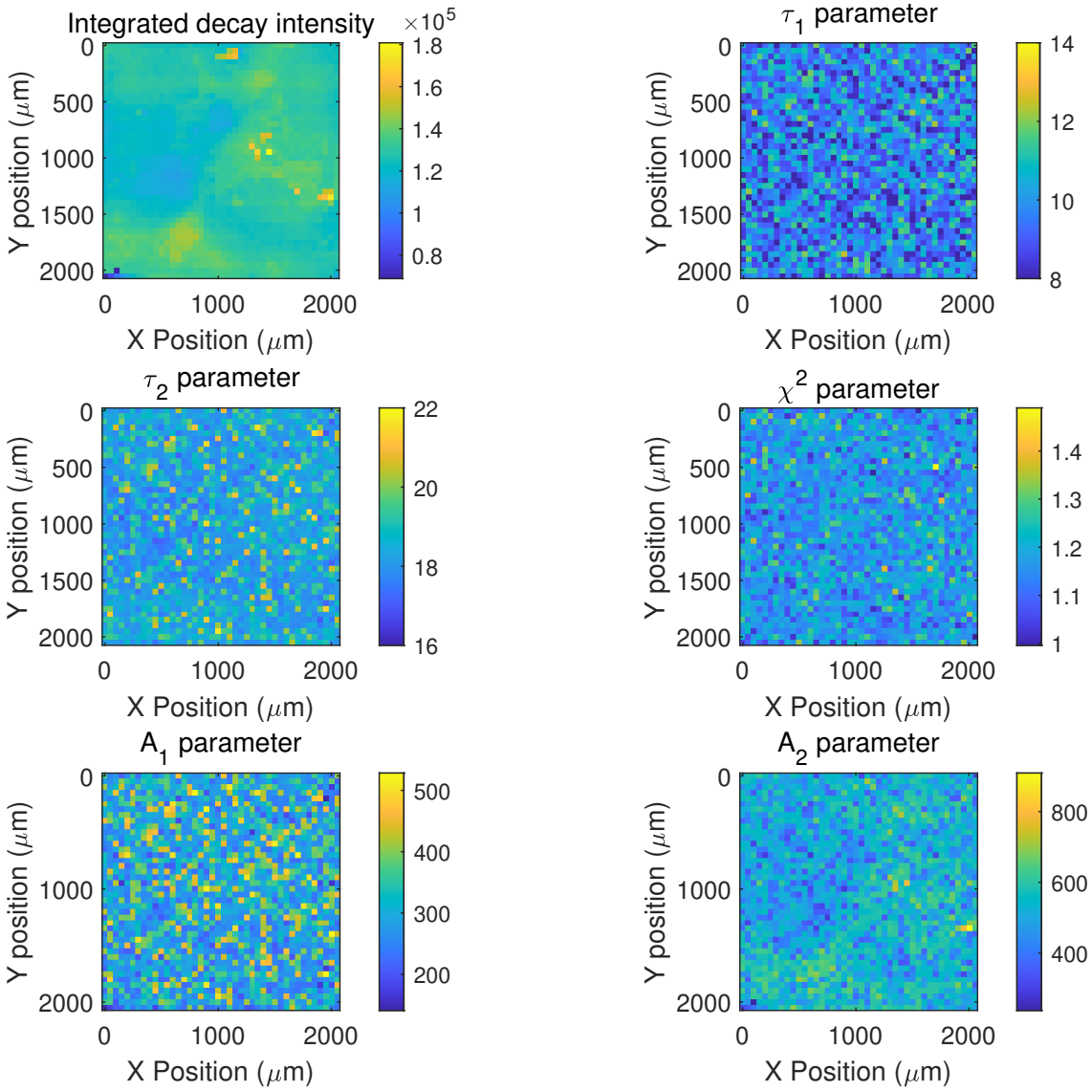


Figure A.4: The fluorescence lifetime mapping using the least square method to analyse the sample 10BA at 532 nm excitation. The subfigures show the integrated decay intensity which is the fluorescence mapping. The first and the second lifetime components, τ_1 and τ_2, and the reduced χ^2 mapping and the amplitude, A_1 and A_2, of the first and the second components respectively.

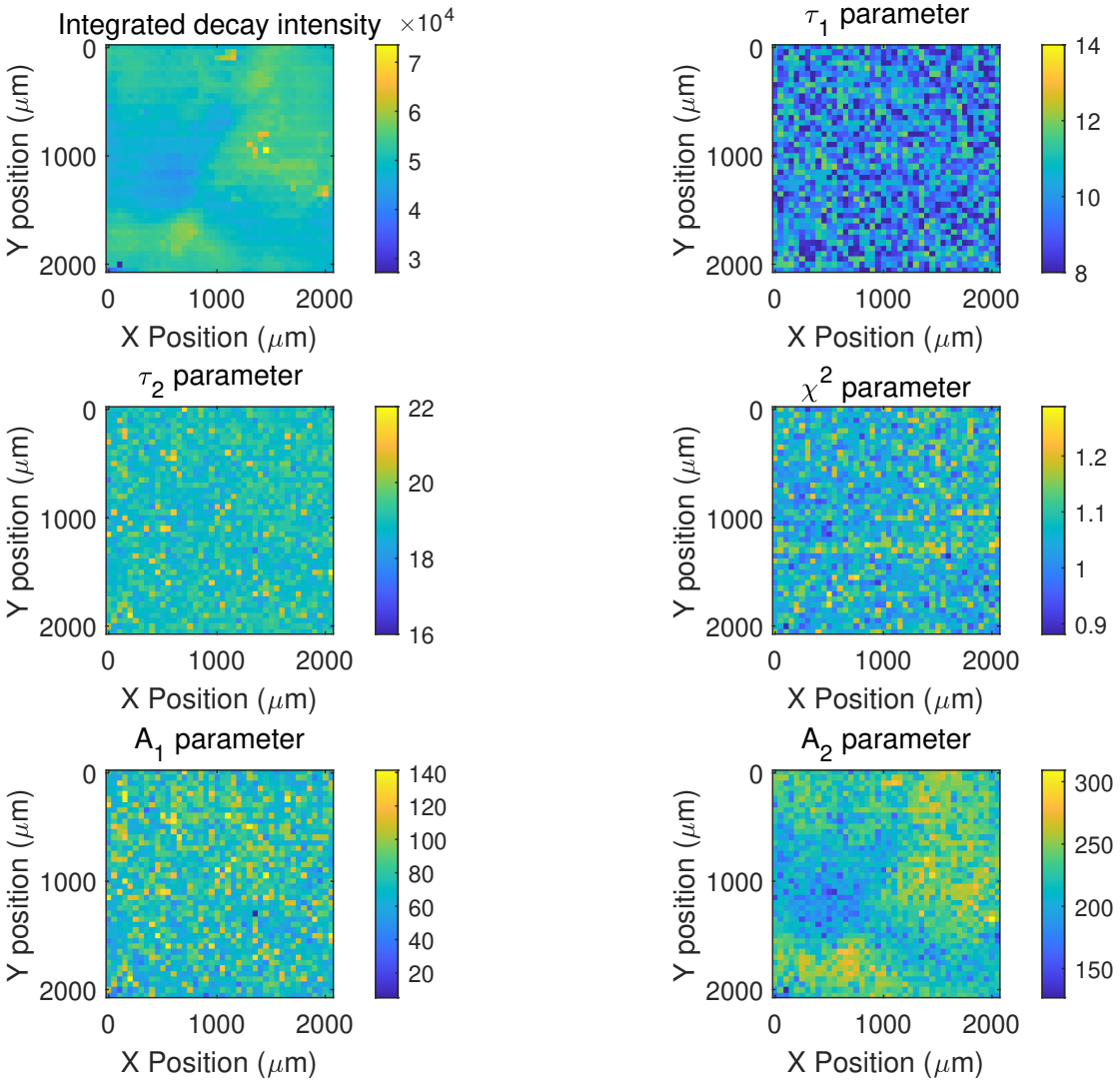


Figure A.5: The fluorescence lifetime mapping using the least square method to analyse the sample 10BA at 502 nm excitation. The subfigures show the integrated decay intensity which is the fluorescence mapping. The first and the second lifetime components, τ_1 and τ_2, and the reduced χ^2 mapping and the amplitude, A_1 and A_2, of the first and the second components respectively.

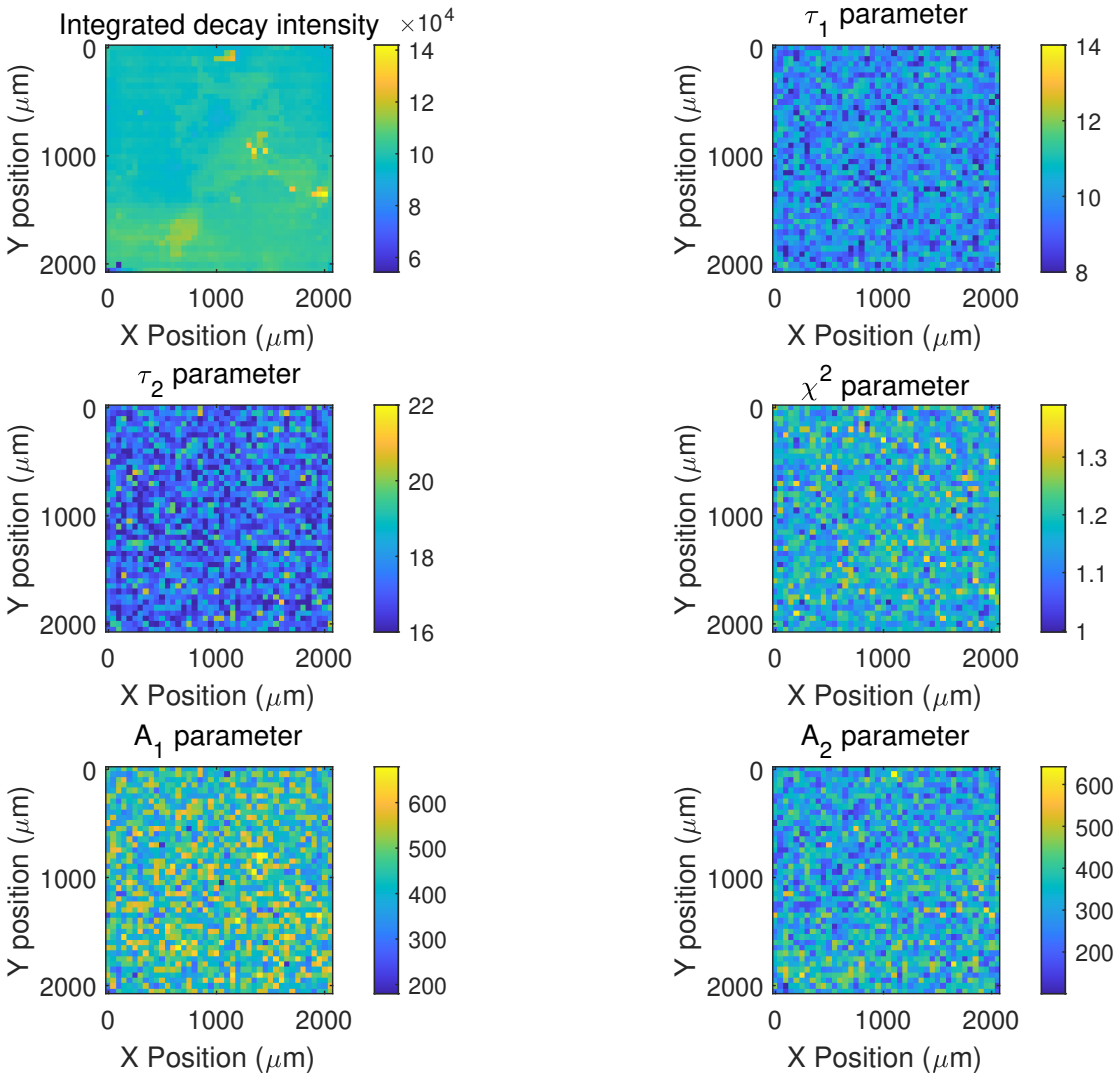


Figure A.6: The fluorescence lifetime mapping using the least square method to analyse the sample 10BA at 562 nm excitation. The subfigures show the integrated decay intensity which is the fluorescence mapping. The first and the second lifetime components, τ_1 and τ_2, and the reduced χ^2 mapping and the amplitude, A_1 and A_2, of the first and the second components respectively.

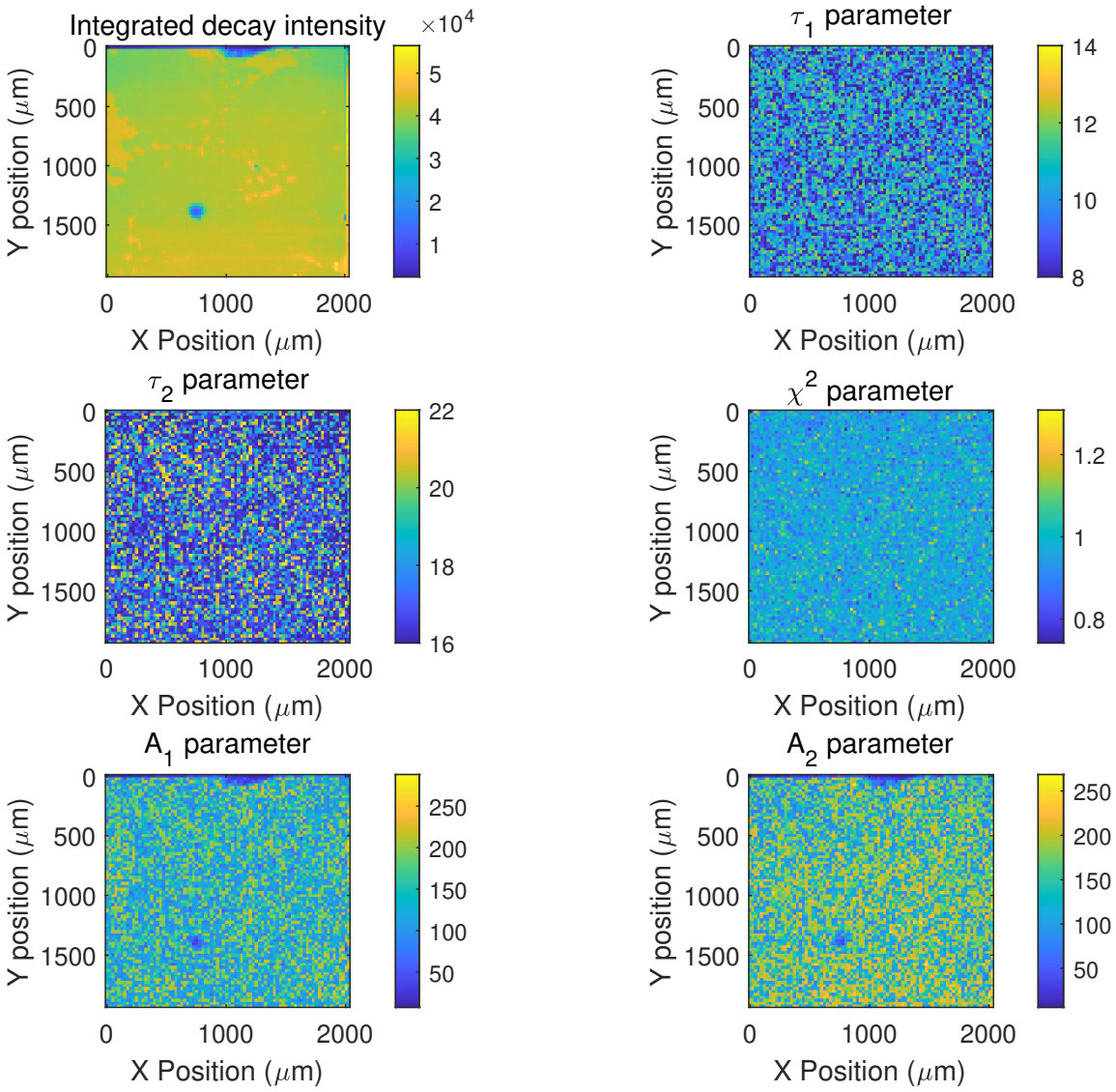


Figure A.7: The fluorescence lifetime mapping using the least square method to analyse the sample 10BB at 532 nm excitation. The subfigures show the integrated decay intensity which is the fluorescence mapping. The first and the second lifetime components, τ_1 and τ_2, and the reduced χ^2 mapping and the amplitude, A_1 and A_2, of the first and the second components respectively.

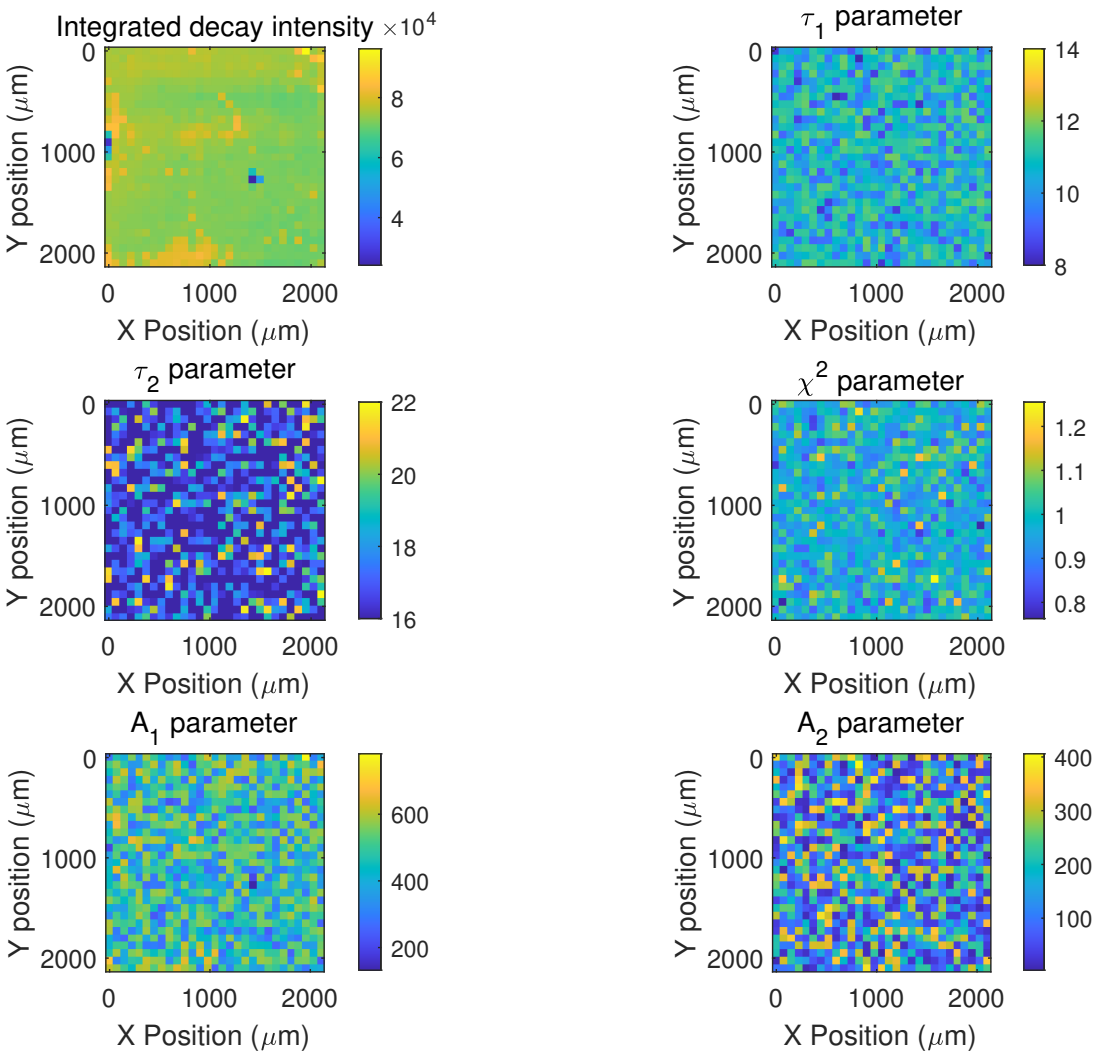


Figure A.8: The fluorescence lifetime mapping using the least square method to analyse the sample 10BB at 592 nm excitation. The subfigures show the integrated decay intensity which is the fluorescence mapping. The first and the second lifetime components, τ_1 and τ_2, and the reduced χ^2 mapping and the amplitude, A_1 and A_2, of the first and the second components respectively.

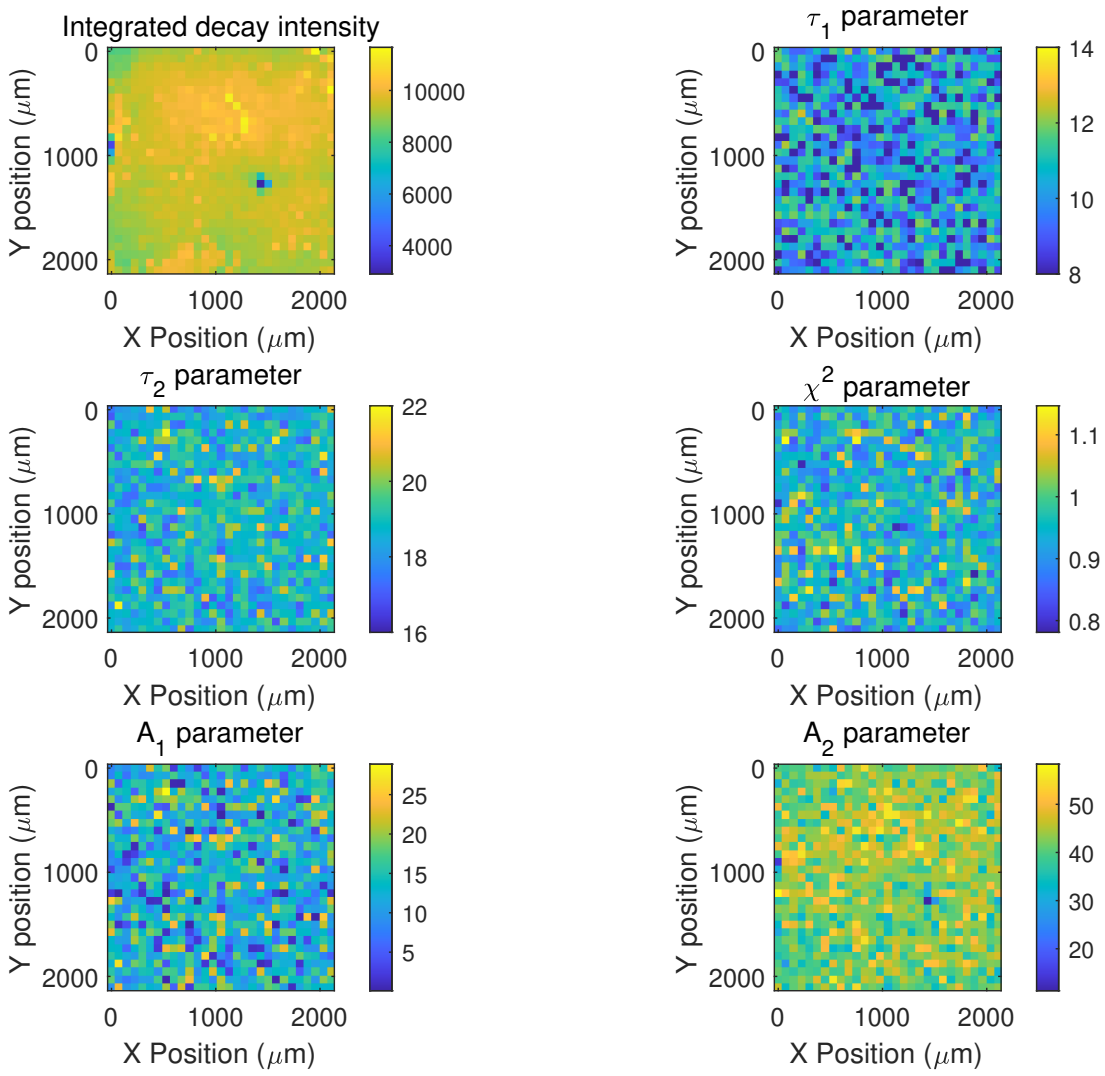


Figure A.9: The fluorescence lifetime mapping using the least square method to analyse the sample 10BB at 482 nm excitation. The subfigures show the integrated decay intensity which is the fluorescence mapping. The first and the second lifetime components, τ_1 and τ_2, and the reduced χ^2 mapping and the amplitude, A_1 and A_2, of the first and the second components respectively.

ns, A_1 is 46.21 and A_2 is 48.16. The pixel level standard deviations of the lifetimes and the amplitudes are 1.13 ns, 1.69 ns, 43.23 and 43.76.

At 592 nm, the mean values of the fitting are τ_1 is 10.67 ± 0.012 ns, τ_2 is 16.62 ± 0.076 ns, A_1 is 459.44 ± 2.27 and A_2 is 158.77 ± 2.28. The mean reduced chi-square is 0.98. The standard deviation of τ_1 is 0.87 ns, τ_2 is 2.15 ns, A_1 is 110.54 and A_2 is 110.71. The pixel level standard deviations of the lifetimes and the amplitudes are 0.31 ns, 1.86 ns, 59.9 and 60.21.

At 482 nm, the mean values of the fitting are τ_1 is 9.99 ± 0.05 ns, τ_2 is 18.80 ± 0.04 ns, A_1 is 12.78 ± 0.20 and A_2 is 43.01 ± 0.19. The mean reduced chi-square is 0.95. The standard deviation of τ_1 is 1.48 ns, τ_2 is 0.87 ns, A_1 is 5.50 and A_2 is 5.42. The pixel level standard deviations of the lifetimes and the amplitudes are 2.04 ns, 1.14 ns, 6.86 and 6.72. The 10BB sample has more NV^- contribution at a longer wavelength and more NV^0 contribution at a shorter wavelength relative to 532 nm.

For the NID_{02} sample, the results are shown in Figure A.10, Figure A.11 and Figure A.12. At 532 nm, the mean values of the fitting are τ_1 is 9.81 ± 0.04 ns, τ_2 is 18.94 ± 0.02 ns, A_1 is 58.65 ± 0.63 and A_2 is 208.57 ± 0.63 The mean reduced chi-square is 1.03. The standard deviation of τ_1 is 1.58 ns, τ_2 is 0.57 ns, A_1 is 21.45 and A_2 is 42.23. The pixel level standard deviations of the lifetimes and the amplitudes are 1.65 ns, 0.80 ns, 26.58 and 26.82.

At 562 nm, the mean values of the fitting are τ_1 is 9.82 ± 0.030 ns, τ_2 is 18.10 ± 0.049 ns, A_1 is 112.6 ± 0.99 and A_2 is 143.99 ± 0.99. The mean reduced chi-square is 0.98. The standard deviation of τ_1 is 1.47 ns, τ_2 is 1.35 ns, A_1 is 39.17 and A_2 is 43.12. The pixel level standard deviations of the lifetimes and the amplitudes are 1.27 ns, 1.58 ns, 37.25 and 37.76. At 502 nm, the mean values of the fitting are τ_1 is 9.56 ± 0.038 ns, τ_2 is 19.17 ns ± 0.012, A_1 is 11.99 ± 0.138 and A_2 is 104.31 ± 0.135. The mean reduced chi-square is 1.00. The standard deviation of τ_1 is 0.58 ns, τ_2 is 1.77 ns, A_1 is 8.82 and A_2 is 20.62. The pixel level standard deviations of the lifetimes and the amplitudes are 1.96 ns, 0.46 ns, 6.22 and 6.24.

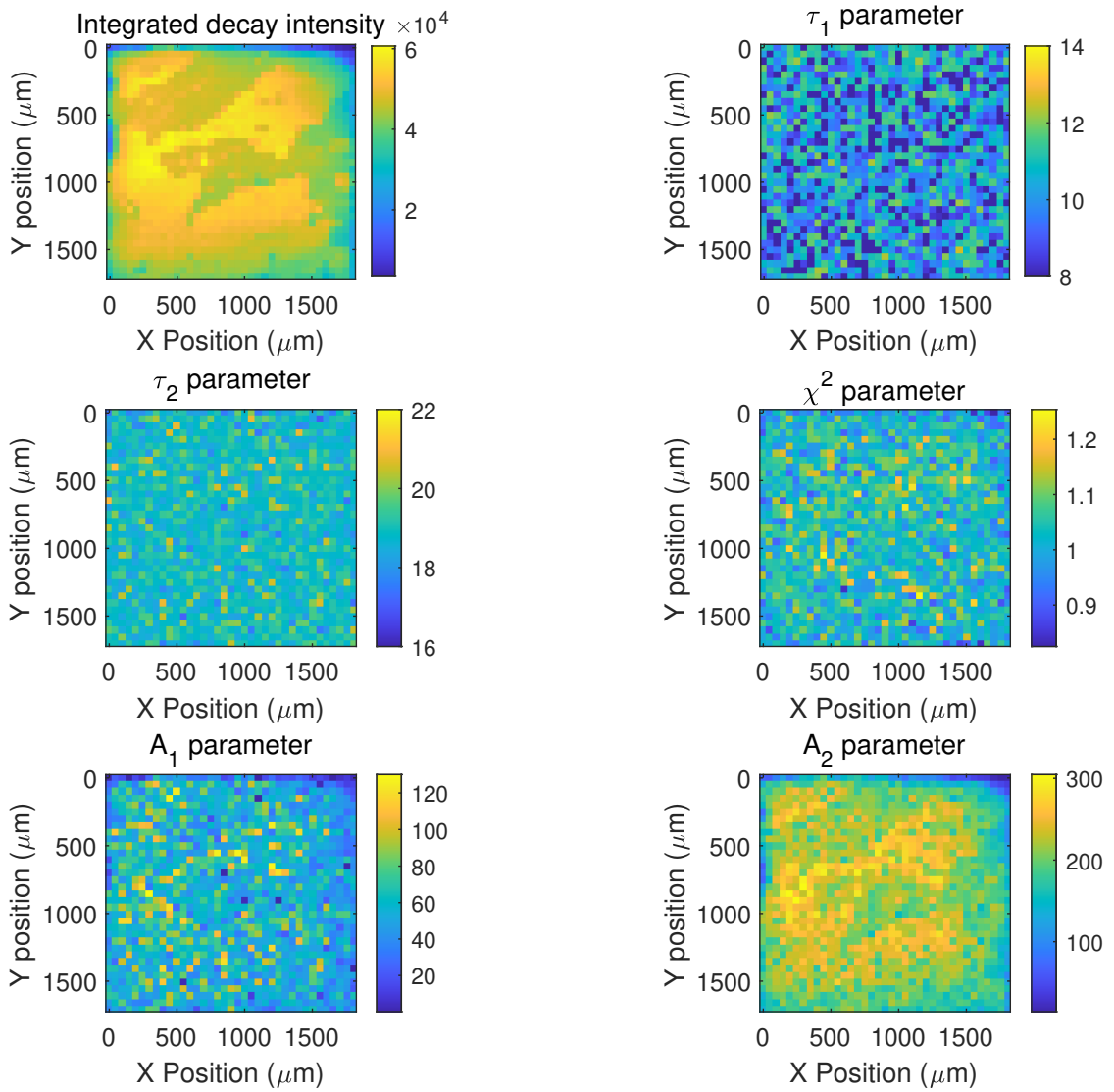


Figure A.10: The fluorescence lifetime mapping using the least square method to analyse the sample NID_{02} at 532 nm excitation. The subfigures show the integrated decay intensity which is the fluorescence mapping. The first and the second lifetime components, τ_1 and τ_2, and the reduced χ^2 mapping and the amplitude, A_1 and A_2, of the first and the second components respectively.

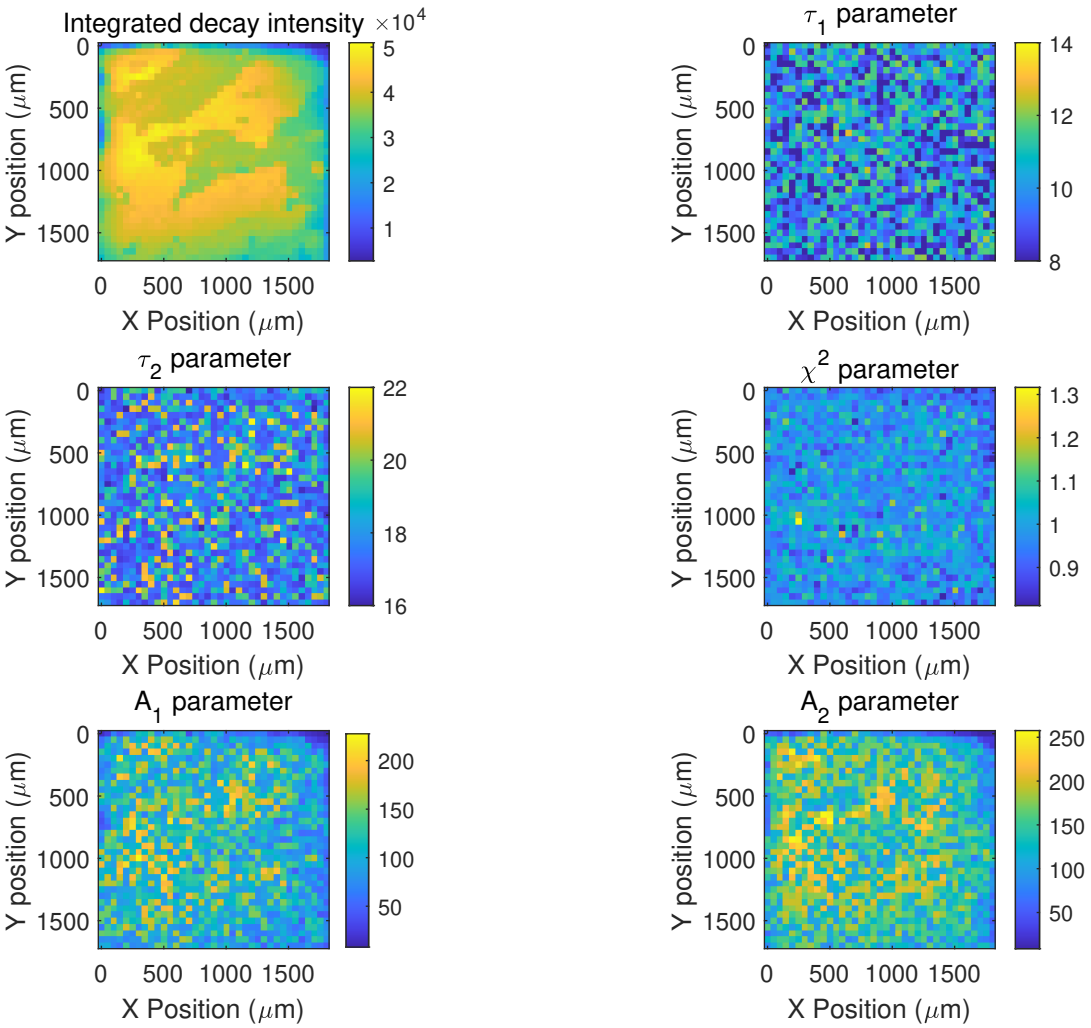


Figure A.11: The fluorescence lifetime mapping using the least square method to analyse the sample NID_{02} at 562 nm excitation. The subfigures show the integrated decay intensity which is the fluorescence mapping. The first and the second lifetime components, τ_1 and τ_2, and the reduced χ^2 mapping and the amplitude, A_1 and A_2, of the first and the second components respectively.

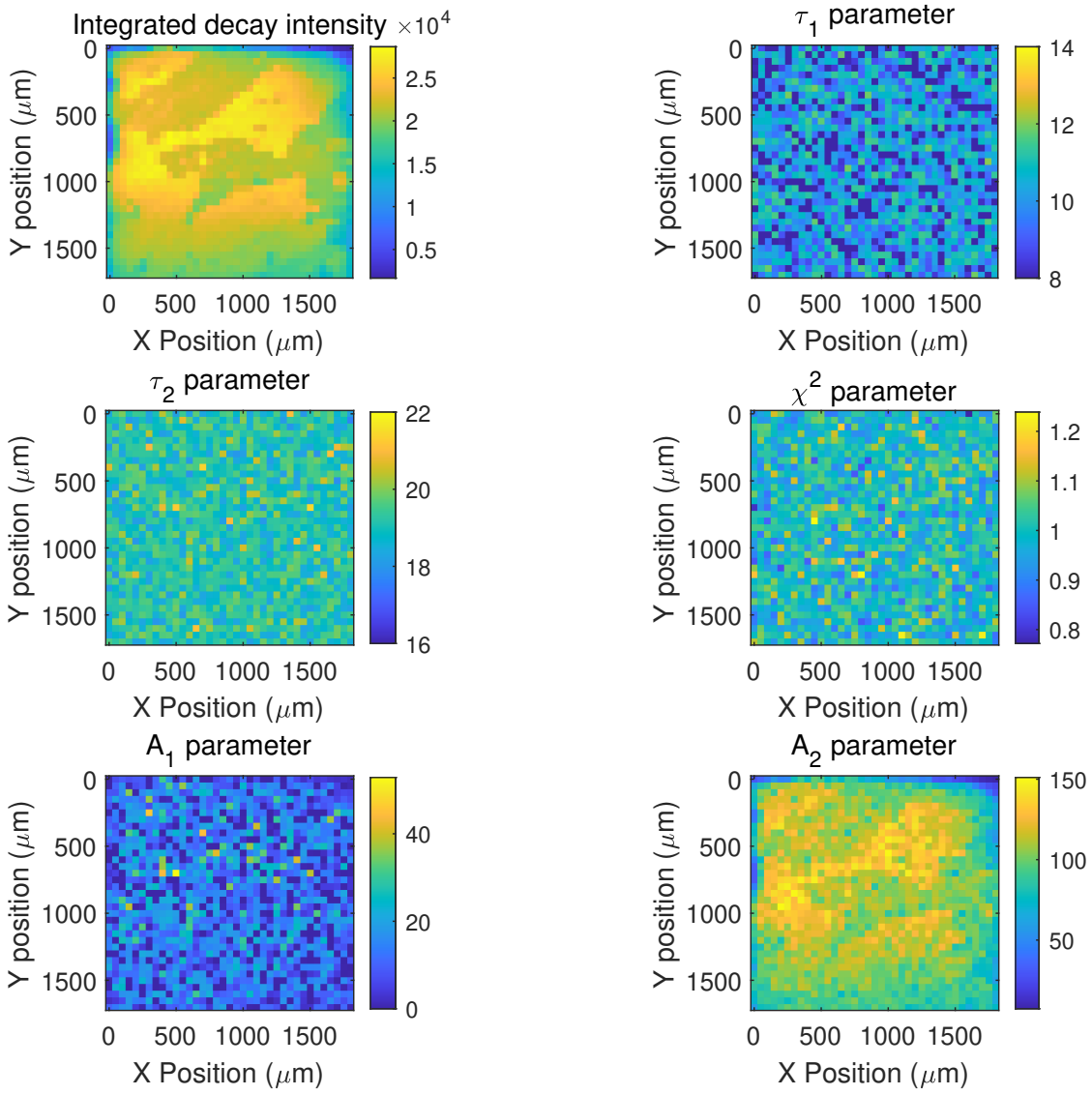
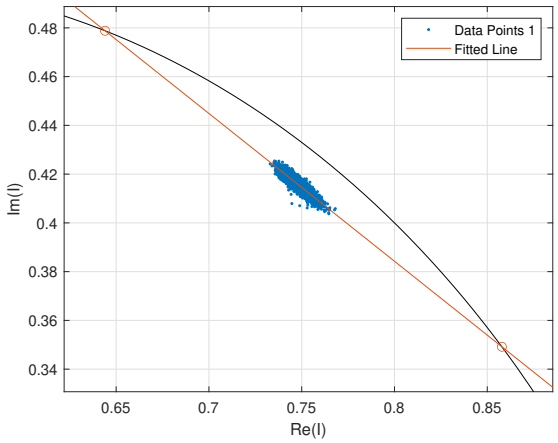
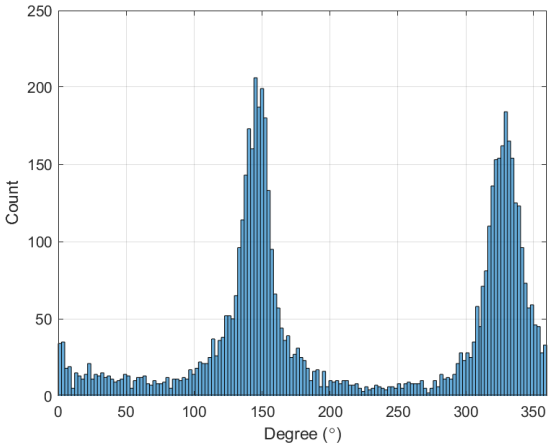


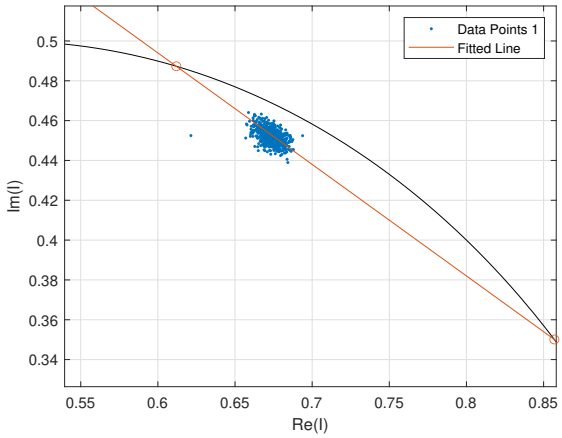
Figure A.12: The fluorescence lifetime mapping using the least square method to analyse the sample NID_{02} at 502 nm excitation. The subfigures show the integrated decay intensity which is the fluorescence mapping. The first and the second lifetime components, τ_1 and τ_2, and the reduced χ^2 mapping and the amplitude, A_1 and A_2, of the first and the second components respectively.



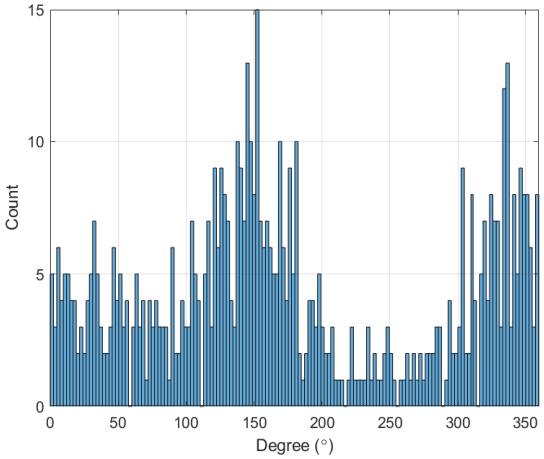
(a) 532 nm



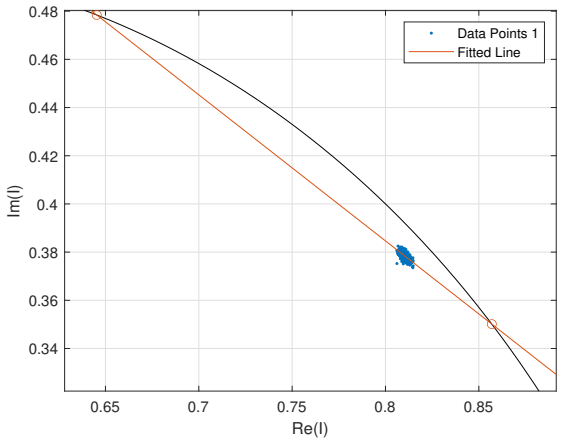
(b) 532 nm



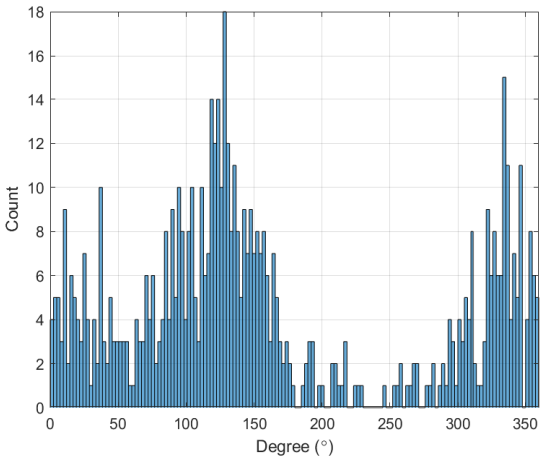
(c) 482 nm



(d) 482 nm



(e) 572 nm



(f) 572 nm

Figure A.13: The phasor diagram of the 10BB sample, (a) for 532 nm, (c) for 482 nm, (e) for 572 nm and the angular histograms of the 10BB sample (b) for the 532 nm, (d) for the 482 nm and (f) for the 572 nm.

A.3

Phasor analysis

Figure A.13 (a) and (b) show the phasor plot and the angular histogram of the sample 10BB using a 532 nm excitation. The results are similar to the 10BA as expected. The shorter lifetime is about 10.80 ns and the longer lifetime is 19.72 ns. The square of the residual is 0.0014. The relative proportion is about 44.9 %.

At the 482 nm excitation, Figure A.13 (c) and (d) display the phasor plot and the angular histogram. The shorter lifetime measures about 10.84 ns, while the longer one is 21.12 ns. The residual's square is 0.0039, and the relative proportion is approximately 24.1%.

At the 572 nm excitation, Figure A.13 (e) and (f) display the phasor plot and the angular histogram. The shorter lifetime measures about 10.84 ns, while the longer one is 19.66 ns. The residual's square is 0.0011, and the relative proportion is approximately 77.8%.

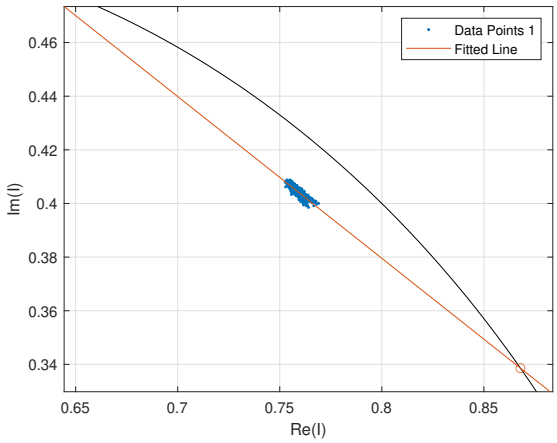
Figure A.14 (a) and (b) show the phasor plot and the angular histogram of the sample D09 using a 532 nm excitation. The shorter lifetime is about 10.35 ns and the longer lifetime is 20.42 ns. The square of the residual is 0.0009. The relative proportion is about 55.0 %.

At the 502 nm excitation, Figure A.14 (c) and (d) display the phasor plot and the angular histogram. The shorter lifetime measures about 9.86 ns, while the longer one is 19.53 ns. The residual's square is 0.0009, and the relative proportion is approximately 33.5%.

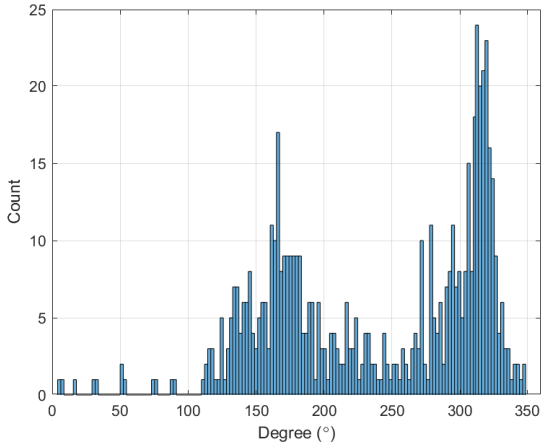
At the 562 nm excitation, Figure A.14 (e) and (f) display the phasor plot and the angular histogram. The shorter lifetime measures about 10.84 ns, while the longer one is 19.66 ns. The residual's square is 0.0003, and the relative proportion is approximately 69.2%.

Figure A.15 (a) and (b) show the phasor plot and the angular histogram of the sample NID_{02} using a 532 nm excitation. The shorter lifetime is about 12.96 ns and the longer lifetime is 20.62 ns. The square of the residual is 0.0015. The relative proportion is about 30.8 %.

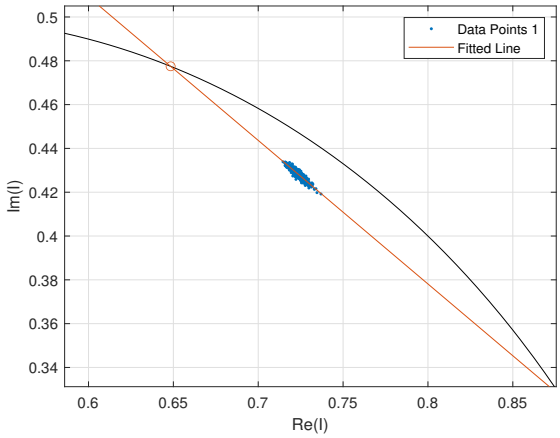
At the 502 nm excitation, Figure A.15 (c) and (d) display the phasor plot and the angular histogram. The shorter lifetime measures about 12.97 ns, while the longer one is 20.78 ns. The residual's square is 0.0025, and the relative proportion is approximately 18.9%.



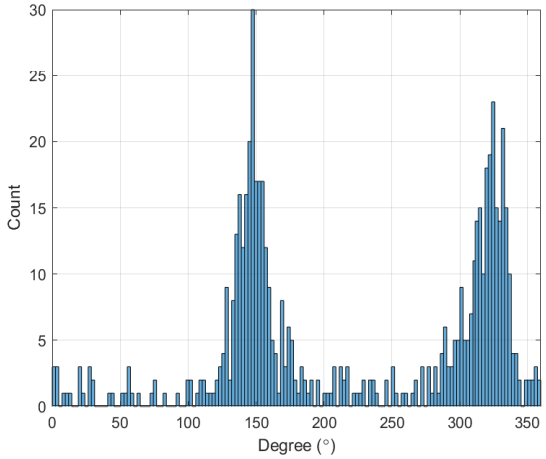
(a) 532 nm



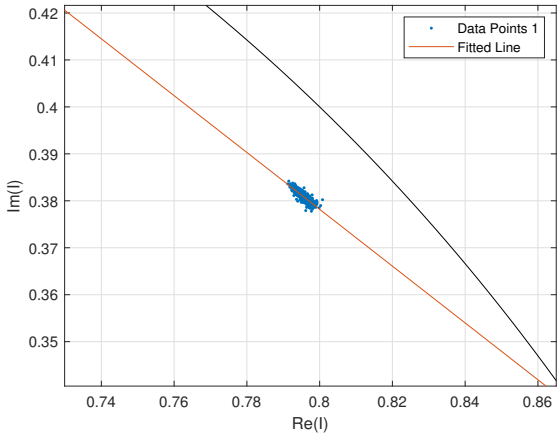
(b) 532 nm



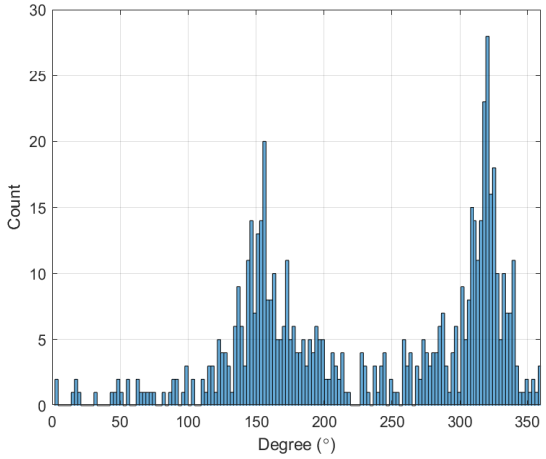
(c) 502 nm



(d) 502 nm

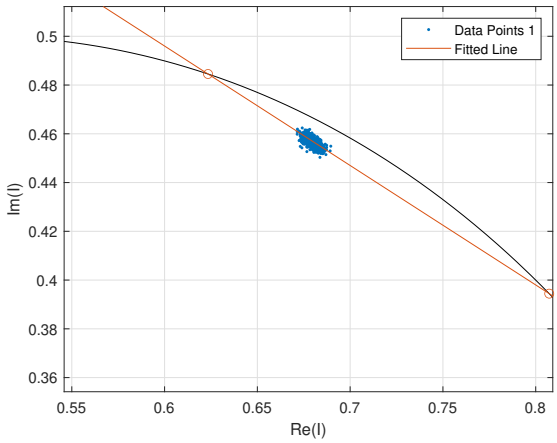


(e) 562 nm

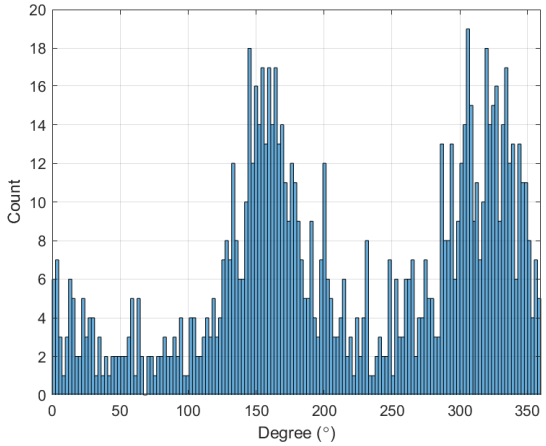


(f) 562 nm

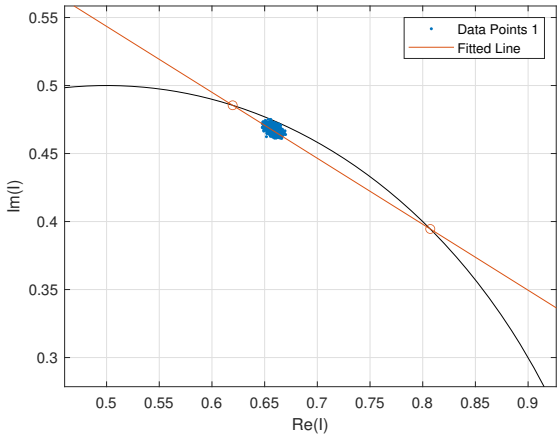
Figure A.14: The phasor diagram of the D09 sample, (a) for 532 nm, (c) for 502 nm, (e) for 562 nm and the angular histograms of the D09 sample (b) for the 532 nm, (d) for the 502 nm and (f) for the 562 nm.



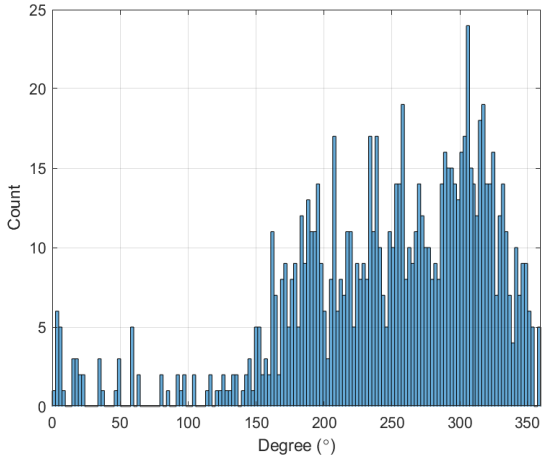
(a) 532 nm



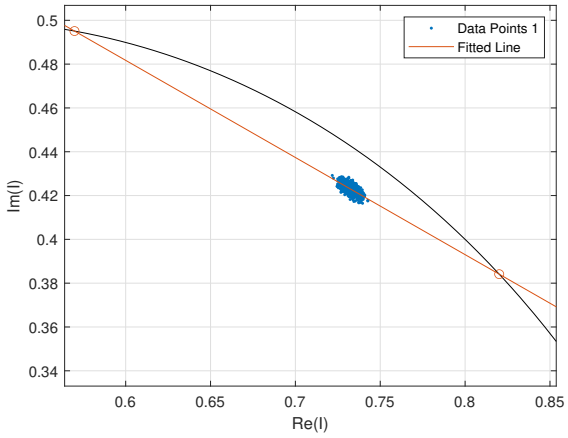
(b) 532 nm



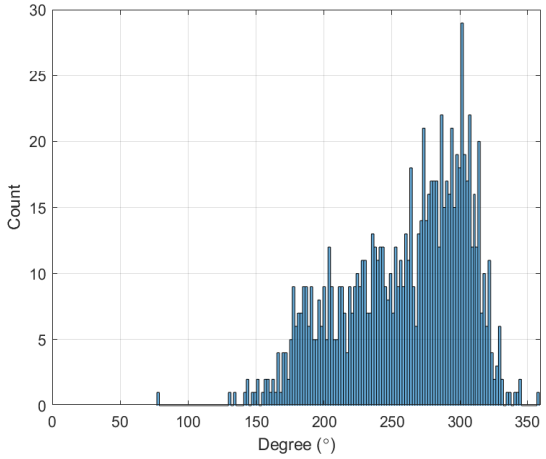
(c) 502 nm



(d) 502 nm



(e) 562 nm



(f) 562 nm

Figure A.15: The phasor diagram of the NID_{02} sample, (a) for 532 nm, (c) for 502 nm, (e) for 562 nm and the angular histograms of the NID_{02} sample (b) for the 532 nm, (d) for the 502 nm and (f) for the 562 nm.

At the 562 nm excitation, Figure A.15 (e) and (f) display the phasor plot and the angular histogram. The shorter lifetime measures about 12.42 ns, while the longer one is 23.05 ns. The residual's square is 0.0016, and the relative proportion is approximately 64.7%. For this sample, the data points are dispersed, and the average square residual of the fittings is the largest among the samples. In the histogram plots, only the 532 nm figures have two peaks. Both the longer wavelength and the shorter wavelength have a very broad peak.

A.4

Halbach array PSO optimisation and experimental field characterisation

A Halbach array is constructed by a number of permanent magnets arranged in a certain way to achieve a high homogeneity and high field magnitude at a position, which was proposed by Mallianson and constructed by Halbach [196, 197]. Halbach arrays have a wide range of applications such as nuclear magnetic resonance [198], electric motors [199] and magnetic refrigeration [200]. One of the most significant advantages over the electromagnetic magnets of Halbach arrays is the fact that they do not need cooling and power consumption and are stable without mechanical noise from cooling or electronic noise [201, 202].

For maser application, high field and high homogeneity are required. In the simulations, the magnets are arranged into a circle where the field of interest is at the centre of the circle. The minimum magnetic field should overcome the level-crossing, which is about 105 mT. The higher the field, the higher the maser operating frequency. The field homogeneity is required so that there are enough NV^- within the maser linewidth, which should be within 1 μT. The inner diameter is limited by the size of the cavity that has to be fitted inside. The method of calculating the field generated from the perfectly homogeneous permanent magnets using analytical solutions. This assumption will neglect demagnetisation effects, which can be added via demagnetisation factor to compensate for most of the effects, such as self-demagnetisation. By neglecting demagnetisation effects, the analytical solution can achieve accurate results with error less than 1 % for permanent magnet $\mu_r < 1.05$ [203].

On the other hand, inhomogeneous effects are harder to estimate using the analytical methods,

but the effects are much smaller than the homogenous effects. In reality, other imperfections such as the random drifts of the magnetisation and the imperfect position of the magnets might have a larger effect. The simulations serve as a guide for constructing a Halbach array with high field and high field homogeneity. The simulations employ open-source Python packages, Magpylib and Pyswarms. The method used magnetostatic Maxwell equations stated below [204].

$$H = -\nabla \cdot \psi \tag{A.1}$$

$$\psi(r) = \frac{1}{4\pi} \int_V \frac{\nabla' \cdot \mathbf{M}(r')dV}{|r - r'|} + \frac{1}{4\pi} \oint_S \frac{\mathbf{n}' \cdot \mathbf{M}(r')dS}{|r - r'|} \tag{A.2}$$

The method is written in numpy and it makes use of vectorised computation, which is an effective CPU computing algorithm. To address the demagnetisation, the magnets are meshed into a user-defined number of triangular meshes, and interactions with each other are incorporated into the method. A PSO optimisation, which is a widely used heuristic optimization technique for structural optimisation, is applied to the structure with constraints such as the diameter of the Halbach array, the positions and angles (P-A) of each permanent magnet, the number of Halbach arrays along the axial direction, and the number of concentric Halbach arrays. The optimisation method employed here can identify the optimal parameters of each magnet to generate the highest homogeneity. Figure A.16 shows the flowchart of the PSO algorithm from creating a basic magnet unit to demagnetisation meshing to the optimised structure.

The first result is a single circular ring of 10 magnets, as shown in Figure A.17 (a). The design is later constructed using 20 mm cubic NdFeB magnets and a 3D-printed frame. Each magnet has a remnant field of 1.3 T and a permeability of 1.005. The demagnetisation method divides the mesh into 1500 cells. Figure A.17 (b) is the X-Y field map without the demagnetisation and Figure A.17 (c) is the same map but with the demagnetisation. Clearly, the demagnetised map has a field magnitude more agrees with the experimental data, shown in Figure A.17 (f) for the X-Z map. Figure A.17 (e) and Figure A.17 (d) are the X-Z and Y-Z field maps. The rest of the magnetic field results are with demagnetisation applied. Figure A.18 shows the histogram of the Halbach array. 97.48 mT is the most populated field point. Figure A.19 shows the 3D field cube of the Halbach array, the size is 3mm by 3mm by 3mm corresponding to the size of the diamond samples.

The X-Y magnetic field at the centre is 99.15 mT for no demagnetisation and 97.45 with demagnetisation. The field difference is 0.432 mT and the field inhomogeneity within a 3 mm

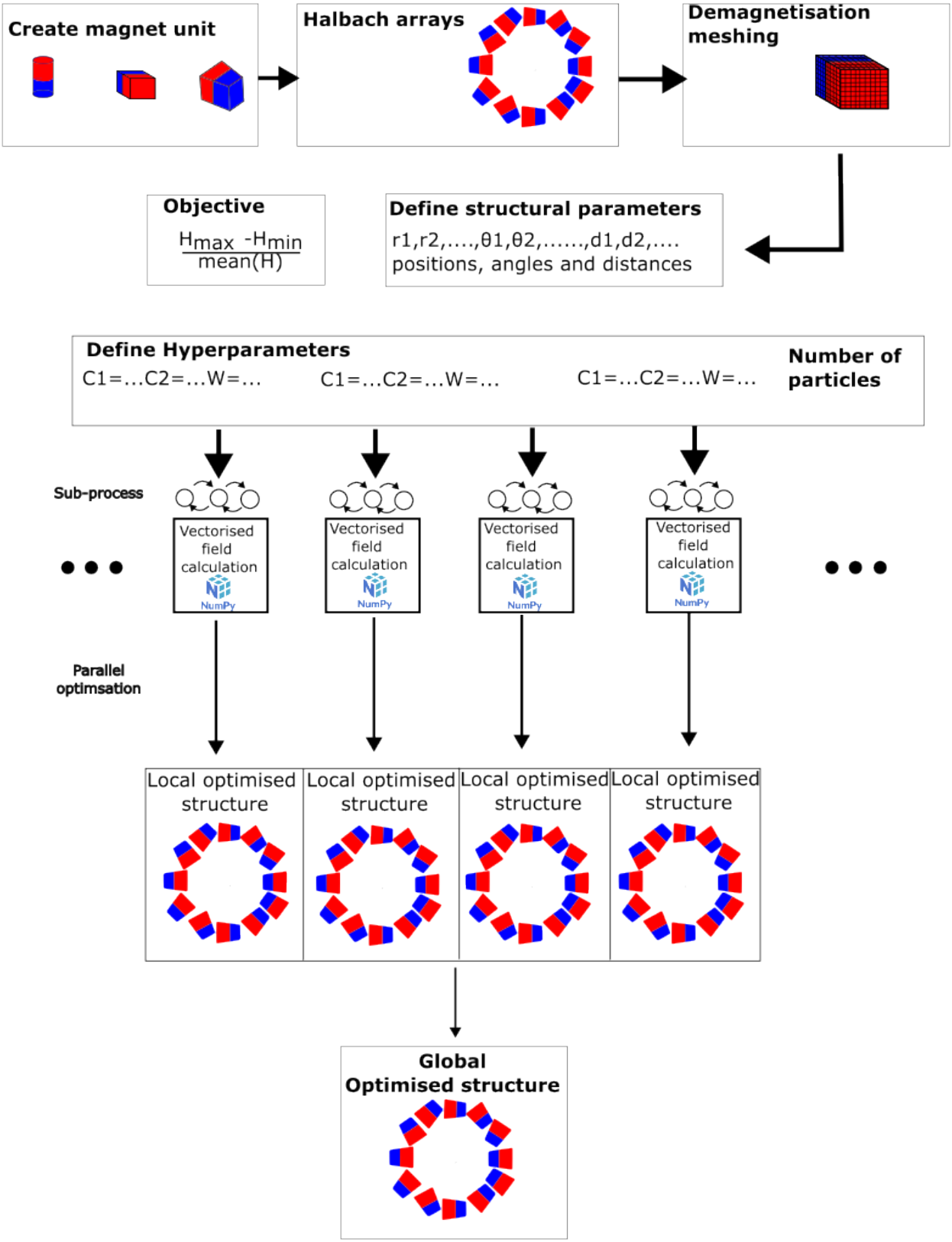
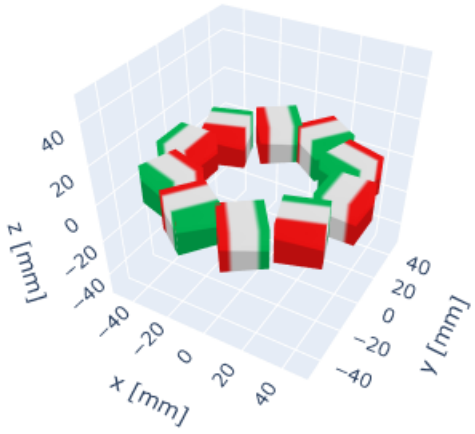
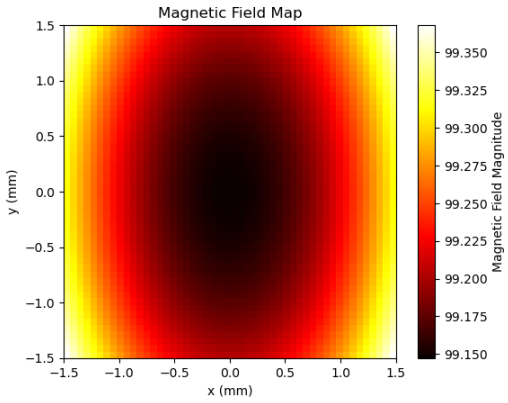


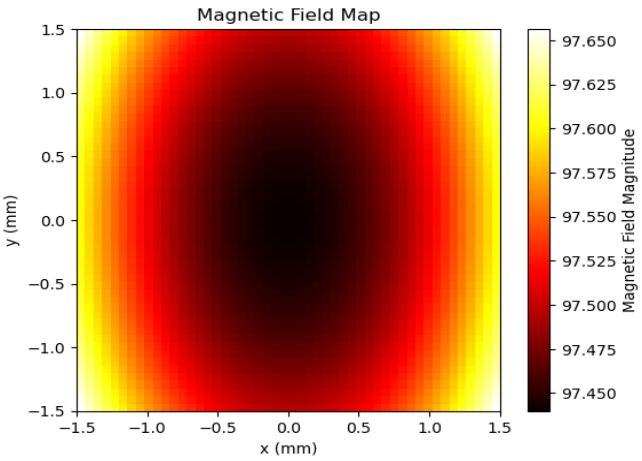
Figure A.16: The PSO algorithm flowchart for optimisation of Halbach arrays for maser application.



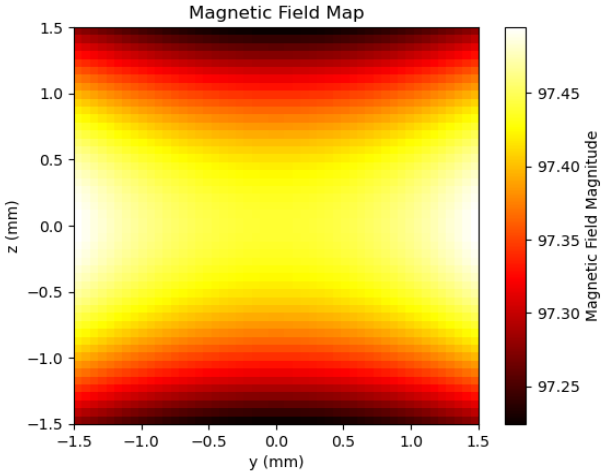
(a) 10-magnet Halbach array



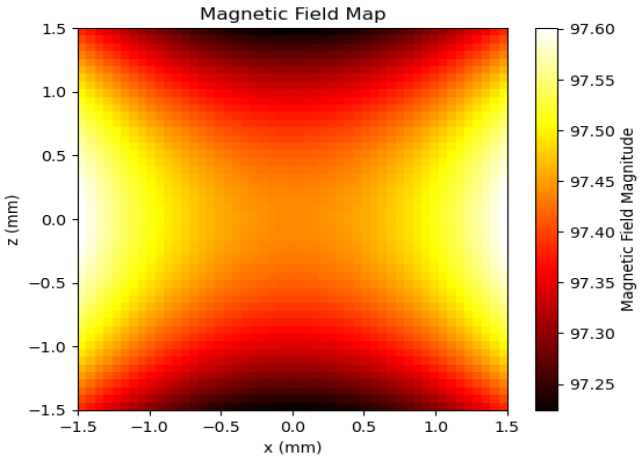
(b) XY field profile without applying the demagnetisation algorithm



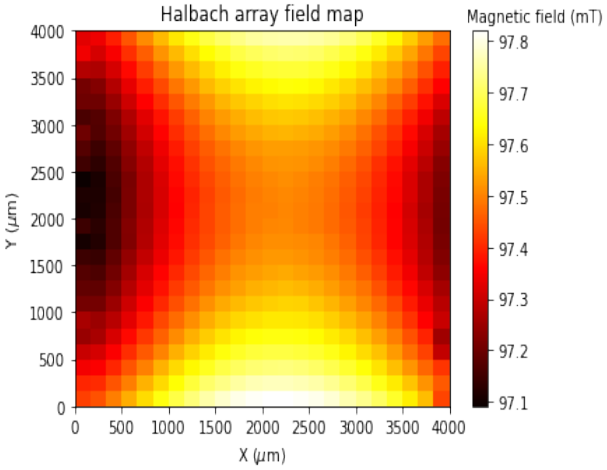
(c) XY field profile



(d) YZ field profile



(e) XZ field profile



(f) Experiment

Figure A.17: 10-magnet Halbach array (a) 3D model (b) The X-Y magnetic field map without applying demagnetisation method (c) The X-Y magnetic field map with applying demagnetisation method (d) The Y-Z magnetic field map (e) The X-Z magnetic field map (f) The X-Z magnetic field map of the 3D printed Halbach array, measured by a teslameter.

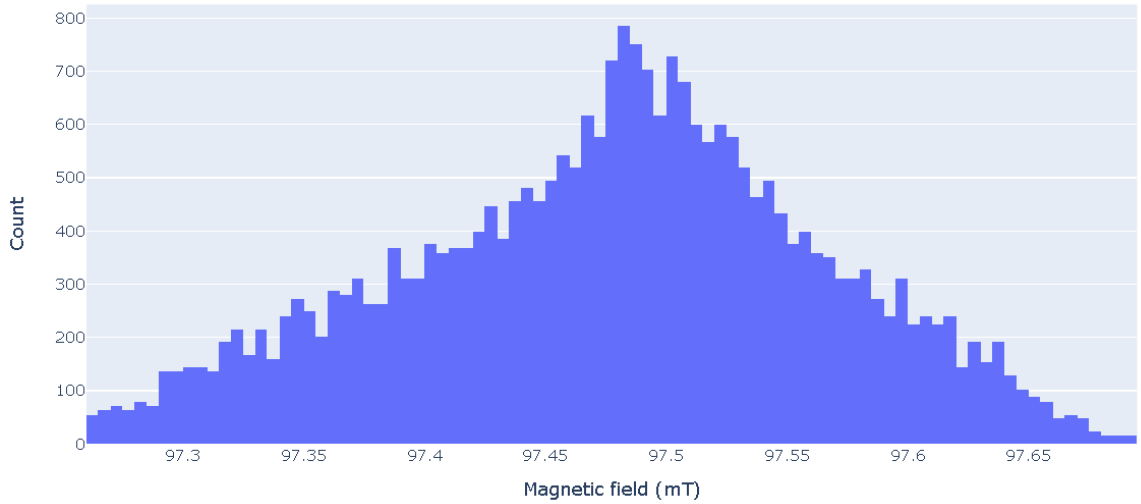


Figure A.18: The histogram of the field map of the Halbach array in a 3 mm × 3 mm × 3 mm cube.

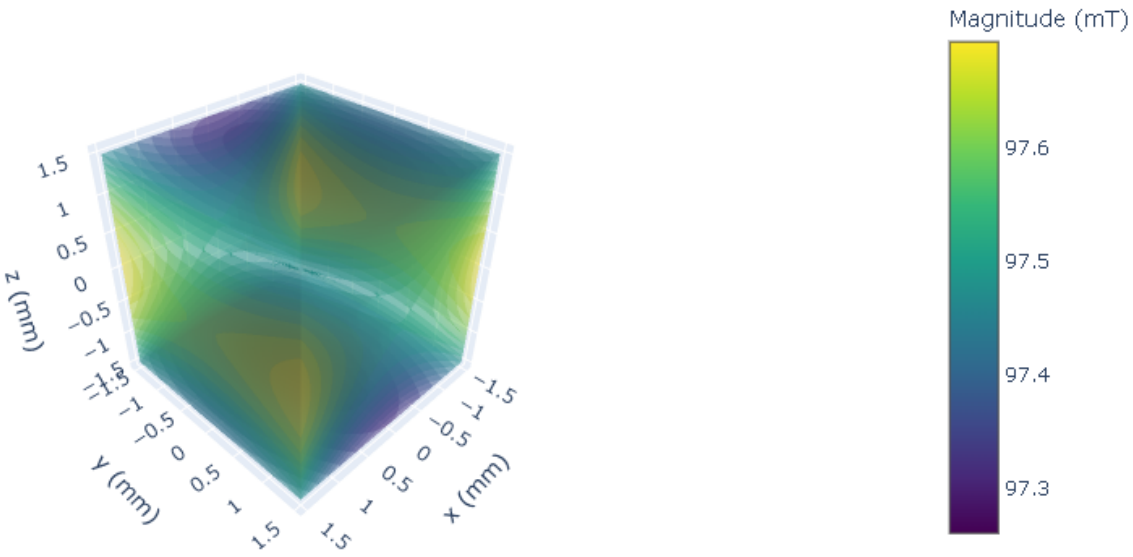


Figure A.19: The 3-dimensional magnetic field map of the Halbach array in a 3 mm × 3 mm × 3 mm cube.

× 3 mm × 3 mm cube is 4431 ppm. The field inhomogeneity, ΔB, is defined below. The diameter of the Halbach array, the distance between the centre of the magnets, is 100 mm. The inner diameter, including the magnet and the 3D-printed structure, is 70 mm.

$$\Delta B = \frac{B_{max} - B_{min}}{B_{mean}} \tag{A.3}$$

where B_{max} is the maximum field, B_{min} is the minimum field and B_{mean} is the mean field.

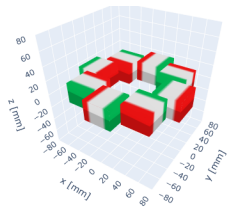
To simulate a better Halbach array that will meet masing requirements. The size of each magnet is decreased so that more magnets can be fitted in a ring to increase the field strength. Commercially available 40 x 40 x 30mm super high-performance N42 Neodymium (NeFeB) magnets are used in the design, as shown in Figure A.20 (a). The diameter is 120 mm. The mean magnetic field at the centre is about 284.31 mT, and the field homogeneity is about 3347.75 ppm, with a field difference of 0.952 mT.

In order to achieve high field and high homogeneity, another pair of Halbach rings is stacked along the z-axis. The position of the stack is carefully estimated using the custom PSO algorithm to maximise the homogeneity. The stacking can help increase the central field and reduce the difference between the maximum field and the minimum field.

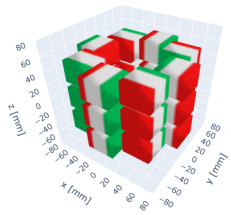
After stacking, at an optimal distance of 38.22 mm without changing the position and rotation, as shown in Figure A.20 (b), (c), (d) and (e), the mean field is 510.244 mT and the homogeneity is 631.66 ppm, with a field difference of 0.322 mT. The homogeneity is slightly better than the commercial Halbach array from Chapter 3. Figure A.21 (a) shows the 3D magnetic field cube.

Figure A.21 (b) shows the random distribution of the mean magnetic field and the magnetic field difference of 10,000 random samples with small deviations in the distance of stacks, angles, and positions of each magnet. The maximum deviation is ± 1 mm in position and ± 1 ° in angle. This result shows that obtaining the optimal homogeneity configuration is difficult, which has a high mean magnetic field and low magnetic field difference. The lower right corner is the high field homogeneity region. The majority of the is located within an ellipse at the centre.

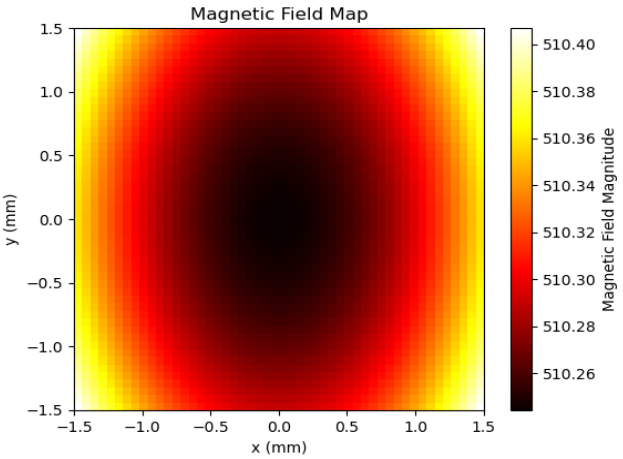
To further improve the homogeneity, the angles and the positions of each magnet are optimised with 10 parallel optimsation in 100 iterations. As a result, the best configuration has a mean of



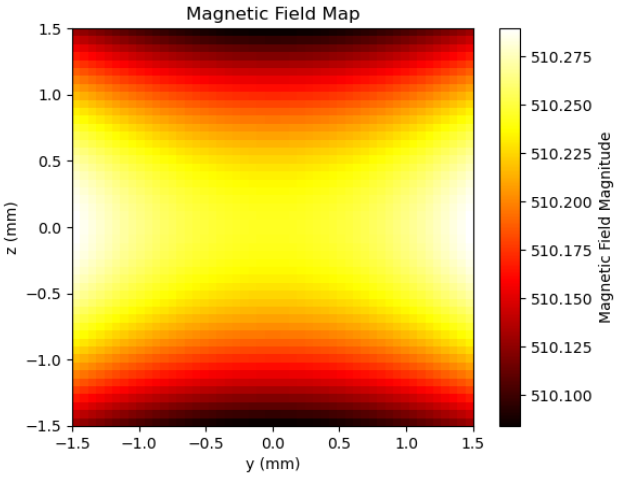
(a) 8-magnet Halbach array



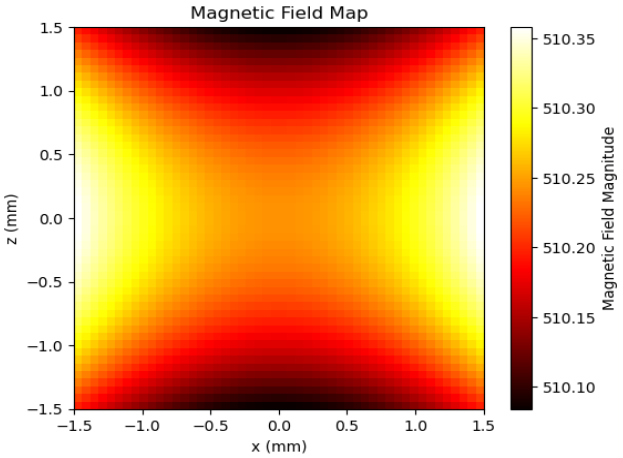
(b) Stack of 8-magnet Halbach array



(c) XY field profile

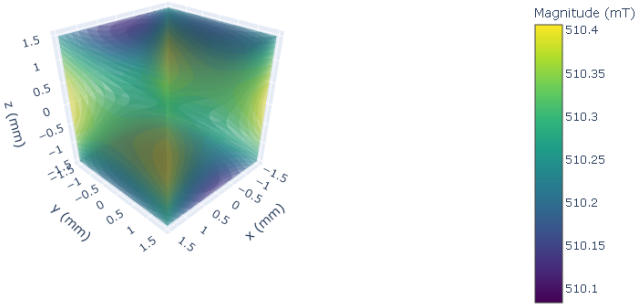


(d) YZ field profile

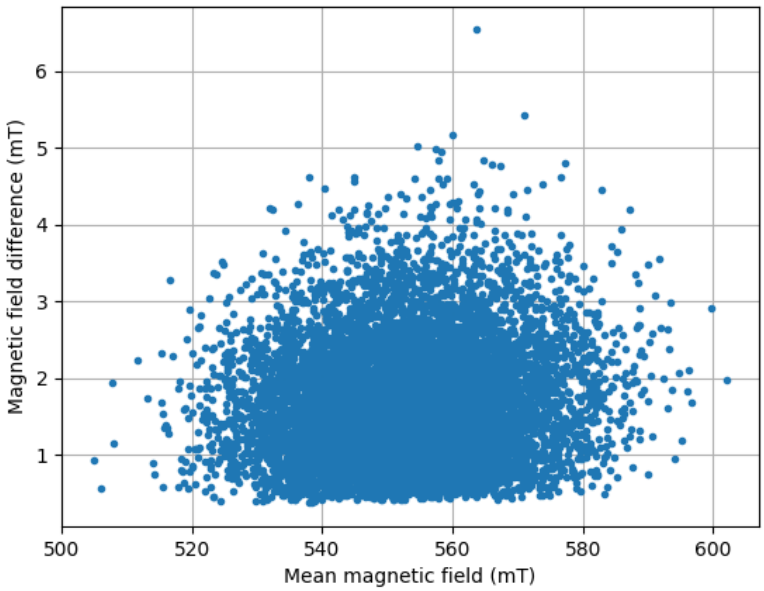


(e) XZ field profile

Figure A.20: 8-magnet Halbach arrays (a) 3D model of a single layer (b) Stack of 3 layers (c) The X-Y magnetic field map (d) The Y-Z magnetic field map (e) The X-Z magnetic field map.



(a) 3D field cube



(b) Field distribution of random varying position and angles.

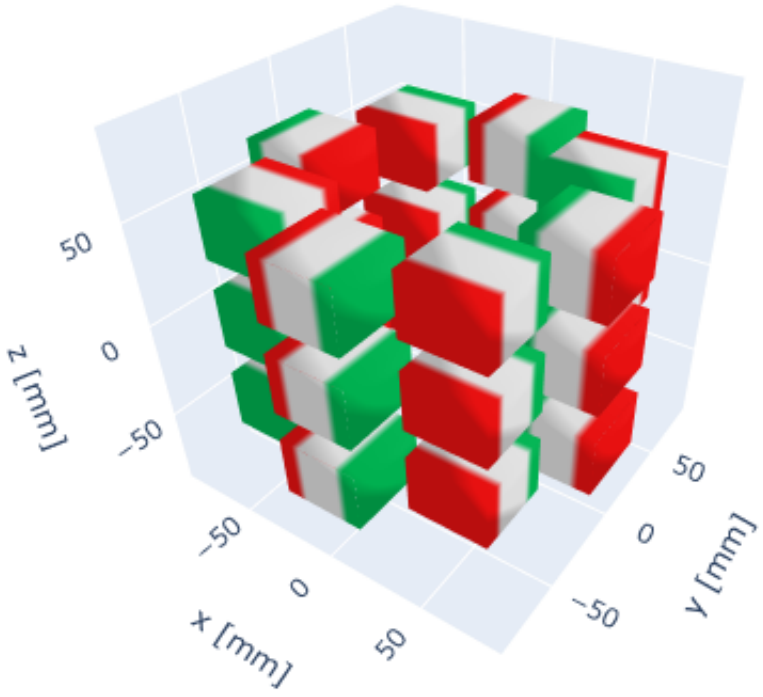
Figure A.21: (a) The 3-dimensional magnetic field map of the Halbach array in a 3 mm × 3 mm × 3 mm cube. (b) Field difference and mean field with random deviation of position and rotation from the ideal Halbach array, ± 1 mm in position and ± 1 °.

443.17 mT and a homogeneity of 594.294 ppm. The optimised structure is shown in Figure A.22 (a). The corresponding field cube and field map are shown in Figure A.22 (b) and Figure A.23. The field difference is reduced to 0.26 mT. The field difference is smaller by more than 18% and the mean field is reduced and closer to the 9.5 GHZ maser frequency as in experiments. From the x-y field map, the contour appears circular with a small distortion which is more homogeneous than the elliptical profile when the angles and the positions are perfect without any deviation from the idea Halbach array. By elongating the x-axis of the Halbach array, making the array elliptical can also help improve the homogeneity, but the angle-position optimsation appears better in homogeneity. In conclusion, the small deviations in angles and position of each magnet will fine-tune the contour line and give a different field profile. The PSO optimisation will find the configuration that will have the best homogeneity in the region of interest.

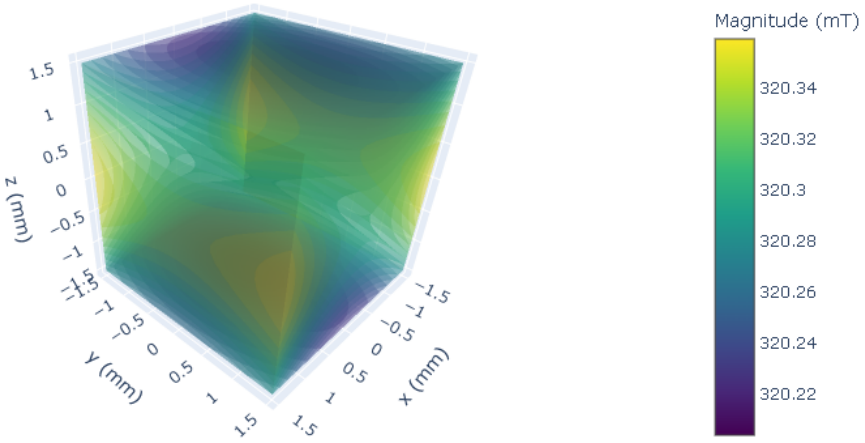
A Halbach array is an array that consists of permanent magnets, such as Neodymium magnets. The magnets are arranged so that the magnetic field at a certain position is either cancelled or magnified.

In this thesis, a cylindrical Halbach array is designed to generate a static magnetic field for the maser for verification with the simulation. In addition, a commercial Halbach array is used. The advantage of the Halbach array is the simplicity over the large, bulky and water-cooled electromagnetic. However, the Halbach array is fixed at a certain magnetic field strength. The Halbach array designed in this thesis consists of identical block magnets forming a circle. The array generates a homogeneous field at the centre of the circle. Starting from the positive x-axis, the magnetisation angle of the magnet rotates gradually from 0° with respect to the x-axis to 180° when the magnet is on the y-axis. Figure A.24 shows the setup of the teslameter that is fixed on a motorised stage. Figure A.25 shows a rendered image of the field map region and the direction of the magnetic field.

The magnetic field profile of a commercial Halbach array made of 8 prism-shaped magnets, Magnetic Solutions LTD, is shown in the figure below. The Halbach array provides a field of 0.345 T at the centre. The greatest difference in the field is about 0.3 mT. The field inhomogeneity of the commerial Halbach array is 869.6 ppm. The field inhomogeneity is particularly important in the diamond maser, as each NV^{-1} centre will experience a different Zeeman shift. From the field profile, the number of NV^{-1} that experiences roughly the same field can be grouped together. The total lineshape of the maser is the sum of the individual emitter's



(a) PSO-optimised Halbach array.



(b) 3D field profile.

Figure A.22: (a) The PSO-optimised Halbach array. (b) The 3-dimensional magnetic field map of the Halbach array in a 3 mm × 3 mm × 3 mm cube.

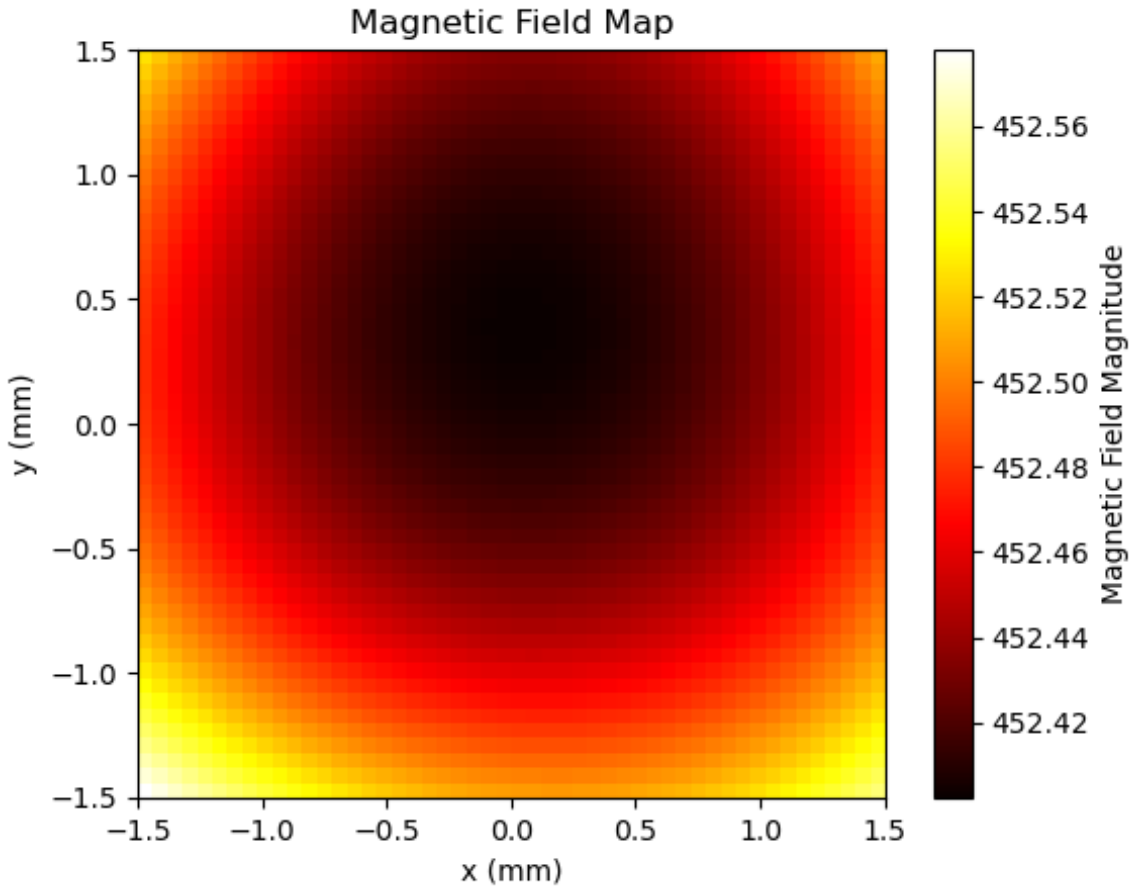


Figure A.23: The 2-dimensional magnetic field map of the angle-position-optimised Halbach array in a 3 mm × 3 mm plane.

lineshape. The resonator acts as a narrow band filter, the resonant frequency is at the maser frequency.

The field profile of a circular Halbach array is slightly elliptical, which is counter-intuitive. This might be explained by the fact that the long axis of the field profile lies along the magnetisation axis. Whereas, in the perpendicular direction, the magnetisation is perpendicular to the axis.

Halbach Array	Mean field (mT)	Field difference (μT)	Homogeneity (ppm)
Single ring	284	952	3347.8
Stacking 3 rings	510.24	322	610.24
P-A optimised stacking 3 rings	443.17	260	594.29
heightTrapezoidal Halbach	463	569	1228

Table A.1: A summary of Halbach array simulations.

Figure A.26 shows the 2D magnetic field map, 3D slice maps and the field distribution histogram of the Halbach array. The Halbach array has a mean field of about 345 mT and the maximum field difference is about 0.3 mT. Figure A.26 (d) shows the magnetic field histogram of the Halbach array. Most of the magnetic field is within 345 mT to 345.1 mT, which is about a third of the maximum field difference. Only a minority has a large field difference. Thus, only the field at the centre area which corresponds to the majority account for the maser. A useful rule of thumb is to assume the Halbach array has a similar field distribution, so the homogeneity can be improved by a factor of three by eliminating the minority field.

Figure A.27 shows the same magnetic field histogram with the maser resonator resonance to show how many field points can be seen from the maser resonance. Assuming the maser frequency is at 345.05 mT. The frequency shift is obtained by the Zeeman shift. The majority is within 2 MHz. The resonator lineshape has a width of 1 MHz. The field points outside the resonance cannot contribute to masing. The resonator will filter out a significant amount of the emitters that experience a different field. The number of emitters within the resonator linewidth is about 1.2×10^{12}. The number of spins is reduced by a factor of 40. This will lead to a significant drop in the cooperativity, which is proportional to the number of active spins, and lead to no maser regime, as the typical diamond maser has a cooperativity of around 10.

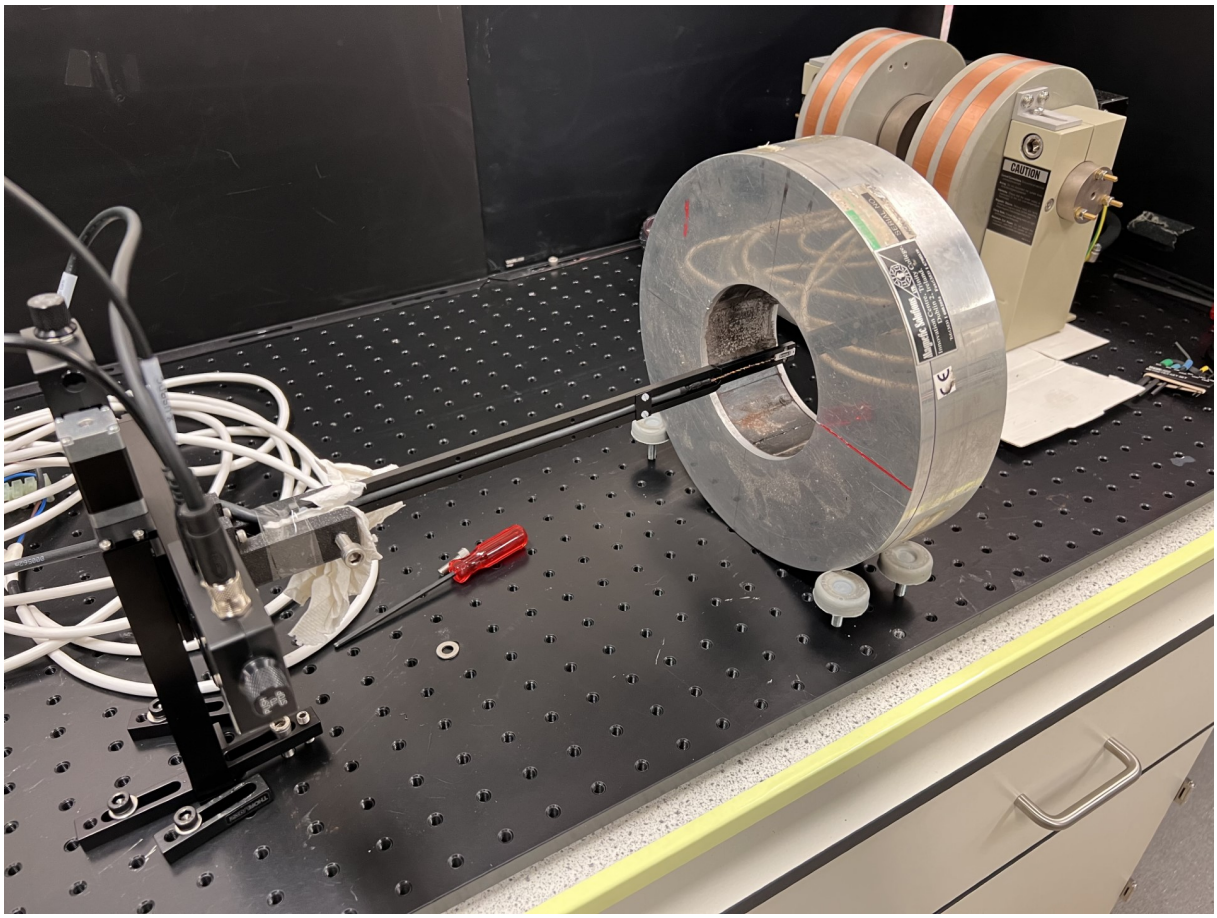


Figure A.24: The teslameter is mounted on the X stage which is mounted on the Z stage. The teslameter scans across a small square at the centre, the size is 2x2 mm. The Halbach array is an 8 prism-shaped Halbach array from Magnetic Solutions. The GMW electromagnet is shown in the background.

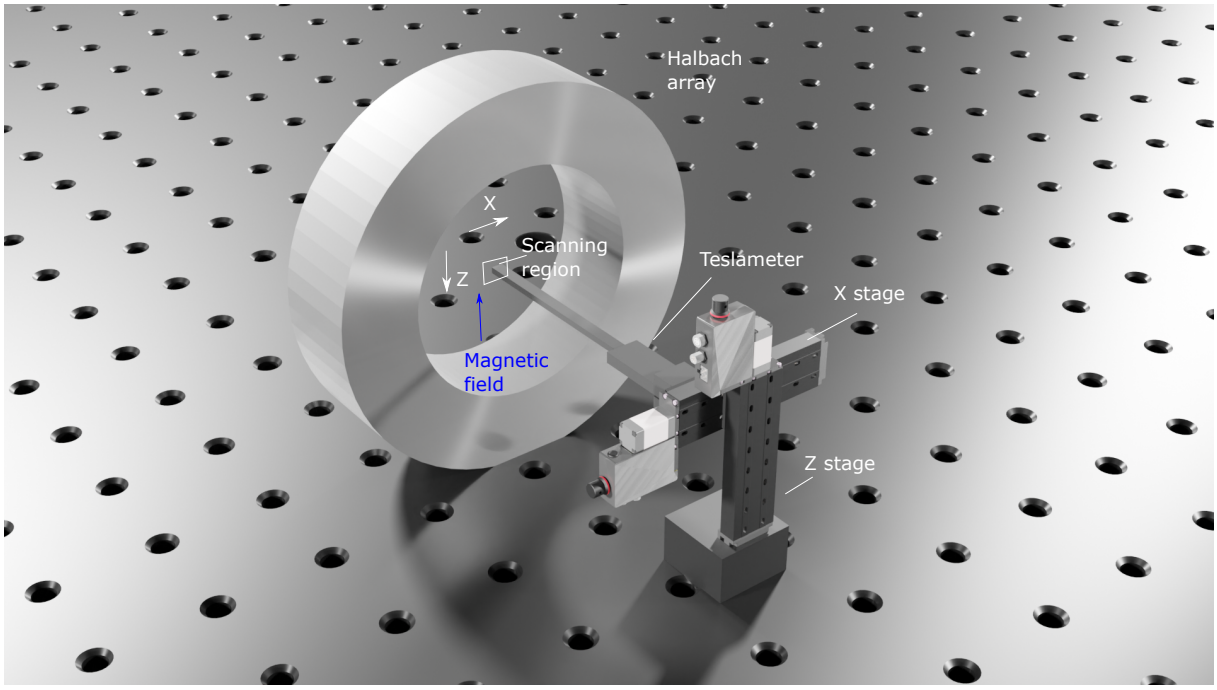
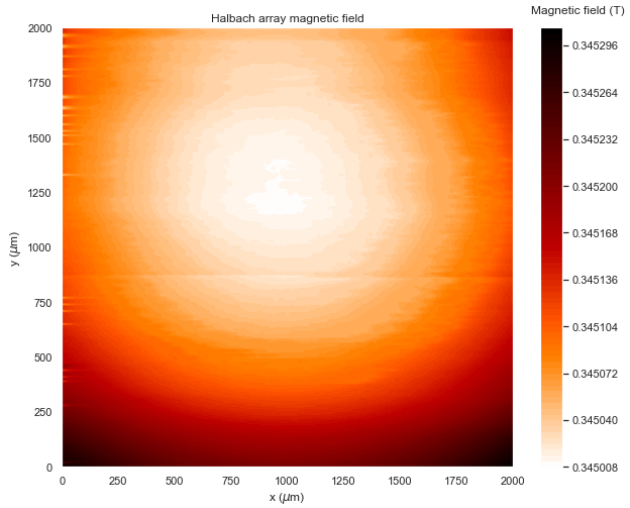
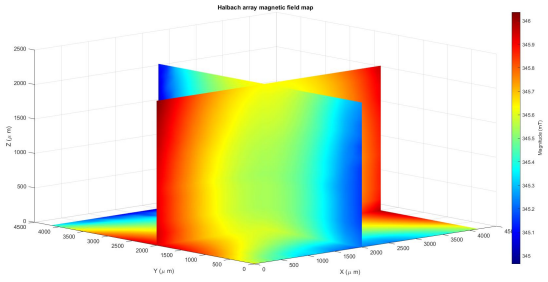


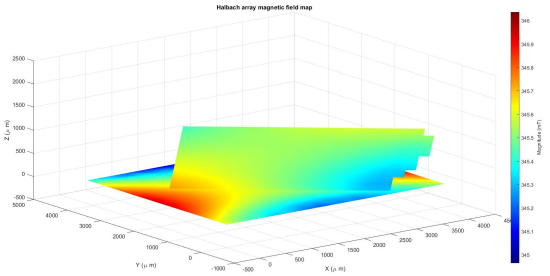
Figure A.25: The rendered image of the magnetic field mapper.



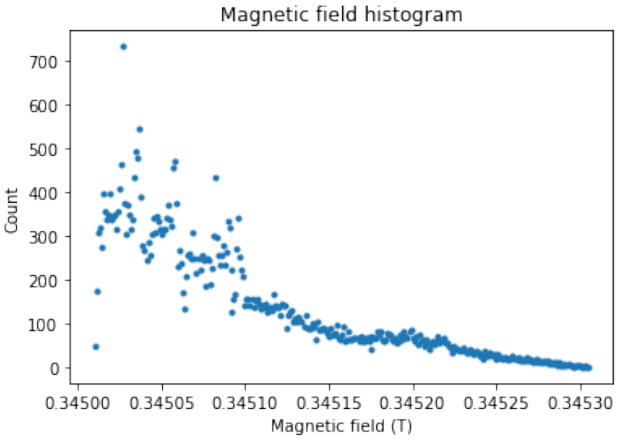
(a) Magnetic field profile



(b) 3D slice plot



(c) 3D slice plot



(d) Magnetic field histogram

Figure A.26: (a) The field profile of the Halbach array. The Halbach array provides a 0.345 T field at the centre, the greatest difference in the field is about 0.3 mT. (b) The 3D magnetic field slice map of the Halbach array. (c) The 3D magnetic field map of the Halbach array with an inclined plane represents the sample along the <111> plane. (d) The histogram of the magnetic field profile in terms of Zeeman shift. The curve represents the lineshape of the maser resonator, represented by a 1 MHz lineshape. It is assumed that the total number of emitters is $4{\cdot}10^{14}$ and only the MW emitter within the lineshape contributes to the maser.

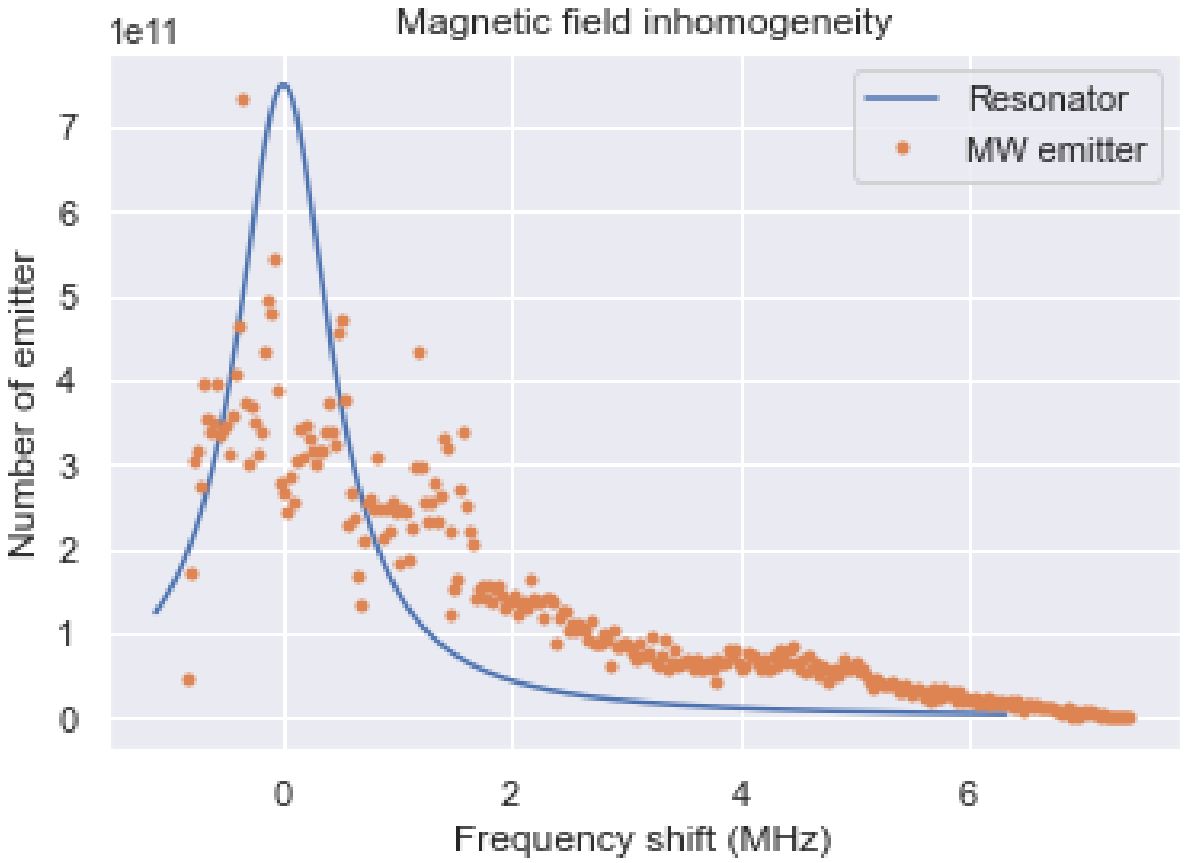


Figure A.27: **Magnetic field histogram.** The histogram of the magnetic field profile in terms of Zeeman shift. The curve represents the lineshape of the maser resonator, represented by a 1 MHz lineshape. It is assumed that the total number of emitters is $4{\cdot}10^{13}$ and only the MW emitter within the lineshape contributes to the maser.

Bibliography

[1] James Klatzow, Jonas N Becker, Patrick M Ledingham, Christian Weinzetl, Krzysztof T Kaczmarek, Dylan J Saunders, Joshua Nunn, Ian A Walmsley, Raam Uzdin, and Eilon Poem. Experimental demonstration of quantum effects in the operation of microscopic heat engines. *Physical Review Letters*, 122(11):110601, 2019.

[2] Jonathan D Breeze, Enrico Salvadori, Juna Sathian, Neil McN Alford, and Christopher WM Kay. Continuous-wave room-temperature diamond maser. *Nature*, 555(7697):493–496, 2018.

[3] Yongqiang Wen, Philip L Diggle, Neil McN Alford, and Daan M Arroo. Exploring the spin dynamics of a room-temperature diamond maser using an extended rate equation model. *Journal of Applied Physics*, 134(19), 2023.

[4] Torsten Gaebel, Michael Domhan, Iulian Popa, Christoffer Wittmann, Philipp Neumann, Fedor Jelezko, James R Rabeau, Nikolas Stavrias, Andrew D Greentree, Steven Prawer, et al. Room-temperature coherent coupling of single spins in diamond. *Nature Physics*, 2(6):408–413, 2006.

[5] Sébastien Pezzagna and Jan Meijer. Quantum computer based on color centers in diamond. *Applied Physics Reviews*, 8(1):011308, 2021.

[6] JM Taylor, Paola Cappellaro, L Childress, Liang Jiang, Dmitry Budker, PR Hemmer, Amir Yacoby, R Walsworth, and MD Lukin. High-sensitivity diamond magnetometer with nanoscale resolution. *Nature Physics*, 4(10):810–816, 2008.

[7] Loïc Rondin, Jean-Philippe Tetienne, Thomas Hingant, Jean-François Roch, Patrick Maletinsky, and Vincent Jacques. Magnetometry with nitrogen-vacancy defects in diamond. *Reports on progress in physics*, 77(5):056503, 2014.

[8] Liang Jin, Matthias Pfender, Nabeel Aslam, Philipp Neumann, Sen Yang, Jörg Wrachtrup, and Ren-Bao Liu. Proposal for a room-temperature diamond maser. *Nature communications*, 6(1):1–8, 2015.

[9] NA Poklonski, NM Lapchuk, AV Khomich, Lu Fan-Xiu, TANG Wei-Zhong, VG Ralchenko, II Vlasov, MV Chukichev, and Sambuu Munkhtsetseg. Nitrogen-doped chemical vapour deposited diamond: a new material for room-temperature solid state maser. *Chinese Physics Letters*, 24(7):2088, 2007.

[10] Mark Oxborrow, Jonathan D Breeze, and Neil M Alford. Room-temperature solid-state maser. *Nature*, 488(7411):353–356, 2012.

[11] Yongqiang Wen, Philip L Diggle, Daan M Arroo, and Neil McN Alford. Exploring the spin dynamics of a room-temperature diamond maser using an extended rate equation model. *arXiv preprint arXiv:2304.03217*, 2023.

[12] David M Pozar. Microwave engineering. *Fourth Editions, University of Massachusetts at Amherst, John Wiley & Sons, Inc*, pages 26–30, 2012.

[13] James P Gordon, Herbert J Zeiger, and Charles H Townes. The maser—new type of microwave amplifier, frequency standard, and spectrometer. *Physical review*, 99(4):1264, 1955.

[14] A Einstein. 7 on the quantum theory of radiation. *The Old Quantum Theory: The Commonwealth and International Library: Selected Readings in Physics*, page 167, 2016.

[15] Anthony E Siegman and HJ Hagger. Microwave solid-state masers. *Physics Today*, 17(10):65, 1964.

[16] Robert C Clauss and James S Shell. Ruby masers. *Low-Noise Systems in the Deep Space Network*, 2008.

[17] Niklas Wadefalk, Anders Mellberg, Iltcho Angelov, Michael E Barsky, Stacey Bui, Emmanuil Choumas, Ronald W Grundbacher, Erik Ludvig Kollberg, Richard Lai, Niklas Rorsman, et al. Cryogenic wide-band ultra-low-noise if amplifiers operating at ultra-low dc power. *IEEE Transactions on Microwave Theory and Techniques*, 51(6):1705–1711, 2003.

[18] JL Caswell, RA Vaile, SP Ellingsen, JB Whiteoak, and RP Norris. Galactic methanol masers at 6.6 ghz. *Monthly Notices of the Royal Astronomical Society*, 272(1):96–138, 1995.

[19] Peter Hofner and Ed Churchwell. A survey of water maser emission toward ultracompact hii regions. *Astronomy and Astrophysics Supplement Series*, 120:283–299, 1996.

[20] KY Lo. Mega-masers and galaxies. *Annual Review of Astronomy and Astrophysics*, 43(1):625–676, 2005.

[21] Theodore H Maiman et al. Stimulated optical radiation in ruby. 1960.

[22] James P Gordon, Herbert J Zeiger, and Charles H Townes. Molecular microwave oscillator and new hyperfine structure in the microwave spectrum of n h 3. *Physical Review*, 95(1):282, 1954.

[23] Koichi Shimoda. Ammonia masers. *IRE Transactions on Instrumentation*, 1(3/4):195–200, 1962.

[24] RJ Collier and TH Wilmshurst. Some characteristics of the ammonia maser amplifier. *British Journal of Applied Physics*, 18(8):1053, 1967.

[25] Daniel Kleppner, H Mark Goldenberg, and Norman F Ramsey. Theory of the hydrogen maser. *Physical Review*, 126(2):603, 1962.

[26] Harold Mark Goldenberg, D Kleppner, and NF Ramsey. Atomic hydrogen maser. *Physical Review Letters*, 5(8):361, 1960.

[27] Ronald L Walsworth Jr, Isaac F Silvera, HP Godfried, Agosta, CC, Robert FC Vessot, and Edward M Mattison. Hydrogen maser at temperatures below 1 k. *Physical Review A*, 34(3):2550, 1986.

[28] D Marcuse. Stimulated emission from hcn gas maser observed at 88.6 kmc. *Journal of Applied Physics*, 32(4):743–743, 1961.

[29] John Wilfred Orton, David Henry Paxman, and John Conway Walling. *The Solid State Maser: The Commonwealth and International Library: Selected Readings in Physics*. Elsevier, 2016.

[30] HED Scovil, G Feher, and H Seidel. Operation of a solid state maser. *Physical Review*, 105(2):762, 1957.

[31] Nicolaas Bloembergen. Proposal for a new type solid state maser. *Physical review*, 104(2):324, 1956.

[32] Anthony G Mann. Ultrastable cryogenic microwave oscillators. In *Frequency Measurement and Control: Advanced Techniques and Future Trends*, pages 37–67. Springer, 2000.

[33] G John Dick and Rabi T Wang. Ultra-stable performance of the superconducting cavity maser. In *Conference on Precision Electromagnetic Measurements*, pages 8–9. IEEE, 1990.

[34] Aharon Blank, Raphael Kastner, and Haim Levanon. Exploring new active materials for low-noise room-temperature microwave amplifiers and other devices. *IEEE transactions on microwave theory and techniques*, 46(12):2137–2144, 1998.

[35] P-Y Bourgeois, N Bazin, Y Kersalé, V Giordano, ME Tobar, and M Oxborrow. Maser oscillation in a whispering-gallery-mode microwave resonator. *Applied Physics Letters*, 87(22), 2005.

[36] H Kraus, VA Soltamov, D Riedel, S Väth, F Fuchs, A Sperlich, PG Baranov, V Dyakonov, and GV Astakhov. Room-temperature quantum microwave emitters based on spin defects in silicon carbide. *Nature Physics*, 10(2):157–162, 2014.

[37] M Fischer, A Sperlich, H Kraus, T Ohshima, GV Astakhov, and V Dyakonov. Highly efficient optical pumping of spin defects in silicon carbide for stimulated microwave emission. *Physical Review Applied*, 9(5):054006, 2018.

[38] Roland Nagy, Matthias Widmann, Matthias Niethammer, Durga BR Dasari, Ilja Gerhardt, Öney O Soykal, Marina Radulaski, Takeshi Ohshima, Jelena Vučković, Nguyen Tien Son, et al. Quantum properties of dichroic silicon vacancies in silicon carbide. *Physical Review Applied*, 9(3):034022, 2018.

[39] Fedor Jelezko and Jörg Wrachtrup. Single defect centres in diamond: A review. *physica status solidi (a)*, 203(13):3207–3225, 2006.

[40] Wern Ng, Shuyao Zhang, Hao Wu, Irena Nevjestic, Andrew JP White, and Mark Oxborrow. Exploring the triplet spin dynamics of the charge-transfer co-crystal phenazine/1, 2, 4, 5-tetracyanobenzene for potential use in organic maser gain media. *The Journal of Physical Chemistry C*, 125(27):14718–14728, 2021.

[41] Supamas Nitnara. A comparison of the glass former 1, 3, 5-tri (naphthyl) benzene and the crystalline p-terphenyl hosts for pentacene masers. 2020.

[42] Max Attwood, Xiaotian Xu, Michael Newns, Zhu Meng, Rebecca Ingle, Hao Wu, Xi Chen, Weidong Xu, Wern Ng, Temitope Abiola, Vasilos Stavros, and Mark Oxborrow. N-heteroacenes as an organic gain medium for room temperature masers. *ChemRxiv*, March 2023.

[43] Wern Ng, Xiaotian Xu, Max Attwood, Hao Wu, Zhu Meng, Xi Chen, and Mark Oxborrow. Move aside pentacene: Diazapentacene-doped para-terphenyl, a zero-field room-temperature maser with strong coupling for cavity quantum electrodynamics. *Advanced Materials*, 35(22):2300441, 2023.

[44] CR Nave. Hydrogen spectrum. *HyperPhysics. Georgia State University. Retrieved March*, 1:2008, 2006.

[45] Thomas Astner, Johannes Gugler, Andreas Angerer, Sebastian Wald, Stefan Putz, Norbert J Mauser, Michael Trupke, Hitoshi Sumiya, Shinobu Onoda, Junichi Isoya, et al. Solid-state electron spin lifetime limited by phononic vacuum modes. *Nature materials*, 17(4):313–317, 2018.

[46] O R Rubinas, VV Vorobyov, VV Soshenko, SV Bolshedvorskii, VN Sorokin, AN Smolyaninov, VG Vins, AP Yelisseyev, and AV Akimov. Spin properties of nv centers in high-pressure, high-temperature grown diamond. *Journal of Physics Communications*, 2(11):115003, 2018.

[47] RD Richtmyer. Dielectric resonators. *Journal of applied physics*, 10(6):391–398, 1939.

[48] A Okaya. The rutile microwave resonator. *Proceedings of the Institute of Radio Engineers*, 48(11):1921–1921, 1960.

[49] A Okaya and LF Barash. The dielectric microwave resonator. *Proceedings of the IRE*, 50(10):2081–2092, 1962.

[50] Jonathan D Breeze, Xavi Aupi, and Neil McN Alford. Ultralow loss polycrystalline alumina. *Applied physics letters*, 81(26):5021–5023, 2002.

[51] N McN Alford, J Breeze, SJ Penn, and M Poole. Layered al2o3–tio2 composite dielectric resonators with tuneable temperature coefficient for microwave applications. *IEE Proceedings-Science, Measurement and Technology*, 147(6):269–273, 2000.

[52] Jonathan Breeze, Jerzy Krupka, Anthony Centeno, and Neil McN Alford. Temperature-stable and high q-factor tio2 bragg reflector resonator. *Applied Physics Letters*, 94(8), 2009.

[53] Rebecca A Parker. Static dielectric constant of rutile (ti o 2), 1.6-1060 k. *Physical Review*, 124(6):1719, 1961.

[54] Won-Sik Jung, Jong-Hyun Kim, Hyun-Tae Kim, and Dang-Hyok Yoon. Effect of temperature schedule on the particle size of barium titanate during solid-state reaction. *Materials Letters*, 64(2):170–172, 2010.

[55] Muhammad Rizwan, Samina Gul, Tahir Iqbal, Uzma Mushtaq, M Hassan Farooq, Muhammad Farman, Rabia Bibi, and Mohsin Ijaz. A review on perovskite lanthanum aluminate (laalo3), its properties and applications. *Materials Research Express*, 6(11):112001, 2019.

[56] Wei Cai, CL Fu, JC Gao, and CX Zhao. Dielectric properties and microstructure of mg doped barium titanate ceramics. *Advances in Applied Ceramics*, 110(3):181–185, 2011.

[57] RS Roth, CJ Rawn, CG Lindsay, and W Wong-Ng. Phase equilibria and crystal chemistry of the binary and ternary barium polytitanates and crystallography of the barium zinc polytitanates. *Journal of solid state chemistry*, 104(1):99–118, 1993.

[58] Neil McN Alford and Stuart J Penn. Sintered alumina with low dielectric loss. *Journal of Applied Physics*, 80(10):5895–5898, 1996.

[59] Stuart J Penn, Neil McN Alford, Alan Templeton, Xiaoru Wang, Meishing Xu, Michael Reece, and Kevin Schrapel. Effect of porosity and grain size on the microwave dielectric properties of sintered alumina. *Journal of the American Ceramic Society*, 80(7):1885–1888, 1997.

[60] VL Gurevich and AK Tagantsev. Intrinsic dielectric loss in crystals. *Advances in Physics*, 40(6):719–767, 1991.

[61] VB Braginsky, VS Ilchenko, and Kh S Bagdassarov. Experimental observation of fundamental microwave absorption in high-quality dielectric crystals. *Physics Letters A*, 120(6):300–305, 1987.

[62] Jonathan Breeze. *Temperature and Frequency Dependence of Complex Permittivity in Metal Oxide Dielectrics: Theory, Modelling and Measurement*. Springer, 2016.

[63] Darko Kajfez and Pierre Guillon. Dielectric resonators, artech house. *Inc.: Norwood, MA, USA*, 1986.

[64] MJ Loboda, TE Parker, and GK Montress. Temperature sensitivity of dielectric resonators and dielectric resonator oscillators. In *Proceedings of the 42nd Annual Frequency Control Symposium, 1988.*, pages 263–271. IEEE, 1988.

[65] Charles E Free and Colin S Aitchison. *RF and Microwave Circuit Design: Theory and Applications*. John Wiley & Sons, 2021.

[66] Joel P.. Dunsmore. *Handbook of microwave component measurements: with advanced VNA techniques*. Wiley, 2012.

[67] Georges A Deschamps. Microstrip microwave antennas. In *Proceedings of the Third Symposium on the USAF Antenna Research and Development Program, Oct*, pages 18–22, 1953.

[68] H Baissinnot and G Gutton. Flat aerial for ultra high frequencies. *French Patent*, 70313, 1955.

[69] Keith Carver and James Mink. Microstrip antenna technology. *IEEE transactions on antennas and propagation*, 29(1):2–24, 1981.

[70] David M Pozar. Microstrip antennas. *Proceedings of the IEEE*, 80(1):79–91, 1992.

[71] Df Pozar. Input impedance and mutual coupling of rectangular microstrip antennas. *IEEE Transactions on Antennas and Propagation*, 30(6):1191–1196, 1982.

[72] David Pozar. Considerations for millimeter wave printed antennas. *IEEE Transactions on antennas and propagation*, 31(5):740–747, 1983.

[73] Kento Sasaki, Yasuaki Monnai, Soya Saijo, Ryushiro Fujita, Hideyuki Watanabe, Junko Ishi-Hayase, Kohei M Itoh, and Eisuke Abe. Broadband, large-area microwave antenna for optically detected magnetic resonance of nitrogen-vacancy centers in diamond. *Review of Scientific Instruments*, 87(5):053904, 2016.

[74] Kai Fong Lee, Kwai Man Luk, and Hau Wah Lai. *Microstrip patch antennas*. World Scientific, 2017.

[75] Michael NR Ashfold, Jonathan P Goss, Ben L Green, Paul W May, Mark E Newton, and Chloe V Peaker. Nitrogen in diamond. *Chemical reviews*, 120(12):5745–5794, 2020.

[76] DC Jones, S Kumar, PMP Lanigan, CD McGuinness, MW Dale, DJ Twitchen, D Fisher, PM Martineau, M Neil, C Dunsby, and P French. Multidimensional luminescence microscope for imaging defect colour centres in diamond. *Methods and Applications in Fluorescence*, 8, 2019.

[77] John Walker. Optical absorption and luminescence in diamond. *Reports on progress in physics*, 42(10):1605, 1979.

[78] W Kaiser and WL Bond. Nitrogen, a major impurity in common type i diamond. *Physical Review*, 115(4):857, 1959.

[79] L Du Preez. *Electron paramagnetic resonance and optical investigations of defect centres in diamond*. PhD thesis, University of the Witwatersrand, Johannesburg, 1965.

[80] Gordon Davies and MF Hamer. Optical studies of the 1.945 ev vibronic band in diamond. *Proceedings of the Royal Society of London. A. Mathematical and Physical Sciences*, 348(1653):285–298, 1976.

[81] CD Clark and CA Norris. Photoluminescence associated with the 1.673, 1.944 and 2.498 ev centres in diamond. *Journal of Physics C: Solid State Physics*, 4(14):2223, 1971.

[82] Lachlan J Rogers, Kay D Jahnke, Tokuyuki Teraji, Luca Marseglia, Christoph Müller, Boris Naydenov, Hardy Schauffert, Christine Kranz, Junichi Isoya, Liam P McGuinness,

et al. Multiple intrinsically identical single-photon emitters in the solid state. *Nature communications*, 5(1):1–6, 2014.

[83] Brendon C Rose, Ding Huang, Zi-Huai Zhang, Paul Stevenson, Alexei M Tyryshkin, Sorawis Sangtawesin, Srikanth Srinivasan, Lorne Loudin, Matthew L Markham, Andrew M Edmonds, et al. Observation of an environmentally insensitive solid-state spin defect in diamond. *Science*, 361(6397):60–63, 2018.

[84] Andreas Dietrich, Kay D Jahnke, Jan M Binder, Tokuyuki Teraji, Junichi Isoya, Lachlan J Rogers, and Fedor Jelezko. Isotopically varying spectral features of silicon-vacancy in diamond. *New Journal of Physics*, 16(11):113019, 2014.

[85] Paul E Barclay, Kai-Mei C Fu, Charles Santori, Andrei Faraon, and Raymond G Beausoleil. Hybrid nanocavity resonant enhancement of color center emission in diamond. *Physical Review X*, 1(1):011007, 2011.

[86] Stefano Lagomarsino, Assegid M Flatae, Haritha Kambalathmana, Florian Sledz, Lukas Hunold, Navid Soltani, Philipp Reuschel, Silvio Sciortino, Nicla Gelli, Mirko Massi, et al. Creation of silicon-vacancy color centers in diamond by ion implantation. *Frontiers in Physics*, page 626, 2021.

[87] Takayuki Iwasaki, Fumitaka Ishibashi, Yoshiyuki Miyamoto, Yuki Doi, Satoshi Kobayashi, Takehide Miyazaki, Kosuke Tahara, Kay D Jahnke, Lachlan J Rogers, Boris Naydenov, et al. Germanium-vacancy single color centers in diamond. *Scientific reports*, 5(1):1–7, 2015.

[88] FP Bundy and HT Hall. H. m strong, rh wentorf. *Nature*, 176:51, 1955.

[89] FP Bundy, WA Bassett, MS Weathers, RJ Hemley, HU Mao, and AF Goncharov. The pressure-temperature phase and transformation diagram for carbon; updated through 1994. *Carbon*, 34(2):141–153, 1996.

[90] John C Angus, Herbert A Will, and Wayne S Stanko. Growth of diamond seed crystals by vapor deposition. *Journal of Applied Physics*, 39(6):2915–2922, 1968.

[91] Peter Deák, Bálint Aradi, Moloud Kaviani, Thomas Frauenheim, and Adam Gali. Formation of nv centers in diamond: A theoretical study based on calculated transitions

and migration of nitrogen and vacancy related defects. *Physical Review B*, 89(7):075203, 2014.

[92] Scott T Alsid. *Optimizing chemical-vapor-deposition diamond for nitrogen-vacancy center ensemble magnetometry*. PhD thesis, Massachusetts Institute of Technology, 2017.

[93] Edwin Kim, Victor M Acosta, Erik Bauch, Dmitry Budker, and Philip R Hemmer. Electron spin resonance shift and linewidth broadening of nitrogen-vacancy centers in diamond as a function of electron irradiation dose. *Applied physics letters*, 101(8):082410, 2012.

[94] Brendan Campbell, Wahid Choudhury, Alison Mainwood, Mark Newton, and Gordon Davies. Lattice damage caused by the irradiation of diamond. *Nuclear Instruments and Methods in Physics Research Section A: Accelerators, Spectrometers, Detectors and Associated Equipment*, 476(3):680–685, 2002.

[95] Gordon Davies. Charge states of the vacancy in diamond. *Nature*, 269(5628):498–500, 1977.

[96] Brian Philip Burton. *Spectroscopic Studies of Radiation Induced Defects in Natural and Synthetic Diamonds*. PhD thesis, King's College London, 1977.

[97] G Davies and EC Lightowlers. The symmetry properties of the nd1 absorption centre in electron-irradiated diamond. *Journal of Physics C: Solid State Physics*, 3(3):638, 1970.

[98] WV Smith, PP Sorokin, IL Gelles, and GJ Lasher. Electron-spin resonance of nitrogen donors in diamond. *Physical Review*, 115(6):1546, 1959.

[99] A Batalov, V Jacques, F Kaiser, P Siyushev, P Neumann, LJ Rogers, RL McMurtrie, NB Manson, F Jelezko, and J Wrachtrup. Low temperature studies of the excited-state structure of negatively charged nitrogen-vacancy color centers in diamond. *Physical review letters*, 102(19):195506, 2009.

[100] LJ Rogers, RL McMurtrie, MJ Sellars, and NB Manson. Time-averaging within the excited state of the nitrogen-vacancy centre in diamond. *New Journal of Physics*, 11(6):063007, 2009.

[101] MW Doherty, F Dolde, H Fedder, Fedor Jelezko, J Wrachtrup, NB Manson, and LCL Hollenberg. Theory of the ground-state spin of the nv- center in diamond. *Physical Review B*, 85(20):205203, 2012.

[102] Christel M Marian. Understanding and controlling intersystem crossing in molecules. *Annual Review of Physical Chemistry*, 72:617–640, 2021.

[103] LJ Rogers, RL McMurtrie, MJ Sellars, and NB Manson. Time-averaging within the excited state of the nitrogen-vacancy centre in diamond. *New Journal of Physics*, 11(6):063007, 2009.

[104] Kasper Jensen, Nathan Leefer, Andrey Jarmola, Yannick Dumeige, Victor M Acosta, Pauli Kehayias, Brian Patton, and Dmitry Budker. Cavity-enhanced room-temperature magnetometry using absorption by nitrogen-vacancy centers in diamond. *Physical review letters*, 112(16):160802, 2014.

[105] Pauli Kehayias. *Exploring Basic Properties and Applications of Nitrogen-Vacancy Color Centers in Diamond*. PhD thesis, UC Berkeley, 2015.

[106] Nabeel Aslam, Gerhald Waldherr, Philipp Neumann, Fedor Jelezko, and Joerg Wrachtrup. Photo-induced ionization dynamics of the nitrogen vacancy defect in diamond investigated by single-shot charge state detection. *New Journal of Physics*, 15(1):013064, 2013.

[107] Kazuya Tsurumoto, Ryota Kuroiwa, Hiroki Kano, Yuhei Sekiguchi, and Hideo Kosaka. Quantum teleportation-based state transfer of photon polarization into a carbon spin in diamond. *Communications Physics*, 2(1):1–6, 2019.

[108] Sen Yang, Ya Wang, DD Bhaktavatsala Rao, Thai Hien Tran, Ali S Momenzadeh, M Markham, DJ Twitchen, Ping Wang, Wen Yang, Rainer Stöhr, et al. High-fidelity transfer and storage of photon states in a single nuclear spin. *Nature Photonics*, 10(8):507, 2016.

[109] Péter Udvarhelyi, Vladyslav O Shkolnikov, Adam Gali, Guido Burkard, and András Pályi. Spin-strain interaction in nitrogen-vacancy centers in diamond. *Physical Review B*, 98(7):075201, 2018.

[110] V Jacques, P Neumann, J Beck, M Markham, D Twitchen, J Meijer, F Kaiser, G Balasubramanian, F Jelezko, and J Wrachtrup. Dynamic polarization of single nuclear spins by optical pumping of nitrogen-vacancy color centers in diamond at room temperature. *Physical review letters*, 102(5):057403, 2009.

[111] Gopalakrishnan Balasubramanian, Philipp Neumann, Daniel Twitchen, Matthew Markham, Roman Kolesov, Norikazu Mizuochi, Junichi Isoya, Jocelyn Achard, Johannes Beck, Julia Tissler, et al. Ultralong spin coherence time in isotopically engineered diamond. *Nature materials*, 8(5):383–387, 2009.

[112] A Gruber, A Dräbenstedt, C Tietz, L Fleury, J Wrachtrup, and C Von Borczyskowski. Scanning confocal optical microscopy and magnetic resonance on single defect centers. *Science*, 276(5321):2012–2014, 1997.

[113] Solveig Felton, AM Edmonds, Mark E Newton, PM Martineau, D Fisher, and DJ Twitchen. Electron paramagnetic resonance studies of the neutral nitrogen vacancy in diamond. *Physical Review B*, 77(8):081201, 2008.

[114] Michael SJ Barson, Elmars Krausz, Neil B Manson, and Marcus W Doherty. The fine structure of the neutral nitrogen-vacancy center in diamond. *Nanophotonics*, 8(11):1985–1991, 2019.

[115] Marcus W Doherty, Neil B Manson, Paul Delaney, Fedor Jelezko, Jörg Wrachtrup, and Lloyd CL Hollenberg. The nitrogen-vacancy colour centre in diamond. *Physics Reports*, 528(1):1–45, 2013.

[116] Richard W Cole, Tushare Jinadasa, and Claire M Brown. Measuring and interpreting point spread functions to determine confocal microscope resolution and ensure quality control. *Nature protocols*, 6(12):1929–1941, 2011.

[117] José-Angel Conchello, John J Kim, and Eric W Hansen. Enhanced three-dimensional reconstruction from confocal scanning microscope images. ii. depth discrimination versus signal-to-noise ratio in partially confocal images. *Applied optics*, 33(17):3740–3750, 1994.

[118] José-Angel Conchello and Jeff W Lichtman. Optical sectioning microscopy. *Nature methods*, 2(12):920–931, 2005.

[119] Fuzhong Bai, Zhen Liu, and Xiaoyan Bao. Two-shot point-diffraction interferometer with an unknown phase shift. *Journal of Optics*, 12(4):045702, 2010.

[120] Donatella Carbonera. Optically detected magnetic resonance (odmr) of photoexcited triplet states. *Photosynthesis research*, 102(2):403–414, 2009.

[121] A Dréau, M Lesik, L Rondin, P Spinicelli, O Arcizet, J-F Roch, and V Jacques. Avoiding power broadening in optically detected magnetic resonance of single nv defects for enhanced dc magnetic field sensitivity. *Physical Review B*, 84(19):195204, 2011.

[122] Colin J Stephen. *Progress towards arrays of qubits using diamond*. PhD thesis, University of Warwick, 2019.

[123] Alexander Stark. Development of measurement protocols for quantum magnetometry. 2017.

[124] Elizabeth A Donley, Thomas P Heavner, Filippo Levi, MO Tataw, and Steven R Jefferts. Double-pass acousto-optic modulator system. *Review of Scientific Instruments*, 76(6):063112, 2005.

[125] Ross A La Rue, Kenneth A Costello, CA Davis, John P Edgecumbe, and Verle W Aebi. Photon counting iii-v hybrid photomultipliers using transmission mode photocathodes. *IEEE Transactions on Electron Devices*, 44(4):672–678, 1997.

[126] A Fukasawa, J Haba, A Kageyama, H Nakazawa, and M Suyama. High speed hpd for photon counting. *IEEE Transactions On Nuclear Science*, 55(2):758–762, 2008.

[127] Wolfgang Becker. *Advanced time-correlated single photon counting techniques*, volume 81. Springer Science & Business Media, 2005.

[128] Joel P Dunsmore. *Handbook of microwave component measurements: with advanced VNA techniques*. John Wiley & Sons, 2020.

[129] Jacques Vanier. The active hydrogen maser: state of the art and forecast. *Metrologia*, 18(4):173, 1982.

[130] Elisabeth Fraczek. Synthesis and assessment of laser related perameters in colour centre containing diamond. 2020.

[131] Daniel C Jones, Yuriy Alexandrov, Nathan Curry, Sunil Kumar, Peter MP Lanigan, Colin D McGuinness, Matthew W Dale, Daniel J Twitchen, David Fisher, Mark AA Neil, et al. Multidimensional spectroscopy and imaging of defects in synthetic diamond: excitation-emission-lifetime luminescence measurements with multiexponential fitting and phasor analysis. *Journal of Physics D: Applied Physics*, 54(4):045303, 2020.

[132] Wouter MJ Franssen, Frank J Vergeldt, Arjen N Bader, Herbert van Amerongen, and Camilla Terenzi. Full-harmonics phasor analysis: unravelling multiexponential trends in magnetic resonance imaging data. *The journal of physical chemistry letters*, 11(21):9152–9158, 2020.

[133] Alexander Vallmitjana, Belén Torrado, Alexander Dvornikov, Suman Ranjit, and Enrico Gratton. Blind resolution of lifetime components in individual pixels of fluorescence lifetime images using the phasor approach. *The journal of physical chemistry B*, 124(45):10126–10137, 2020.

[134] Lucio Robledo, Hannes Bernien, Toeno Van Der Sar, and Ronald Hanson. Spin dynamics in the optical cycle of single nitrogen-vacancy centres in diamond. *New Journal of Physics*, 13(2):025013, 2011.

[135] Lukas Razinkovas, Marek Maciaszek, Friedemann Reinhard, Marcus W Doherty, and Audrius Alkauskas. Photoionization of negatively charged nv centers in diamond: Theory and ab initio calculations. *Physical Review B*, 104(23):235301, 2021.

[136] Morgan Hedges Priya Singh Sophie Stearn Y Chen Lachlan Oberg Carlos A Meriles Marcus W Doherty Neil B Manson, Michael SJ Barson. Nv with nitrogen. *arXiv preprint arXiv:2311.09570*, 2023.

[137] Jason T Smith, Ruoyang Yao, Nattawut Sinsuebphon, Alena Rudkouskaya, Nathan Un, Joseph Mazurkiewicz, Margarida Barroso, Pingkun Yan, and Xavier Intes. Fast fit-free analysis of fluorescence lifetime imaging via deep learning. *Proceedings of the National Academy of Sciences*, 116(48):24019–24030, 2019.

[138] Dylan G Stone and Carlo Bradac. Machine and quantum learning for diamond-based quantum applications. *Materials for Quantum Technology*, 3(1):012001, 2023.

[139] Dong Xiao, Natakorn Sapermsap, Yu Chen, and David Day Uei Li. Deep learning enhanced fast fluorescence lifetime imaging with a few photons. *Optica*, 10(7):944–951, 2023.

[140] Peng Qian, Xue Lin, Feifei Zhou, Runchuan Ye, Yunlan Ji, Bing Chen, Guangjun Xie, and Nanyang Xu. Machine-learning-assisted electron-spin readout of nitrogen-vacancy center in diamond. *Applied Physics Letters*, 118(8), 2021.

[141] Rupsa Datta, Tiffany M Heaster, Joe T Sharick, Amani A Gillette, and Melissa C Skala. Fluorescence lifetime imaging microscopy: fundamentals and advances in instrumentation, analysis, and applications. *Journal of biomedical optics*, 25(7):071203–071203, 2020.

[142] Dong Xiao, Yu Chen, and David Day-Uei Li. One-dimensional deep learning architecture for fast fluorescence lifetime imaging. *IEEE Journal of Selected Topics in Quantum Electronics*, 27(4):1–10, 2021.

[143] Sergey V Titkov, Valentina V Yakovleva, Ilya D Breev, Roman A Babunts, Pavel G Baranov, and Nikolay S Bortnikov. Nv- center in natural diamonds: Optically detected magnetic resonance study. *Diamond and Related Materials*, 136:109938, 2023.

[144] P Kehayias, MJ Turner, R Trubko, JM Schloss, CA Hart, M Wesson, DR Glenn, and RL Walsworth. Imaging crystal stress in diamond using ensembles of nitrogen-vacancy centers. *Physical Review B*, 100(17):174103, 2019.

[145] K Jensen, VM Acosta, A Jarmola, and D Budker. Light narrowing of magnetic resonances in ensembles of nitrogen-vacancy centers in diamond. *Physical Review B*, 87(1):014115, 2013.

[146] A. M. Zaitsev. *Optical Properties of Diamond*. Springer-Verlag, Berlin Heidelberg, 2001.

[147] John F Barry, Jennifer M Schloss, Erik Bauch, Matthew J Turner, Connor A Hart, Linh M Pham, and Ronald L Walsworth. Sensitivity optimization for nv-diamond magnetometry. *Reviews of Modern Physics*, 92(1):015004, 2020.

[148] S. M. Graham, A. T. M. A. Rahman, L. Munn, R. L. Patel, A. J. Newman, C. J. Stephen, G. Colston, A. Nikitin, A. M. Edmonds, D. J. Twitchen, M. L. Markham, and G. W. Morley. Fiber-coupled diamond magnetometry with an unshielded 30 pt/$\sqrt{\text{hz}}$ sensitivity, 2023.

[149] RL Patel, LQ Zhou, AC Frangeskou, GA Stimpson, BG Breeze, A Nikitin, MW Dale, EC Nichols, W Thornley, BL Green, et al. Subnanotesla magnetometry with a fiber-coupled diamond sensor. *Physical Review Applied*, 14(4):044058, 2020.

[150] Maximilian Ruf, Noel H Wan, Hyeongrak Choi, Dirk Englund, and Ronald Hanson. Quantum networks based on color centers in diamond. *Journal of Applied Physics*, 130(7):070901, 2021.

[151] Bas Hensen, Hannes Bernien, Anaïs E Dréau, Andreas Reiserer, Norbert Kalb, Machiel S Blok, Just Ruitenberg, Raymond FL Vermeulen, Raymond N Schouten, Carlos Abellán, et al. Loophole-free bell inequality violation using electron spins separated by 1.3 kilometres. *Nature*, 526(7575):682–686, 2015.

[152] Conor E Bradley, Joe Randall, Mohamed H Abobeih, RC Berrevoets, MJ Degen, Michiel A Bakker, Matthew Markham, DJ Twitchen, and Tim H Taminiau. A ten-qubit solid-state spin register with quantum memory up to one minute. *Physical Review X*, 9(3):031045, 2019.

[153] JR Weber, WF Koehl, JB Varley, Anderson Janotti, BB Buckley, CG Van de Walle, and David D Awschalom. Quantum computing with defects. *Proceedings of the National Academy of Sciences*, 107(19):8513–8518, 2010.

[154] Wern Ng, Xiaotian Xu, Max Attwood, Hao Wu, Zhu Meng, Xi Chen, and Mark Oxborrow. Move aside pentacene: Diazapentacene doped para-terphenyl, a zero-field room-temperature maser with strong coupling for cavity quantum electrodynamics. *Advanced Materials*, page 2300441, March 2023.

[155] Alexander Sherman, Lotem Buchbinder, Siyuan Ding, and Aharon Blank. Performance analysis of diamond-based masers. *Journal of Applied Physics*, 129(14):144503, 2021.

[156] Alexander Sherman, Oleg Zgadzai, Boaz Koren, Idan Peretz, Eyal Laster, and Aharon Blank. Diamond-based microwave quantum amplifier. *Science Advances*, 8(49):eade6527, 2022.

[157] Christoph W Zollitsch, Stefan Ruloff, Yan Fett, Haakon TA Wiedemann, Rudolf Richter, Jonathan D Breeze, and Christopher WM Kay. Maser threshold characterization by resonator q-factor tuning. *Communications Physics*, 6(1):295, 2023.

[158] Daan M Arroo, Neil McN Alford, and Jonathan D Breeze. Perspective on room-temperature solid-state masers. *Applied Physics Letters*, 119(14):140502, 2021.

[159] Ananda Roy and Michel Devoret. Introduction to parametric amplification of quantum signals with josephson circuits. *Comptes Rendus Physique*, 17(7):740–755, 2016.

[160] A Jarmola, VM Acosta, K Jensen, S Chemerisov, and D Budker. Temperature-and magnetic-field-dependent longitudinal spin relaxation in nitrogen-vacancy ensembles in diamond. *Physical review letters*, 108(19):197601, 2012.

[161] Paul L Stanwix, Linh M Pham, Jeronimo R Maze, David Le Sage, Tsun Kwan Yeung, Paola Cappellaro, Philip R Hemmer, Amir Yacoby, Mikhail D Lukin, and Ronald L Walsworth. Coherence of nitrogen-vacancy electronic spin ensembles in diamond. *Physical Review B*, 82(20):201201, 2010.

[162] Alexander Savvin, Alexander Dormidonov, Evgeniya Smetanina, Vladimir Mitrokhin, Evgeniy Lipatov, Dmitriy Genin, Sergey Potanin, Alexander Yelisseyev, and Viktor Vins. Nv–diamond laser. *Nature communications*, 12(1):7118, 2021.

[163] Wern Ng, Hao Wu, and Mark Oxborrow. Quasi-continuous cooling of a microwave mode on a benchtop using hyperpolarized nv- diamond. *Applied Physics Letters*, 119(23):234001, 2021.

[164] Iulian Popa. Pulsed magnetic resonance on single defect centers in diamond. 2006.

[165] Audrius Alkauskas, Bob B Buckley, David D Awschalom, and Chris G Van de Walle. First-principles theory of the luminescence lineshape for the triplet transition in diamond nv centres. *New Journal of Physics*, 16(7):073026, 2014.

[166] William T Vetterling, William H Press, Saul A Teukolsky, and Brian P Flannery. *Numerical recipes example book (c++): The art of scientific computing*. Cambridge University Press, 2002.

[167] ME Hosea and LF Shampine. Analysis and implementation of tr-bdf2. *Applied Numerical Mathematics*, 20(1-2):21–37, 1996.

[168] Edward Mills Purcell. Spontaneous emission probabilities at radio frequencies. In *Confined electrons and photons*, pages 839–839. Springer, 1995.

[169] Vladimir Borisovich Berestetskii, Evgenii Mikhailovich Lifshitz, and Lev Petrovich Pitaevskii. *Quantum Electrodynamics: Volume 4*, volume 4. Butterworth-Heinemann, 1982.

[170] Isabel Cardoso Barbosa, Jonas Gutsche, and Artur Widera. Impact of charge conversion on nv-center relaxometry. *arXiv e-prints*, pages arXiv–2301, 2023.

[171] Shengran Lin, Changfeng Weng, Yuanjie Yang, Jiaxin Zhao, Yuhang Guo, Jian Zhang, Liren Lou, Wei Zhu, and Guanzhong Wang. Temperature-dependent coherence properties of nv ensemble in diamond up to 600 k. *Physical Review B*, 104(15):155430, 2021.

[172] X-D Chen, C-H Dong, F-W Sun, C-L Zou, J-M Cui, Z-F Han, and G-C Guo. Temperature dependent energy level shifts of nitrogen-vacancy centers in diamond. *Applied Physics Letters*, 99(16):161903, 2011.

[173] Zhi-Hui Wang and Susumu Takahashi. Spin decoherence and electron spin bath noise of a nitrogen-vacancy center in diamond. *Physical Review B*, 87(11):115122, 2013.

[174] Andrew M Edmonds, Connor A Hart, Matthew J Turner, Pierre-Olivier Colard, Jennifer M Schloss, Kevin S Olsson, Raisa Trubko, Matthew L Markham, Adam Rathmill, Ben Horne-Smith, et al. Characterisation of cvd diamond with high concentrations of nitrogen for magnetic-field sensing applications. *Materials for Quantum Technology*, 1(2):025001, 2021.

[175] Tai-Sang Ahn, Rabih O Al-Kaysi, Astrid M Müller, Katherine M Wentz, and Christopher J Bardeen. Self-absorption correction for solid-state photoluminescence quantum yields obtained from integrating sphere measurements. *Review of Scientific Instruments*, 78(8):086105, 2007.

[176] Benjamin Fortman and Susumu Takahashi. Understanding the linewidth of the esr spectrum detected by a single nv center in diamond. *The Journal of Physical Chemistry A*, 123(29):6350–6355, 2019.

[177] Andreas Gottscholl, Maximilian Wagenhöfer, Manuel Klimmer, Selina Scherbel, Christian Kasper, Valentin Baianov, Georgy V Astakhov, Vladimir Dyakonov, and Andreas Sperlich. Superradiance of spin defects in silicon carbide for maser applications. *Frontiers in Photonics*, 3:886354, 2022.

[178] Wern Ng, Yongqiang Wen, Neil Alford, and Daan M Arroo. Portable diamond maser with reduced magnetic field through orientation. *arXiv preprint arXiv:2404.05000*, 2024.

[179] R Vilaseca and R Corbalán. Lorenz chaos in optically pumped lasers. *Europhysics News*, 23(2):27–30, 1992.

[180] Wenkai Pang, Zekang Wu, Yu Xiao, and Cuimei Jiang. Chaos control and synchronization of a complex rikitake dynamo model. *Entropy*, 22(6):671, 2020.

[181] Valeria Teppati, Andrea Ferrero, and Mohamed Sayed. *Modern RF and microwave measurement techniques*. Cambridge University Press, 2013.

[182] Harald T Friis. Noise figures of radio receivers. *Proceedings of the IRE*, 32(7):419–422, 1944.

[183] H Rothe. The theory of noisy four-poles. *Transactions of the IRE Professional Group on Electron Devices*, 1(4):258–259, 1954.

[184] HA Haus, WR Atkinson, GM Branch, WB Davenport, WH Fonger, WA Harris, SW Harrison, WW McLeod, EK Stodola, and TE Talpey. Representation of noise in linear twoports. *Proceedings of the IRE*, 48(1):69–74, 1960.

[185] SW Harrison and NY Bayside. Description of the noise performance of amplifiers and receiving systems.

[186] Agilent Technologies. Fundamentals of rf and microwave noise figure measurements. 2010.

[187] V Adamian. A novel procedure for receiver noise characterization. *IEEE Trans. Instrum. Meas.*, 33(2):136–140, 1984.

[188] TJ Henry. Ire standards on methods of measuring noise in linear twoports, 1959.

[189] David B Leeson. A simple model of feedback oscillator noise spectrum. *Proceedings of the IEEE*, 54(2):329–330, 1966.

[190] Hao Chi Zhang, Shuo Liu, Xiaopeng Shen, Lin Hui Chen, Lianming Li, and Tie Jun Cui. Broadband amplification of spoof surface plasmon polaritons at microwave frequencies. *Laser & Photonics Reviews*, 9(1):83–90, 2015.

[191] Andreas Gottscholl, Maximilian Wagenhöfer, Manuel Klimmer, Selina Scherbel, Christian Kasper, Valentin Baianov, Georgy V Astakhov, Vladimir Dyakonov, and Andreas Sperlich. Superradiance of spin defects in silicon carbide for maser applications. *Frontiers in Photonics*, 3:886354, 2022.

[192] William F Koehl, Bob B Buckley, F Joseph Heremans, Greg Calusine, and David D Awschalom. Room temperature coherent control of defect spin qubits in silicon carbide. *Nature*, 479(7371):84–87, 2011.

[193] J Mossbrucker and TA Grotjohn. Determination of local crystal orientation of diamond using polarized raman spectra. *Diamond and related materials*, 5(11):1333–1343, 1996.

[194] David Schiferl, Malcolm Nicol, Joseph M Zaug, SK Sharma, TF Cooney, S-Y Wang, Thomas R Anthony, and James F Fleischer. The diamond c 13/12 c isotope raman pressure sensor system for high-temperature/pressure diamond-anvil cells with reactive samples. *Journal of Applied Physics*, 82(7):3256–3265, 1997.

[195] Andrea Mari, Thomas R Bromley, Josh Izaac, Maria Schuld, and Nathan Killoran. Transfer learning in hybrid classical-quantum neural networks. *Quantum*, 4:340, 2020.

[196] J Mallinson. One-sided fluxes–a magnetic curiosity? *IEEE Transactions on magnetics*, 9(4):678–682, 1973.

[197] Klaus Halbach. Strong rare earth cobalt quadrupoles. *IEEE Transactions on Nuclear Science*, 26(3):3882–3884, 1979.

[198] Michael CD Tayler and Dimitrios Sakellariou. Low-cost, pseudo-halbach dipole magnets for nmr. *Journal of Magnetic Resonance*, 277:143–148, 2017.

[199] Ramu Krishnan. *Permanent magnet synchronous and brushless DC motor drives*. CRC press, 2017.

[200] Paulo V Trevizoli, Jaime A Lozano, Guilherme F Peixer, and Jader R Barbosa Jr. Design of nested halbach cylinder arrays for magnetic refrigeration applications. *Journal of Magnetism and Magnetic Materials*, 395:109–122, 2015.

[201] Huijie Zheng, Georgios Chatzidrosos, Arne Wickenbrock, Lykourgos Bougas, Reinis Lazda, Andris Berzins, Florian Helmuth Gahbauer, Marcis Auzinsh, Ruvin Ferber, and Dmitry Budker. Level anti-crossing magnetometry with color centers in diamond. In *Slow Light, Fast Light, and Opto-Atomic Precision Metrology X*, volume 10119, pages 115–122. SPIE, 2017.

[202] Oleg Tretiak, Peter Blümler, and Lykourgos Bougas. Variable single-axis magnetic-field generator using permanent magnets. *AIP Advances*, 9(11), 2019.

[203] Perla Malagò, Florian Slanovc, Stefan Herzog, Stefano Lumetti, Thomas Schaden, Andrea Pellegrinetti, Mohssen Moridi, Claas Abert, Dieter Suess, and Michael Ortner. Magnetic position system design method applied to three-axis joystick motion tracking. *Sensors*, 20(23):6873, 2020.

[204] ZJ Yang, TH Johansen, H Bratsberg, G Helgesen, and AT Skjeltorp. Potential and force between a magnet and a bulk y1ba2cu3o7-δ superconductor studied by a mechanical pendulum. *Superconductor Science and Technology*, 3(12):591, 1990.